

Irreducible antiferroite electrolytes

Landgraf, V.R.

DOI

[10.4233/uuid:2d81960f-8d9b-41e4-9b49-fd49ad2474f9](https://doi.org/10.4233/uuid:2d81960f-8d9b-41e4-9b49-fd49ad2474f9)

Publication date

2025

Document Version

Final published version

Citation (APA)

Landgraf, V. R. (2025). *Irreducible antiferroite electrolytes*. [Dissertation (TU Delft), Delft University of Technology]. <https://doi.org/10.4233/uuid:2d81960f-8d9b-41e4-9b49-fd49ad2474f9>

Important note

To cite this publication, please use the final published version (if applicable).
Please check the document version above.

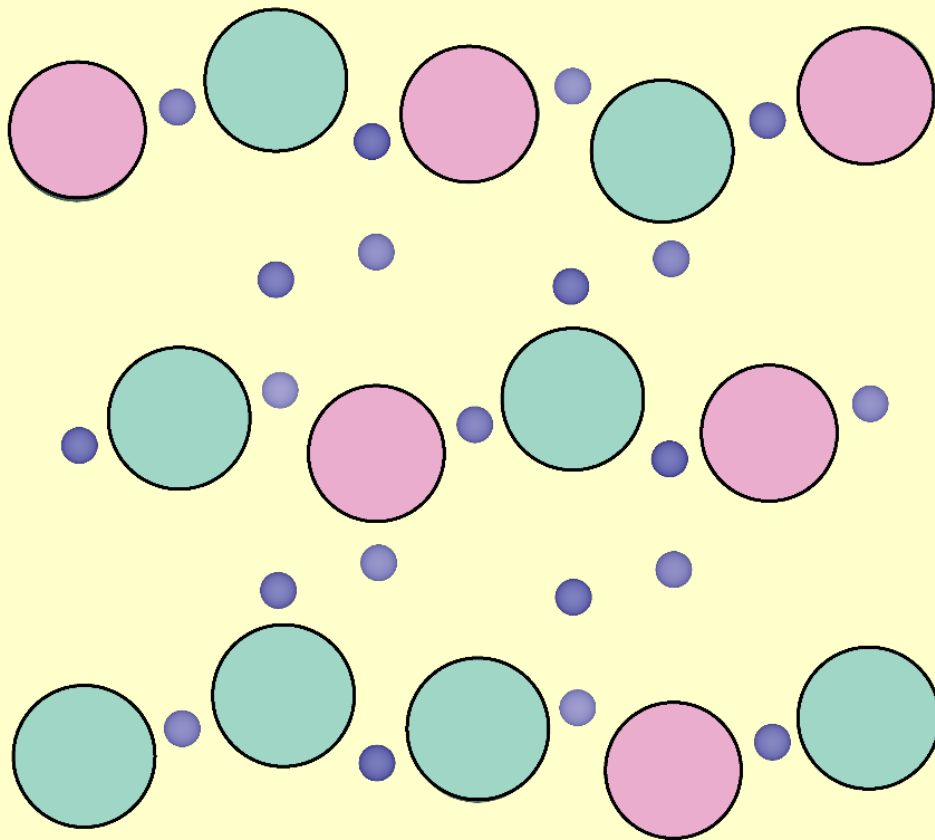
Copyright

Other than for strictly personal use, it is not permitted to download, forward or distribute the text or part of it, without the consent of the author(s) and/or copyright holder(s), unless the work is under an open content license such as Creative Commons.

Takedown policy

Please contact us and provide details if you believe this document breaches copyrights.
We will remove access to the work immediately and investigate your claim.

Irreducible antifluorite electrolytes



Victor Ruben Landgraf

Irreducible antiferroite electrolytes

Proefschrift

ter verkrijging van de graad van doctor
aan de Technische Universiteit Delft,
op gezag van de Rector Magnificus prof. dr. ir. T.H.J.J. Van der Hagen,
voorzitter van het College voor Promoties,
in het openbaar te vertedigen op 21.05.2025 .

door

Victor Ruben LANDGRAF

Master of Science in Chemistry, Imperial College London, United Kingdom,
Associate of the Royal College of Science
geboren te Brussels

Samenstelling van de promotiecommissie bestaat uit

Rector magnificus

Prof. Dr. ir. Marnix Wagemaker

Dr. Theodosios Famprikis

voorzitter

Technische Universiteit Delft, promotor

Technische Universiteit Delft, advisor

Onafhankelijke leden:

Prof. Dr. Philipp Adelhelm

Prof. Dr. Ferdinand Grozema

Prof. Dr. Saiful Islam

Dr. Yaolin Xu

Prof. Pieter Dorenbos

Humboldt Universität, Berlin

Technische Universiteit, Delft

University of Oxford

Aalto University

Technische Universiteit Delft, reservelid

Contents

1	Introduction	4
	1.1 Electrochemical stability and the fully-reduced state.....	5
	1.2 Effect of positional disorder on ion diffusion in crystalline solids.....	9
	1.3 Disordered fully reduced antiferroite-like phases.....	12
	1.4 Outline of this thesis.....	13
	References.....	15
2	Li₅NCl₂ – a fully-reduced, highly-disordered nitride-halide electrolyte for solid-state batteries with lithium-metal anodes	18
	2.1 Abstract.....	18
	2.2 Introduction.....	19
	2.3 Results and Discussion.....	20
	2.4 Conclusion.....	34
	2.5 Methods.....	34
	References.....	37
3	Disorder-mediated ionic conductivity in irreducible solid electrolytes	40
	3.1 Abstract.....	40
	3.2 Introduction.....	40
	3.3 Results and Discussion.....	41
	3.4 Conclusion.....	55
	3.5 Methods.....	56
	References.....	59

4	Compositional flexibility in irreducible antiferroite electrolytes for next generation battery anodes	64
	4.1 Abstract.....	64
	4.2 Introduction.....	65
	4.3 Results and Discussion.....	66
	4.4 Conclusion.....	78
	4.5 Methods.....	78
	References.....	81
5	High conductivity in irreducible nitridophosphide solid electrolytes	84
	5.1 Chapter Summary.....	84
	5.2 Introduction.....	84
	5.3 Results and Discussion.....	85
	5.4 Conclusion.....	93
	5.5 Methods.....	94
	References.....	96
	Appendix 1: Supporting Information for chapter 2	97
	Appendix 2: Supporting Information for chapter 3	116
	Appendix 3: Supporting Information for chapter 4	166
	Appendix 4: Supporting Information for chapter 5	189
	Summary	199
	Samenvating	201
	Acknowledgments	203
	Curriculum Vitae Victor Landgraf	204

Chapter 1: Introduction

Lithium ion (Li-ion) batteries were commercialized in 1991 and were a step-up in energy density compared to the previously known battery chemistries.¹ This leap forward in energy density enabled the progress of energy-intensive mobile electronics such as smartphones, laptops and electric vehicles over the last two decades.¹ For their tremendous impact on humanity the three main developers of the Li-ion battery chemistry M.S. Whittingham, A. Yoshino and J.B. Goodenough received the Nobel prize in Chemistry in 2019.^{2,3} Despite tremendous improvements in energy density and cost since their first commercialization, Li-ion batteries are now approaching their fundamental limits.⁴

Novel battery chemistries to enable the next step-up in energy density are currently developed.⁵ The solid-state battery is a novel type of battery that may enable the sought advancement in energy density.⁶ In solid-state batteries the liquid electrolyte is replaced by a solid ceramic and/or polymer.⁶ The projected advantages of solid-state batteries over state-of-the-art Li-ion batteries are (1) the possibility of bipolar stacking, (2) the usage of low-voltage anodes such as lithium (Li) metal or silicon (Li_xSi) and (3) increased device safety.⁶ To supersede Li-ion batteries in terms of energy density, solid-state batteries need to feature high-energy anodes such as Li metal or potentially silicon (Li_xSi).⁶⁻⁸ Moreover, solid state batteries hinge on the development of solid electrolytes that are at once highly conducting and (electro)chemically compatible with the cathode and anode active materials.⁹

Several solid phases have been developed with conductivities $> 1 \text{ mS cm}^{-1}$.¹⁰ These highly-conducting electrolytes can be broadly segregated into three chemistries: halides, oxides and sulfides.¹⁰ Within these three groups further subgroups exist such as the argyrodite and LGPS-type for sulfides and NaSICON and garnet-type for oxides.¹⁰ Representative electrochemical stability windows of the highly-conducting electrolyte types are shown in Figure 1.1. None of the known highly-conducting electrolytes ($>1 \text{ mS cm}^{-1}$) is at once electrochemically stable at the high potentials of high-energy oxide cathodes ($>3.6 \text{ V vs Li/Li}^+$) and the low potentials of high-energy anodes such as Li metal or Li_xSi (i.e. “silicon”) anodes ($\sim 0 \text{ V vs Li/Li}^+$).^{11,12} The electrochemical instability of solid electrolytes with electrodes likely leads to electrolyte decomposition at the electrolyte-electrode interfaces.^{9,11} Electrolyte decomposition at the electrode interfaces causes Li loss, formation of resistive interphases and contact loss between solid electrolyte- and electrode particles, which are all directly linked to battery degradation and failure.^{8,13}

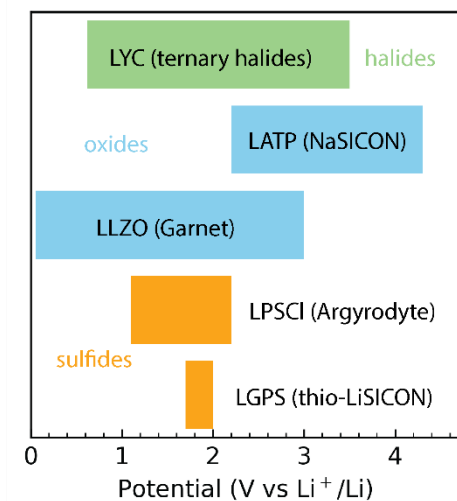


Figure 1.1 Representative calculated electrochemical stability windows of the highly conducting ($>1 \text{ mS cm}^{-1}$) solid electrolyte-groups currently known. As a representative of the ternary halides the stability window of Li_3YCl_6 (LYC) is shown. The stability windows of $\text{Li}_{1.3}\text{Al}_{0.3}\text{Ti}_{1.7}(\text{PO}_4)_3$ (LTP), $\text{Li}_7\text{La}_3\text{Zr}_2\text{O}_{12}$ (LLZO) are shown as representatives of NaSICON and garnet oxide electrolytes. The stability window of $\text{Li}_6\text{PS}_5\text{Cl}$ (LPSCI) and $\text{Li}_{10}\text{GeP}_2\text{S}_{12}$ (LGPS) are shown as representatives of argyrodite and thio-LiSICON-type sulfide electrolytes. For other representatives of the electrolyte-groups than the ones shown, the exact stability window might slightly vary. For the ternary halides for example, BrCl substitution slightly lowers the oxidation stability.^{14,15} The stability windows for LLZO, LTP and LGPS were obtained from ref 16. The ones for LYC and LPSCI from refs (14,17) respectively.

1.1 Electrochemical stability and the fully-reduced state

Lithium-garnet electrolytes are considered compatible with Li metal.¹⁸ But lithium-garnets require energy-intensive sintering processes (ref²⁰) which are difficult to scale and motivate the development of new solid electrolytes that are at once electrochemically stable against low-potential anodes and highly conductive; developing such novel phases is the focus of the present thesis.

For phases to be stable against Li metal they need to be resistant to (electro)chemical reduction. A pertinent subset of phases that are (electro)chemically stable against Li metal are *fully-reduced* phases which are *irreducible* and which are the phases explored in this thesis. The exact definition of the terms fully-reduced and irreducible will be further explored in the next section.

The focus of this thesis is on a subset of solid phases that are electrochemically stable against Li metal. Before further introducing this subset of phases the terms chemical and electrochemical stability will be explained.

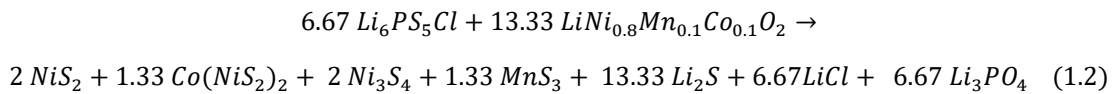
Chemical and electrochemical stability are two approaches to assess the stability of an interface. The conceptual differences between chemical and electrochemical stability will be explained on the example of a Li-argyrodite ($\text{Li}_6\text{PS}_5\text{Cl}$) phase in contact with a $\text{LiNi}_{0.8}\text{Mn}_{0.1}\text{Co}_{0.1}\text{O}_2$ (NMC) phase. But in principle, for this entire subsection, $\text{Li}_6\text{PS}_5\text{Cl}$ and NMC could be replaced by a more general phase A and phase B. The presented explanations are based on ref (11).

Chemical stability

Chemical stability means that no reaction products exist that make the general reaction expressed in equation 1.1 spontaneous (i.e. $\Delta_r G > 0$ for all possible reactions).

$$\Delta_r G = \sum c_i \Delta G_{f,i} - (a * \Delta G_{f, Li_6PS_5Cl} + b * \Delta G_{f, NMC}) \quad (1.1)$$

In equation (1.1), $\Delta G_{f, Li_6PS_5Cl}$ stands for the Gibbs free energy of formation of the Li_6PS_5Cl phase, $\Delta G_{f, NMC}$ stands for the Gibbs free energy of formation of the NMC phase. The coefficients a, b and c_i are stoichiometric factors and “i” is a possible reaction product between a*NMC and b* Li_6PS_5Cl . An example of such a possible chemical reaction for which the free energy of reaction $\Delta_r G$ can be calculated with equation (1.1) is given below in equation (1.2):



Electrochemical stability

If a Li_6PS_5Cl phase is in contact with an NMC cathode comprising an electron conducting network in the context of an electrochemical cell then the Li_6PS_5Cl phase is also in contact with a reservoir of Li^+ ions and electrons (e^-) and the phase-space of potentially possible decomposition products extends. Electrochemical stability means that no reaction products exist that make the general reaction expressed in equation 1.3 spontaneous (i.e. $\Delta_r G > 0$ for all possible reactions).

$$\Delta_r G = \sum c_i \Delta G_{f,i} - [a * \Delta G_{f, Li_6PS_5Cl} + b * \Delta G_{f, NMC} + n * (\mu_{Li^+, NMC} + \mu_{e^-, NMC})] \quad (1.3)$$

since $(\mu_{Li^+, NMC} + \mu_{e^-, NMC}) = \mu_{Li, NMC}$ equation (1.3) may be rewritten as shown in equation (1.4)

$$\Delta_r G = \sum c_i \Delta G_{f,i} - (a * \Delta G_{f, Li_6PS_5Cl} + b * \Delta G_{f, NMC} + n * \mu_{Li, NMC}) \quad (1.4)$$

where $\mu_{Li^+, NMC}$, $\mu_{e^-, NMC}$ and $\mu_{Li, NMC}$ are the chemical potentials Li^+ , electrons and of Li atoms in NMC and “n” is a stoichiometric factor (note $n < 0$ is permitted). $\mu_{Li, NMC}$ can be related to an electrode potential as follows:

$$\Phi = \frac{\mu_{Li, Li-metal} - \mu_{Li, NMC}}{e} \quad (1.5)$$

where Φ is the electrode potential of a Li-metal || NMC electrochemical cell. Equation (1.6) is equation (1.4) combined with equation (1.5) to introduce the cell potential. We can thus rephrase: electrochemical stability means that no reaction products exist that make the general reaction expressed in equation (1.6) spontaneous (i.e. $\Delta_r G > 0$ for all possible reactions).

$$\Delta_r G = \sum c_i \Delta G_{f,i} - [a * \Delta G_{f, Li_6PS_5Cl} + b * \Delta G_{f, NMC} + n * (\mu_{Li, Li-metal} - e \Phi)] \quad (1.6)$$

In summary, chemical and electrochemical stability are two approaches to assess the stability of an interface and they apply in different cases. Chemical stability applies when Li_6PS_5Cl is in contact with NMC in a context where NMC is not the active electrode material of an electrochemical cell. In a context where NMC is the active electrode material of an electrochemical cell, comprising the presence of an

electronically conducting carbon network, electrochemical stability needs to be considered to assess the stability of the interface. Figure 1.2 illustrates the above distinctions between chemical and electrochemical stability. It should be noted that the above are thermodynamic definitions of chemical and electrochemical stability. In principle, effective (electro)chemical stability can be also obtained even if exergonic decomposition reactions exist provided these decomposition reactions are kinetically inhibited.

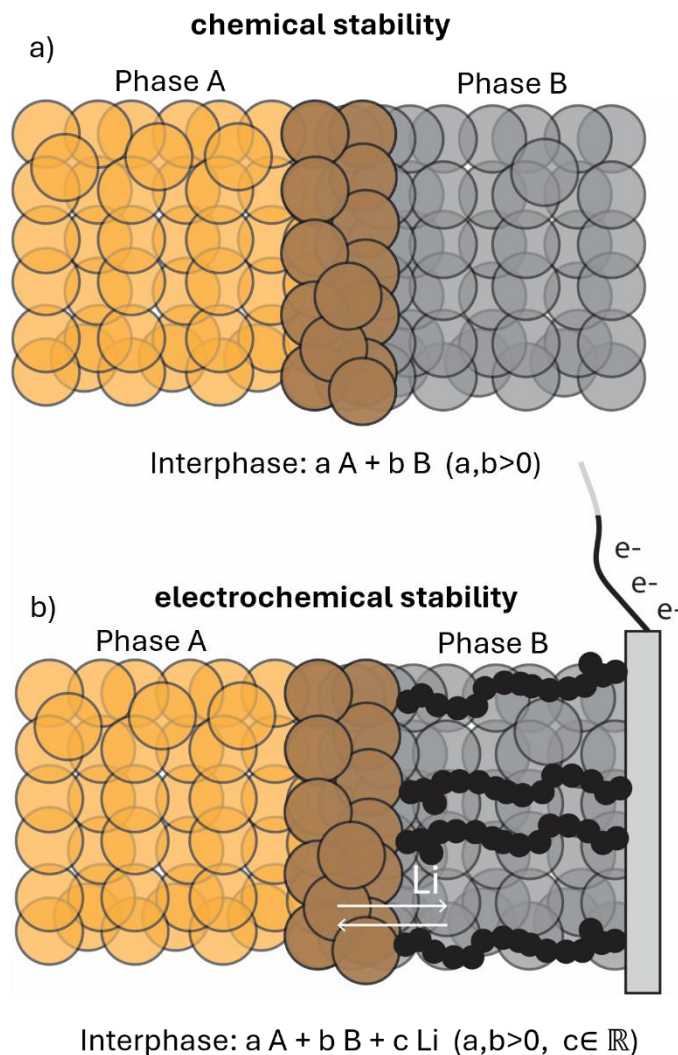


Figure 1.2. Chemical versus electrochemical stability. Yellow spheres phase A. Grey spheres phase B. Brown spheres interphase after (electro)chemical decomposition. (a) Schematic illustration of chemical decomposition of a phase A in contact with a phase B. (b) Schematic illustration of electrochemical decomposition of phase A with phase B where phase B is an active cathode material in a composite cathode featuring a carbon additive (black spheres) for electronic conductivity throughout the cathode. The Li exchange that is possible in such a case between phase B and the interphase is also shown as well as a schematic of a current collector.

In the next section a subset of phases that are (electro)chemically stable even at the low potentials of Li metal will be introduced.

The fully-reduced state and irreducible electrolytes

Following the explanation of chemical and electrochemical stability in the previous section, this section will introduce subset of phases that are (electro)chemically stable against Li metal. The highly conducting electrolytes known today, are not electrochemically stable against Li metal because they contain elements that are in oxidation states that are further reducible which in contact with highly-reducing electrodes -- such as Li metal or Li_xSi -- leads to their electrochemical reduction. For example, P in the Li-argyrodite (e.g. $\text{Li}_6\text{PS}_5\text{Cl}$) has a formal oxidation state of +5. In contact with Li metal, the Li-argyrodite decomposes and forms Li_3P , Li_2S and LiCl .¹²



The $\text{Li}_6\text{PS}_5\text{Cl}$ phase is thus reducible. In contrast to $\text{Li}_6\text{PS}_5\text{Cl}$, none of the three decomposition products above have reducible elements; P, S and Cl in Li_3P , Li_2S and LiCl have formal oxidation states of -3, -2 and -1 which are the lowest permitted oxidation states for these elements. The three decomposition products are thus fully-reduced and inert to further reductive decomposition —that is they are irreducible.

More formally, fully reduced (Li-)phases have Li as their only cation and all anions in their lowest permitted oxidation state. Examples of fully reduced Li-phases are LiCl , Li_2S , LiF , LiBr , LiI , Li_3N , Li_3P , Li_2Se , Li_3OCl , [...]. A benefit of fully reduced and thus irreducible phases is that no interphase of decomposition products forms when they are in contact with highly-reducing electrodes which eliminates performance impediments associated with interphase formation. While many fully-reduced phases are known, few exhibit ionic conductivities beyond 0.01 mS cm^{-1} .²¹ Exceptions are the newly-discovered disordered antiperovskite-like phases —investigated and developed in the body of this thesis—and Li_3N .^{22–25} Note that high conductivities ($>1 \text{ mS cm}^{-1}$) have been reported for the antiperovskite Li_3OX ($\text{X}=\text{Cl}, \text{Br}$) phases but could not be substantiated.²⁶

Li_3N has been investigated in the last four decades.²⁷ Conductivities of $> 1 \text{ mS cm}^{-1}$ have been reported for Li_3N but were obtained on single crystals and along specific crystallographic axes.²⁸ It was shown also that these highly-conducting Li_3N samples were likely contaminated with hydrogen.²⁹ Polycrystalline $\beta\text{-Li}_3\text{N}$ and $\alpha\text{-Li}_3\text{N}$ samples pressed to pellets reproducibly yield conductivities of $\sim 0.5 \text{ mS cm}^{-1}$.^{30–33} Li_3N has a low oxidation limit (0.8 V, ref²⁴). Thus, Li_3N cannot be used in contact with high-energy cathode materials so that its main application is as anolyte in bilayer separator setups which are separators that consists of two solid electrolyte layers, one layer – the anolyte or ‘artificial SEI’– facing the anode and the second layer facing the cathode.^{19,34–36}

Sufficient conductivity and stability, however, are not the only suitability criteria of anolytes. Mechanical and microstructural properties of solid electrolytes play a key role, for instance in dendrite formation of metal electrodes.^{37,38} Chemical compatibilities of anolytes with the paired catholytes also need to be considered.³⁹ Additionally, the oxidation limit of anolytes needs to be considered; for example, the operation window of Li_xSi anodes ranges from 0.01 V to 1.1 V.⁸ Due to the low oxidation limit of Li_3N (0.8 V, ref²⁴), Li_3N would be inert to reduction but not inert to oxidation when in contact with Li_xSi anodes. All of the above, motivates the search for further fully-reduced electrolytes beyond Li_3N . In the present thesis a novel class of highly-conducting irreducible electrolytes has been developed based on the antiperovskite structure with a focus on Li diffusion mechanism and conductivity on these phases. In the following sections the general mechanism by which ion diffusion occurs in solids will be introduced followed by an

introduction of the structure and diffusion paths in the fully-reduced phases which are explored in this thesis.

1.2 Effect of positional disorder on ion diffusion in crystalline solids

A brief introduction to ion diffusion

Experiments show that ion-conductivity and diffusivity in solids are temperature dependent and their temperature dependence obeys Arrhenius' law; ^{22,39,40} this suggests that ion diffusion occurs through a series of thermally activated events.⁴⁰ A widely adopted model for ion diffusion that explains this temperature dependence is the hopping model. Within a crystal, ions majorly occupy the energetically most favourable positions, that is their sites. Within the hopping model diffusion requires an ion to 'hop' between sites.⁴⁰ These ion hops necessitate ions to overcome an energy barrier since a hop entails that the ion will move through positions between sites which are by definition energetically less favourable.⁴⁰ In several solids diffusion between sites is energetically impeded by steric bottlenecks.^{41,42} Steric bottlenecks are positions along the diffusion path where the diffusing ion is too close to the average positions of peripheral ions (that is non-diffusing ions) which is energetically unfavourable.^{41,42} The above description of the hopping model for ion diffusion are illustrated in figures 1.3a and 1.3b.

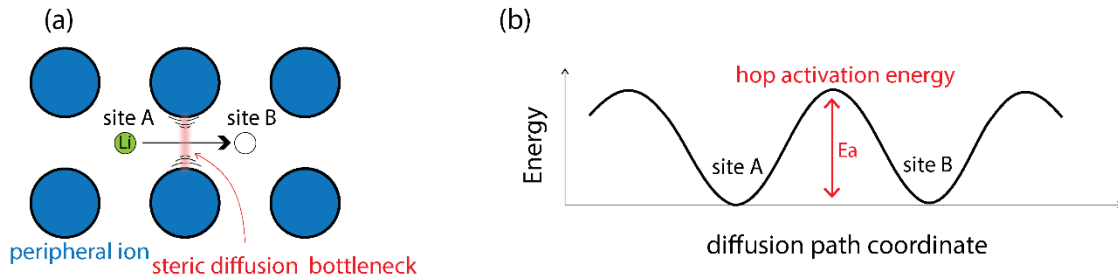


Figure 1.3. Schematic illustration of ion hopping. (a) schematic illustration of Li as the mobile ion hopping from site A to site B through a steric bottleneck highlighted in red where the diffusing ion is too close to the peripheral ions which is energetically unfavourable. (b) Schematic of the energy of the Li-ion as it diffuses through this path from site A to site B.

Ion hops are thus thermally activated processes and have an activation energy associated with them. The hop frequency between two sites thus depends on the hop's activation energy and an attempt frequency ν_0 which typically assumes values of 10^{11} - 10^{13} Hz in crystalline solids.⁴³

$$\nu_{A \rightarrow B} = \nu_0 * \exp\left(\frac{-E_{a,A \rightarrow B}}{kT}\right) \quad (1.8)$$

The hop frequency ($\nu_{A \rightarrow B}$) between sites may be obtained from molecular dynamics simulations by counting the hops between two sites. Given the hop frequency and provided the attempt frequency is

known (or a reasonable approximate) – the average activation energy for specific ion hops ($E_{a,A \rightarrow B}$) can be calculated:

$$E_{a,A \rightarrow B} = -k_b T * \ln\left(\frac{v_{A \rightarrow B}}{v_0}\right) \quad (1.9)$$

A reasonable approximation for the average attempt frequency may also be obtained from MD simulations by studying the Li oscillations within Li sites. ⁴⁴

The overall activation energy for macroscopic bulk diffusion of Li ions will be close to the largest hop activation energy across percolating paths through a crystallite. ⁴⁰ Based on the hopping model the following expression may be derived for ion conductivity (ref. ⁴⁰):

$$\sigma = \frac{fc(ze)^2 a^2}{6H_R k_b T} v_0 * \exp\left(\frac{-E_a}{k_b T}\right) \quad (1.10)$$

Where “a” is the distance between sites, f is a correlation factor capturing the correlation between the hops made by individual ions and H_R is Haven’s ratio capturing the correlation of the hops of different ions with respect to each other, (ze) is the charge on the diffusion ion, c is the concentration of the diffusing ion, k_b is Boltzmann’s constant, T is the temperature in Kelvin, and E_a is activation energy for macroscopic diffusion.

Inspection of equation (1.10) shows that one viable strategy to improve ion diffusivity and conductivity is thus to lower the activation energy for macroscopic diffusion which may be achieved by lowering the hop activation energy for specific ion hops. One strategy that enables the lowering of the activation energy for macroscopic diffusion is to introduce positional disorder into crystal structures, – as will be explained in the next section.

The effect of positional disorder on ion diffusivity

Several types of disorder exist in crystalline solids, compositional, orientational or displacive disorder, [...], to name a few. ⁴⁵ In this section the term ‘disorder’ will be used to refer to positional disorder which comprises partial and shared occupancy on crystallographic sites. ⁴⁵ Disorder in ceramic solid electrolytes is often correlated with high conductivity. ^{23,46,47} Positional disorder may be obtained in two ways: (1) increasing the number of elements in a phase so that several elements occupy the same site (e.g ref ⁴⁶) or (2) modifying the synthesis so that ions present in the original phase are forced to share sites (e.g. ref ⁴⁷). Both variants are illustrated in Figure 1.5. Figure 1.5a shows an array of tetrahedral Li sites with an ordered arrangement of N and S. Figure 1.5b shows the case where disorder was introduced by partial Cl_S-substitution. Figure 1.5c shows a variant of the second disordering case, where disorder was introduced by disordering the S and N anion arrangement compared to Figure 1.5a.

The general mechanism behind disorder-induced conductivity enhancements is a perturbation of the potential energy landscape for Li diffusion, that is the degeneracy of site energies and barrier energies is broken^{23,48} For instance, in the ordered case in Figure 1.4a, only one type of tetrahedral Li-sites exist with 2N and 2S at the corners. These sites which are all of the same type are also all connected by the same Li-hop steric bottleneck consisting of N and S. It follows that in the ordered case in Figure 1.4a only one type of jump with one associated hop activation energy exists. Figures 1.4b and 1.4c schematically illustrate

how disordering introduces new site types and new types of diffusion-bottlenecks that all have different hop activation energies associated with them.

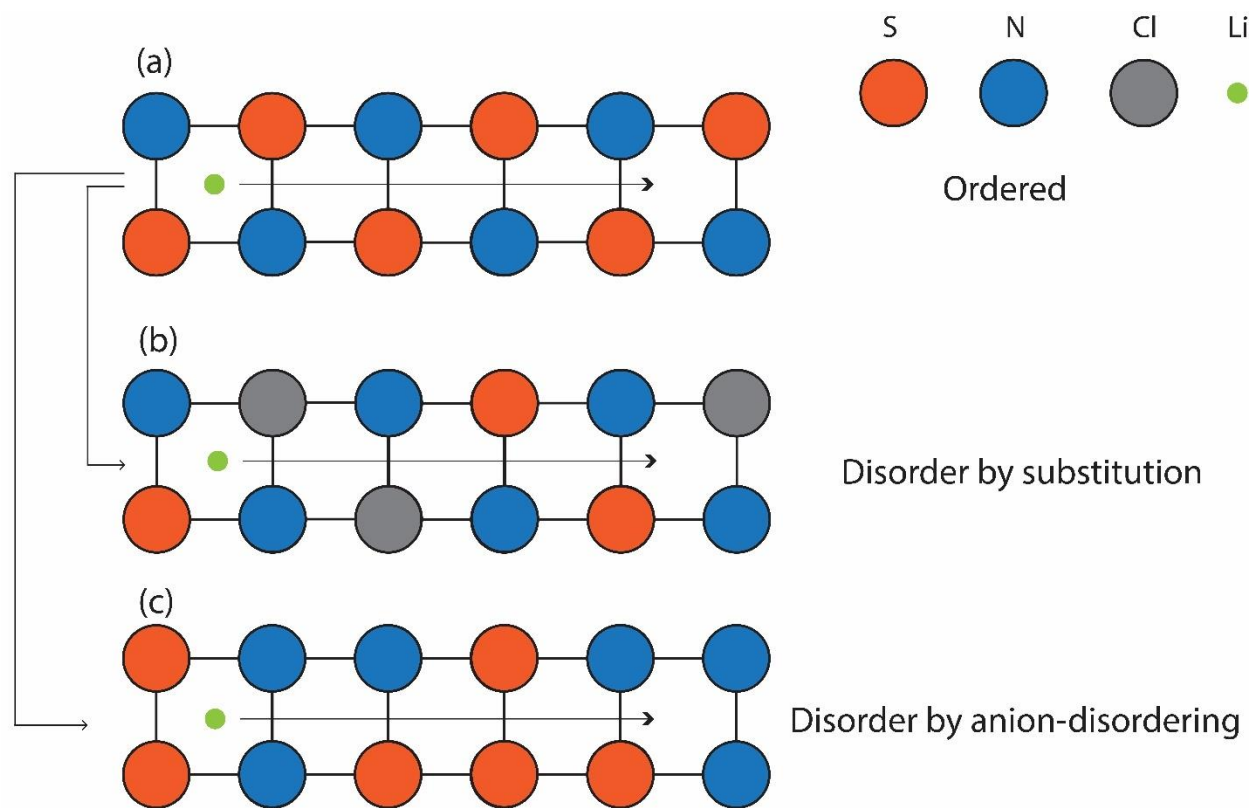


Figure 1.4 Schematic illustration of three 1D arrays of tetrahedral Li sites with the large spheres representing anions and the small sphere representing a Li cation. (a) 1D array of tetrahedral Li sites with an ordered anionic framework. (b) 1D array of tetrahedral Li sites with disorder introduced by partial ClS substitution. (c) 1D array of tetrahedral Li sites with disorder introduced by shuffling the arrangement of the anions in (a).

It follows that in disordered materials a distribution of hop activation energies exists instead of few discrete hop activation energies in ordered phases allowing for lower hop activation energies than exist in the ordered counterpart, schematically illustrated in Figure 1.5. In the event that percolating paths of these jump types with low activation energies exist, faster diffusion can be obtained in disordered phases compared to the ordered counterpart.^{23,46} The diffusion paths in a phase and their respective energy thresholds can be analysed by building percolation-energy diagrams. An example of a percolation-energy diagram is shown in Figure 1.5b. The y-axis in energy percolation diagrams shows how many Li sites are connected in percolating networks where no ion jump has an activation energy higher than the threshold on the x axis. Percolation energy diagrams enable to see whether disordering introduces sufficient low-activation-energy ion hops for percolating paths at lower energy thresholds compared to the ordered case. In the illustrative example of a percolation energy diagram in Figure 1.5b, the disordering would indeed provide percolating paths at lower energy thresholds than the ordered case as can be seen from the earlier onset of the percolation-energy trace of the disordered phase. In the next section the antifluorite structure of the fully-reduced phases investigated in this thesis will be introduced.

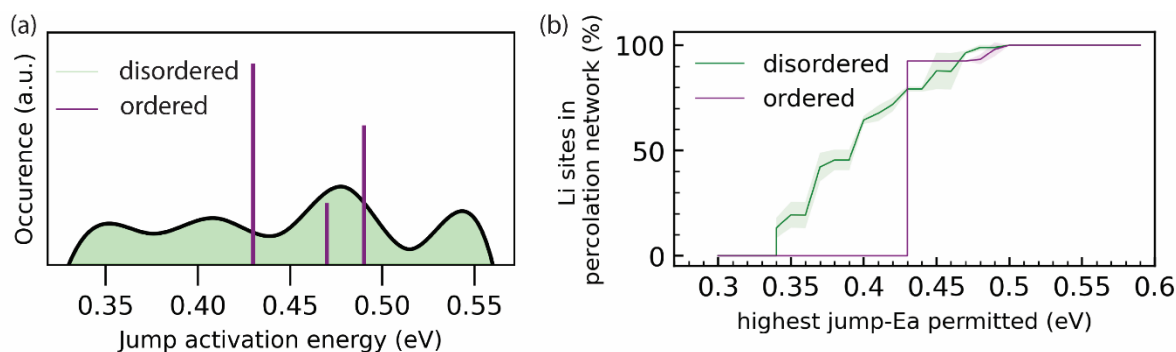


Figure 1.5. Effect of disordering on Li diffusion. (a) Schematic illustration of the distribution of Li jump activation energies in disordered phases compared to the few discrete jump activation energies in ordered phases. (b) Example of a percolation energy diagram for a disordered and ordered phases featuring the respective manifold of Li-jump activation energies activation energies shown in (a).

1.3 Disordered fully reduced antiferite-like phases

The fully reduced phases that are newly-reported in this thesis are all fully reduced antiferite-like phases. In this section the antiferite and antiferite-like crystal structures will be presented.

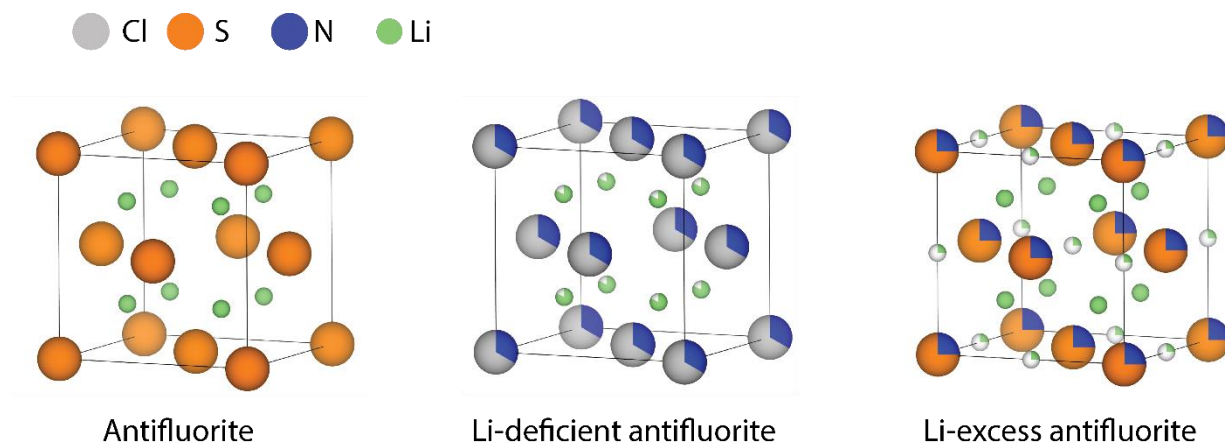


Figure 1.6. From left to right: representative unit cells of an antiferite, Li-deficient antiferite and Li-excess antiferite phase.

The antiferite structure is an archetypical crystal structure with the $Fm-3m$ space group. The Antiferite structure characterized by a face centred cubic arrangement of anions. A face centred cubic arrangement of anions creates two tetrahedral and one octahedral interstitial per anion. In the archetypical antiferite structure the tetrahedral interstitials are fully occupied leading to a cation/anion ratio of 2. Li-deficient antiferite phases are characterized by a cation/anion ratio < 2 with partially depleted tetrahedral positions. Li-excess antiferite phases are characterized by a cation/anion ratio > 2 with fully-occupied tetrahedral positions and partially occupied octahedral positions. Figure 1.3 shows the unit cells of Li_2S , Li_5NCl_2 and Li_9S_3N (refs ^{23,24,39}) as examples for antiferite, Li-deficient and Li-excess antiferite,

respectively. Both Li-excess and Li-deficient antiferite phases can be referred to as *antiferite-like* phases but in some scientific literature they are also simply referred to as *antiferite* phases.^{22,25}

In antiferite-like phases Li diffusion occurs either via ion hops between tetrahedral sites (tet-tet) or ion hops between octahedral and tetrahedral sites (tet->oct). Hops between tetrahedra occur through linear bottlenecks consisting of two anions while hops between octahedra occur via triangular bottlenecks consisting of three anions as shown in Figure 1.7.

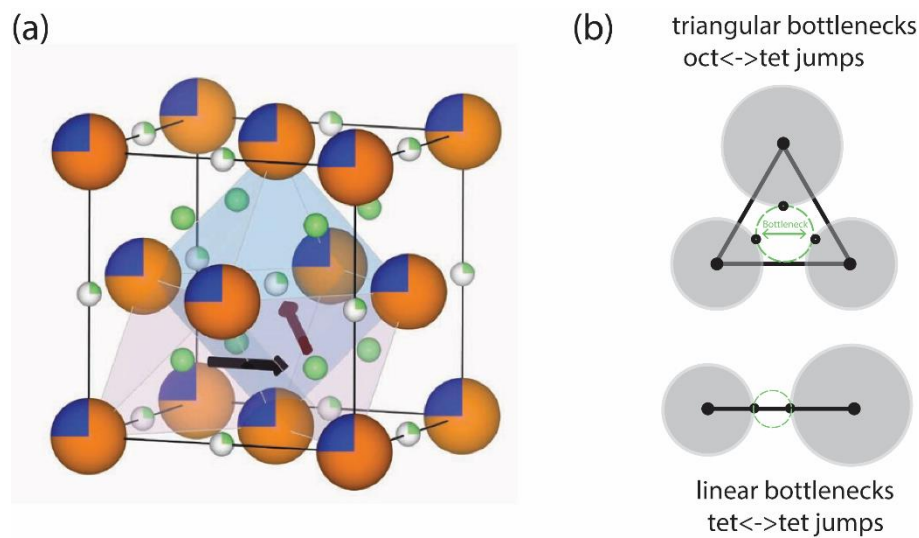


Figure 1.7 Lidiffusion in fully-reduced antiferite-like phases. (a) Unit cell of a Li-excess antiferite phase. The pink highlighting shows two tetrahedral 8c Li-site, the blue highlighting shows octahedral 4b Li-site. The arrows indicate the possible Li-hops in these phases. Hops from one tetrahedron to another tetrahedron are possible (tet-tet) and hops from a tetrahedron to an octahedron (and vice versa of course, tet->oct). Tet-tet hops occur through linear bottlenecks consisting of two anions and tet->oct hops occur through triangular bottlenecks consisting of three anions. (b) Schematic illustrations of the steric diffusion bottlenecks for tet-tet and oct->tet Li jumps. The grey spheres represent anions. The green circle indicates the diameter of the largest spherical particle that fits through this steric bottleneck. The diameter of this sphere is the bottleneck diameter.

1.4 Outline of this thesis

The main objective of the studies presented in the following 4 chapters was to identify new fully-reduced phases and to better understand Li-diffusion in these phases to optimize their conductivity combining experiments and density functional theory (DFT) calculations. At the beginning of the work on this thesis, the highest-conducting fully-reduced antiferite-like phase had a conductivity of $1 \cdot 10^{-3}$ mS cm⁻¹ which was the nitride-halide phase that is also investigated in Chapter 2.⁴⁹ The work presented in this thesis demonstrates a large compositional modifiability of this phase, S²⁻, Br⁻ and P³⁻ can additionally be introduced on the Wyckoff 4a anion-site (see Chapters 3,4,5). Through the work in this thesis the conductivity of fully-reduced antiferite phases could be improved by 3 orders of magnitude and the mechanism enabling this was investigated.

Chapter 2: In this chapter we revisit the fully-reduced antifluorite-like Li_5NCl_2 phase which had been previously discovered. Combining DFT computations and experiments we found that the disordering of the Cl and N anions inflicts a large distribution of hop activation energies for Li-ion hops. This distribution of hop activation energies leads to diffusion with different energy thresholds at different length-scales and may be the origin of different activation energies obtained from NMR-line narrowing measurements and EIS spectroscopy. Furthermore, we reinvestigated the oxidation limit of the Li_5NCl_2 phase which had previously been reported to be at 2 V (vs Li). We found computationally and experimentally that the oxidation limit of the Li_5NCl_2 phase is around ~ 0.6 V (vs Li). Finally, we computationally investigated the driving force for chemical reactions between Li_5NCl_2 and other common solid electrolytes including sulfides, oxides and halides which is relevant when Li_5NCl_2 is considered as an anolyte in bilayer separators.

Chapter 3: In this chapter we report on the discovery a new family of *irreducible* (i.e. *fully reduced*) electrolytes by mechanochemically dissolving lithium nitride into the Li_2S antifluorite structure, yielding highly conducting crystalline Li-excess $\text{Li}_{2+x}\text{S}_{1-x}\text{N}_x$ ($0 < x < \sim 0.55$) phases reaching > 0.2 mS cm^{-1} at ambient temperatures. Combining impedance spectroscopy experiments and *ab initio* density functional theory calculations we clarify the mechanism by which the disordering of the sulfide and nitride ions in the anion sublattice boosts ionic conductivity in $\text{Li}_{2+x}\text{S}_{1-x}\text{N}_x$ phases by a factor 10^5 compared to the Li_2S host structure. This advance is achieved through a novel theoretical framework, leveraging percolation analysis with local-environment-specific activation energies and is widely applicable to disordered ion conductors. The same methodology allows us to rationalize how increasing nitrogen content in $\text{Li}_{2+x}\text{S}_{1-x}\text{N}_x$ antifluorite-like samples leads to both increased ionic conductivity and lower conductivity-activation energy.

Chapter 4: In this chapter we discover a solid solution of Li-deficient antifluorite phases $\text{Li}_{1+2x}\text{Cl}_{1-x}\text{N}_x$ ($0.33 < x < \sim 0.5$) that exists on the Li_3N -LiCl tieline. The Li_5NCl_2 and the $\text{Li}_9\text{N}_2\text{Cl}_3$ phases that were previously reported are part of this solid solution. Furthermore we investigate why the conductivity of the newly-discovered $\text{Li}_{1+2x}\text{Cl}_{1-x}\text{N}_x$ ($0.33 < x < \sim 0.5$) phases is 5 orders of magnitude higher than that of the structurally related LiCl phase. Additionally, we show that increased metastability lowers the oxidation limit of fully-reduced antifluorite phases. Finally, thus far only fully-reduced antifluorite phases with at most 2 anions on the anion site were synthesized and investigated. In this chapter the compositional flexibility of the fully-reduced antifluorite phases is demonstrated and phases with up to four anions (N^{3-} , Cl^- , Br^- , S^{2-}) on the anion site were synthesized for the first time in the context of a systematic investigation of the $\text{Li}_{1.9+0.55y}\text{Cl}_{0.55(1-y-z)}\text{S}_{0.55y}\text{Br}_{0.55z}\text{N}_{0.45}$ phase space.

Chapter 5 : In this chapter we experimentally demonstrate that N_p substitutions can be obtained on irreducible Li-excess antifluorite $\text{Li}_{2+x}\text{S}_{1-x}\text{P}_x$ phases: we successfully synthesized antifluorite $\text{Li}_{2.6}\text{S}_{0.4}\text{P}_{0.6}$, $\text{Li}_{2.6}\text{S}_{0.4}\text{P}_{0.35}\text{N}_{0.15}$ and $\text{Li}_{2.6}\text{S}_{0.4}\text{P}_{0.35}\text{N}_{0.25}$. $\text{Li}_{2.6}\text{S}_{0.4}\text{P}_{0.35}\text{N}_{0.25}$ has a conductivity of ~ 0.75 mS and is thus, at the time of writing, the highest-conducting irreducible solid electrolyte reported. Computationally we demonstrate that N_p substitutions increase the void space in steric diffusion bottlenecks due to the smaller ionic radius of N^{3-} compared to P^{3-} ions which correlates with facilitated Li diffusion.

1.5 References

- (1) Whittingham, M. S. History, Evolution, and Future Status of Energy Storage. *Proc. IEEE* **2012**, *100* (Special Centennial Issue), 1518–1534.
- (2) Whittingham, M. S.; Yoshino, A. Lithium-Ion Batteries. *R. Swedish Acad. Sci.* **2019**.
- (3) Hu, Y.-S.; Lu, Y. 2019 Nobel Prize for the Li-Ion Batteries and New Opportunities and Challenges in Na-Ion Batteries. *ACS Energy Letters*. ACS Publications 2019, pp 2689–2690.
- (4) Berg, E. J.; Villevieille, C.; Streich, D.; Trabesinger, S.; Novák, P. Rechargeable Batteries: Grasping for the Limits of Chemistry. *J. Electrochem. Soc.* **2015**, *162* (14), A2468–A2475.
- (5) Luntz, A. Beyond Lithium Ion Batteries. *The journal of physical chemistry letters*. ACS Publications 2015, pp 300–301.
- (6) Janek, J.; Zeier, W. G. Challenges in Speeding up Solid-State Battery Development. *Nat. Energy* **2023**, *8* (3), 230–240.
- (7) Janek, J.; Zeier, W. G. A Solid Future for Battery Development. *Nat. Energy* **2016**, *1* (9), 1–4.
- (8) Huo, H.; Janek, J. Silicon as Emerging Anode in Solid-State Batteries. *ACS Energy Lett.* **2022**, *7* (11), 4005–4016.
- (9) Famprakis, T.; Canepa, P.; Dawson, J. A.; Islam, M. S.; Masquelier, C. Fundamentals of Inorganic Solid-State Electrolytes for Batteries. *Nat. Mater.* **2019**, *18*, 1278–1291.
- (10) Jun, K.; Chen, Y.; Wei, G.; Yang, X.; Ceder, G. Diffusion Mechanisms of Fast Lithium-Ion Conductors. *Nat. Rev. Mater.* **2024**, 1–19.
- (11) Zhu, Y.; He, X.; Mo, Y. First Principles Study on Electrochemical and Chemical Stability of Solid Electrolyte-Electrode Interfaces in All-Solid-State Li-Ion Batteries. *J. Mater. Chem. A* **2016**, *4* (9), 3253–3266.
- (12) Schwietert, T. K.; Arszewska, V. A.; Wang, C.; Yu, C.; Vasileiadis, A.; J Klerk, N. J.; Hageman, J.; Hupfer, T.; Kerkamm, I.; Xu, Y.; Maas, E.; Kelder, E. M.; Ganapathy, S.; Wagemaker, M. Clarifying the Relationship between Redox Activity and Electrochemical Stability in Solid Electrolytes. *Nat. Mater.* **2020**, *19* (4), 428–435.
- (13) Zaman, W.; Hatzell, K. B. Processing and Manufacturing of next Generation Lithium-Based All Solid-State Batteries. *Curr. Opin. Solid State Mater. Sci.* **2022**, *26* (4), 101003.
- (14) Wang, S.; Bai, Q.; Nolan, A. M.; Liu, Y.; Gong, S.; Sun, Q.; Mo, Y. Lithium Chlorides and Bromides as Promising Solid-State Chemistries for Fast Ion Conductors with Good Electrochemical Stability. *Angew. Chemie - Int. Ed.* **2019**, *58* (24), 8039–8043.
- (15) van der Maas, E.; Zhao, W.; Cheng, Z.; Famprakis, T.; Thijs, M.; Parnell, S. R.; Ganapathy, S.; Wagemaker, M. Investigation of Structure, Ionic Conductivity, and Electrochemical Stability of Halogen Substitution in Solid-State Ion Conductor Li₃YBr_xCl_{6-x}. *J. Phys. Chem. C* **2023**, *127* (1), 125–132.
- (16) Zhu, Y.; He, X.; Mo, Y. Origin of Outstanding Stability in the Lithium Solid Electrolyte Materials: Insights from Thermodynamic Analyses Based on First-Principles Calculations. *ACS Appl. Mater. Interfaces* **2015**, *7* (42), 23685–23693.
- (17) Schwietert, T. K.; Arszewska, V. A.; Wang, C.; Yu, C.; Vasileiadis, A.; de Klerk, N. J. J.; Hageman, J.; Hupfer, T.; Kerkamm, I.; Xu, Y. Clarifying the Relationship between Redox Activity and Electrochemical Stability in Solid Electrolytes. *Nat. Mater.* **2020**, *19* (4), 428–435.
- (18) Wang, C.; Fu, K.; Kammampata, S. P.; McOwen, D. W.; Samson, A. J.; Zhang, L.; Hitz, G. T.; Nolan, A. M.; Wachsman, E. D.; Mo, Y. Garnet-Type Solid-State Electrolytes: Materials, Interfaces, and Batteries. *Chem. Rev.* **2020**, *120* (10), 4257–4300.
- (19) Xu, H.; Li, Y.; Zhou, A.; Wu, N.; Xin, S.; Li, Z.; Goodenough, J. B. Li₃N-Modified Garnet Electrolyte for All-Solid-State Lithium Metal Batteries Operated at 40 °C. *Nano Lett.* **2018**, *18* (11), 7414–7418.
- (20) Allen, J. L.; Wolfenstine, J.; Rangasamy, E.; Sakamoto, J. Effect of Substitution (Ta, Al, Ga) on the Conductivity of Li₇La₃Zr₂O₁₂. *J. Power Sources* **2012**, *206*, 315–319.

- (21) Park, S.; Chaudhary, R.; Han, S. A.; Qutaish, H.; Moon, J.; Park, M.-S.; Kim, J. H. Ionic Conductivity and Mechanical Properties of the Solid Electrolyte Interphase in Lithium Metal Batteries. *ENERGY Mater.* **2023**, *3* (1).
- (22) Szczuka, C.; Karasulu, B.; Groh, M. F.; Sayed, F. N.; Sherman, T. J.; Bocarsly, J. D.; Vema, S.; Menkin, S.; Emge, S. P.; Morris, A. J.; Grey, C. P. Forced Disorder in the Solid Solution $\text{Li}_3\text{P-Li}_2\text{S}$: A New Class of Fully Reduced Solid Electrolytes for Lithium Metal Anodes. *J. Am. Chem. Soc.* **2022**, *144* (36), 16350–16365.
- (23) Landgraf, V.; Tu, M.; Zhao, W.; Lavrinenko, A.; Cheng, Z.; Canals, J.; de Leeuw, J.; Ganapathy, S.; Vasileiadis, A.; Wagemaker, M. Disorder-Mediated Ionic Conductivity in Irreducible Solid Electrolytes. **2024**.
- (24) Landgraf, V.; Tu, M.; Cheng, Z.; Vasileiadis, A.; Wagemaker, M.; Famprikis, T. Compositional Flexibility in Irreducible Antifluorite Electrolytes for Next-Generation Battery Anodes. **2024**.
- (25) Yu, P.; Zhang, H.; Hussain, F.; Luo, J.; Tang, W.; Lei, J.; Gao, L.; Butenko, D.; Wang, C.; Zhu, J.; Yin, W.; Zhang, H.; Han, S.; Zou, R.; Chen, W.; Zhao, Y.; Xia, W.; Sun, X. Lithium Metal-Compatible Antifluorite Electrolytes for Solid-State Batteries. *J. Am. Chem. Soc.* **2024**.
- (26) Zheng, J.; Perry, B.; Wu, Y. Antiperovskite Superionic Conductors: A Critical Review. *ACS Mater. Au* **2021**, *1* (2), 92–106.
- (27) Alpen, U. v. Li_3N : A Promising Li Ionic Conductor. *J. Solid State Chem.* **1979**, *29* (3), 379–392.
- (28) You, A.; Be, M. A. Y.; In, I. Ionic Conductivity in Li_3N Single Crystals. **2014**, *621* (August 2008), 10–13.
- (29) Lapp, T.; Skaarup, S.; Hooper, A. Ionic Conductivity of Pure and Doped Li_3N . *Solid State Ionics* **1983**, *11* (2), 97–103.
- (30) Rea, J. R.; Foster, D. L.; Mallory, P. R.; Co. Inc. High Ionic Conductivity in Densified Polycrystalline Lithium Nitride. *Mater. Res. Bull.* **1979**, *14* (6), 841–846.
- (31) Xu, X.; Du, G.; Cui, C.; Liang, J.; Zeng, C.; Wang, S.; Ma, Y.; Li, H. Stabilizing the Halide Solid Electrolyte to Lithium by a $\beta\text{-Li}_3\text{N}$ Interfacial Layer. *ACS Appl. Mater. Interfaces* **2022**, *14* (35), 39951–39958.
- (32) Boukamp, B. A.; Huggins, R. A. Fast Ionic Conductivity in Lithium Nitride. *Mater. Res. Bull.* **1978**, *13* (1), 23–32.
- (33) Li, W.; Wu, G.; Araújo, C. M.; Scheicher, R. H.; Blomqvist, A.; Ahuja, R.; Xiong, Z.; Feng, Y.; Chen, P. Li⁺ Ion Conductivity and Diffusion Mechanism in $\alpha\text{-Li}_3\text{N}$ and $\beta\text{-Li}_3\text{N}$. *Energy Environ. Sci.* **2010**, *3* (10), 1524–1530.
- (34) Xu, X.; Du, G.; Cui, C.; Liang, J.; Zeng, C.; Wang, S.; Ma, Y.; Li, H. Stabilizing the Halide Solid Electrolyte to Lithium by a $\beta\text{-Li}_3\text{N}$ Interfacial Layer. *ACS Appl. Mater. Interfaces* **2022**, *14* (35), 39951–39958.
- (35) Yang, M.; Yang, K.; Wu, Y.; Wang, Z.; Ma, T.; Wu, D.; Yang, L.; Xu, J.; Lu, P.; Peng, J. Dendrite-Free All-Solid-State Lithium Metal Batteries by In Situ Phase Transformation of the Soft Carbon– Li_3N Interface Layer. *ACS Nano* **2024**, *18* (26), 16842–16852.
- (36) Kizilaslan, A.; Akbulut, H. Assembling All-Solid-State Lithium–Sulfur Batteries with Li_3N -Protected Anodes. *Chempluschem* **2019**, *84* (2), 183–189.
- (37) Krauskopf, T.; Richter, F. H.; Zeier, W. G.; Janek, J. Physicochemical Concepts of the Lithium Metal Anode in Solid-State Batteries. *Chem. Rev.* **2020**, *120* (15), 7745–7794.
- (38) Hatzell, K. B.; Chen, X. C.; Cobb, C. L.; Dasgupta, N. P.; Dixit, M. B.; Marbella, L. E.; McDowell, M. T.; Mukherjee, P. P.; Verma, A.; Viswanathan, V.; Westover, A. S.; Zeier, W. G. Challenges in Lithium Metal Anodes for Solid-State Batteries. **2020**.
- (39) Landgraf, V.; Famprikis, T.; de Leeuw, J.; Bannenberg, L. J.; Ganapathy, S.; Wagemaker, M. Li_5NCl_2 : A Fully-Reduced, Highly-Disordered Nitride-Halide Electrolyte for Solid-State Batteries with Lithium-Metal Anodes. *ACS Appl. Energy Mater.* **2023**, *6* (3), 1661–1672.
- (40) Tilley, R. J. D. *Defects in Solids*; John Wiley & Sons, 2008.
- (41) West, A. R. *Solid State Chemistry and Its Applications*; John Wiley & Sons, 2022.
- (42) Bruce, P. G. *Solid State Electrochemistry*; Cambridge University Press, 1997.

- (43) Van der Ven, A.; Ceder, G.; Asta, M.; Tepesch, P. D. First-Principles Theory of Ionic Diffusion with Nondilute Carriers. *Phys. Rev. B* **2001**, *64* (18), 184307.
- (44) De Klerk, N. J. J.; Van Der Maas, E.; Wagemaker, M. Analysis of Diffusion in Solid-State Electrolytes through MD Simulations, Improvement of the Li-Ion Conductivity in β -Li3PS4 as an Example. *ACS Appl. energy Mater.* **2018**, *1* (7), 3230–3242.
- (45) Parsonage, N. G.; Staveley, L. A. K. Disorder in Crystals. *Clarendon Press*, **1978**.
- (46) Zeng, Y.; Ouyang, B.; Liu, J.; Byeon, Y.-W.; Cai, Z.; Miara, L. J.; Wang, Y.; Ceder, G. High-Entropy Mechanism to Boost Ionic Conductivity. *Science (80-.)*. **2022**, *378* (6626), 1320–1324.
- (47) Morgan, B. J. Mechanistic Origin of Superionic Lithium Diffusion in Anion-Disordered Li6PS5X Argyrodites. *Chem. Mater.* **2021**, *33* (6), 2004–2018.
- (48) Zeng, Y.; Ouyang, B.; Liu, J.; Byeon, Y. W.; Cai, Z.; Miara, L. J.; Wang, Y.; Ceder, G. High-Entropy Mechanism to Boost Ionic Conductivity. *Science (80-.)*. **2022**, *378* (6626), 1320–1324.
- (49) Jia, Y.; Yang, J. Study of the Lithium Solid Electrolytes Based on Lithium Nitride Chloride (Li9N2Cl3). *Solid State Ionics* **1997**, *96* (1–2), 113–117.

Chapter 2: Li_5NCl_2 – a fully-reduced, highly-disordered nitride-halide electrolyte for solid-state batteries with lithium-metal anodes

Victor Landgraf, Theodosios Famprikis, Swapna Ganapathy, Lars Bannenberg, Joris de Leeuw, Marnix Wagemaker

2.1 Abstract

Most highly Li-conducting solid electrolytes ($\sigma_{\text{RT}} > 10^{-3} \text{ S cm}^{-1}$) are thermodynamically unstable against lithium-metal and suffer from detrimental solid-electrolyte decomposition at the lithium-metal/solid-electrolyte interface. Solid electrolytes that are thermodynamically stable against Li-metal thus offer a direct way to stabilize lithium-metal/solid-electrolyte interfaces which is crucial for realizing all solid-state batteries that outperform conventional lithium-ion batteries. In this study we investigate Li_5NCl_2 (LNCl) a fully-reduced solid electrolyte that is thermodynamically stable against lithium-metal. Combining experiments and simulations we investigate the lithium diffusion mechanism, different synthetic routes and the electrochemical stability window of LNCl. Li nuclear magnetic resonance (NMR) experiments suggest fast Li motion in LNCl which is however locally-confined and not accessible in macroscopic LNCl pellets via electrochemical impedance spectroscopy (EIS). With the help of ab-initio calculations we develop an in-depth understanding of Li diffusion in LNCl which features a disorder-induced wide spread of different lithium jumps. We identify diffusion-limiting jumps providing an explanation for the high local diffusivity from NMR and the lower macroscopic conductivity from EIS. The fundamental understanding of the diffusion mechanism we develop herein will guide future synthesis optimizations for LNCl to further improve its conductivity (currently $\sigma_{\text{RT}} = 0.015 \text{ mS cm}^{-1}$) and may be applied to other highly-disordered fully-reduced electrolytes. We further show experimentally that the previously reported anodic limit ($>2\text{V}$ vs Li+/Li) is an overestimate and find the true anodic limit at 0.6 V which is in close agreement with our first-principles calculations. Because of LNCl's stability against lithium-metal we identify LNCl as a prospective artificial protection layer between highly-conducting solid electrolytes and strongly-reducing lithium-metal anodes and thus provide a computational investigation of the chemical compatibility of LNCl with common highly-conducting solid electrolytes ($\text{Li}_6\text{PS}_5\text{Cl}$, Li_3YCl_6 ,...). Our results set a framework to better understand and improve highly-disordered fully-reduced electrolytes and highlight their potential in enabling lithium-metal solid-state batteries.

2.2 Introduction

Conventional lithium-ion batteries are reaching their theoretical limits in term of energy density and rely on flammable liquid electrolytes.^{1, 2} A promising alternative for the next generation of energy storage devices are all-solid-state batteries (ASSBs), which may enable the next step-up in terms of energy density and safety required for the ongoing energy transition and the electrification of transport.^{2, 3}

Numerous solid electrolytes (SEs) have been developed, reaching Li-ion conductivities of up to $10^{-2} \text{ S cm}^{-1}$, are comparable with liquid electrolytes.^{4, 5} However, the interfacial stability of SEs with both lithium (Li)

metal and common high-voltage cathodes remains a tremendous challenge and hampers their application in ASSBs.^{6 7 4} A Li-metal anode may be indispensable for ASSBs to surpass conventional lithium-ion batteries in terms of energy density³ thus stable Li-metal/SE interfaces are crucial for the full-scale commercialization of ASSBs.

The stability of the Li-metal/SE interface can be separated into two inter-linked properties: chemical and contact stability. Chemical stability may potentially be achieved in two ways. (i) In the simplest case, the SE is thermodynamically stable against Li-metal and no interphase is formed. (ii) If the SE is thermodynamically unstable against Li-metal, chemical stability can be achieved if it decomposes into an electronically insulating and ion conducting interphase, self-limiting further decomposition and thus effectively serving as a passivation layer^{4 8} Such interphases, however, may lead to inhomogeneous Li plating which favors the growth of lithium dendrites and cell short-circuiting. Additionally, volume changes during decomposition may incite contact losses.⁶ It was previously believed that SEs could inhibit the growth of Li dendrites due to their high stiffness (large elastic moduli) compared to Li-metal.⁹ This assumption has now been refuted theoretically¹⁰ and experimentally.^{11 12} Recently, the crucial role of microstructural aspects to inhibit Li dendrite growth has also been established.² This convoluted interplay of mechanical and microstructural properties, dendritic growth, (electro)chemical and contact stability renders the designing of stable Li-metal/SE interfaces a difficult task. Uncontrollable SE decomposition at the Li-metal/SE interface poses an additional engineering challenge and motivates the investigation of SEs that are thermodynamically stable against Li-metal as they may facilitate the Li-metal/SE interface.

In search of new SEs, researchers investigated the compositional space between Li_3N and LiX ($\text{X}=\text{Cl}, \text{Br}, \text{I}$).¹³ As Li_3N and the LiX salts are thermodynamically stable against Li-metal all members on the quasi-binary $\text{Li}_3\text{N-LiX}$ phase cuts were equally expected to be stable against Li-metal. The numerous new phases discovered are called lithium nitride-halides. Cubic LNCl which crystallizes in the antifluorite structure emerged as the best lithium-ion conducting lithium nitride halide ($\sigma_{\text{RT}} = 1 \cdot 10^{-3} \text{ mS cm}^{-1}$),¹³ demonstrating excellent (electro)chemical stability against Li-metal, an anodic limit of $>2 \text{ V}$ (vs Li^+/Li) and low electronic conductivity of $<1 \cdot 10^{-10} \text{ S cm}^{-1}$.¹³ Marx and coworkers revisited numerous lithium nitride halides, better refined their structures and often corrected the initially reported stoichiometries.^{14 15 16 17} LNCl was found to have a stoichiometry of Li_5NCl_2 , not $\text{Li}_9\text{N}_2\text{Cl}_3$.¹⁵ Thereafter, LNCl was not revisited until Galvez-Aranda and Seminario investigated the solid-solid Li-metal/ LNCl interface with ab-initio molecular dynamics (AIMD) simulations and confirmed the stability of the interface.¹⁸ Sang and coworkers recently performed an ab-initio high-throughput investigation and identified new lithium nitride halide phases that may potentially be synthesizable and of which some are predicted to be highly Li-ion conducting ($>10^{-4} \text{ S cm}^{-1}$).¹⁹

LNCl crystallizes in the antifluorite structure with the Fm-3m space group. N/Cl partially occupy the $(0,0,0)$ site with a 1:2 ratio (Figure 2.1a).¹⁵ The tetrahedral interstitials $(0.25, 0.25, 0.25)$ site are partially occupied by lithium ions (82.5 %) and LNCl thus features a partially occupied lithium sub-lattice which is a good predisposition for high lithium-ion conductivity.²⁰ Reinvestigating materials with promising structural features recently led to the discovery of high ionic conductivities in materials that were thought to be poorly conducting. Lithium halide ceramics with trivalent metals (Li_3MX_6 , $\text{M}=\text{Y}, \text{Er}, \text{Zr}, \text{In} \dots$; $\text{X} = \text{Cl}, \text{Br}, \text{I}$), for example, had been known for decades.²¹ However, their high ionic conductivities were only discovered after Asano and coworkers in 2018 first demonstrated that ionic conductivities in the range of $0.03\text{-}1.7 \text{ mS cm}^{-1}$ could be obtained for Li_3YCl_6 and Li_3YBr_6 via a mechanochemical synthesis route.^{22 23} In contrast, reinvestigating the electrochemical stability window of SEs, showed that previously reported stability

windows were frequently too large; the stability window of SEs was systematically overestimated because of the use of semi-blocking electrodes that provide poor contact at the SE/electrode interface.^{24 25}

In view of the above and because of its excellent stability against Li-metal it is due time to reinvestigate LNCl. Combining experiment and calculation we investigate (i) the fundamental bulk ion-conduction mechanism in LNCl, (ii) the effects of mechanochemical treatments on LNCl and (iii) its anodic limit. Based on our findings we reassess the applicability of LNCl for ASSBs.

2.3 Results and Discussion

Computational investigation of Li diffusion in LNCl. LNCl is a material with partial occupancies and constructing a 2x2x2 supercell that can be used in ab initio \simulations necessitates the probing of different possible atom arrangements. Inspired by references²⁶ and²⁷ we obtained a model supercell of LNCl by a combination of electrostatic energy minimization and the screening >10,000 atom arrangements. We adopted the supercell with the lowest internal energy as our model LNCl supercell. Our model supercell is slightly distorted from cubic symmetry (Table S2.1) which is likely a consequence of the limited size of our model supercell. Similar distortions from cubic symmetry of an LNCl supercell have been observed in a previous computational investigation (Table S2.1) of LNCl.¹⁸ Overall, good agreement is found between the unit cell parameters measured from Rietveld refinement of X-ray diffraction (XRD) data and our model supercell (Table S2.1). The side lengths of the supercell deviate by at most 2.5% and the supercell volume and density differ by less than 0.6% from experiments (Table S2.1). In LNCl the Li sites are enclosed by tetrahedra composed of nitride and chloride ions. The tetrahedra are composed of either 1 nitride and 3 chlorides (from here on referred to as a Cl₃N₁ site), 2 nitrides and 2 chlorides (Cl₂N₂), 3 nitride and 1 chlorides (Cl₁N₃), 4 chlorides (Cl₄) or 4 nitrides (N₄). In mixed N/Cl tetrahedra we found that Li was displaced from the center of the tetrahedron towards the nitride ions (Figure S2.1). Figure 2.1e shows the radial-distribution function (RDF) of the Li-N and Li-Cl distances throughout an ab-initio molecular dynamics (AIMD) simulation. The Li-N peak in Figure 2.1e appears at shorter radii than the Li-Cl peak suggesting that a shorter Li-N distance is maintained not only in the fully relaxed state at 0 K (Figure S2.1) but also during diffusion between sites throughout the AIMD simulation. Figures 2.1b and 2.1c are lithium density maps of our AIMD simulations at 910 K. The density maps show that Li diffuses through the shared edge of two neighboring tetrahedra. The density maps also reveal that the Li-density through shared-edges composed of two chloride ions (Cl-Cl edges, red highlighting in Figure 2.1b) is lower than through Cl-N and N-N edges. This suggests that diffusion through N-N and Cl-N edges is more favorable than through Cl-Cl edges.

As done in previous studies,^{28 29} we dissected our AIMD simulations into individual jumps between lithium sites. This enabled us to estimate the average attempt-frequency ν^* in LNCl ($1.08 \cdot 10^{13}$ Hz) and the jump frequency between different sites $\nu_{A \rightarrow B}$ as explained in detail elsewhere.²⁸ The activation energy for a jump event was estimated with the following expression:

$$E_{a,A \rightarrow B} = -k_b T \ln \left(\frac{\nu_{A \rightarrow B}}{\nu^*} \right) \quad (2.1)$$

where k_b is Boltzmann's constant, T the temperature in K and $E_{a,A \rightarrow B}$ the activation energy of a generalized jump event from site A to site B. We would like to highlight that a site-independent, isotropic attempt frequency of $1.08 \cdot 10^{13}$ Hz is assumed. $E_{a, \text{jump}}$ calculated with equation 2.1 can thus not be interpreted as the actual energy-barrier for diffusion between two sites. $E_{a, \text{jump}}$ should rather be interpreted as a metric

for the affinity for jumps between two sites. The affinity for jumps between two sites is also represented by the jump frequency $v_{A \rightarrow B}$ but we favor the use of $E_{a, \text{jump}}$ over $v_{A \rightarrow B}$, because $v_{A \rightarrow B}$ is temperature dependent. The temperature dependence of $v_{A \rightarrow B}$ is moderated by the temperature term T in equation 2.1, making $E_{a, \text{jump}}$ a temperature-independent metric for the affinity for jumps between two sites.

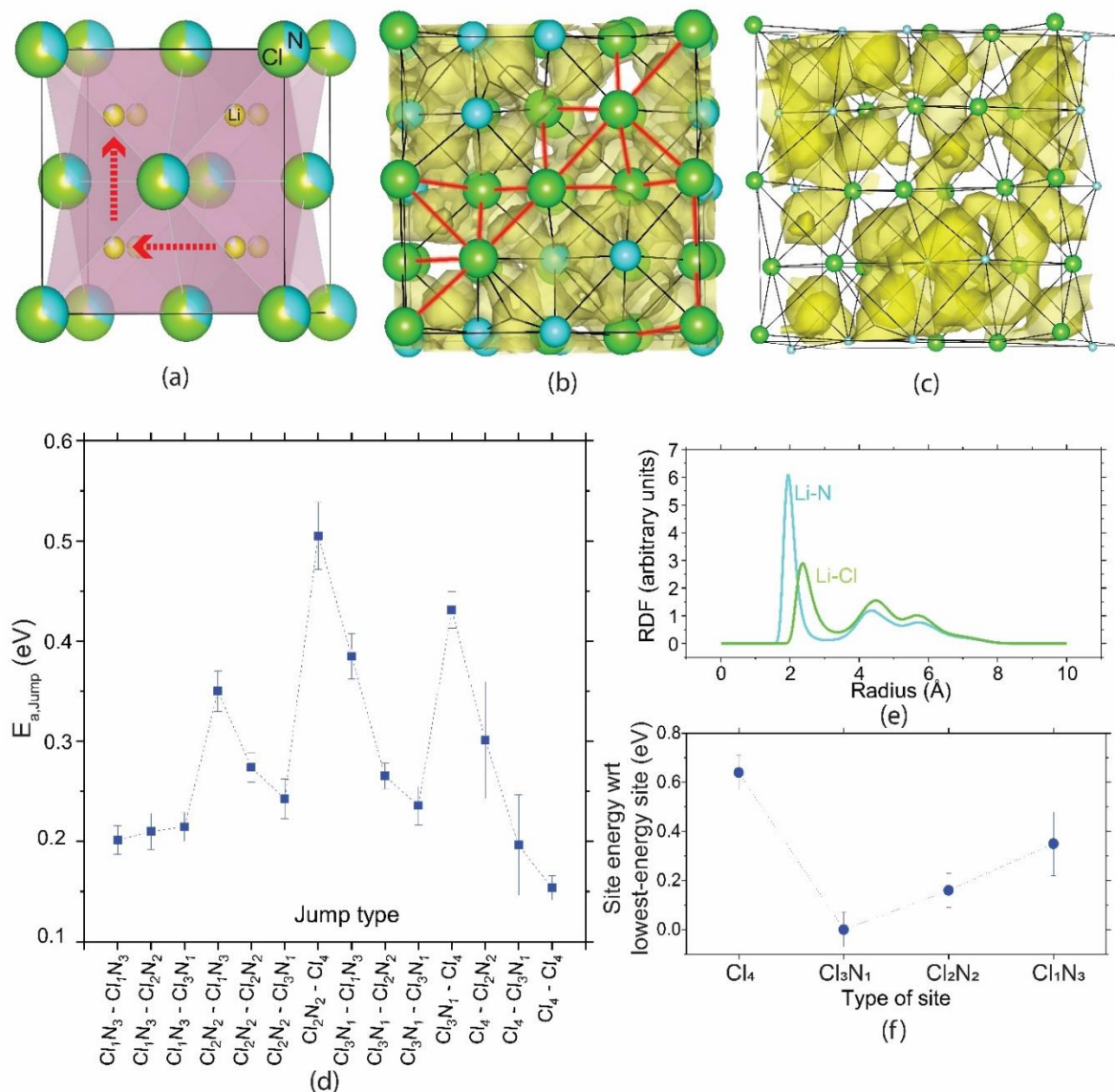


Figure 2.1. a) Unit cell of LNCI. The green and turquoise spheres represent Cl and N, respectively. The red arrows schematically show the Li diffusion pathways in LNCI. b) LNCI supercell with the Li density maps obtained from an AIMD simulation at 910 K. The tetrahedra surrounding Li sites are shown as black lines and edges composed of two chlorides (Cl-Cl) are highlighted in red. c) Same supercell as in b. For better readability only one layer is shown, the supercell is slightly turned and the N/Cl ions are made smaller. d) $E_{a, \text{jump}}$ for different Li jumps. The average $E_{a, \text{jump}}$ values and their respective standard errors plotted here are obtained from 7 AIMD simulations at 910 K, 860 K, 800 K, 720 K, 700 K, 680 K 650 K, respectively. e) The RDFs obtained from an AIMD simulation at 910 K. f) Relative energies of the different Li-sites as obtained from the Li vacancy displacements to different sites.

Figure 2.1d shows the activation energy $E_{a, \text{jump}}$ for individual jump events in LNCl. The $E_{a, \text{jump}}$ values in LNCl span a wide range from 0.2 to 0.5 eV and it becomes apparent that jumps originating from Cl_2N_2 and Cl_3N_1 sites towards Cl_4 sites show particularly high $E_{a, \text{jump}}$ values (>0.4 eV). Figure 2.1f shows the energy differences between the Li sites. This energy difference between Li sites was obtained by displacing a Li ion in a site A to a vacant site B. We then interpreted the energy difference between the two supercells as the energy difference between sites A and B. It becomes apparent that Cl_4 sites are >100 meV higher in energy than all other sites. The large $E_{a, \text{jump}}$ values for $\text{Cl}_2\text{N}_2 \rightarrow \text{Cl}_4$ and $\text{Cl}_3\text{N}_1 \rightarrow \text{Cl}_4$ jumps thus likely originate from the large site-energy differences between $\text{Cl}_2\text{N}_2/\text{Cl}_3\text{N}_1$ and Cl_4 sites.

In LNCl Li diffuses through the edge of edge-sharing tetrahedra and thus diffuses through bottleneck (BN) edges that are composed of either two chlorides (Cl-Cl), one chloride and one nitride (Cl-N) or two nitrides (N-N). To deconvolute the effects of the jump type ($\text{Cl}_2\text{N}_2 \rightarrow \text{Cl}_3\text{N}_1$, $\text{Cl}_2\text{N}_2 \rightarrow \text{Cl}_2\text{N}_2$, ...) and of the BN composition on $E_{a, \text{jump}}$ we focused on jumps between the same type of sites through different BN compositions (Table 2.1). Examining jumps between Cl_3N_1 and Cl_2N_2 sites, respectively, we found that the more nitrogen the BN contains, the lower $E_{a, \text{jump}}$ (Table 2.1). This observation suggests that the $E_{a, \text{jump}}$ values are affected by an intrinsic characteristic of the BN.

BN size is often considered to influence the activation barrier.^{20 30 31} We define the bottleneck size in LNCl as such:

$$R_b = R_{A,B} - (r_A + r_B) \quad (2.2)$$

where $R_{A,B}$ is the distance between the peripheral atoms and r_A and r_B the ionic radii of the peripheral ions A and B. In the optimal case, R_b should be equal to the diameter of Li^+ which is 1.18 \AA .^{20 32} If the bottleneck is too large or too small, thermal energy may be required to adjust the bottleneck size, which increases the activation energy for a jump process.²⁰ Using the Shannon radii³² of Cl^- and N^{3-} we calculated the R_b for Cl-Cl, Cl-N and N-N bottlenecks to be 0.10 \AA , 0.50 \AA and 0.72 \AA . In each case R_b is smaller than 1.18 \AA and thermal energy is likely required to open the bottleneck for Li^+ diffusion. Interestingly, the Cl-Cl BN with (for a fixed jump type) the largest $E_{a, \text{jump}}$ has a R_b that is furthest from the optimum and the N-N BN with (for a fixed jump type) the lowest $E_{a, \text{jump}}$ has a R_b that is closest to the optimum. Bottleneck size could thus provide an explanation for the $E_{a, \text{jump}}$ dependence on BN composition. We conclude from Table 2.1 that for the same jump type, altering the BN composition affects $E_{a, \text{jump}}$. In contrast, for the same BN composition, $E_{a, \text{jump}}$ varies for different jump types. Thus, $E_{a, \text{jump}}$ depends in a convoluted manner on both, the jump type and the BN composition.

Table 2.1. $E_{a, \text{jump}}$ values for jumps between equal sites through different types of bottlenecks and the average of all types of jumps through different types of bottlenecks.

Type of jump	$E_{a, \text{jump}}$ through different bottlenecks (eV)		
	Cl-Cl	Cl-N	N-N
$\text{Cl}_3\text{N}_1 \rightarrow \text{Cl}_3\text{N}_1$	0.41 ± 0.03	0.23 ± 0.01	-
$\text{Cl}_2\text{N}_2 \rightarrow \text{Cl}_2\text{N}_2$	0.43*	0.34 ± 0.02	0.21 ± 0.01
$\text{Cl}_1\text{N}_3 \rightarrow \text{Cl}_1\text{N}_3$	-	-	0.18 ± 0.01
$\text{Cl}_4 \rightarrow \text{Cl}_4$	0.13 ± 0.01	-	-
Average of all types of jumps	0.32 ± 0.02	0.27 ± 0.01	0.22 ± 0.01

Note: The averages and their respective standard errors listed in this table are obtained from three AIMD simulations at 910 K, 860 K and 800 K. $\text{Cl}_2\text{N}_2 \rightarrow \text{Cl}_2\text{N}_2$ jumps through Cl-Cl bottlenecks were only observed at 910 K and only between one of the two $\text{Cl}_2\text{N}_2 \rightarrow \text{Cl}_2\text{N}_2$ site pairs that are connected by a Cl-Cl bottleneck (Table S2.5) which is why we do not report a standard error for this value (marked with *).

From AIMD simulations of LNCl at different temperatures, we obtained the tracer diffusivity (D_{tr}) at different temperatures which enables the estimation of an activation energy (Figure S2.2) as done in previous studies.³³ The ion conductivity σ can be obtained from the diffusivity using the Nernst-Einstein equation³³:

$$\sigma = \frac{n(ze)^2}{k_b T H_R} D_{\text{tr}} \quad (2.3)$$

where n and z are the number density of charge carriers and the charge of the charge carrier as a multiple of the elementary charge e , respectively. We assumed a Haven ratio H_R of 1. Our tracer-diffusivity analysis predicts an activation energy of 0.35 ± 0.03 eV and a conductivity of 0.3 mS cm^{-1} at 300 K for LNCl. Dissecting our AIMD simulations into individual jump events enabled the estimation of the jump-diffusivity D_J which can be obtained from the Einstein-Smoluchowski equation^{28 34}

$$D_J = \frac{1}{N2dt} \sum_{i=1}^M a_{A \rightarrow B}^2 \quad (2.4)$$

where N is the total number of diffusing ions, d the dimensionality of diffusion, t the total simulation time, M the total number of jumps observed and $a_{A \rightarrow B}$ the jump distance of a generalized jump-event. From D_J the conductivity can be estimated by inserting D_J into equation 2.3 instead of D_{tr} . Our jump-diffusivity analysis predicts an activation energy of 0.27 ± 0.01 eV and a conductivity of 4.1 mS cm^{-1} at 300 K. Conductivities derived from D_J are typically larger than conductivities derived from D_{tr} because every jump is assumed to contribute to macroscopic diffusion. However, “back and forth” jumps between two sites and locally confined diffusion do not effectively contribute to macroscopic diffusion and thus tracer diffusivities better describe macroscopic bulk diffusion.

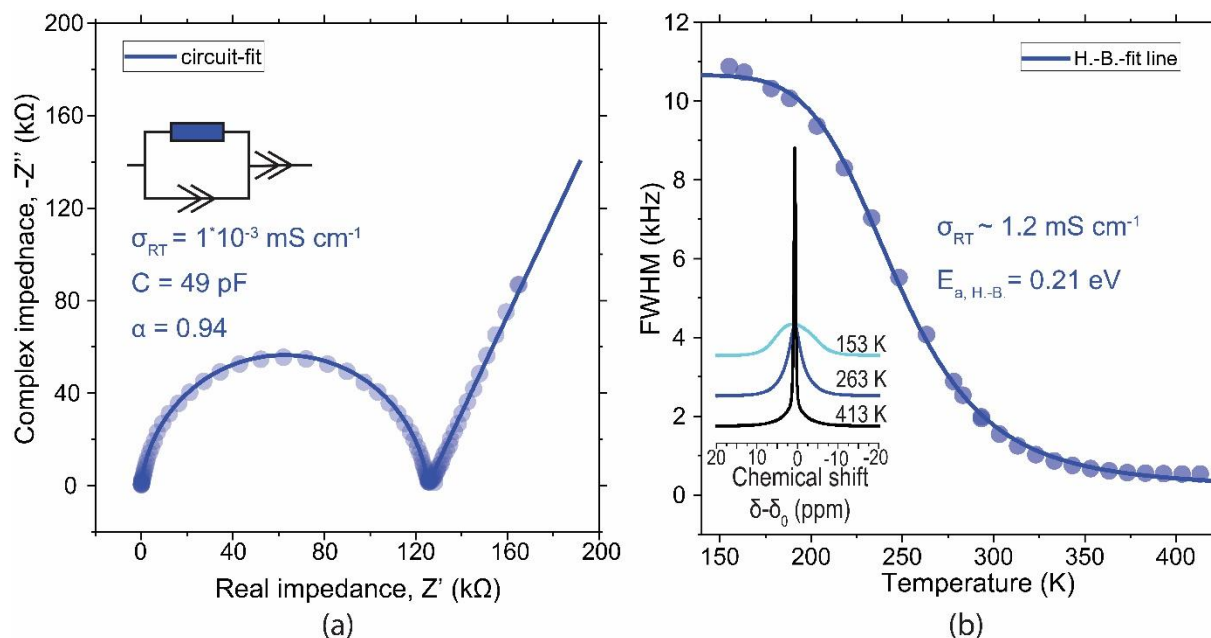


Figure 2.2. a) Nyquist plot of LNCl-I at RT. Experiments were done in a SS|LNCl-I|SS cell (SS=stainless steel). The inset shows the equivalent circuit. b) FWHM of the ^7Li NMR signal of LNCl at different temperatures. The inset shows the NMR signal at three distinct temperatures. The solid line is the fit obtained from the Hendrickson-Bray equation.

Experimental investigation of Li conductivity in LNCl.

We synthesized LNCl via a solid-state synthesis route by heating stoichiometric amounts of LiCl and Li_3N at 600°C for 3h and subsequent air quenching as following in ref³⁵. LNCl synthesized in this way is from now on referred to as LNCl-I. The lattice constants previously reported for LNCl range from 5.386 Å to 5.416 Å.³⁶¹⁵³⁷ This variation in the lattice parameter may be a consequence of the different annealing protocols employed for LNCl synthesis in refs. 15,³⁶ and ³⁷. Also the exact quenching procedure is not described in detail in refs.³⁶ and ³⁷. The lattice constant 5.396 Å that we determined from our XRD Rietveld refinements (Figure S2.3, Table S2.1) for LNCl fits well into the range of lattice parameters determined in previous studies (5.386 Å to 5.416 Å).¹⁵³⁶³⁷ The purity of LNCl-I was verified by XRD and no impurities were observed (Figure S2.3). Figure 2.2a shows the electrochemical impedance spectrum (EIS) Nyquist plot of LNCl-I at room temperature (RT). The impedance of LNCl-I could be fitted with a resistor (R) parallel to a constant phase element (CPE). The effective capacitance of the CPE calculated with Brug's formula³⁸³⁹ is 49 pF which is a value typically associated with ion conduction in the bulk of solid ion conductors.⁴⁰ A prominent secondary process in the impedance that may for instance arise from grain boundaries was not observed even at -30°C (Figure S2.4). We thus interpret the impedance of LNCl-I at RT as bulk dominated. We calculated the ionic conductivity of LNCl to be $1 \cdot 10^{-3} \text{ mS cm}^{-1}$ at RT, which comparable with previous reports.¹³ The activation energy measured from temperature dependent impedance spectroscopy was $0.471 \pm 0.005 \text{ eV}$ which is close to the value of 0.49 eV previously reported for LNCl.¹³

Complimentary to EIS, ^7Li NMR provides insights on Li diffusion in ion conductors.⁴¹ Figure 2.2b shows the ^7Li NMR signal linewidth evolution with increasing temperature for LNCl-I and the typical line shape narrowing profile was observed.⁴¹⁴²⁴³ The activation energy of the diffusion process that inflicts the line-narrowing can be obtained from the phenomenological equation derived by

Hendrickson and Bray (H.-B.)⁴³:

$$\Delta\nu(T) = \Delta\nu_R \left[1 + \left(\frac{\Delta\nu_R}{B} - 1 \right) \exp \left(-\frac{E_a}{k_b T} \right) \right]^{-1} + D \quad (2.5)$$

where $\Delta\nu(T)$ is the linewidth at temperature T , and $\Delta\nu_R$ is the linewidth in the rigid-lattice regime. B is the linewidth that would be obtained at extreme narrowing in the absence of magnetic field inhomogeneity and D is a correction factor accounting for broadening arising from the inhomogeneity of the static magnetic field. From this model we obtain an activation energy of 0.21 ± 0.01 eV for lithium diffusion in LNCl. The value of B is an indicator for the ‘range’ of motion. The larger B , the more ‘short-range’ the motion because locally confined motion is not expected to entirely eliminate dipole-dipole interactions.⁴³ For different ion conductors values for B ranged from 10^{-3} to 10^{-13} kHz.⁴³ The value of B obtained for LNCl ($5 \cdot 10^{-4}$ kHz) thus suggests that the line-narrowing is caused by locally confined motion.⁴³ To what range exactly this motion may be confined, goes beyond the predictive scope of the Hendrickson-Bray equation.

An additional estimate of the activation energy can be obtained from the empirical expression of

Waugh and Fedin (W.-F.)⁴⁴:

$$E_a^{WF} = 1.617 \cdot 10^{-3} \frac{T_c}{K} \quad (2.6)$$

where T_c is the onset temperature of motional narrowing in Kelvin. A drawback of the W.-F. approach is the difficulty to estimate the exact onset of motional narrowing. We observe the onset of narrowing at ~ 180 K and from the W.-F. expression we obtain an activation energy of 0.29 eV. Generally, ^{6,7}Li NMR-measurements also capture Li motion that does not effectively contribute to macroscopic diffusion such as locally-confined diffusion and “back and forth” jumps. Activation energies obtained from D_j values thus better match activation energies obtained from ^{6,7}Li NMR-measurements than activation energies obtained with D_{tr} values. The activation energies obtained from the H.-B. and the W.-F. expressions and the activation energy obtained from the D_j values in our AIMD simulations are all in a range between 0.21 eV and 0.29 eV (Table 2.2). Generally, at temperatures below the onset of line narrowing the jump frequency is lower than the rigid-lattice-regime NMR line width.⁴¹ At temperatures where narrowing is observed the jump frequency is higher than the rigid-lattice-regime NMR line width.⁴¹ When extrapolating the jump frequencies obtained from AIMD simulations to temperatures of the rigid-lattice regime (< 150 K) we indeed obtain jump frequencies lower than the rigid-lattice-regime NMR line width of 10 kHz. Extrapolating the jump frequencies obtained from AIMD simulations to temperatures of narrowing (> 180 K) we obtain jump frequencies > 100 kHz and thus much larger than the rigid-lattice-regime NMR line width. We thus observe reasonable agreement between our AIMD simulations and NMR measurements.

The activation energies obtained from NMR can be used to calculate the Li conductivity at 300 K in LNCl as follows⁴¹:

$$\sigma = \frac{fn(ze)^2 a^2}{6k_b T} v^* \exp \left(\frac{-E_a}{k_b T} \right) \quad (2.7)$$

where a is the average jump distance taken as 2.7 Å which is the average distance between Li sites in LNCl and f is the correlation factor; the correlation factor is a measure for how efficiently jumps contribute to macroscopic diffusion and can be calculated from the ratio D_{tr}/D_j .²⁸ From the extrapolated values of D_{tr} and D_j at 300 K we obtained a correlation factor $f=0.06$.

Using the range of activation energies obtained from the linewidth narrowing (0.21-0.29 eV), the correlation factor ($f = 0.06$) and assuming an attempt frequency ν^* of $1 \cdot 10^{13}$ Hz, a range for the ion conductivity at 300 K as probed by ^7Li NMR was calculated (Table 2.2).

Table 2.2. Ion Conductivity and E_a obtained by different methods.

Method	E_a (eV)	σ_{RT} (mS cm ⁻¹) [lower boundary; upper boundary]	Length scale probed
AIMD _{Tracer}	0.35 ± 0.03	0.3 [0.07; 1.2]	10 Å
AIMD _{Jump}	0.27 ± 0.01	4.9 [4.4; 5.5]	10 Å
^7Li NMR signal			
line shape narrowing	0.25 [0.29; 0.21]	1.2 [0.18; 6.9]	<500 μm
EIS	0.471 ± 0.005	$1.0 \cdot 10^{-3}$	~500 μm

Note: The lower and upper boundaries for σ_{RT} are obtained by using the respective extremes of the E_a values for extrapolation (e.g. 0.32 and 0.38 eV in the case of AIMD_{Tracer}). For ^7Li NMR line shape narrowing the lower and upper boundaries originate from the different E_a values obtained from different models.

Table 2.2 summarizes the activation energies and RT conductivities obtained from different techniques. We observe reasonable agreement between our NMR measurements and the jump-analysis of our AIMD simulations (Table 2.2). The activation energy obtained from the tracer-analysis of our AIMD simulations is 0.08 eV larger than that of the jump-analysis. This is most likely a consequence of the difference in how the mean square displacement is calculated (see Methodology) which may affect the respective temperature dependence of D_j and D_{tr} . Diffusivities obtained from the jump-analysis (D_j) tend to be overestimates because the jump-analysis captures locally confined motion that does not effectively contribute to macroscopic diffusion. Activation energies and conductivities obtained from the tracer-analysis (D_{tr}) of AIMD simulations thus better compare to the bulk properties of materials measured by EIS. Interestingly, the activation energy obtained from EIS is by 0.1 eV larger than the activation energy obtained from our AIMD tracer analysis. We would like to bring forward two conceivable explanations for this discrepancy. (i) The length scale probed by EIS is 5 orders of magnitude larger than the one probed in our AIMD simulations (Table 2.2). EIS may potentially capture a diffusion limitation occurring at the

mesoscale of our LNCl pellets. Such a diffusion limitation may for example arise from potential amorphous impurities in our LNCl pellets that would not be detected by XRD. (ii) A second explanation for the discrepancy between our AIMD tracer-analysis and our EIS experiments may be diffusion limiting Cl_4 sites and/or Cl-Cl edges in the bulk of our LNCl pellets: Our AIMD analysis shows a poor affinity for jumps through Cl_4 -sites and Cl-Cl edges ($E_{a,\text{jump}} > 0.4$ eV). In our model LNCl supercell (side length 10 Å) the Li diffusion pathways are not limited by Cl_4 sites and/or Cl-Cl edges. However, with EIS we capture effects at the scale of our polycrystalline LNCl pellets (thickness ~ 500 μm). Between different crystallites the distribution of the Li sites likely varies and the likelihood of diffusion-limiting Cl_4 sites and/or Cl-Cl bottlenecks increases and may restrict the macroscopic conductivity, measured by EIS.

Mechanochemical treatment of LNCl.

It has been repeatedly demonstrated that mechanochemical processing can dramatically improve the ion conductivity of inorganic ceramics.^{23 42}

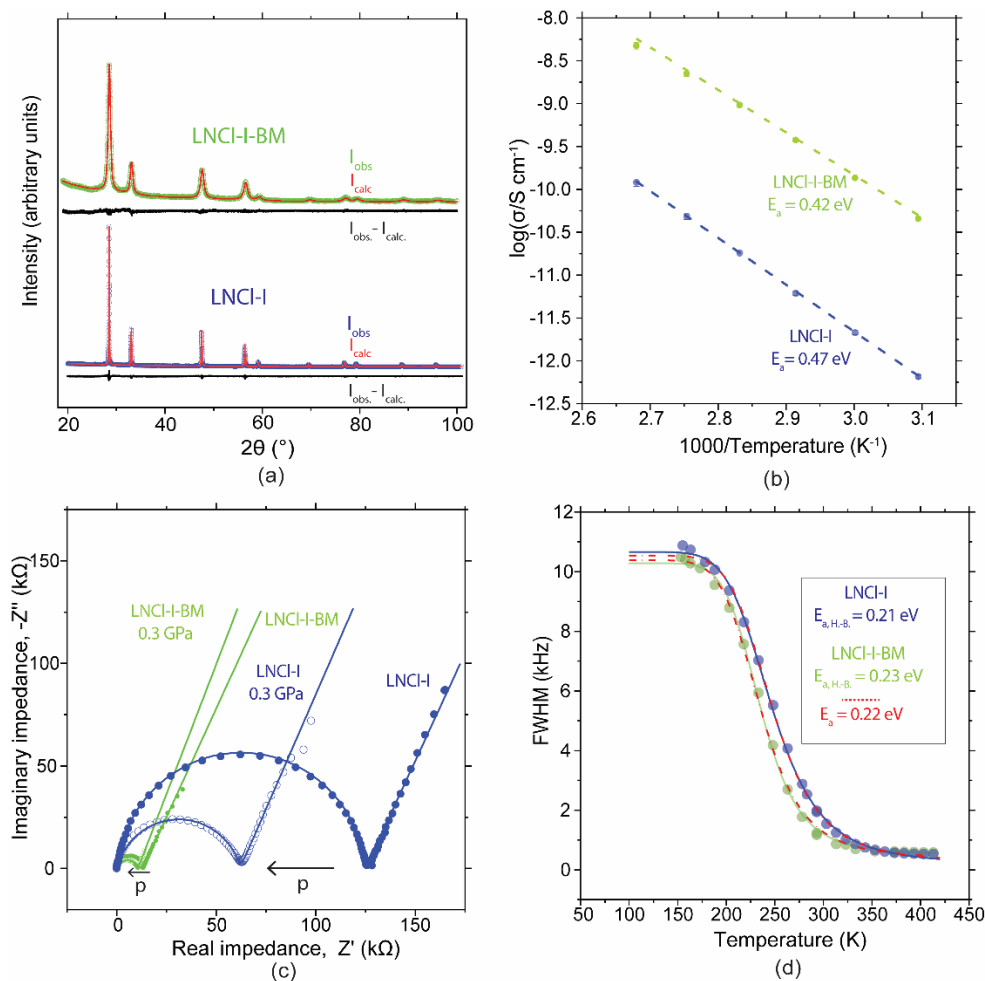


Figure 2.3. a) XRDs of LNCl-I and LNCl-I-BM with Rietveld refinements and the difference profile. b) Arrhenius fits of the conductivities obtained at different temperatures from EIS for LNCl-I and LNCl-I-BM. The individual points are the averages of three measurements, error bars are smaller than the point symbol and therefore not visible. c) Nyquist plot of LNCl-I and LNCl-I-BM with and without pressure applied during measurement. d) ^7Li NMR signal line shape evolution with temperature for LNCl-I and LNCl-I-BM, the solid lines are the H.-B. fits, the red dashed lines are obtained from H.-B. fits with E_a as a fixed parameter set to 0.22 eV.

To investigate potential benefits of mechanical milling we processed LNCl-I for 4h in a planetary ball mill after solid-state synthesis. Samples prepared in this way are from now on referred to as LNCl-I-BM. LNCl-I remains stable during the milling as no impurity peaks are detected in the XRD of LNCl-I-BM. The XRD of LNCl-I-BM shows dramatic peak-broadening compared to LNCl-I (Figure S2.5). Rietveld refinements show that the lattice parameter of LNCl-I is decreased from 5.39(6) Å to 5.37(6) Å after the mechanical milling

process. Additionally, Williamson-Hall analysis (Figure S2.6) shows that after milling the average crystallite size is dramatically reduced from the μm range to ~ 60 nm. Milling also imposes significant strain on the LNCl lattice so that we obtain a residual microstrain of $\epsilon = 1.04\%$ for LNCl-I-BM.

Interestingly, EIS shows that the ion conductivity of LNCl increases by an order of magnitude after milling reaching 0.01 mS cm^{-1} . Additionally, fits of the conductivities at different temperatures to Arrhenius' law (Figure 2.3b) show that the (macroscopic) E_a of LNCl-I is decreased from 0.471 ± 0.005 eV to 0.426 ± 0.005 eV after milling. As the crystallite size of LNCl-I-BM is substantially smaller, a larger volume fraction of grain boundary regions is expected in LNCl-I-BM as compared to non-BM LNCl. However, the EIS of LNCl-I-BM-4h could be excellently fitted with a single R-CPE with an effective capacitance of ~ 40 pF. As for LNCl-I we thus interpret the impedance in LNCl-I-BM to be bulk dominated. Longer milling of LNCl-I, for 8h and 12h did not further increase the conductivity and no significant further decrease of the crystallite size was obtained (Figure S2.6).

Reduced particle size is a proposed explanation for the improved ion conductivity in mechanically processed materials.^{45 46} Under the same pelletization conditions a smaller particle size facilitates compression and consolidation which improves the area-contact between particles and reduces the tortuosity for ion conduction.^{45 46} Famprakis and coworkers demonstrated that applying pressure during measurement on non-ball-milled (non-BM) Na_3PS_4 improved its observable conductivity by a factor of ~ 10 so that it matched the conductivity of ball milled (BM) Na_3PS_4 .⁴⁶ In contrast, applying pressure on the BM- Na_3PS_4 sample had a negligible effect on its conductivity. They concluded that the better conductivity of BM- Na_3PS_4 was a consequence of better compression/consolidation of the BM- Na_3PS_4 pellets used for EIS measurements.⁴⁶ Inspired by this study, we investigated the conductivity of LNCl-I and LNCl-I-BM under pressure. We found that the conductivity of LNCl-I increased by a factor of ~ 2 (Figure 2.3c). In contrast, the ion conductivity of LNCl-I-BM hardly improved when applying pressure. We thus observe a similar trend to Famprakis and coworkers and explain our results as follows. For LNCl-I leeway for better consolidation was available and we observed an increase in conductivity when applying pressure. For the LNCl-I-BM sample, the conductivity hardly improved because the smaller particle size enabled near-optimal consolidation during pelletization. However, two observations indicate that the improved conductivity of LNCl-I-BM is not solely a consequence of better consolidation. (i) Despite the pressure-induced conductivity improvement of LNCl-I by a factor of 2, even under pressure, the conductivity of LNCl-I-BM is still higher by a factor of 5. (ii) An improved conductivity solely originating from superior consolidation would not be expected to show a change in activation energy but the Arrhenius fits in Figure 2.3b clearly show that the activation energy for LNCl-I-BM is decreased by 40 meV as compared to LNCl-I.

Interestingly the Arrhenius prefactor of LNCl-I-BM is hardly larger than for LNCl-I. For LNCl-I-BM we obtain $\log_{10}(\sigma_0/S\text{ cm}^{-1}) = 2.22$ and for LNCl-I $\log_{10}(\sigma_0/S\text{ cm}^{-1}) = 2.05$. The Arrhenius prefactor comprises factors such as the charge-carrier concentration, the attempt frequency, the jump distance and the correlation factor. These factors are thus only slightly modified by milling and the improved RT conductivity of LNCl-I-BM is predominantly a consequence of the decreased (macroscopic) activation energy. The origin of the reduced macroscopic activation energy of LNCl-I-BM is not entirely understood. Previous studies suggested that amorphous fractions in SEs introduced by high-energy milling may reduce the macroscopic activation energy and consequently improve ion conductivity.^{42 47 48} It was equally suggested that surface-related regions show faster ion diffusion due to increased structural disorder. An increased volume fraction of surface-related regions (concomitant with smaller particle size) may thus enhance bulk diffusion in nanocrystalline ceramics.^{42 47 49}

The activation energy of LNCl-I-BM obtained from a Hendrickson-Bray fit of the ^7Li NMR lineshape narrowing profile is increased by 20 meV as compared to LNCl-I. This may suggest an increased activation barrier in LNCl-I-BM for the fast, locally confined Li diffusion probed by NMR. However, the accuracy of activation energies obtained from motional narrowing data relies on highly precise line-width measurements. Small errors in the line-width measurements may largely impact the fit result, so that the uncertainty in activation energies obtained by this method typically amounts to a few tens of meV.⁵⁰ This argument is visualized in Figure 2.3d where a fit line obtained from a H.B.-fit with E_a as a fixed parameter set to 0.22 eV shows a good fit for the narrowing profile of LNCl-I and LNCl-I-BM.

To investigate the effects of further annealing on LNCl-I-BM we re-annealed LNCl-I-BM at 600°C for 3h and subsequent air-quenching restored the initial crystallinity of LNCl-I and the conductivity was reduced to $1 \cdot 10^{-3} \text{ mS cm}^{-1}$. Annealing LNCl-I-BM also increased the activation energy to $0.486 \pm 0.005 \text{ eV}$ which is close to the LNCl-I value of $0.471 \pm 0.005 \text{ eV}$ (Figure S2.7). We thus conclude that the beneficial effects of mechanochemical milling on LNCl-I are reversed when annealing the ball milled samples. This result supports that the reduced particle size and the increased strain obtained after milling LNCl-I may potentially explain the increased Li conductivity of LNCl-I-BM.

Finally we report that LNCl can be synthesized directly via a mechanochemical route without any annealing step. After milling stoichiometric amounts of LiCl and Li_3N for 10 h at 600 rpm LNCl was obtained (Figure S2.7). Samples synthesized in this way are referred to as BM-LNCl. The RT conductivity of BM-LNCl was found to be 0.015 mS cm^{-1} and is the highest conductivity ever reported for LNCl. The activation energy of this sample is $0.416 \pm 0.005 \text{ eV}$. Analogously to LNCl-I-BM, the conductivity of BM-LNCl is reduced to $5 \cdot 10^{-3} \text{ mS cm}^{-1}$ after annealing and the activation energy is increased to $0.466 \pm 0.005 \text{ eV}$ which are values comparable to well consolidated LNCl-I (Figure S2.7).

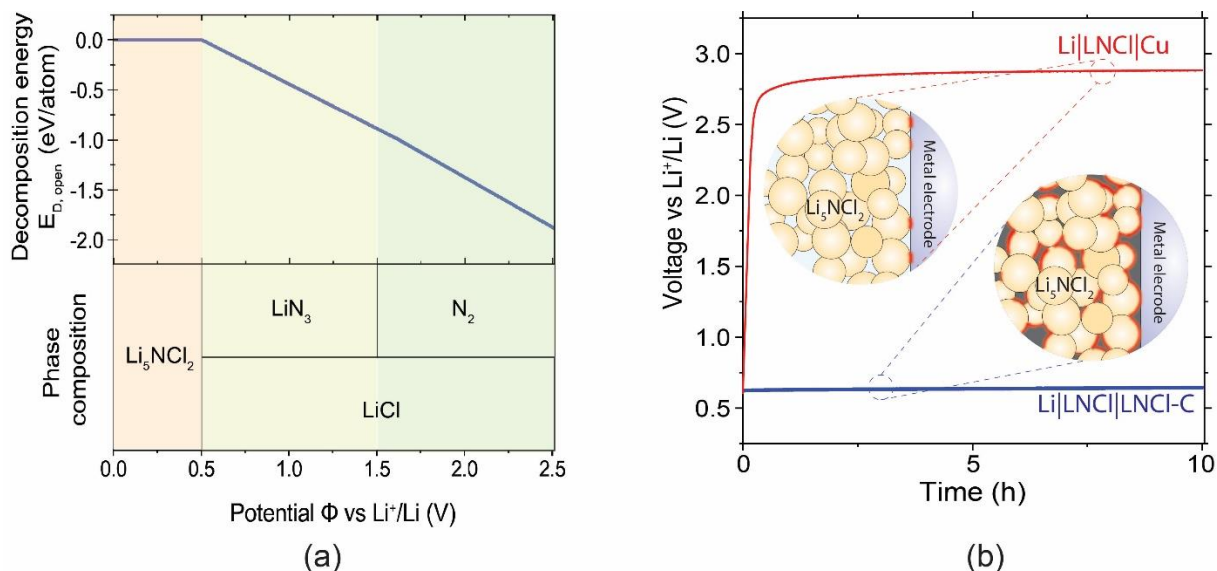


Figure 2.4. a) Phase equilibria of the Li_xNCl_2 $\{x \in \mathbb{R} | x \geq 0\}$ phase space at different potentials ϕ vs Li^+/Li . Additionally this figure shows the decomposition energy $E_{D, \text{open}}$ as defined by Zhu and Mo51 of LNCl at different ϕ . b) Galvanostatic oxidation of a composite LNCl-C cathode and of LNCl in contact with an ion-blocking Cu disk. The two schematics represent the cathode compositions. In the case of LNCl-C composite cathodes the contact area with the electronic network is much larger as sketched by the red highlighting. The constant current for both curves in b was $0.5 \mu\text{A}$ ($0.64 \mu\text{A cm}^{-2}$).

Electrochemical stability window of LNCl.

The anodic limit of LNCl was previously found to be > 2 V vs (Li⁺/Li).¹³ Figure 2.4a shows the results of our electrochemical stability calculations for LNCl, which were obtained by constructing grand potential diagrams at different chemical potentials of Li (μ_{Li}) leveraging the materials project data base.^{51 52} Our calculations predict that LNCl is thermodynamically stable against Li metal and has an anodic limit of 0.50 V vs (Li⁺/Li). Beyond 0.5 V, LNCl was predicted to decompose to lithium azide (LiN₃) and LiCl (Figure 2.4a)

Overestimated anodic limits for SE were recently often reported.^{25 53} It was previously shown that employing SE-carbon composite electrode in a Li|SE|SE-C cell instead of a simple ion-blocking metal (M) electrode in a Li|SE|M cell, enabled a more accurate measurement of the anodic limit of SEs.^{25 53} The anodic limits obtained when using composite SE-C electrodes are typically significantly lower than the anodic limits obtained with ion-blocking metal electrodes. The smaller anodic limit measured, is a consequence of the increased electrochemical surface area in a SE-C composite electrode; this increases the current signal at the onset of oxidation making the onset of oxidation better observable.^{25 53} Figure 2.4b shows the galvanostatic charge of a Li|LNCl|LNCl-C cell with an extremely low current of 0.5 μA (0.64 $\mu\text{A cm}^{-2}$). The current onset at 0.62 V indicated an experimental anodic limit of 0.62 V for LNCl which is in much closer agreement with the calculated value of 0.50 V than the previous experimental values of >2 V. We repeated the same experiment with a Li|LNCl|Cu cell equally shown in Figure 2.4b; for this cell the voltage stabilized at 2.7 V and may explain the overestimate in previous reports.

The predicted oxidation of LNCl to LiN₃ calculated to occur at 0.50 V may potentially be kinetically inhibited even at very slow currents because LiN₃ formation necessitates a complex anionic rearrangement to form the [N₃]⁻ moieties present in azides. Such complex anionic rearrangements are additionally hampered by the likely limited RT diffusivity of Cl⁻/N³⁻ in LNCl. In the potential scenario of kinetically inhibited LiN₃ formation the calculated anodic decomposition voltage would be extended from 0.50 V to 0.63 V vs (Li⁺/Li) (Figure S2.8), which is even closer to our experimental value of ~ 0.6 V. In principle, the cathodic limit of SEs can be measured in an analogous way to the anodic limit. However, the use of composite SE-C electrodes makes it difficult to distinguish between the lithiation of carbon additives and the lithiation of the SE at potentials close to 0 V vs Li⁺/Li.⁵⁴ Hartwig and coworkers reported chemical stability of LNCl against Li-metal.⁵⁵ This stability was investigated by dipping LNCl into molten Li and the absence of any observed reaction.⁵⁵ We repeated this experiment keeping LNCl powder submerged in molten Li at 210 °C for 2h. No new peaks were observed after this in our XRD experiments (Figure S2.9). Additionally symmetric Li|LNCl|Li cells display flat stripping/plating plateaus and no increase in the cell voltage (Figure S2.9) over time, indicating a stable Li-metal /LNCl interface.

Based on our findings on LNCl it convenes to reflect on its applicability in ASSBs. A key property of LNCl is its thermodynamic stability against Li-metal which is uncommon for SEs. However, its low anodic limit (~ 0.6 V) inhibits its application in combination with common high-voltage cathodes and confines the applicability of LNCl to an artificial buffer layer between Li-metal and alternative SEs that face the cathode. In such a hybrid bilayer SE architecture, LNCl would be in close contact with a partner SE. The realization of such systems thus hinges on the chemical compatibility between LNCl and other common SEs.

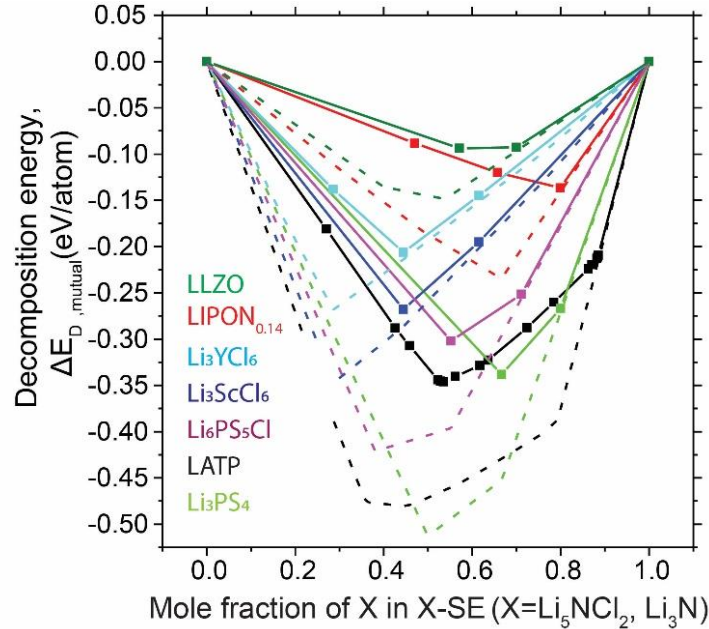


Figure 2.5. Pseudo-binaries between LNCl/Li₃N and common highly-conducting SEs. The solid lines are pseudo-binaries between LNCl and different SEs and the dashed lines are for pseudo-binaries between Li₃N and different SEs

We investigated the thermodynamic driving force of LNCl to chemically react with common SEs by constructing pseudo-binaries in phase space (Figure 2.5) leveraging the materials project database, as explained in detail elsewhere.⁵¹ Figure 2.5 shows the pseudo binaries between LNCl and different SEs. $\Delta E_{D,mutual}$ as defined by Zhu and Mo⁵¹ is the reaction energy for the reaction between LNCl and the SE of interest. We would like to highlight that a thermodynamic driving force for chemical reaction ($\Delta E_{D,mutual} < 0$) between two SEs does not necessarily imply immediate reaction upon contact; the diffusivity of elements in Li⁺-conducting SEs (excluding Li⁺) is limited at ambient temperatures so that an immediate solid-state reaction upon contact may be kinetically inhibited. $\Delta E_{D,mutual}$ can be treated as a propensity for reaction especially if the hybrid bilayer electrolyte is subjected to annealing/heating steps.⁵¹

Figure 2.5 shows that LNCl has the strongest propensity for chemical decomposition with LAMP and sulfide-based SEs such as the argyrodite Li₆PS₅Cl and Li₃PS₄. With halide (Li₃MCl₆) electrolytes the decomposition energy is reduced and seems to be mainly driven by the formation of strong M³⁺-N³⁻ bonds. The decomposition energy $\Delta E_{D,mutual}$ of Li₃ScCl₆ is 100 meV/atom larger than for Li₃YCl₆ which can be explained by a stronger Sc-N affinity compared to Y-N. The propensity for chemical decomposition is further reduced between LNCl and LIPON-type electrolytes and the garnet (LLZO) electrolyte. Figure 2.5 equally shows the pseudo-binaries of Li₃N and the SEs of interest (dashed lines). α -Li₃N has a larger ion conductivity than LNCl (0.1-1 mS cm⁻¹)^{56, 57} and is equally thermodynamically stable against Li metal.⁵⁶ Similar to LNCl, the applicability of α -Li₃N is confined by its limited anodic limit (0.44 V).^{56, 58} However, the driving force for chemical decomposition with common SEs is larger with Li₃N by 50 - 200 eV/atom than with LNCl. This suggests a stronger propensity for decomposition at the Li₃N|SE interface than at the LNCl|SE interface. Hybrid bilayer electrolytes are scarcely investigated but bear the potential to enable ASSBs.⁵⁹ Beyond good ion conductivity (~ 0.1 mS cm⁻¹), the anolyte needs to balance chemical stability, contact stability and lithium dendrite suppression on the Li-metal side and compatibility with the catholyte. This complex interplay of chemical, mechanical and microstructural properties of the anolyte motivates the exploration

and optimization of different phases that are thermodynamically stable against Li-metal such as the lithium nitride halides. However, the future practicality of LNCl will depend on whether its practical conductivity can be increased.

2.4 Conclusion

We investigated the fundamental Li diffusion mechanism in LNCl using AIMD simulations. We found that Li diffuses through the edge of edge-sharing tetrahedral Li sites. The affinity for jumps between two Li sites depends on the N/Cl-composition of the tetrahedra enclosing the Li sites and of the bottleneck-edge composition. We found that jumps into Cl_4 Li sites and jumps through Cl-Cl edges have the largest $E_{a, \text{jump}}$ values indicating that they are unfavorable compared to other jump events. Our EIS experiments confirmed the previously reported Li conductivity of $1 \cdot 10^{-3} \text{ mS cm}^{-1}$ and an E_a of 0.47 eV. Much faster Li motion was detected with ^7Li NMR ($>0.1 \text{ mS cm}^{-1}$) with a lower $E_a \sim 0.25$ eV. We propose that the fast Li motion may arise from readily occurring jumps with low $E_{a, \text{jump}}$ values and that the long-range conductivity probed by EIS is limited by jumps with large $E_{a, \text{jump}}$ values. Introducing a 4h mechanochemical milling step after solid state synthesis improves the RT conductivity of LNCl by an order of magnitude to 0.01 mS cm^{-1} and lowers the activation energy to 0.42 eV. It was shown that LNCl can be synthesized mechanochemically without any annealing step and these samples reached conductivities of 0.015 mS cm^{-1} . Re-annealing of milled LNCl samples at 600°C eliminates the beneficial effects of milling as the conductivity is reduced and the activation energy increased to values obtained for non-milled samples. Our experiments showed that the anodic limit of LNCl is $\sim 0.6 \text{ V}$ (vs Li^+/Li) which is significantly lower than the previously reported $>2 \text{ V}$ (vs Li^+/Li) and matches our first principles thermodynamic calculations. We established that the anodic limit of LNCl confines its potential role in ASSBs to an artificial buffer layer between Li-metal and other highly-conducting SEs where the thermodynamic stability of LNCl against Li-metal may be beneficial. Our calculations show that from a thermodynamic viewpoint, LNCl is chemically better compatible with common highly-conducting SEs than Li_3N . Future investigations on LNCl should focus on different synthesis approaches of LNCl, how they affect sub-ordering of the N/Cl anionic framework and how this may potentially affect Li ion conductivity. Additionally, doping strategies have previously been investigated³⁵ and should be further explored.

2.5 Methodology

Synthesis. *LNCl-I*: The synthesis precursors were LiCl (Sigma-Aldrich, 99%) and Li_3N (Sigma-Aldrich, $>99.5\%$). Stoichiometric amounts of the precursors with 10% wt. excess Li_3N were milled in a planetary ball mill (Jar: ZrO_2 , 45 mL) with 10 mm ZrO_2 balls and a ball/powder ratio of 13 at 270 rpm for 4.5 h (5 min milling; 15 min pause) to ensure good mixing of the precursors. Subsequently the precursor mix was pressed into a pellet (1.3 tons) and transferred to an airtight Cu crucible. The crucible was placed in a furnace and heated with a rate of 300°C/h to 600°C , maintained at this temperature for 3 h and then air quenched. *LNCl-I-BM*: To obtain LNCl-I-BM, LNCl-I was transferred to a planetary ball mill (Jar: ZrO_2 , 45 mL) with 1 mm ZrO_2 balls and a ball/powder ratio of 25 and milled for 4h (5 min milling; 5 min pause). After each hour of milling, all powder was removed from the inner walls of the jar to ensure effective milling. *BM-LNCl*: Stoichiometric amounts of LiCl and Li_3N with 10% wt. excess Li_3N were milled in a planetary ball mill (Jar: ZrO_2 , 45 mL) with 10 mm ZrO_2 balls and a ball/powder ratio of 13 at 600 rpm for 10 h (5 min milling; 5 pause). All preparation steps were done in an argon atmosphere ($\text{H}_2\text{O} < 1 \text{ ppm}$, $\text{O}_2 < 1 \text{ ppm}$). *LNCl-I in contact with molten Li*: LNCl-I was placed between two Li-metal disks in a W crucible

which was sealed in a quartz ampoule. The ampoule was exposed to 210 °C for 2 h and then removed from the furnace.

Electrochemical Characterization. *EIS:* Pellets of the LNCl probes were pressed (3.2 tons) in custom-made solid-state lab cells. The cell configuration was SS|LNCl|SS (SS=stainless steel). AC impedance was performed with an Autolab (AUT86298) in the frequency range 10 MHz to 0.1 Hz with a voltage amplitude of 10 mV. *Galvanostatic measurements:* Galvanostatic measurements were also performed with an Autolab (AUT86298). To measure the anodic limit of LNCl, Li|LNCl-I-BM|LNCl-I-C were used. To make the LNCl-I-C composite cathode a mixture of LNCl-I: Super P:carbon-nanotubes with a weight ratio of 0.7:0.15:0.15 was milled in a planetary ball mill (Jar: ZrO₂, 45 mL) with 10 mm ZrO₂ balls and a ball/powder ratio of 30 at 400 rpm for 2 h (5 min milling; 5 min pause). After the first hour of milling, all powder was removed from the inner walls of the jar to ensure good mixing. Li|LNCl-I-BM|LNCl-I-C cells were assembled by pressing a LNCl-I-BM pellet (130 mg, 3.2 tons) and subsequently the LNCl-I-C composite (15 mg, 3.2 tons) on top of it. Finally a Li disk was pasted on the opposite side of the LNCl-I-BM pellet. LNCl-I-BM was used as the SE because it is 10 times more conductive than LNCl-I so that voltage drops in the SE becomes negligible (<0.01 V) at the current used 0.5 μA (0.64 μA cm⁻²). *Conductivity measurements at different temperatures for Arrhenius fits:* SS|LNCl|SS cells were kept at 30°C for 1h, then heated in 5 min to 50°C and kept at this temperature for 30 min followed by heating to 60°C in 5 min and maintaining the temperature for 30 min. This procedure was continued up to 100°C. The EIS obtained at the end of the 30 min temperature-plateaus were used for Arrhenius fits.

Solid state NMR. Solid state NMR measurements were done on a Bruker Ascend 500 MHz spectrometer with a ⁷Li resonance frequency of 194.381 MHz. The 90° pulse length was typically 2.7-2.8 μs. Air sensitive LNCl probes were sealed in 4 mm diameter Teflon rotors in an Ar glove box. The variable temperature ⁷Li NMR experiments were conducted statically without MAS in a temperature range from -120°C to 160°C. The chemical shifts were referenced to a 0.1 M aqueous LiCl solution.

X-ray diffraction. Powder diffractograms were collected in the 2θ range 10 – 100° using Cu Kα X-rays (1.54 Å, 45 kV, 40 mA) on a PANalytical X'Pert Pro X-ray diffractometer. The air sensitive LNCl probes were loaded into air-tight holders in an Ar glovebox prior to the measurements. An LaB₆ NIST (NIST660c) standard was employed to calibrate instrumental broadening. The JANA2006 program⁶⁰ was used for LeBail and Rietveld refinements and the Williamson-Hall analysis.

Computational details. All DFT calculations were performed with the Vienna ab-initio simulation package VASP with computational settings consistent with those used in the Materials Project database.⁵² Calculations were done on a 2x2x2 LNCl supercell. Because of the partial occupancies in LNCl different atomic arrangements were generated. Starting point was an initial guess of a 2x2x2 supercell with all Li positions occupied (real supercell stoichiometry Li₆₄N₁₁Cl₂₁) the N/Cl arrangement was optimized by minimizing the electrostatic energy using the *OrderDisorderStandardTransformation* tool as implemented in pymatgen.⁶¹ Subsequently, for the 20 arrangements with the lowest electrostatic energy, 20 further supercells were generated by removing Li, again minimizing the electrostatic energy with the *PartialRemoveSpeciesTransformation* tool as implemented in pymatgen.⁶¹ From this pool of 400 supercells, the 40 supercells with the lowest electrostatic energy were relaxed with DFT. Additionally >10 000 supercells were generated randomly. The 40 “random” supercells with the lowest electrostatic energy were relaxed with DFT. The supercell with the lowest internal energy as calculated by DFT was taken and the N/Cl arrangement was re-optimized minimizing the electrostatic energy and the 40 supercells with the

lowest electrostatic energy were relaxed with DFT. Of all supercells generated, the supercell with the lowest internal energy as calculated by DFT was adopted as the model supercell. The stoichiometry of the supercells was always $\text{Li}_{4.82}\text{NCl}_{1.91}$ ($\text{Li}_{53}\text{N}_{11}\text{Cl}_{21}$) and approximates the Li_5NCl_2 ($\text{Li}_{53.333}\text{N}_{10.666}\text{Cl}_{21.333}$) stoichiometry as good as possible given the supercell-size constraints in AIMD simulations. The electrochemical stability window and the pseudo-binaries were calculated as described in the work by Zhu and Mo.⁵¹ For the pseudo-binaries, the SE phase compositions with energies above the hull set to zero were added to the materials project phase space. Subsequently $E_{D, \text{mutual}}$ as defined by Zhu and Mo⁵¹ was calculated between LNCl and respective SEs. AIMD simulations were done in the NVT ensemble and with 2 fs time steps. The kpoint grid used was 1x1x1 and the energy cutoff was 400 eV. For the AIMD simulations the Li pseudopotential was changed from Li_sv (which was used for relaxations) to Li as this enables the use of a lower energy cutoff. The simulation time was > 200 ps for every AIMD simulation and the error on the obtained diffusivities was estimated as done by He and Mo.³³ The dissection of AIMD simulations into individual jump events and subsequent analysis of the prefactor frequency, jump-diffusivity, jump frequencies and individual $E_{a, \text{jump}}$ values was done as first described by de Klerk and Wagemaker;²⁸ a comprehensive account can be found in ref 28 but crucial aspects for the understanding of the reported data is presented here. *Calculation of $E_{a, \text{jump}}$ values between two sites:* The sites are defined around the 0 K equilibrium positions of the Li ions. At every simulation step it is recorded in which site each Li ions is located or whether it is currently between two sites. From this information the jump frequency between two site $v_{A \rightarrow B}$ can be calculated according to equation 2.8:

$$v_{A \rightarrow B} = \frac{N_{A \rightarrow B}}{\tau_A} \quad (2.8)$$

where $v_{A \rightarrow B}$ is the jump frequency for jumps from site A to site B, $N_{A \rightarrow B}$ is the number of recorded jumps from A to B, and τ_A is the time of occupation of site A. $E_{a, \text{jump}}$ is then obtained from equation 2.1. *Calculation of Jump diffusivities and tracer diffusivities D_J and D_{tr} :* D_J and D_{tr} are in principle calculated with the same formula:

$$D = \frac{\langle x^2 \rangle}{2dt} \quad (2.9)$$

Where $\langle x^2 \rangle$ is the mean square displacement of the lithium ions, d the dimensionality of diffusion and t the simulation time. D_J and D_{tr} differ in the way $\langle x^2 \rangle$ is calculated. For D_{tr} , $\langle x^2 \rangle$ is directly obtained from the AIMD simulation. For D_J , $\langle x^2 \rangle$ is calculated by summing up the jump-distances and averaging over the number of Li ions:

$$\langle x^2 \rangle_{\text{for } D_J} = \frac{1}{N} \sum_{i=1}^M a_i^2 \quad (2.10)$$

where N is the total number of diffusing ions and $a_{A \rightarrow B}$ the jump distance of a generalized jump-event “i” and M the total number of jumps observed. Combining equations (2.9) and (2.10) yields equation (2.4). *Calculation of the relative site energies:* LNCl intrinsically contains Li vacancies. The site-energy difference between a site A and a site B was obtained by displacing a Li in site A to an empty site B. The energy difference between the two supercells was interpreted as the site-energy difference between sites A and B. The average site-energy difference between sites A and B was calculated from 10 such displacements.

2.6 References

- (1) Berg, E. J.; Villevieille, C.; Streich, D.; Trabesinger, S.; Novák, P. Rechargeable Batteries: Grasping for the Limits of Chemistry. *J. Electrochem. Soc.* **2015**, *162* (14), A2468–A2475.
- (2) Cao, D.; Sun, X.; Li, Q.; Natan, A.; Xiang, P.; Zhu, H. Lithium Dendrite in All-Solid-State Batteries: Growth Mechanisms, Suppression Strategies, and Characterizations. *Matter* **2020**, *3* (1), 57–94.
- (3) Janek, J.; Zeier, W. G. A Solid Future for Battery Development. *Nat. Energy* **2016**, *1* (9), 1–4.
- (4) Park, K. H.; Bai, Q.; Kim, D. H.; Oh, D. Y.; Zhu, Y.; Mo, Y.; Jung, Y. S. Design Strategies, Practical Considerations, and New Solution Processes of Sulfide Solid Electrolytes for All-Solid-State Batteries. *Adv. Energy Mater.* **2018**, *8* (18), 1–24.
- (5) Abakumov, A. M.; Fedotov, S. S.; Antipov, E. V.; Tarascon, J. M. Solid State Chemistry for Developing Better Metal-Ion Batteries. *Nat. Commun.* **2020**, *11* (1), 1–14.
- (6) Famprikis, T.; Canepa, P.; Dawson, J. A.; Islam, M. S.; Masquelier, C. Fundamentals of Inorganic Solid-State Electrolytes for Batteries. *Nat. Mater.* **2019**, *18*, 1278–1291.
- (7) Zhang, Z.; Shao, Y.; Lotsch, B.; Hu, Y. S.; Li, H.; Janek, J.; Nazar, L. F.; Nan, C. W.; Maier, J.; Armand, M.; Chen, L. New Horizons for Inorganic Solid State Ion Conductors. *Energy Environ. Sci.* **2018**, *11* (8), 1945–1976.
- (8) Riegger, L. M.; Schlem, R.; Sann, J.; Zeier, W. G.; Janek, J. Lithium-Metal Anode Instability of the Superionic Halide Solid Electrolytes and the Implications for Solid-State Batteries. *Angew. Chemie* **2021**, *133* (12), 6792–6797.
- (9) Monroe, C.; Newman, J. The Impact of Elastic Deformation on Deposition Kinetics at Lithium/Polymer Interfaces. *J. Electrochem. Soc.* **2005**, *152* (2), A396.
- (10) Ahmad, Z.; Viswanathan, V. Stability of Electrodeposition at Solid-Solid Interfaces and Implications for Metal Anodes. *Phys. Rev. Lett.* **2017**, *119* (5), 1–6.
- (11) Porz, L.; Swamy, T.; Sheldon, B. W.; Rettenwander, D.; Frömling, T.; Thaman, H. L.; Berendts, S.; Uecker, R.; Carter, W. C.; Chiang, Y. M. Mechanism of Lithium Metal Penetration through Inorganic Solid Electrolytes. *Adv. Energy Mater.* **2017**, *7* (20), 1–12.
- (12) Yu, S.; Schmidt, R. D.; Garcia-Mendez, R.; Herbert, E.; Dudney, N. J.; Wolfenstine, J. B.; Sakamoto, J.; Siegel, D. J. Elastic Properties of the Solid Electrolyte Li₇La₃Zr₂O₁₂ (LLZO). *Chem. Mater.* **2016**, *28* (1), 197–206.
- (13) Weppner, W.; Hartwig, P.; Rabenau, A. Consideration of Lithium Nitride Halides as Solid Electrolytes in Practical Galvanic Cell Applications. *J. Power Sources* **1981**, *6* (3), 251–259.
- (14) Marx, R. Preparation and Crystal Structure of Lithium Nitride Chloride Li₄NCl. *J. Solid State Chem.* **1997**, *128* (2), 241–246.
- (15) Marx, R.; Mayer, H. M. Preparation and Crystal Structure of Ordered and Disordered Lithium Nitride Dichloride, Li₅NCl₂. *J. Solid State Chem.* **1997**, *130* (1), 90–96.
- (16) Marx, R.; Mayer, H. M. Reindarstellung Und Kristallstruktur von Lithiumnitridibromid, Li₅NBr₂. *Zeitschrift für Naturforsch. - Sect. B J. Chem. Sci.* **1995**, *50* (9), 1353–1358.
- (17) Marx, R.; Mayer, H.-M. Darstellung Und Lithiumteilstruktur von Lithiumnitridtribromid, Li₆NBr₃ Und Lithiumnitridtriiodid, Li₆NI₃. *Z. Naturforsch.* **1996**, *3*, 525–530.
- (18) Galvez-Aranda, D. E.; Seminario, J. M. Ab Initio Study of the Interface of the Solid-State Electrolyte Li₉N₂Cl₃ with a Li-Metal Electrode. *J. Electrochem. Soc.* **2019**, *166* (10), A2048–A2057.
- (19) Sang, J.; Yu, Y.; Wang, Z.; Shao, G. Theoretical Formulation of Li₃: A + BNaX_b (X = Halogen) as a Potential Artificial Solid Electrolyte Interphase (ASEI) to Protect the Li Anode. *Phys. Chem. Chem. Phys.* **2020**, *22* (23), 12918–12928.
- (20) Bruce, P. G. *Solid State Electrochemistry*; Cambridge university press, 1997.

- (21) Halogenide, T.; Chloride, T.; Lithium, D. S.; Synthese, S.; Ionenbewegung, K.; Bohnsack, A.; Stenzel, F.; Zajonc, A.; Balzer, G.; Wickleder, M. S.; Synthesis, S.; Structures, C.; Motion, I. *Zeitschrift Fur Anorganische Und Allgemeine Chemie Ternary Halides of the A3MX6 Type . VI .* **1997**, *623*, 1067–1073.
- (22) Li, X.; Liang, J.; Yang, X.; Adair, K. R.; Wang, C.; Zhao, F.; Sun, X. Progress and Perspectives on Halide Lithium Conductors for All-Solid-State Lithium Batteries. *Energy Environ. Sci.* **2020**, *13* (5), 1429–1461.
- (23) Asano, T.; Sakai, A.; Ouchi, S.; Sakaida, M.; Miyazaki, A.; Hasegawa, S. Solid Halide Electrolytes with High Lithium-Ion Conductivity for Application in 4 V Class Bulk-Type All-Solid-State Batteries. *Adv. Mater.* **2018**, *30* (44), 1–7.
- (24) Mo, Y.; Ong, S. P.; Ceder, G. First Principles Study of the Li₁₀GeP₂S₁₂ Lithium Super Ionic Conductor Material. *Chem. Mater.* **2012**, *24* (1), 15–17.
- (25) Han, F.; Zhu, Y.; He, X.; Mo, Y.; Wang, C. Electrochemical Stability of Li₁₀GeP₂S₁₂ and Li₇La₃Zr₂O₁₂ Solid Electrolytes. *Adv. Energy Mater.* **2016**, *6* (8), 1501590.
- (26) Liu, Y.; Wang, S.; Nolan, A. M.; Ling, C.; Mo, Y. Tailoring the Cation Lattice for Chloride Lithium-Ion Conductors. *Adv. Energy Mater.* **2020**, *10* (40), 1–11.
- (27) He, X.; Mo, Y. Accelerated Materials Design of Na_{0.5}Bi_{0.5}TiO₃ Oxygen Ionic Conductors Based on First Principles Calculations. *Phys. Chem. Chem. Phys.* **2015**, *17* (27), 18035–18044.
- (28) De Klerk, N. J. J.; Van Der Maas, E.; Wagemaker, M. Analysis of Diffusion in Solid-State Electrolytes through MD Simulations, Improvement of the Li-Ion Conductivity in β-Li₃PS₄ as an Example. *ACS Appl. Energy Mater.* **2018**, *1* (7), 3230–3242.
- (29) Yu, C.; Ganapathy, S.; De Klerk, N. J. J.; Roslon, I.; Van Eck, E. R. H.; Kentgens, A. P. M.; Wagemaker, M. Unravelling Li-Ion Transport from Picoseconds to Seconds: Bulk versus Interfaces in an Argyrodite Li₆PSSCl-Li₂S All-Solid-State Li-Ion Battery. *J. Am. Chem. Soc.* **2016**, *138* (35), 11192–11201.
- (30) Chen, F.; Xu, L.; Li, J.; Yang, Y.; Shen, Q. Effect of Bottleneck Size on Lithium Migration in Lithium Garnets Li₇La₃Zr₂O₁₂ (LLZO). *Ionics (Kiel)*. **2020**, *26* (6), 3193–3198.
- (31) Fu, Z. H.; Chen, X.; Zhao, C. Z.; Yuan, H.; Zhang, R.; Shen, X.; Ma, X. X.; Lu, Y.; Liu, Q. B.; Fan, L. Z.; Zhang, Q. Stress Regulation on Atomic Bonding and Ionic Diffusivity: Mechanochemical Effects in Sulfide Solid Electrolytes. *Energy and Fuels* **2021**, *35* (12), 10210–10218.
- (32) Shannon, R. D. Revised Effective Ionic Radii and Systematic Studies of Interatomic Distances in Halides and Chalcogenides. *Acta Crystallogr. Sect. A Cryst. physics, diffraction, Theor. Gen. Crystallogr.* **1976**, *32* (5), 751–767.
- (33) He, X.; Zhu, Y.; Epstein, A.; Mo, Y. Statistical Variances of Diffusional Properties from Ab Initio Molecular Dynamics Simulations. *npj Comput. Mater.* **2018**, *4* (1), 1–9.
- (34) Tilley, R. J. D. *Defects in Solids*; John Wiley & Sons, 2008.
- (35) Jia, Y.; Yang, J. Study of the Lithium Solid Electrolytes Based on Lithium Nitride Chloride (Li₉N₂Cl₃). *Solid State Ionics* **1997**, *96* (1–2), 113–117.
- (36) Hartwig, P.; Rabenau, A.; Weppner, W. Phase Equilibria and Thermodynamic Properties of the Li-N-Cl, Li-N-Br and Li-N-I Systems. **1981**, *80*, 81–90.
- (37) Sattlegger, H.; Hahn, H. Über Das System Li₃N/LiCl. *Zeitschrift für Anorg. und Allg. Chemie* **1971**, *379* (3), 293–299.
- (38) Brug, G. J.; van den Eeden, A. L. G.; Sluyters-Rehbach, M.; Sluyters, J. H. The Analysis of Electrode Impedances Complicated by the Presence of a Constant Phase Element. *J. Electroanal. Chem.* **1984**, *176* (1–2), 275–295.
- (39) Hirschorn, B.; Orazem, M. E.; Tribollet, B.; Vivier, V.; Frateur, I.; Musiani, M. Determination of Effective Capacitance and Film Thickness from Constant-Phase-Element Parameters. *Electrochim. Acta* **2010**, *55*, 6218–6227.
- (40) West, A.; Irvine, J.; Sinclair, D. Electroceramics : Characterization by Impedance Spectroscopy. *Adv. Mater.* **1990**, *2* (3), 132–138.
- (41) Epp, V.; Wilkening, M. Li-Ion Dynamics in Solids as Seen Via Relaxation NMR. In *Handbook of Solid State Batteries*; 2016; pp 133–190.

- (42) Brinek, M.; Hiebl, C.; Wilkening, H. M. R. Understanding the Origin of Enhanced Li-Ion Transport in Nanocrystalline Argyrodite-Type Li₆PS₅I. *Chem. Mater.* **2020**, *32* (11), 4754–4766.
- (43) Hendrickson, J. R.; Bray, P. J. A Phenomenological Equation for NMR Motional Narrowing in Solids. *J. Magn. Reson.* **1973**, *9* (3), 341–357.
- (44) Waugh, J.; Fedin, E. No Title. *Sov. Phys. Solid State* **1963**, *1633* (4), 4754–4766.
- (45) Schlem, R.; Burmeister, C. F.; Michalowski, P.; Ohno, S.; Dewald, G. F.; Kwade, A.; Zeier, W. G. Energy Storage Materials for Solid-State Batteries: Design by Mechanochemistry. *Adv. Energy Mater.* **2021**, *11* (30), 2101022.
- (46) Famprikis, T.; Kudu, O. U.; Dawson, J. A.; Canepa, P.; Fauth, F.; Suard, E.; Zbiri, M.; Dambournet, D.; Borkiewicz, O. J.; Bouyanfif, H.; Emge, S. P.; Cretu, S.; Chotard, J. N.; Grey, C. P.; Zeier, W. G.; Islam, M. S.; Masquelier, C. Under Pressure: Mechanochemical Effects on Structure and Ion Conduction in the Sodium-Ion Solid Electrolyte Na₃PS₄. *J. Am. Chem. Soc.* **2020**, *142* (43), 18422–18436.
- (47) Wilkening, M.; Bork, D.; Indris, S.; Heitjans, P. Diffusion in Amorphous LiNbO₃ Studied by ⁷Li NMR - Comparison with the Nano- and Microcrystalline Material. *Phys. Chem. Chem. Phys.* **2002**, *4* (14), 3246–3251.
- (48) Boulineau, S.; Courty, M.; Tarascon, J. M.; Viallet, V. Mechanochemical Synthesis of Li-Argyrodite Li₆PS₅X (X = Cl, Br, I) as Sulfur-Based Solid Electrolytes for All Solid State Batteries Application. *Solid State Ionics* **2012**, *221*, 1–5.
- (49) Breuer, S.; Uitz, M.; Wilkening, H. M. R. Rapid Li Ion Dynamics in the Interfacial Regions of Nanocrystalline Solids. *J. Phys. Chem. Lett.* **2018**, *9* (8), 2093–2097.
- (50) Kuhn, A.; Narayanan, S.; Spencer, L.; Goward, G.; Thangadurai, V.; Wilkening, M. Li Self-Diffusion in Garnet-Type Li₇La₃Zr₂O₁₂ as Probed Directly by Diffusion-Induced Li⁷ Spin-Lattice Relaxation NMR Spectroscopy. *Phys. Rev. B - Condens. Matter Mater. Phys.* **2011**, *83* (9), 1–11.
- (51) Zhu, Y.; He, X.; Mo, Y. First Principles Study on Electrochemical and Chemical Stability of Solid Electrolyte-Electrode Interfaces in All-Solid-State Li-Ion Batteries. *J. Mater. Chem. A* **2016**, *4* (9), 3253–3266.
- (52) Jain, A.; Ong, S. P.; Hautier, G.; Chen, W.; Richards, W. D.; Dacek, S.; Cholia, S.; Gunter, D.; Skinner, D.; Ceder, G.; Persson, K. A. Commentary: The Materials Project: A Materials Genome Approach to Accelerating Materials Innovation. *APL Mater.* **2013**, *1* (1), 001002.
- (53) Schwietert, T. K.; Arszlewska, V. A.; Wang, C.; Yu, C.; Vasileiadis, A.; J Klerk, N. J.; Hageman, J.; Hupfer, T.; Kerkamm, I.; Xu, Y.; Maas, E.; Kelder, E. M.; Ganapathy, S.; Wagemaker, M. Clarifying the Relationship between Redox Activity and Electrochemical Stability in Solid Electrolytes. *Nat. Mater.* **2020**, *19* (4), 428–435.
- (54) Peng, B.; Xu, Y.; Wang, X.; Shi, X.; Mulder, F. M. The Electrochemical Performance of Super P Carbon Black in Reversible Li/Na Ion Uptake. *Sci. China Physics, Mech. Astron.* **2017**, *60* (6), 1–8.
- (55) Hartwig, P.; Weppner, W.; Wichelhaus, W. Fast Ionic Lithium Conduction in Solid Lithium Nitride Chloride. *Mat. Res. Bull.* **1979**, *14*, 493–498.
- (56) Alpen, U. v. Li₃N: A Promising Li Ionic Conductor. *J. Solid State Chem.* **1979**, *29* (3), 379–392.
- (57) Boukamp, B. A.; Huggins, R. A. Lithium Ion Conductivity in Lithium Nitride. *Phys. Lett. A* **1976**, *58* (4), 231–233.
- (58) Rea, J. R.; Foster, D. L.; Mallory, P. R.; Co. Inc. High Ionic Conductivity in Densified Polycrystalline Lithium Nitride. *Mater. Res. Bull.* **1979**, *14* (6), 841–846.
- (59) Weiss, M.; Simon, F. J.; Busche, M. R.; Nakamura, T.; Schröder, D.; Richter, F. H.; Janek, J. From Liquid- to Solid-State Batteries: Ion Transfer Kinetics of Heteroionic Interfaces. *Electrochem. Energy Rev.* **2020**, *3* (2), 221–238.
- (60) Petříček, V.; Dušek, M.; Palatinus, L. Crystallographic Computing System JANA2006: General Features. *Zeitschrift für Krist. - Cryst. Mater.* **2014**, *229* (5), 345–352.
- (61) Ong, S. P.; Richards, W. D.; Jain, A.; Hautier, G.; Kocher, M.; Cholia, S.; Gunter, D.; Chevrier, V. L.; Persson, K. A.; Ceder, G. Python Materials Genomics (Pymatgen): A Robust, Open-Source Python Library for Materials Analysis. *Comput. Mater. Sci.* **2013**, *68*, 314–319.

Chapter 3: Disorder-mediated ionic conductivity in irreducible solid electrolytes

Victor Landgraf, Mengfu Tu, Wenxuan Zhao, Anastasia K. Lavrinenko, Zhu Cheng, Jef Canals, Joris de Leeuw, Swapna Ganapathy, Alexandros Vasileiadis, Marnix Wagemaker, Theodosios Famprikis

3.1 Abstract

Solid-state batteries currently receive extensive attention due to their potential to outperform lithium-ion batteries in terms of energy density when featuring next-generation anodes such as Li metal or silicon. However, most highly conducting solid electrolytes decompose at the low operating voltages of next-generation anodes leading to irreversible lithium loss and increased cell resistance. Such performance losses may be prevented by designing electrolytes which are thermodynamically stable at low operating voltages (anolytes). Here, we report on the discovery a new family of *irreducible* (i.e. *fully reduced*) electrolytes by mechanochemically dissolving lithium nitride into the Li_2S antifluorite structure, yielding highly conducting crystalline $\text{Li}_{2+x}\text{S}_{1-x}\text{N}_x$ phases reaching $> 0.2 \text{ mS cm}^{-1}$ at ambient temperatures. Combining impedance spectroscopy experiments and *ab initio* density functional theory calculations we clarify the mechanism by which the disordering of the sulfide and nitride ions in the anion sublattice boosts ionic conductivity in $\text{Li}_{2+x}\text{S}_{1-x}\text{N}_x$ phases by a factor 10^5 compared to the Li_2S host structure. This advance is achieved through a novel theoretical framework, leveraging percolation analysis with local-environment-specific activation energies and is widely applicable to disordered ion conductors. The same methodology allows us to rationalize how increasing nitrogen content in $\text{Li}_{2+x}\text{S}_{1-x}\text{N}_x$ antifluorite-like samples leads to both increased ionic conductivity and lower conductivity-activation energy. These findings pave the way to understanding disordered solid electrolytes and eliminating decomposition-induced performance losses on the anode side in solid-state batteries.

3.2 Introduction

Solid-state batteries (SSBs) are recently receiving considerable attention in the scientific community because of their potential to outperform conventional lithium-ion batteries.^{1,2} The potential advantages of SSBs originate from their solid nature and single-ion conductivity, improved safety and the possibility of efficient cell stacking (*bipolar stacking*).¹ SSBs will likely only overcome conventional lithium-ion batteries in terms of energy density, if they feature low-potential, high-energy-density anodes such as Si (ref. ³) or Li-metal anodes.^{4,5} Most highly-conducting solid electrolytes decompose at the low potentials of Si and Li metal anodes.⁶⁻⁸ The decomposition into solid electrolyte interphase (SEI) entails irreversible Li-loss – particularly an issue for industrially attractive *zero-Li-excess* battery cells.⁹ Irreversible Li loss from SEI formation may be mediated in three ways: (i) by limiting the contact area between the solid-electrolyte and anode^{10,11}, (ii) by adding sacrificial Li agents such as for instance Li_3N to the cathode^{12,13} or (iii) by designing solid electrolytes which are thermodynamically stable at the operating potentials of low-potential anodes.

Irreducible or *fully reduced* phases are thermodynamically stable against Li metal and are thus inherently irreducible against low-potential anodes. *Irreducible* refers to all elements (except for Li) in the material being in their lowest possible formal oxidation state (i.e. *fully reduced*) and thus not further reducible.

Examples of irreducible phases are lithium binaries (e.g. Li_2S , LiCl , LiBr , Li_2O , Li_3N), lithium-rich antiperovskites (e.g. Li_3OCl , Li_3OBr ; see refs. ^{14,15}), Li_5NCl_2 (refs. ^{16,17}) and the recently discovered $\text{Li}_{2+x}\text{S}_{1-x}\text{P}_x$ ($0 < x < 0.75$) solid solution. ¹⁸ An issue with irreducible phases thus far has been that their ambient-temperature conductivities do not typically reach values above 0.05 mS cm^{-1} — Li_3N and $\text{Li}_{2.75}\text{S}_{0.25}\text{P}_{0.75}$ are exceptions with RT conductivities of 0.5 mS cm^{-1} (ref. ¹⁹) and $\sim 0.25 \text{ mS cm}^{-1}$ (ref. ¹⁸), respectively. The latter $\text{Li}_{2+x}\text{S}_{1-x}\text{P}_x$ ($0 < x < 0.75$) solid solution ¹⁸ is characterized by a disordered anion lattice, yet the effect of the structural disorder on ion conductivity has not yet been clarified.

Structural disorder on the atomic scale —often occupational (i.e. characterized by multiple partially occupied cation positions) and/or compositional (i.e. characterized by mixed occupation of framework sites by multiple different atoms)—is in fact a common feature of most highly conductive solid electrolytes. Both of these types of disorder feature, for example, in the well-studied argyrodite family of ion conductors with the archetypical formula $\text{Li}_6\text{PS}_5\text{X}$ (X: Cl, Br). Nevertheless, the correlation between disorder and ionic conductivity remains a qualitative one. Zeng et al. argued in a recent study that the (often) enhanced conductivity in compositionally disordered solid electrolytes originates from the increased energy-overlap between individual carrier-ion (Li, Na, ...) sites, enabling low-energy percolation paths through solid-electrolyte crystallites —without explicitly considering the energetics of ion hops but instead based on the assumption that sites similar in energy are connected by low activation barriers.²⁰

In the present study, we report the discovery of a new family of irreducible solid electrolytes with the general formula $\text{Li}_{2+x}\text{S}_{1-x}\text{N}_x$ ($0 < x < 0.55$) reaching high conductivities above 0.2 mS cm^{-1} . These are metastable phases, accessible by mechanochemistry and feature a disordered face-centered-cubic arrangement of nitride and sulfide anions. We further develop a widely applicable methodology to investigate the effect of disorder on conductivity that explains the often observed conductivity increase with increased structural disorder. The herein developed methodology comprises the analysis of ion-hop activation energies from molecular dynamics (MD) as a function of local environments and their connectivity via percolation analysis.

We leverage this MD-percolation methodology to rationalize the conductivity boost in the disordered $\text{Li}_{2+x}\text{S}_{1-x}\text{N}_x$ phases. We find that the disordered N/S anion arrangement in $\text{Li}_{2+x}\text{S}_{1-x}\text{N}_x$ electrolytes is causally related to their vastly increased ionic conductivity compared to the structurally and chemically related anion-ordered Li_2S and $\text{Li}_9\text{S}_3\text{N}$ (refs. ^{21,22}), by allowing low-activation-energy ion jumps through locally nitrogen-rich bottlenecks. We show how the MD-percolation methodology may be applied to other disordered solid electrolytes which we demonstrate on the example of the $\text{Li}_6\text{PS}_5\text{Br}$ argyrodite.

3.3 Results and Discussion

Synthesis of disordered- $\text{Li}_9\text{S}_3\text{N}$

Previous investigations on the Li_2S - Li_3N tieline identified the anion-ordered $\text{Li}_9\text{S}_3\text{N}$ phase accessible by conventional solid-state synthesis^{21,22}. After reproducing said synthesis (SI Figure S3.1, Table S3.1), we attempted to synthesize $\text{Li}_9\text{S}_3\text{N}$ mechanochemically, through milling stoichiometric amounts of the precursors (Li_2S and Li_3N). The x-ray and neutron diffraction patterns of the resulting product did not show any leftover precursors (Figure 3.1, Figure S3.1) and we verified through diffraction that no significant amorphous fraction or amorphous impurities are present in samples synthesized with this approach (see Supplementary Note 1).

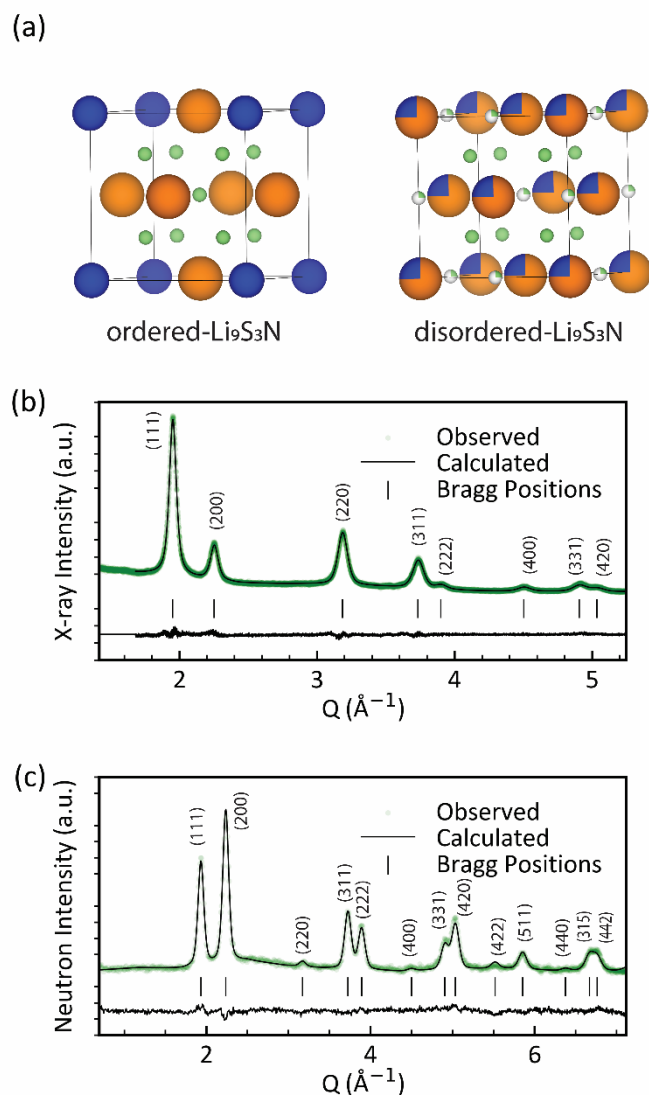


Figure 3.1. Neutron and x-ray powder diffraction on mechanochemically-synthesized anion-disordered $\text{Li}_9\text{S}_3\text{N}$. (a) Unit cell of anion-ordered ($Pm\bar{3}m$) and anion-disordered ($Fm\bar{3}m$) $\text{Li}_9\text{S}_3\text{N}$. (b) x-ray- and (c) neutron diffraction patterns of mechanochemically-synthesized anion-disordered $\text{Li}_9\text{S}_3\text{N}$ along with Rietveld refinements.

Interestingly, poor Rietveld refinements were obtained when attempting to fit the same $Pm\bar{3}m$ - $\text{Li}_9\text{S}_3\text{N}$ structure solution proposed by Marx et al.²¹ to the neutron and x-ray diffraction patterns of the mechanochemically prepared product (SI Figure S3.2). The $Pm\bar{3}m$ - $\text{Li}_9\text{S}_3\text{N}$ structure solution proposed by Marx et al.²¹ (inset Figure 3.1a, Table S3.1) is closely related to the antifluorite ($Fm\bar{3}m$) structure of Li_2S but the face-centered symmetry is broken by the ordered arrangement of sulfur and nitrogen and an additional Li yielding a unit cell with a lower-symmetry $Pm\bar{3}m$ space group and more non-zero-intensity diffraction peaks.

The absence of certain diffraction peaks in the measured diffraction pattern of mechanochemically synthesized $\text{Li}_9\text{S}_3\text{N}$ suggests that the crystal structure of mechanochemically prepared $\text{Li}_9\text{S}_3\text{N}$ has a higher

symmetry than the $Pm\bar{3}m$ structure that Marx et al.²¹ proposed for ampoule-synthesized $\text{Li}_9\text{S}_3\text{N}$. The increased symmetry may originate from a mechanochemically-induced disordering of the S and N atoms. Inspired by the crystal structure of the cubic lithium-deficient antifluorite lithium-nitride-halide Li_5NCl_2 (ref. ¹⁶), we propose the following structure for mechanochemically-prepared $\text{Li}_9\text{S}_3\text{N}$ (SI Table S3.2) : Cubic $Fm\bar{3}m$ with S and N sharing occupation of the Wyckoff 4a (0,0,0) position in a 3:1 proportion as imposed by the $\text{Li}_9\text{S}_3\text{N}$ stoichiometry. The tetrahedral interstitial on the Wyckoff 8c (0.25, 0.25, 0.25) position is fully occupied by Li and the octahedral interstitial on the Wyckoff 4b (0.5, 0.5, 0.5) position is partially occupied (25 %) by Li (Figure 3.1a). In that sense the structure can be considered as an intermediate between the antifluorite (only tetrahedral sites fully occupied; e.g. Na_2O , Li_2S) and Li_3Bi (both tetrahedral and octahedral sites fully occupied) archetypical structures based on interstitial-filling of face-centered lattices.

The proposed lithium-rich disordered antifluorite ($Fm\bar{3}m$) structure solution is supported by the much improved neutron and x-ray Rietveld refinements (SI Figure S3.1). We thus discovered a new material which can be interpreted as a disordered polymorph of the previously known $Pm\bar{3}m$ phase²¹. Based on our structure solution we will from now on refer to the mechanochemically synthesized, anion-disordered ($Fm\bar{3}m$) $\text{Li}_9\text{S}_3\text{N}$ as *disordered*- $\text{Li}_9\text{S}_3\text{N}$ and to solid-state-synthesized, anion-ordered ($Pm\bar{3}m$) $\text{Li}_9\text{S}_3\text{N}$ as *ordered*- $\text{Li}_9\text{S}_3\text{N}$.

We note that the structure solution we propose for disordered- $\text{Li}_9\text{S}_3\text{N}$ (Figure 3.1a, Table S3.2) features large thermal parameters on the Li-sites ($U_{\text{iso}} > 0.07 \text{ \AA}^2$). An in-depth structure analysis supported by molecular dynamics simulations (Supplementary Note 2) demonstrates that these large U_{iso} values originate from displacive relaxations of lithium ions off their ideal positions correlated to the specific local N/S coordination. We also propose an alternative structure solution, in which the octahedral lithium positions are further resolved via site-splitting in combination with lower U_{iso} values. Still, the simple structure solution presented in Figure 3.1a and Table S3.2 captures all the essential features to describe the disordered- $\text{Li}_9\text{S}_3\text{N}$ phase for all following discussions.

Effect of S/N disordering on the conductivity in disordered- $\text{Li}_9\text{S}_3\text{N}$

To compare the ionic conductivities of ordered- and the newly discovered disordered- $\text{Li}_9\text{S}_3\text{N}$ we performed variable-temperature impedance spectroscopy experiments on pelletized powder samples (Figure 3.2). Interestingly, we found an activation energy reduced by 80 meV and a significant ambient-temperature conductivity increase by a factor 30 for disordered- $\text{Li}_9\text{S}_3\text{N}$ (0.064 mS cm^{-1}), compared to ordered- $\text{Li}_9\text{S}_3\text{N}$ ($0.0018 \text{ mS cm}^{-1}$). Next, we occupy ourselves with the underlying mechanism that enabled the 30-fold conductivity increase and the reduced activation energy in disordered- $\text{Li}_9\text{S}_3\text{N}$ compared to ordered- $\text{Li}_9\text{S}_3\text{N}$.

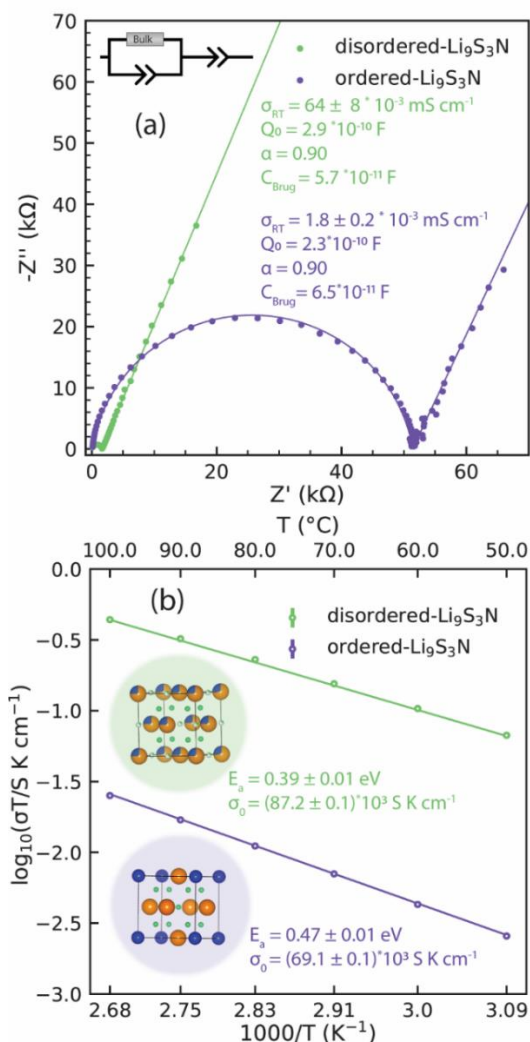


Figure 3.2. Impedance spectroscopy results for ordered and disordered-Li₉S₃N. (a) Room-temperature impedance spectra fitted with the equivalent circuit inset. (b) The Arrhenius plots and fits. All data points obtained from at least two measurements. Error bars often smaller than marker symbol. Inset: structural models with Li, S, N in green, orange, blue, respectively.

Ordered- and disordered-Li₉S₃N feature the same face-centered-cubic anion framework and the same lithium (and thus, vacancy) content and so the change in conductivity cannot be ascribed to the overall concentration of charge carriers. Thus we hypothesize that the vastly different ionic conductivity observed in Figure 3.2 should originate in changes to the relative mobility of Li⁺ ions as a function of the different local structure. To probe this hypothesis we initiated a series of *ab initio* molecular dynamics (AIMD) simulations with ordered-Li₉S₃N and disordered-Li₉S₃N supercells. In disordered supercells the Wyckoff 4a position was randomly decorated with N and S, respecting the 1:3 ratio imposed by the Li₉S₃N stoichiometry. The Wyckoff 4b position was also randomly decorated with Li atoms and vacancies respecting the overall stoichiometry. As done in previous studies we dissected our AIMD simulations into individual jump events.^{16,23–26} In-depth analysis of the AIMD simulations shows that well-defined sites exist in (dis)ordered Li₉S₃N and that jumps between these sites occur mostly independently (i.e. *no* evidence of correlated ion jumps, correlated “cascades” of jumps or correlated “strings” of jumps is found

which have been reported in other high-conducting solid electrolytes such as $\text{Li}_6\text{PS}_5\text{Cl}$ (ref.²⁷) and $\text{Li}_{10}\text{GeP}_2\text{S}_{12}$ (ref.²⁸), see Supplementary Note 5).

From the frequency of jumps between two sites ($\nu_{A \rightarrow B}$) we calculate so-called jump-activation energies (jump- E_a) by using equation (3.1):

$$\text{jump}E_{a,A \rightarrow B} = -k_b T \cdot \ln\left(\frac{\nu_{A \rightarrow B}}{\nu_0}\right) \quad (3.1)$$

where jump- $E_{a,A \rightarrow B}$ the jump-activation energy of a jump event from site A to site B, k_b the Boltzmann constant, T the temperature in K, $\nu_{A \rightarrow B}$ the observed frequency of jumps between sites A and B and ν_0 the *attempt* frequency, which we assume to be 10^{13} Hz. The latter is a widely accepted approximation for ceramic ion conductors^{29–32} and we additionally verified that this approximation applies for the $\text{Li}_9\text{S}_3\text{N}$ system (see Supplementary Note 4).

The jump- $E_{a,A \rightarrow B}$ is a rescaled jump frequency that we interpret as a proxy for the time-averaged local ion hop activation energies and thus the ease of the ion jump from site A to site B. We note that, while both quantify the ease of migration, energy barriers obtained from nudged-elastic-band calculations and the jump- E_a values from AIMD used here are conceptually different and not necessarily equivalent as explained in Supplementary Note 5).

Adopting the above described approach, we could assign an individual jump- E_a values to each different jump type based on local coordination and bottleneck composition. Irrespective of local anion ordering, three general families of jumps are observed through the face-centered anion arrangement in $\text{Li}_9\text{S}_3\text{N}$. (i) tetrahedron(8c)-to-octahedron(4b) (tet-oct), (ii) octahedron(4b)-to-tetrahedron(8c) (oct-tet) and (iii) tetrahedron(8c)-to-tetrahedron(8c) (tet-tet) jumps. Tetrahedral sites are connected to adjacent octahedral sites via triangular bottlenecks composed of three anions, whereas two tetrahedral sites are connected through linear bottlenecks composed of two anions. Both, triangular and linear bottlenecks are shown schematically in Figure 3.2 for ordered- and disordered- $\text{Li}_9\text{S}_3\text{N}$.

We characterize a jump event by its start-site, its end-site and the bottleneck connecting the two sites and use a *start-end(bottleneck)* notation. For example, a $\text{S}_3\text{N-S}_6(\text{SSS})$ jump is a tet-oct jump which starts at a tetrahedral-Li site where the corners of the tetrahedron are occupied by three sulfide and one nitride ion for which we use the notation S_3N_1 . From there on the jump path proceeds through a triangular bottleneck consisting of three sulfide ions for which we use the notation SSS. The end-point of this jump is an octahedral Li site where the corners of the octahedron are all occupied by sulfide ions for which we use the notation S_6 .

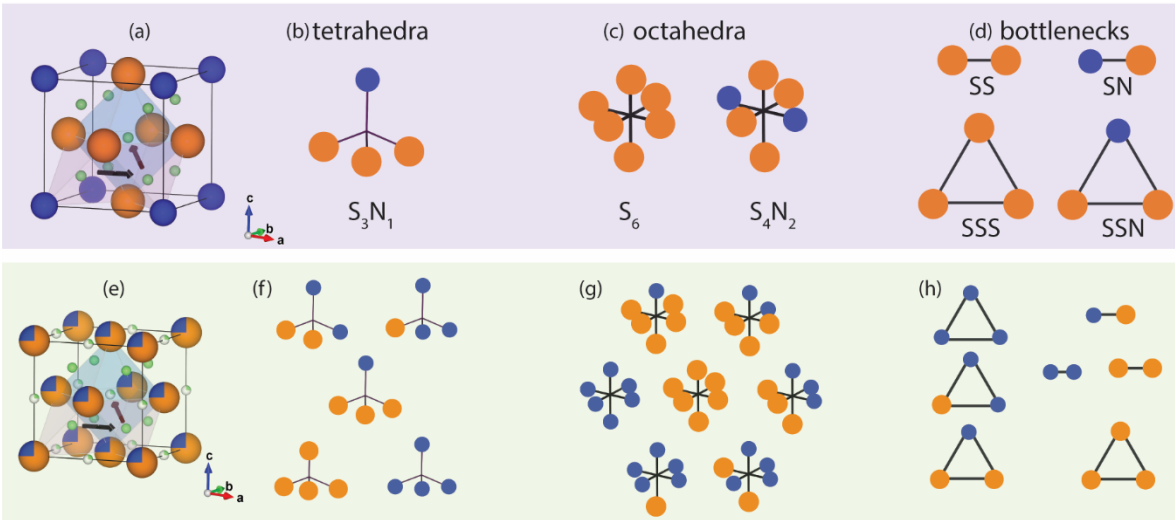


Figure 3.2. Local environments in ordered- and disordered- $\text{Li}_9\text{S}_3\text{N}$. (a) unit cell of ordered- $\text{Li}_9\text{S}_3\text{N}$ ($Pm\bar{3}m$). Example, tetrahedral and octahedral lithium positions in pink and blue, respectively. Black arrows indicate tet-tet and oct-tet jump paths. (b) single tetrahedral site, S_3N_1 present in ordered- $\text{Li}_9\text{S}_3\text{N}$. (c) Two octahedral sites present in ordered- $\text{Li}_9\text{S}_3\text{N}$: S_6 and S_4N_2 . (d) Two linear bottlenecks (SS, NS) and two triangular bottlenecks (SSS, SSN) present in ordered- $\text{Li}_9\text{S}_3\text{N}$. (e) unit cell of disordered- $\text{Li}_9\text{S}_3\text{N}$ ($Fm\bar{3}m$). (f) All five possible tetrahedral compositions in disordered- $\text{Li}_9\text{S}_3\text{N}$. (g) all seven possible octahedral coordinations in disordered- $\text{Li}_9\text{S}_3\text{N}$. (h) all three linear and four triangular bottlenecks possible in disordered- $\text{Li}_9\text{S}_3\text{N}$. Li, S, N in green, orange, blue, respectively.

Figures 3.3a and 3.3e schematically illustrate the tet-tet and oct-tet jump paths through the linear and triangular bottlenecks for the crystal structure of ordered- $\text{Li}_9\text{S}_3\text{N}$ and disordered- $\text{Li}_9\text{S}_3\text{N}$, respectively. Figure 3.3 shows that the disorderly arrangement of S/N in disordered- $\text{Li}_9\text{S}_3\text{N}$ enables a large manifold of different jump types (91 jump-types, Table S3.3), as a result of the possible permutations between starting site, ending site and bottleneck compositions. For instance, taking the example of triangular bottlenecks, in disordered- $\text{Li}_9\text{S}_3\text{N}$, SSS, NSS, NNS and NNN bottlenecks may exist whereas in ordered- $\text{Li}_9\text{S}_3\text{N}$ only SSS and NSS bottlenecks exist (Figure 3.3d,h).

To enable high conductivity, SEs should feature low-energy percolating paths consisting of a series of connected Li jumps with low jump-activation energies. Figure 3.4a demonstrates the jump- E_a values of individual jump types segregated by local environment and determined by equation (3.1) from the MD trajectories. Because of its ordered S/N arrangement, ordered- $\text{Li}_9\text{S}_3\text{N}$ merely features 6 discrete jumps which are shown as discrete points in Figure 3.4a. The uncertainty on individual jump- E_a values is in the range of 10-30 meV and comprises uncertainty associated to convergence as further explored in Supplementary Note 6. The tet-oct jumps being generally higher in energy than the oct-tet jumps is coherent with the fact that the octahedral sites are generally higher in energy compared to the tetrahedral ones (Figure S3.4), which in turn is coherent in the crystallographic model of full tetrahedral- and only partial octahedral Li occupation.

In both phases, ordered- and disordered- $\text{Li}_9\text{S}_3\text{N}$, long-range bulk diffusion occurs along *tet-oct-tet* or *tet-tet* diffusion paths. To illustrate the effect of the determined jump- E_a values on Li diffusion we take the example of a jump- E_a threshold of 0.4 eV: Ordered- $\text{Li}_9\text{S}_3\text{N}$ does not feature tet-oct or tet-tet jumps with a jump- $E_a < 0.4$ eV. Thus *oct-tet-oct* or *tet-tet-tet* diffusion paths —necessary for percolation— where each

individual jump has a jump- $E_a < 0.4$ eV cannot exist and thus no percolation is possible with an overall activation-energy threshold < 0.4 eV.

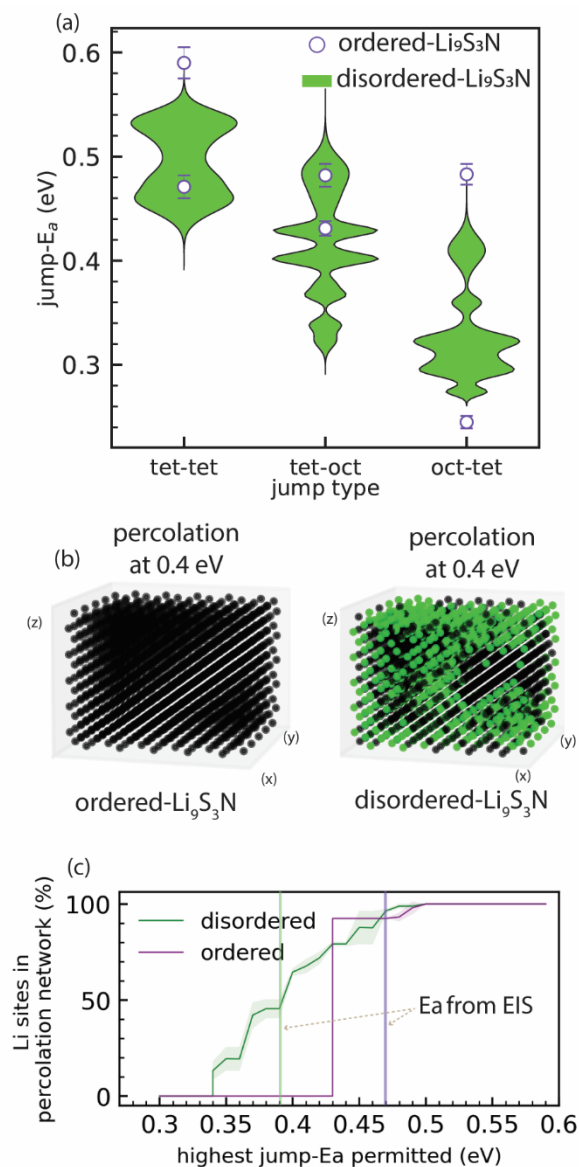


Figure 3.4. Effect of different jump-types existing in ordered and disordered Li₉S₃N. (a) Comparison of the observable jump-activation energies in ordered and disordered-Li₉S₃N. Purple markers indicate jump- E_a of six distinct jump types possible in ordered-Li₉S₃N, labelled with the start-end(bottleneck) notation explained in the main text. In disordered-Li₉S₃N 91 different jumps are observable, listed in SI Table S3.8 and shown here as density plots (violins). The horizontal scale of the violins represent the relative occurrence of jump types at that energy. (b) Lattice of 1500 lithium sites for ordered and disordered Li₉S₃N (5x5x5) supercells. Sites highlighted in green are part of percolating networks with an energy threshold ≤ 0.4 eV. (c) Percolation-energy diagram showing the fraction of Li sites that are connected to percolating networks (averaged over 50 disordered 5x5x5 supercells) for ordered- and disordered-Li₉S₃N. Shading is the standard deviation over 50 supercells. The vertical lines indicate the experimental activation energy $E_{a,EIS}$ obtained experimentally from EIS for ordered- and disordered- Li₉S₃N (see Figure 3.2).

In contrast to ordered-Li₉S₃N, the disordering of S/N in disordered-Li₉S₃N enables a large manifold of 91 different jump types, of which the distribution of jump-activation energies are shown in Figure 3.4 as density (*violin*) plots. In contrast to the ordered case, the disordering of anions creates tet-oct and tet-tet jumps with jump-Ea's < 0.4 eV. Thus *oct-tet-oct* and *tet-tet* diffusion paths where each individual jump has a jump-Ea < 0.4 eV are conceivable —and thus percolation with an overall activation-energy threshold <0.4 eV is possible. From a comparison of the same jump types in ordered and disordered Li₉S₃N supercells it becomes apparent that the long-range anion ordering in ordered-Li₉S₃N has a Li-diffusion hampering effect in addition to the local N/S occupation of polyhedra and bottlenecks as further explored in Supplementary Note 7.

In summary, the above analysis presented in Figures 3.3 and 3.4 suggests that the improved conductivity of disordered-Li₉S₃N originates from the disorder-induced numerous possibilities of octahedral and tetrahedral local coordination environments which introduce new jump-types with low jump-activation energies which enable lower-energy percolating paths that cannot exist in the ordered case.

To consolidate the hypothesis that percolating lower-energy diffusion paths exist in disordered-Li₉S₃N we designed a percolation model. In this percolation model, 5x5x5 supercells are considered, containing 125 formula units of Li₉S₃N, and 1500 lithium sites (Figure 3.4b). Each Li site is related to its neighbors based on the jump-activation energies determined previously. A connection is made between two Li sites if the jump-Ea for both the forward and the backward jump are below a defined jump-Ea cutoff value. If —for a defined jump-Ea cutoff value— a connected path can be found spanning the supercell, then the path is *percolating*, provided that the end-point of percolation is itself a starting-point of a percolating path (as illustrated in Figure S3.5).

The results of our percolation analysis are demonstrated in Figures 3.4b and 3.4c. Figure 3.4b shows that for ordered-Li₉S₃N no percolating path exists when the jump-Ea cutoff is set to 0.4 eV. In contrast, for a disordered-Li₉S₃N supercell with the same jump-Ea cutoff of 0.4 eV a clear percolating network is obtained. Our model also determines the number of Li sites that are connected to the percolating network. As the example in Figure 3.4b demonstrates, even if a percolating network exists, a fraction of Li sites may still be disconnected which may lead to a fraction of Li sites which do not (or significantly more slowly) participate in Li-ion diffusion than Li sites in the percolating network. Li sites in disordered-Li₉S₃N may thus be segregated in *active* and *inactive* sites with regards to long-range lithium diffusion¹. In other words, the majority of jump events involves only a subset of sites that predominantly contribute to the diffusivity (*active*) while the rest remain invariantly vacant or occupied throughout much of the simulation (*inactive*); as may be directly observed from the frequency of occupation change in our AIMD simulations (Figure S3.6).

Figure 3.4c is a percolation-energy diagram and shows the fraction of Li sites in percolating networks for ordered-Li₉S₃N and disordered-Li₉S₃N (average of 50, 5x5x5 supercells) as a function the highest jump-Ea value allowed in the percolation network. The onset of percolation —that is the lowest activation energy for which a percolation network can exist— is markedly lower in the disordered case (0.34 eV) compared to the ordered case (0.43 eV). This is a direct reflection of the lower energy tet-tet and tet-oct jumps available in the disordered case shown in Figure 3.4a but additionally highlights that their connectivity is

¹ We note that the ‘active’ versus ‘inactive’ nomenclature used here, is conceptually comparable to the ‘accessible’ and ‘inaccessible’ nomenclature used in the disordered rock-salt cathode literature⁶⁹

sufficiently likely to enable percolation paths at lower energy thresholds. The lower energy of percolation onset of disordered-Li₉S₃N suggests that long-range diffusion can be sustained more easily in disordered-Li₉S₃N than in ordered-Li₉S₃N. The presence of diffusion at lower energy thresholds is indeed experimentally reflected in the lower activation energy of disordered-Li₉S₃N (0.39 eV) compared to ordered-Li₉S₃N (0.47 eV, Figure 3.2b). In both cases the conductivity-activation energy is 0.04-0.05 eV higher than the simulated percolation-onset energy.

The fact that the experimental *conductivity-activation* energy values are slightly higher than the simulated *percolation-onset* energy values is consistent with the expectation that percolation networks at higher energies than the percolation onset also contribute to the overall diffusion (see Supplementary Note 8).

We conclude at this stage that the increased conductivity of disordered-Li₉S₃N is a consequence of the disordered anionic sublattice which enables numerous octahedral and tetrahedral lithium coordination by combinations of sulfide and nitride ions. Instead of only having S₆, S₄N₂ and N₁S₃ polyhedra like in ordered-Li₉S₃N, disordered-Li₉S₃N features a wide manifold of polyhedra (N₂S₂, S₃N₃, S₂N₄, S₃N₁....). The diverse configurations of the polyhedra in disordered-Li₉S₃N create new sites and bottlenecks which are simply not present in ordered-Li₉S₃N. Some among these new sites and low-energy bottlenecks enable lower-energy percolation and thus the increased conductivity in disordered-Li₉S₃N. The presented mechanism for disorder-induced conductivity enhancement and the analysis approach developed here for Li₉S₃N are widely applicable to other solid electrolytes as we demonstrate using the example of the entirely different Li₆PS₅Br argyrodite system in Supplementary Note 9.

The presented analysis of local jump environments and percolation also enables to optimize ion diffusion by identifying diffusion-promoting and diffusion-hampering local environments. Subsequently, ion diffusion may be optimized by tuning the phase composition to increase the occurrence of diffusion-promoting environments as presented in the following sections.

Understanding diffusion bottlenecks in disordered-Li₉S₃N

Next we explore the relationship between bottleneck composition and local jump-activation energy in disordered-Li₉S₃N. It is expected that the composition of the bottlenecks affects the bottleneck size through the different sizes of the sulfide and nitride anions. The empty space available for Li⁺ in the bottlenecks for different oct-tet ion jumps may be estimated from geometrical considerations by determining the diameter of the circle inscribed in the triangle spanned by the surrounding anions (taking into account their anionic radii) as shown in Figure 3.5a (Table S3.5 summarizes the ionic radii used for the following considerations, Figure S3.7 shows how the bottleneck diameter is analogously obtained for linear bottlenecks between tet-tet jumps). The average bottleneck size and its standard deviation were calculated from 50 DFT-relaxed (2x2x2) disordered Li₉S₃N supercells (>9000 bottlenecks) to account for local distortions which may not be present in long-range averaged crystallographic unit cells.

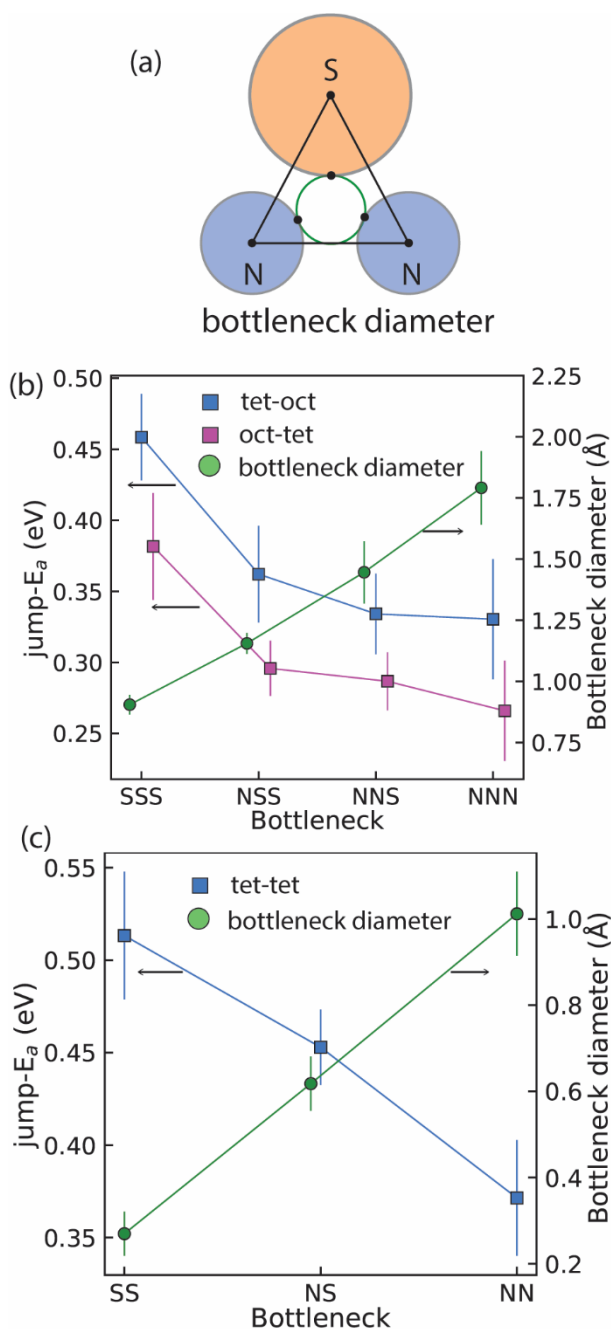


Figure 3.5. Relation between jump activation energies and bottleneck sizes in disordered- $\text{Li}_9\text{S}_3\text{N}$. (a) Illustration of bottleneck definition based on ionic radii of peripheral anions for tet-oct and oct-tet jumps. Analogous definition for tet-tet bottlenecks in Figure S7 (b) Average jump- E_a and bottleneck diameter for tet-oct and oct-tet jumps segregated by bottleneck composition. (c) Average jump- E_a and bottleneck diameter for tet-tet jumps segregated by bottleneck composition. Error bars represent standard deviations from the multiple occurrences of each bottleneck considered.

Figure 3.5b shows the bottleneck size and average jump- E_a for tet-oct and oct-tet jumps in disordered- $\text{Li}_9\text{S}_3\text{N}$ as a function of the different possible jump bottlenecks. This analysis shows that the more nitrogen the bottleneck contains the larger the bottleneck which can be rationalized based on the small ionic radius of N^{3-} (1.46 Å, ref³³) compared to S^{2-} (1.84 Å, ref³³). Further, the more nitrogen a bottleneck contains the lower the jump- E_a . The same trends hold for tet-tet jumps, shown in Figure 3.5c.

We thus observe a correlation between bottleneck size and jump-Ea. In order to rationalize this observation, a useful benchmark is to compare the bottleneck sizes to the diameter of Li⁺ at about 1.18 Å. As the bottleneck size approaches the size of Li⁺, the jump-activation decreases, presumably because of the lessened energy penalty associated with an anion-cation approach smaller than the sum of their ionic radii. This is observed for the tet-tet cases (Figure 3.5c) and partly for the tet-oct cases (Figure 3.5b). For the latter, there is a stark effect in going from an SSS bottleneck (diameter: 0.90 Å) to NSS (1.15 Å) resulting in a decrease in jump-Ea of approximately 100 meV.

As the bottleneck size reaches and surpasses the size of Li⁺ —that is, in the case of NSS, NNS and NNN triangular bottlenecks— the effect of bottleneck-diameter widening on decreasing jump-Ea is lessened and the corresponding jump-activation energies plateau. We quantify the amount of time lithium ions are in unfavorable proximity to the anions (defined as closer than the sum of their respective radii) in SI Figure S3.8, and show indeed that the lower jump-Ea correlates with less time spent too close to the anions.

We have thus established that the jump-Ea generally decreases the more nitrogen the bottleneck contains and we thus identified diffusion-promoting local environments. Based on this observation, we hypothesize that introducing more nitrogen into disordered-Li₉S₃N would increase the number of low-energy nitrogen-containing bottlenecks, thus increasing the number of lower-energy percolation paths, in turn leading to more facile ion conduction.

Solid Solution between Li₃N and Li₂S: Lithium-rich disordered antifluorite phases Li_{2+x}S_{1-x}N_x

To probe the hypothesis that nitrogen content controls ionic conductivity in the sulfide-nitride antifluorites, we synthetically explored compositions on the tie line between Li₂S and Li₃N. The two Li₉S₃N phases lie on the (1-x)Li₂S-xLi₃N tie line with x=0.25. Our findings so far suggest that nitrogen-richer Li_{2+x}S_{1-x}N_x antifluorite phases—if existing— would likely have even higher conductivities than the disordered-Li₉S₃N (i.e. Li_{2.25}S_{0.75}N_{0.25}) because of the higher occurrence of low-energy, nitrogen-rich bottlenecks.

Figure 3.6 shows the results of our synthetic exploration of the Li₂S-Li₃N tie line via mechanochemistry. For samples of overall stoichiometry (1-x)Li₂S-xLi₃N with 0<x<0.55, a single (*Fm* $\bar{3}$ *m*) antifluorite-like phase was observed in the diffractograms (shown in Figure S3.9), indicating that Li₃N dissolves in the antifluorite structure of Li₂S to form a Li_{2+x}S_{1-x}N_x solid solution of anion-disordered phases illustrated in Figure 3.6a. Nitrogen-richer Li_{2+x}S_{1-x}N_x phases have expectedly smaller lattice parameters as obtained from refinements of x-ray diffraction patterns and plotted in Figure 3.6b.

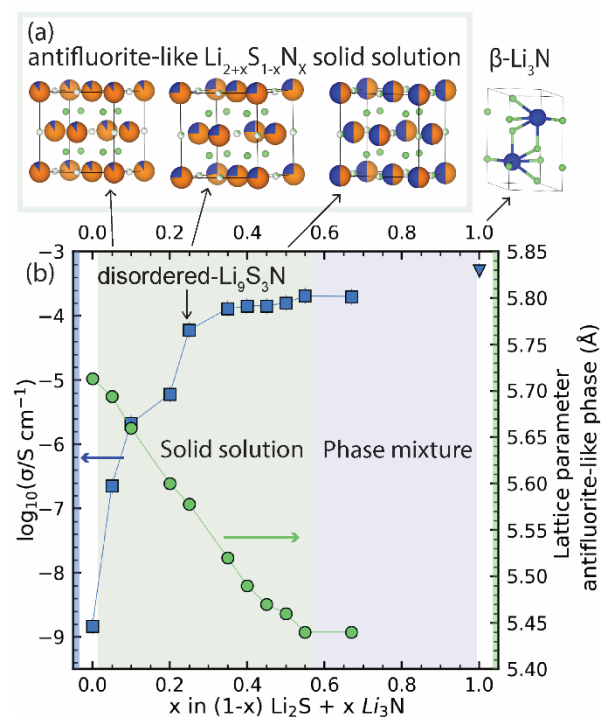


Figure 3.6. Conductivity of the antifluorite-like solid solution on the $(1-x)\text{Li}_2\text{S}-x\text{Li}_3\text{N}$ tie line ($0 < x < 0.55$). (a) Schematic illustration of the $\text{Li}_{2+x}\text{S}_{1-x}\text{N}_x$ ($0 < x < 0.55$) solid solution and hexagonal $\beta\text{-Li}_3\text{N}$ (b) Ionic conductivity and lattice parameter (of antifluorite-like phase) for $(1-x)\text{Li}_2\text{S}-x\text{Li}_3\text{N}$ samples. Green and blue shading indicates antifluorite-like solid solution ($0 < x < 0.55$) and phase separation ($0.55 < x < 1$) regions, respectively. Lines are guides to the eye.

At $x=0.55$ the lattice parameter ceases to decrease with increasing nitrogen content. The diffraction pattern of an attempted synthesis with nominal stoichiometry $0.33\text{Li}_2\text{S}-0.67\text{Li}_3\text{N}$ (i.e. $x=0.67$) showed a phase mixture of Li_3N and an antifluorite $\text{Li}_{2+x}\text{S}_{1-x}\text{N}_x$ phase (Figure S3.9) with the same lattice parameter as $\text{Li}_{2.55}\text{S}_{0.45}\text{N}_{0.55}$ indicating that the solubility limit of Li_3N in Li_2S is reached at $x=0.55$. The nitrogen-richest phase in the $\text{Li}_{2+x}\text{S}_{1-x}\text{N}_x$ antifluorite solid solution is thus $\text{Li}_{2.55}\text{S}_{0.45}\text{N}_{0.55}$.

Figure 3.6b shows that the conductivity increases with increasing nitrogen content in antifluorite-like $\text{Li}_{2+x}\text{S}_{1-x}\text{N}_x$ ($0 < x < 0.55$). For antifluorite Li_2S , mechanochemically milled without Li_3N (i.e. $x=0$), we measured a room-temperature conductivity of 10^{-9} S cm^{-1} . Dissolving a small fraction ($x=0.05$) of nitrogen into the Li_2S host structure already improves the room-temperature conductivity by more than 2 orders of magnitude to $2.2 \times 10^{-7}\text{ S cm}^{-1}$. The conductivity then steadily increases with increasing nitrogen content reaching a high conductivity of 0.22 mS cm^{-1} near the solubility limit at $x=0.55$. Li_3N can thus be dissolved in Li_2S leading to a series of fully reduced solid electrolytes with high ionic conductivities. The conductivity of $\beta\text{-Li}_3\text{N}$ (0.5 mS cm^{-1}) is also shown in Figure 3.6b for comparison —though we note that $\beta\text{-Li}_3\text{N}$ is structurally unrelated to the antifluorite-like $\text{Li}_{2+x}\text{S}_{1-x}\text{N}_x$ solid solution.

We measured the conductivity-activation energy of several synthesized $\text{Li}_{2+x}\text{S}_{1-x}\text{N}_x$ phases ($x=0.05, 0.1, 0.2, 0.25, 0.45$) via impedance spectroscopy at varying temperatures. Figure 3.7a shows that the experimental activation energy of $\text{Li}_{2+x}\text{S}_{1-x}\text{N}_x$ phases decreases with increasing nitrogen content, suggesting lithium diffusivity at lower energy thresholds. The observation of higher room-temperature conductivity and

lower conductivity-activation energy is consistent with our expectation from the analysis of jump-Ea values and their dependence on the bottleneck composition.

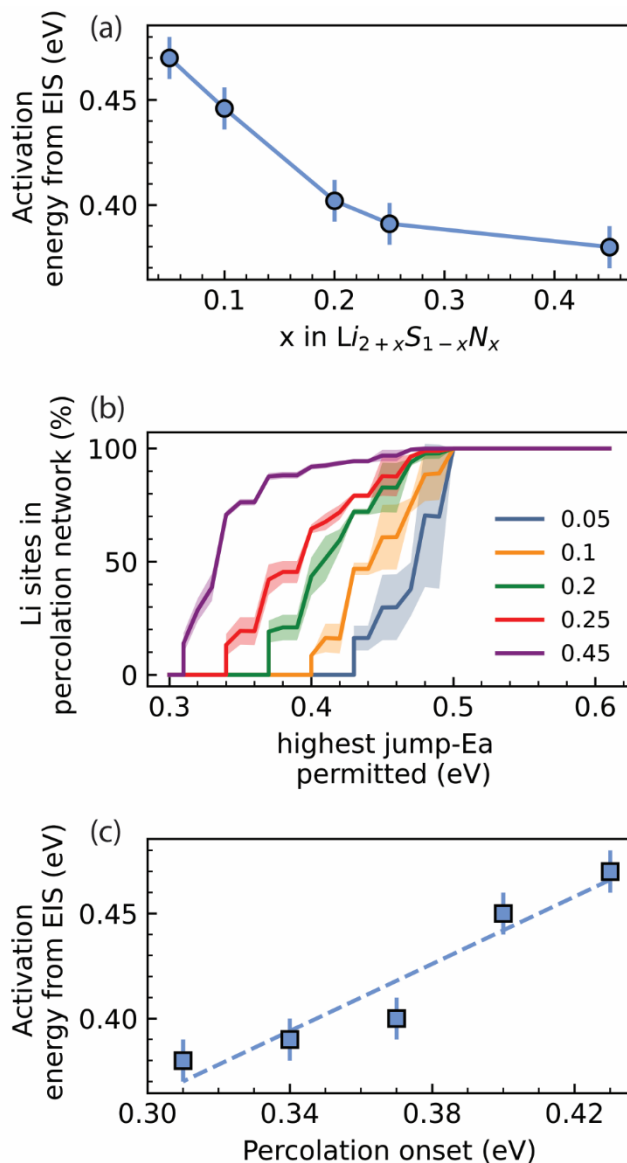


Figure 3.7. Rationalizing the decreasing activation energy for increased nitrogen content in $\text{Li}_{2+x}\text{S}_{1-x}\text{N}_x$ ($0 < x < 0.55$) antifluorite-like phases. (a) Activation energy obtained from impedance spectroscopy at varying temperatures for phases of the $\text{Li}_{2+x}\text{S}_{1-x}\text{N}_x$ solid solution (i.e. $x=0.05, 0.1, 0.2, 0.25, 0.45$) (b) Percolation-energy diagram for different phases in the $\text{Li}_{2+x}\text{S}_{1-x}\text{N}_x$ solid-solution. (c) Correlation between the energy of percolation onset and the activation energies from impedance spectroscopy experiments.

We further calculated the corresponding percolation-energy diagrams for the $\text{Li}_{2+x}\text{S}_{1-x}\text{N}_x$ ($x=0.05, 0.1, 0.2, 0.25, 0.45$) phases (Figure 3.7b) which show increasingly lower energies of percolation onset demonstrating that indeed higher nitrogen content enables diffusion at lower energy thresholds. Taken together with the experimental conductivity results, we arrive at a coherent picture of how nitrogen content in the disordered $\text{Li}_{2+x}\text{S}_{1-x}\text{N}_x$ ($0 < x < 0.55$) solution, modulates lithium-ion diffusion by controlling the energy and distribution of local transition states.

Figure 3.7c highlights the correlation between low-energy percolation onsets and the ability of phases to feature diffusion at low-energy thresholds which is reflected in low experimental conductivity-activation energies. This correlation between the atomistic ($\text{\AA}/\text{nm}$) simulation results and the macroscopic (mm) experimental results underlines the applicability of the MD-percolation approach to rationalize property-composition relationships in disordered systems.

In conclusion, we demonstrate here a previously unknown partial solid solution in the $(1-x)\text{Li}_2\text{S}-x\text{Li}_3\text{N}$ tieline, spanning $0 < x < 0.55$, accessible only by mechanochemistry and crystallizing in antifluorite-like $Fm\bar{3}m$. The increasing conductivity with increasing nitrogen content in antifluorite-like $\text{Li}_{2+x}\text{S}_{1-x}\text{N}_x$ ($0 < x < 0.55$) phases can be rationalized by the increased number of low-energy N-rich bottlenecks enabling more percolating lithium-diffusion paths with lower energy thresholds.

Perspectives for disordered, fully-reduced antifluorite solid electrolytes

Solid electrolytes should feature high ionic conductivity and (electro-)chemical stability against both electrodes. The $\text{Li}_{2+x}\text{S}_{1-x}\text{N}_x$ phases presented here reach $\sim 0.2 \text{ mS cm}^{-1}$ and further improvements of the ionic conductivity may be achieved by further compositional modifications which are very likely possible based on reports nitride-chloride^{16,34,35} and phosphide-sulfide¹⁸ phases with similar antifluorite-like structures, suggesting a large chemical space remaining to be investigated. The $\text{Li}_{2+x}\text{S}_{1-x}\text{N}_x$ phases are structurally analogous to the recently discovered $\text{Li}_{2+x}\text{S}_{1-x}\text{P}_x$ phases which highlights the possibility to substitute phosphide P^{3-} anions ($r \approx 1.89 \text{ \AA}$, Table S3.5) by significantly smaller N^{3-} anions ($r \approx 1.46 \text{ \AA}$, Table S3.5). For a given pnictide content (x) the $\text{Li}_{2+x}\text{S}_{1-x}\text{N}_x$ phases feature higher conductivities than the $\text{Li}_{2+x}\text{S}_{1-x}\text{P}_x$ phases (see SI Figure S3.10) possibly because the smaller N^{3-} radii increases the bottleneck diameter.

Regarding (electro-)chemical stability against electrodes, due to their irreducible nature $\text{Li}_{2+x}\text{S}_{1-x}\text{N}_x$ phases are thermodynamically stable at low potentials down to 0 V vs Li/Li^+ (see also Supplementary Note 11) and thus intrinsically inert to reduction in contact with low-voltage next-generation anodes such as Li-metal or silicon. Indeed we demonstrate in Figure 3.8a stable lithium stripping/deposition in $\text{Li}/\text{Li}_{2.55}\text{S}_{0.45}\text{N}_{0.55}/\text{Li}$ cells over hundreds of hours.

While irreducible, based on our preliminary linear-sweep voltammetry experiments shown in SI Figure S3.11 the $\text{Li}_{2+x}\text{S}_{1-x}\text{N}_x$ phases can be oxidized at modest voltages. For low nitrogen content the anodic limit lies close to 2 V (vs Li/Li^+) which is close to the anodic limit of Li_2S . With increasing nitrogen content, while the ionic conductivity increases, the anodic limit decreases to $\sim 1.25 \text{ V}$ (for $x=0.45$). These low anodic limits are still significantly higher than the anodic limit of Li_3N of ca. 0.8 V vs Li/Li^+ (SI Figure S3.11). While equally inert to reductive decomposition, the increased oxidative stability may be a key advantage of antifluorite-like $\text{Li}_{2+x}\text{S}_{1-x}\text{N}_x$ ($0 < x < 0.55$) phases over Li_3N to enable next-generation anodes.

For example, considering that the operation window of Li_xSi anodes ranges from 0.01 V to 1.1 V, Li_3N would oxidize against Li_xSi anodes due to its low anodic limit of $\sim 0.8 \text{ V}$ vs Li (Figure 3.8c). In contrast, antifluorite-like $\text{Li}_{2+x}\text{S}_{1-x}\text{N}_x$ phases would be more suitable protection layers against Li_xSi anodes as they would be inert to reduction **and** oxidation against Li_xSi anodes. We thus envisage that $\text{Li}_{2+x}\text{S}_{1-x}\text{N}_x$ and related irreducible electrolytes could be applied as anolytes or protective layers against low-potential anodes, in conjunction with a catholyte. As a proof of concept, we demonstrate in Figure 3.8b and in Supplementary Note 11 that $\text{Li}_{2+x}\text{S}_{1-x}\text{N}_x$ ($0 < x < 0.55$) phases may be used to prevent catastrophic decomposition of the Li_2ZrCl_6 solid electrolyte against Li-metal electrodes. These examples demonstrate that inertness to reduction is not the

sole suitability criterion of anolytes and highlights the potential of new highly conducting irreducible phases for enabling next-generation solid-state batteries.

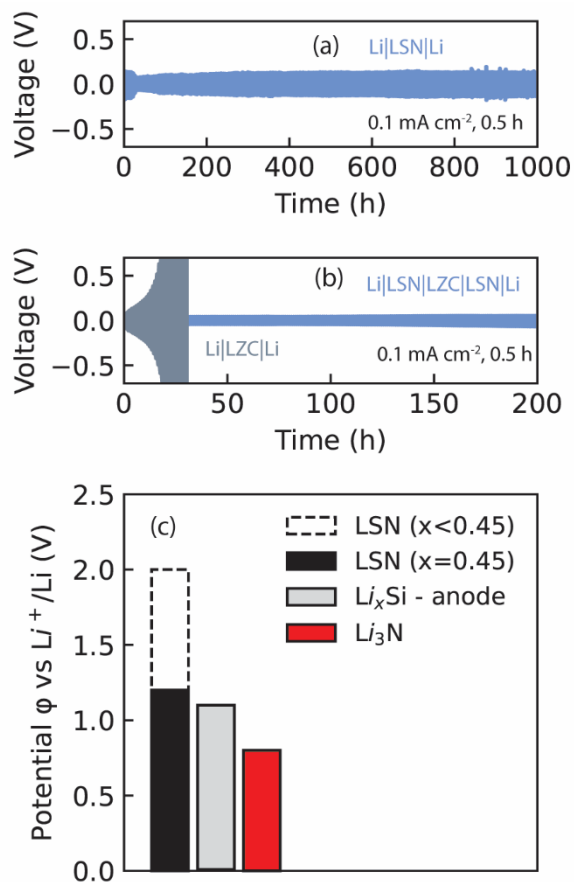


Figure 3.8. Electrochemical characterization of $\text{Li}_{2+x}\text{S}_{1-x}\text{N}_x$ ($0 < x < 0.55$) phases. (a) Symmetric $\text{Li}/\text{Li}_{2.45}\text{S}_{0.45}\text{N}_{0.55}/\text{Li}$ cell cycled at 0.1 mA cm^{-2} , 0.5 h of plating and stripping. (b) Symmetric $\text{Li}/\text{Li}_{2.45}\text{S}_{0.45}\text{N}_{0.55}/\text{Li}_2\text{ZrCl}_6/\text{Li}_{2.45}\text{S}_{0.45}\text{N}_{0.55}/\text{Li}$ and symmetric $\text{Li}/\text{Li}_2\text{ZrCl}_6/\text{Li}$ cells. Catastrophic voltage increase of $\text{Li}/\text{Li}_2\text{ZrCl}_6/\text{Li}$ cells is inhibited by protection against Li-metal with a $\text{Li}_{2+x}\text{S}_{1-x}\text{N}_x$ phase. (c) Black: Stability window of the of $\text{Li}_{2+x}\text{S}_{1-x}\text{N}_x$ phases, increasing with nitrogen content. Red: Stability window of Li_3N . Grey: Potential window over which Li_xSi (silicon) anodes operate.

3.4 Conclusion

In this study we report the discovery of a new family of irreducible solid electrolytes by dissolving lithium nitride into the antifluorite Li_2S resulting in crystalline $\text{Li}_{2+x}\text{S}_{1-x}\text{N}_x$ ($0 < x < 0.55$) lithium-rich antifluorite phases reaching high conductivities $>0.2 \text{ mS cm}^{-1}$ at room temperature. Leveraging a thorough diffusion-percolation analysis, we develop a widely applicable analysis approach and clarify the mechanism by which compositional disorder unlocks high conductivities in these solid electrolytes.

Using the examples of ordered and disordered- $\text{Li}_9\text{S}_3\text{N}$ we demonstrate how the rich diversity of coordination-environment compositions creates new lithium sites and bottlenecks, enabling low-energy-percolating diffusion pathways. In particular, we identify the composition of the bottlenecks as highly correlated with the local jump-activation energy, with nitride-rich bottlenecks favoring diffusion. Based on this observation we endeavor to maximize nitrogen content, in the process discovering a solid solution of

$\text{Li}_{2+x}\text{S}_{1-x}\text{N}_x$ ($0 < x < 0.55$) antifluorite electrolytes reaching 0.2 mS cm^{-1} for the maximum nitrogen composition of $\text{Li}_{2.55}\text{S}_{0.45}\text{N}_{0.55}$.

Based on our combined experimental (EIS)-computational (AIMD-percolation) analyses on $\text{Li}_{2+x}\text{S}_{1-x}\text{N}_x$ we establish that nitrogen-richer compositions indeed show higher conductivities and lower conductivity-activation energies that can be rationalized by lower percolation onset energies due to the increased occurrence of low jump-activation energy, nitrogen-rich bottlenecks.

The new $\text{Li}_{2+x}\text{S}_{1-x}\text{N}_x$ ($0 < x < 0.55$) electrolytes we discovered are irreducible, thus thermodynamically stable against all known next-generation low-potential anode materials for batteries. Their high conductivities and stability at low potentials make these new electrolytes a natural choice for much needed anolytes and protection layers combination with low-potential, high-capacity anodes such as Si or Li metal.

Most relevantly, our results shed light on the mechanism by which structural disorder can affect ionic conductivity in solids. Contrary to recent research trends, we show that high compositional complexity (e.g. in so called *high-entropy* materials) is not necessary to access the disorder-mediated improvements of ionic conductivity. Instead, by comparing disordered $\text{Li}_9\text{S}_3\text{N}$ and $\text{Li}_6\text{PS}_5\text{Br}$ argyrodite to their ordered counterparts of the same composition, we demonstrate that stabilizing metastable configurations of compositionally simple (*low entropy*) materials —e.g. through mechanochemistry, quenching or soft-chemical approaches— can be sufficient to effect dramatic ionic conductivity improvements without invoking compositional complexity.

3.5 Methodology

Synthesis. $\text{Li}_{2+x}\text{S}_{1-x}\text{N}_x$ phases: The synthesis precursors were Li_2S (Sigma-Aldrich, 99%) and Li_3N (Sigma-Aldrich, >99.5%). Stoichiometric amounts of the precursors were milled in a planetary ball mill (Jar: ZrO_2 , 45 mL) with 10 mm ZrO_2 balls and a ball:powder mass ratio of 30 at 550 rpm for 99 (5-min milling-5 min-pause) cycles. *Ordered*- $\text{Li}_9\text{S}_3\text{N}$: We closely followed the procedure described by Miara and coworkers²². A planetary ball mill jar with 10 mm ZrO_2 balls and a ball/powder ratio of 30 at 550 rpm for 99 (5-min-milling-5 min-pause) cycles was used to mix the precursors Li_2S and Li_3N . Subsequently the powder mixture was transferred to tungsten crucibles and sealed into quartz glass ampoules under 200 mbar of argon. The ampoules were then heated ($100^\circ\text{C}/\text{h}$) to 600°C held at this temperature for 24 h and then slowly (over the course of 24 h) cooled down to RT. All preparation steps were performed in an argon atmosphere ($\text{H}_2\text{O} < 1 \text{ ppm}$, $\text{O}_2 < 1 \text{ ppm}$).

Electrochemical Characterization. *Electrochemical Impedance Spectroscopy (EIS)*: Pellets (diameter=10 mm) of the $\text{Li}_{2+x}\text{S}_{1-x}\text{N}_x$ probes were pressed (3.2 tons) in custom-made solid-state lab cells. These lab cells consist of an alumina tube and two stainless steel plungers. Solid electrolyte powder is filled in the alumina tube and compressed on both sides with the stainless steel plungers. The cell configuration used was SS | $\text{Li}_{2+x}\text{S}_{1-x}\text{N}_x$ | SS (SS=stainless steel). AC impedance was performed with a Metrohm Autolab (AUT86298) in the frequency range 10 MHz to 0.1 Hz with a voltage amplitude of 10 mV. *Linear sweep voltammetry (LSV)*: LSV measurements were also performed with an Metrohm Autolab (AUT86298). To measure the anodic limit of $\text{Li}_{2+x}\text{S}_{1-x}\text{N}_x$ phases, $\text{Li} | \text{Li}_{2+x}\text{S}_{1-x}\text{N}_x | \text{Li}_{2+x}\text{S}_{1-x}\text{N}_x$ -C cells were used. To make the $\text{Li}_{2+x}\text{S}_{1-x}\text{N}_x$ -C composite cathode a mixture of $\text{Li}_{2+x}\text{S}_{1-x}\text{N}_x$:Super P with a weight ratio of 0.7:0.3 was milled in

a planetary ball mill (Jar: ZrO₂, 45 mL) with 10 mm ZrO₂ balls and a ball/powder ratio of 30 at 400 rpm for 2 h (5 min milling; 5 min pause). Li | Li_{2+x}S_{1-x}N_x | Li_{2+x}S_{1-x}N_x -C cells were assembled by pressing a Li_{2+x}S_{1-x}N_x pellet (130 mg, 3.2 tons) and subsequently the Li_{2+x}S_{1-x}N_x -C composite (15 mg, 3.2 tons) on top of it. Finally, a Li disk was placed on the opposite side of the Li_{2+x}S_{1-x}N_x pellet. The LSV scanning rate was 0.01 mV s⁻¹. *Conductivity measurements at different temperatures for Arrhenius fits:* SS | Li_{2+x}S_{1-x}N_x | SS cells were kept at 30°C for 1h, then heated in 5 min to 50°C and kept at this temperature for 30 min followed by heating to 60°C in 5 min and maintaining the temperature for 30 min. This procedure was continued up to 100°C. The EIS obtained at the end of the 30 min temperature-plateaus were used for Arrhenius fits.

X-ray diffraction. Powder diffraction patterns were collected using Cu K α X-rays (1.54 Å) on a PANalytical X'Pert Pro X-ray diffractometer in Bragg-Brenano (*reflection*) geometry up to a 2 θ _{max} ≈ 80° (q_{max} ≈ 5.2 Å⁻¹). The air sensitive Li_{2+x}S_{1-x}N_x probes were loaded into air-tight holders in an Ar-filled glovebox prior to the measurements. GSAS-II³⁶ and FullProf³⁷ (through the user interface implemented in the “Match!” software) were used for LeBail and Rietveld refinements.

Neutron diffraction. Neutron powder diffraction data were collected on the PEARL neutron powder diffractometer at the research reactor of TU Delft.³⁸ Approximately 4 g of samples were loaded on 6-mm diameter cylindrical vanadium holders and sealed using indium wire under Ar atmosphere. Measurements were collected of the powder samples at room temperature with a neutron wavelength of 1.667 Å selected using the 533 reflection of a Ge monochromator, in transmission geometry up to a 2 θ _{max} ≈ 155° (q_{max} ≈ 7.3 Å⁻¹).

Computational details. All DFT calculations were performed with the Vienna ab-initio simulation package VASP with computational settings consistent with those used in the Materials Project database.³⁹ For the generation and analysis of supercells the calculations were done on 2x2x2 Li_{2+x}S_{1-x}N_x supercells. Because of the shared site occupations and partial occupancies in Li_{2+x}S_{1-x}N_x phases different atomic arrangements were generated by random decoration of the Wyckoff 4a (0,0,0) position with nitrogen and sulfur and the 4b (0.5,0.5,0.5) positions were randomly decorated with Li and vacancies. The Wyckoff 8c (0.25,0.25,0.25) position was fully occupied with Li for all stoichiometries. For the generation and analysis of supercells the pymatgen package was used.⁴⁰ For the AIMD simulations the Li pseudopotential was changed from Li_sv (which was used for relaxations) to Li as this enables the use of a lower energy cutoff. The simulation time was > 200 ps for every AIMD simulation. The AIMD simulations were executed at 900 K. The dissection of AIMD simulations into individual jump events and subsequent analysis of jump frequencies and individual E_{a, Jump} values was done as first described by de Klerk and Wagemaker;²³ a comprehensive account can be found in ref²³ but crucial aspects for the understanding of the reported data is presented here: *Partitioning of the supercell volume into site and non-site voxels:* The lithium site centers are obtained from crystallography and the site radii are set to the average vibrational amplitude of the Li-ions as described in ref.²³. Given the site center and site radius, spherical sites are defined around the site-center. *Calculation of E_{a, jump} values between two sites:* The sites are defined around the 0 K equilibrium positions of the Li ions. At every simulation step it is recorded in which site each Li ion is located or whether it is currently between two sites. From this information the jump frequency between two site v_{A→B} can be calculated according to equation 3.2:

$$v_{A \rightarrow B} = \frac{N_{A \rightarrow B}}{\tau_A} \quad (3.2)$$

where $v_{A \rightarrow B}$ is the jump frequency for jumps from site A to site B, $N_{A \rightarrow B}$ is the number of recorded jumps from A to B, and τ_A is the time of occupation of site A. $E_{a, \text{jump}}$ is then obtained from equation (3.1). The uncertainty on the average jump-Ea value for a jump type can be obtained from the standard deviation of the mean (ϵ_{mean}) and the uncertainty associated with convergence ($\epsilon_{\text{convergence}}$, as further detailed in Supplementary Note 6) so that the total uncertainty on average jump-Ea values is $\epsilon_{\text{jump-ea}} = \epsilon_{\text{mean}} + \epsilon_{\text{convergence}}$ and is typically on the range of 10-30 meV. This whole analysis is strongly supported by the gemdat (ref⁴¹) python package currently developed in our group.

Percolation model: We performed AIMD simulations on 8 selected supercells that in sum contained all jump events present in the disordered $\text{Li}_{2+x}\text{S}_{1-x}\text{N}_x$ phases (incl. disordered- $\text{Li}_9\text{S}_3\text{N}$); this enabled the construction of a *jump library* with an average jump-Ea value for each jump event, shown in SI Tables S3.3 and S3.4. The jump events for ordered- $\text{Li}_9\text{S}_3\text{N}$ were obtained from an AIMD simulation of an ordered- $\text{Li}_9\text{S}_3\text{N}$ supercell. Subsequently a percolation analysis could be performed on 50 (5x5x5) supercells for each of the different $\text{Li}_{2+x}\text{S}_{1-x}\text{N}_x$ stoichiometries ($x=0.05, 0.1, 0.2, 0.25, 0.3, 0.4, 0.5, 0.6, 0.7, 0.8, 0.9$). The percolation analysis works as follows: An activation energy cutoff is defined. Two sites A and B are connected if a randomly picked element in the range [$\text{jump-Ea}_{(A \rightarrow B)} - \text{uncertainty}, \text{jump-Ea}_{(A \rightarrow B)} + \text{uncertainty}$] and a randomly picked element in the range [$\text{jump-Ea}_{(B \rightarrow A)} - \text{uncertainty}, \text{jump-Ea}_{(B \rightarrow A)} + \text{uncertainty}$] are below the activation energy cutoff. In this way a graph can be constructed which we did using the rustworkX package ref⁴². If a path extends throughout the supercell the path is considered percolating, provided that the endpoint of the percolation path is equally a starting point of a percolating path (see SI Figure S3.5). For a given supercell and a given energy cutoff the analysis needs to be repeated until the average fraction of sites in the percolation network converges. In cases where only a subset of supercells were percolating at a given cutoff the average fraction of percolating sites was obtained from percolating supercells. The standard deviation of the distribution of fractions at one cutoff energy was taken as the uncertainty on the fraction of active Li sites. *Bottleneck size calculations:* 50 disordered $\text{Li}_9\text{S}_3\text{N}$ supercells were relaxed (containing > 9000 bottlenecks) to account for local distortions which may not be present in long-range averaged crystallographic unit cells. The three atoms at the vertices of triangular bottlenecks connecting sites were identified and the inner-circle diameter using the sympy Triangle package. For the calculation of bottleneck diameters the bisecting line (line that “cuts an angle in half”) was followed by the distance of the ion-radius of the ion located at the vertex. This was done at all three vertices so that a new triangle is formed. The outer-circle diameter of this new triangle is determined by the sympy (ref⁴³) Triangle package and is the bottleneck diameter. For each type of bottleneck (i.e. NSS, NNS...) the average diameter is determined and the standard deviation of the distribution of diameters is shown as the error bar.

3.6 References

- (1) Janek, J.; Zeier, W. G. Challenges in Speeding up Solid-State Battery Development. *Nat. Energy* **2023**, *8* (3), 230–240.
- (2) Betz, J.; Bieker, G.; Meister, P.; Placke, T.; Winter, M.; Schmuch, R. Theoretical versus Practical Energy: A Plea for More Transparency in the Energy Calculation of Different Rechargeable Battery Systems. *Adv. energy Mater.* **2019**, *9* (6), 1803170.
- (3) Lewis, J. A.; Cavallaro, K. A.; Liu, Y.; McDowell, M. T. The Promise of Alloy Anodes for Solid-State Batteries. *Joule* **2022**, *6* (7), 1418–1430.
- (4) Janek, J.; Zeier, W. G. A Solid Future for Battery Development. *Nat. Energy* **2016**, *1* (9), 1–4.
- (5) Krauskopf, T.; Richter, F. H.; Zeier, W. G.; Janek, J. Physicochemical Concepts of the Lithium Metal Anode in Solid-State Batteries. *Chem. Rev.* **2020**, *120* (15), 7745–7794.
- (6) Zhu, Y.; He, X.; Mo, Y. First Principles Study on Electrochemical and Chemical Stability of Solid Electrolyte-Electrode Interfaces in All-Solid-State Li-Ion Batteries. *J. Mater. Chem. A* **2016**, *4* (9), 3253–3266.
- (7) Schwietert, T. K.; Arszewska, V. A.; Wang, C.; Yu, C.; Vasileiadis, A.; de Klerk, N. J. J.; Hageman, J.; Hupfer, T.; Kerkamm, I.; Xu, Y. Clarifying the Relationship between Redox Activity and Electrochemical Stability in Solid Electrolytes. *Nat. Mater.* **2020**, *19* (4), 428–435.
- (8) Kim, K.; Park, D.; Jung, H.-G.; Chung, K. Y.; Shim, J. H.; Wood, B. C.; Yu, S. Material Design Strategy for Halide Solid Electrolytes Li_3MX_6 (X= Cl, Br, and I) for All-Solid-State High-Voltage Li-Ion Batteries. *Chem. Mater.* **2021**, *33* (10), 3669–3677.
- (9) Lohrberg, O.; Voigt, K.; Maletti, S.; Auer, H.; Nikolowski, K.; Heubner, C.; Michaelis, A. Benchmarking and Critical Design Considerations of Zero-Excess Li-Metal Batteries. *Adv. Funct. Mater.* **2023**, 2214891.
- (10) Han, F.; Zhu, Y.; He, X.; Mo, Y.; Wang, C. Electrochemical Stability of $\text{Li}_{10}\text{GeP}_2\text{S}_{12}$ and $\text{Li}_7\text{La}_3\text{Zr}_2\text{O}_{12}$ Solid Electrolytes. *Adv. Energy Mater.* **2016**, *6* (8), 1501590.
- (11) Huo, H.; Janek, J. Silicon as Emerging Anode in Solid-State Batteries. *ACS Energy Lett.* **2022**, *7* (11), 4005–4016.
- (12) Sun, Y.; Li, Y.; Sun, J.; Li, Y.; Pei, A.; Cui, Y. Stabilized Li_3N for Efficient Battery Cathode Prelithiation. *Energy Storage Mater.* **2017**, *6* (October 2016), 119–124.
- (13) Park, S. W.; Choi, H. J.; Yoo, Y.; Lim, H.; Park, J.; Lee, Y.; Ha, Y.; Lee, S.; Kim, B. G. Stable Cycling of All-solid-state Batteries with Sacrificial Cathode and Lithium-free Indium Layer. *Adv. Funct. Mater.* **2022**, *32* (5), 2108203.
- (14) Zheng, J.; Perry, B.; Wu, Y. Antiperovskite Superionic Conductors: A Critical Review. *ACS Mater. Au* **2021**, *1* (2), 92–106.
- (15) Dawson, J. A.; Famprikis, T.; Johnston, K. E. Anti-Perovskites for Solid-State Batteries: Recent

- Developments, Current Challenges and Future Prospects. *J. Mater. Chem. A* **2021**, *9* (35), 18746–18772.
- (16) Landgraf, V.; Famprikis, T.; de Leeuw, J.; Bannenberg, L. J.; Ganapathy, S.; Wagemaker, M. Li_5NCl_2 : A Fully-Reduced, Highly-Disordered Nitride-Halide Electrolyte for Solid-State Batteries with Lithium-Metal Anodes. *ACS Appl. Energy Mater.* **2023**, *6* (3), 1661–1672.
- (17) Li, W.; Li, M.; Chien, P.; Wang, S.; Yu, C.; King, G.; Hu, Y.; Xiao, Q.; Shakouri, M.; Feng, R.; Fu, B.; Abdolvand, H.; Fraser, A.; Li, R.; Huang, Y.; Liu, J.; Mo, Y.; Sham, T.; Sun, X. Lithium-Compatible and Air-Stable Vacancy-Rich $\text{Li}_9\text{N}_2\text{Cl}_3$ for High – Areal Capacity, Long-Cycling All – Solid-State Lithium Metal Batteries. **2023**.
- (18) Szczuka, C.; Karasulu, B.; Groh, M. F.; Sayed, F. N.; Sherman, T. J.; Bocarsly, J. D.; Vema, S.; Menkin, S.; Emge, S. P.; Morris, A. J.; Grey, C. P. Forced Disorder in the Solid Solution $\text{Li}_3\text{P-Li}_2\text{S}$: A New Class of Fully Reduced Solid Electrolytes for Lithium Metal Anodes. *J. Am. Chem. Soc.* **2022**, *144* (36), 16350–16365.
- (19) Xu, X.; Du, G.; Cui, C.; Liang, J.; Zeng, C.; Wang, S.; Ma, Y.; Li, H. Stabilizing the Halide Solid Electrolyte to Lithium by a $\beta\text{-Li}_3\text{N}$ Interfacial Layer. *ACS Appl. Mater. Interfaces* **2022**, *14* (35), 39951–39958.
- (20) Zeng, Y.; Ouyang, B.; Liu, J.; Byeon, Y. W.; Cai, Z.; Miara, L. J.; Wang, Y.; Ceder, G. High-Entropy Mechanism to Boost Ionic Conductivity. *Science (80-.)*. **2022**, *378* (6626), 1320–1324.
- (21) Marx, R.; Lissner, F.; Schleid, T. $\text{Li}_9\text{N}_2\text{S}_3$: Das Erste Nitridsulfid Der Alkalimetalle in Einer Li_2O -Typ-Variante. *Zeitschrift für Anorg. und Allg. Chemie* **2006**, *632* (12-13), 2151.
- (22) Miara, L. J.; Suzuki, N.; Richards, W. D.; Wang, Y.; Kim, J. C.; Ceder, G. Li-Ion Conductivity in $\text{Li}_9\text{S}_3\text{N}$. *J. Mater. Chem. A* **2015**, *3* (40), 20338–20344.
- (23) De Klerk, N. J. J.; Van Der Maas, E.; Wagemaker, M. Analysis of Diffusion in Solid-State Electrolytes through MD Simulations, Improvement of the Li-Ion Conductivity in $\beta\text{-Li}_3\text{PS}_4$ as an Example. *ACS Appl. Energy Mater.* **2018**, *1* (7), 3230–3242.
- (24) Yu, C.; Ganapathy, S.; De Klerk, N. J. J.; Roslon, I.; Van Eck, E. R. H.; Kentgens, A. P. M.; Wagemaker, M. Unravelling Li-Ion Transport from Picoseconds to Seconds: Bulk versus Interfaces in an Argyrodite $\text{Li}_6\text{PS}_5\text{Cl-Li}_2\text{S}$ All-Solid-State Li-Ion Battery. *J. Am. Chem. Soc.* **2016**, *138* (35), 11192–11201.
- (25) De Klerk, N. J. J.; Rosłoń, I.; Wagemaker, M. Diffusion Mechanism of Li Argyrodite Solid Electrolytes for Li-Ion Batteries and Prediction of Optimized Halogen Doping: The Effect of Li Vacancies, Halogens, and Halogen Disorder. *Chem. Mater.* **2016**, *28* (21), 7955–7963.
- (26) De Klerk, N. J. J.; Wagemaker, M. Diffusion Mechanism of the Sodium-Ion Solid Electrolyte Na_3PS_4 and Potential Improvements of Halogen Doping. *Chem. Mater.* **2016**, *28* (9), 3122–3130.
- (27) Morgan, B. J. Mechanistic Origin of Superionic Lithium Diffusion in Anion-Disordered $\text{Li}_6\text{PS}_5\text{X}$ Argyrodites. *Chem. Mater.* **2021**, *33* (6), 2004–2018.
- (28) He, X.; Zhu, Y.; Mo, Y. Origin of Fast Ion Diffusion in Super-Ionic Conductors. *Nat. Commun.* **2017**, *8* (May), 1–7.

- (29) Van der Ven, A.; Ceder, G.; Asta, M.; Tepesch, P. D. First-Principles Theory of Ionic Diffusion with Nondilute Carriers. *Phys. Rev. B* **2001**, *64* (18), 184307.
- (30) Almond, D. P.; Duncan, G. K.; West, A. R. The Determination of Hopping Rates and Carrier Concentrations in Ionic Conductors by a New Analysis of Ac Conductivity. *Solid State Ionics* **1983**, *8* (2), 159–164.
- (31) Wang, Z.; Mishra, T. P.; Xie, W.; Deng, Z.; Gautam, G. S.; Cheetham, A. K.; Canepa, P. Kinetic Monte Carlo Simulations of Sodium Ion Transport in NaSICON Electrodes. *ACS Mater. Lett.* **2023**, *5* (9), 2499–2507.
- (32) Deng, Z.; Mishra, T. P.; Mahayoni, E.; Ma, Q.; Tieu, A. J. K.; Guillon, O.; Chotard, J.-N.; Seznec, V.; Cheetham, A. K.; Masquelier, C. Fundamental Investigations on the Sodium-Ion Transport Properties of Mixed Polyanion Solid-State Battery Electrolytes. *Nat. Commun.* **2022**, *13* (1), 4470.
- (33) Shannon, R. D. Revised Effective Ionic Radii and Systematic Studies of Interatomic Distances in Halides and Chalcogenides. *Acta Crystallogr. Sect. A Cryst. physics, diffraction, Theor. Gen. Crystallogr.* **1976**, *32* (5), 751–767.
- (34) Li, W.; Li, M.; Chien, P.-H.; Wang, S.; Yu, C.; King, G.; Hu, Y.; Xiao, Q.; Shakouri, M.; Feng, R. Lithium-Compatible and Air-Stable Vacancy-Rich Li₉N₂Cl₃ for High-Areal Capacity, Long-Cycling All-Solid-State Lithium Metal Batteries. *Sci. Adv.* **2023**, *9* (42), eadh4626.
- (35) Marx, R.; Mayer, H. M. Preparation and Crystal Structure of Ordered and Disordered Lithium Nitride Dichloride, Li₅NCl₂. *J. Solid State Chem.* **1997**, *130* (1), 90–96.
- (36) Toby, B. H.; Von Dreele, R. B. GSAS-II: The Genesis of a Modern Open-Source All Purpose Crystallography Software Package. *J. Appl. Crystallogr.* **2013**, *46* (2), 544–549.
- (37) Rodriguez-Carvajal, J. In Satellite Meeting on Powder Diffraction of the XV Congress of the IUCr, 1990, 127. *Toulouse, Fr.*
- (38) Van Eijck, L.; Cussen, L. D.; Sykora, G. J.; Schooneveld, E. M.; Rhodes, N. J.; Van Well, A. A.; Pappas, C. Design and Performance of a Novel Neutron Powder Diffractometer: PEARL at TU Delft. *J. Appl. Crystallogr.* **2016**, *49* (5), 1398–1401.
- (39) Jain, A.; Ong, S. P.; Hautier, G.; Chen, W.; Richards, W. D.; Dacek, S.; Cholia, S.; Gunter, D.; Skinner, D.; Ceder, G.; Persson, K. A. Commentary: The Materials Project: A Materials Genome Approach to Accelerating Materials Innovation. *APL Mater.* **2013**, *1* (1), 001002.
- (40) Ong, S. P.; Richards, W. D.; Jain, A.; Hautier, G.; Kocher, M.; Cholia, S.; Gunter, D.; Chevrier, V. L.; Persson, K. A.; Ceder, G. Python Materials Genomics (Pymatgen): A Robust, Open-Source Python Library for Materials Analysis. *Comput. Mater. Sci.* **2013**, *68*, 314–319.
- (41) Azizi, V.; Smeets, S.; Lavrinenko, A. K.; Ciarella, S.; Famprikis, T. GEMDAT. Zenodo July 2024.
- (42) Treinish, M.; Carvalho, I.; Tsilimigkounakis, G.; Sá, N. Rustworkx: A High-Performance Graph Library for Python. *arXiv Prepr. arXiv2110.15221* **2021**.
- (43) Meurer, A.; Smith, C. P.; Paprocki, M.; Čertík, O.; Kirpichev, S. B.; Rocklin, M.; Kumar, Am.; Ivanov, S.; Moore, J. K.; Singh, S. SymPy: Symbolic Computing in Python. *PeerJ Comput. Sci.* **2017**, *3*, e103.

- (44) Harris, C. R.; Millman, K. J.; Van Der Walt, S. J.; Gommers, R.; Virtanen, P.; Cournapeau, D.; Wieser, E.; Taylor, J.; Berg, S.; Smith, N. J. Array Programming with NumPy. *Nature* **2020**, *585* (7825), 357–362.
- (45) Hunter, J. D. Matplotlib: A 2D Graphics Environment. *Comput. Sci. & Eng.* **2007**, *9* (3), 90–95.
- (46) Conrad Szczuka; Bora Karasulu; Matthias F. Groh; Svetlana Menkin; Steffen P. Emge; Farheen N. Sayed; Andrew J. Morris; Clare P. Grey. Forced Disorder in the Solid Solution Li₃P–Li₂S: A New Class of Fully Reduced Solid Electrolytes for Lithium Metal Anodes, (Manuscript Submitted). **2022**.
- (47) Dong, Y.; DiSalvo, F. J. Reinvestigation of Trilithium Phosphide, Li₃P. *Acta Crystallogr. Sect. E Struct. Reports Online* **2007**, *63* (4), i97–i98.
- (48) Van der Ven, A.; Ceder, G.; Asta, M.; Tepesch, P. D. First-Principles Theory of Ionic Diffusion with Nondilute Carriers. *Phys. Rev. B - Condens. Matter Mater. Phys.* **2001**, *64* (18), 1–17.
- (49) Catlow, C. R. A. STATIC LATTICE SIMULATION OF STRUCTURE AND TRANSPORT IN SUPERIONIC CONDUCTORS. *Solid State Ionics* **1983**, *8* (SUPPL. 3), 89–107.
- (50) Gautam, A.; Sadowski, M.; Ghidui, M.; Minafra, N.; Senyshyn, A.; Albe, K.; Zeier, W. G. Engineering the Site-Disorder and Lithium Distribution in the Lithium Superionic Argyrodite Li₆PS₅Br. *Adv. Energy Mater.* **2021**, *11* (5).
- (51) Zhao, E.; He, L.; Zhang, Z.; Doux, J.-M.; Tan, D. H. S.; Wu, E. A.; Deysher, G.; Chen, Y.-T.; Zhao, J.; Wang, F. New Insights into Li Distribution in the Superionic Argyrodite Li₆PS₅Cl. *Chem. Commun.* **2021**, *57* (82), 10787–10790.
- (52) Zhou, L.; Minafra, N.; Zeier, W. G.; Nazar, L. F. Innovative Approaches to Li-Argyrodite Solid Electrolytes for All-Solid-State Lithium Batteries. *Acc. Chem. Res.* **2021**, *54* (12), 2717–2728.
- (53) Zhou, L.; Zhang, Q.; Nazar, L. F. Li-Rich and Halide-Deficient Argyrodite Fast Ion Conductors. *Chem. Mater.* **2022**, *34* (21), 9634–9643.
- (54) Hogrefe, K.; Minafra, N.; Hanghofer, I.; Banik, A.; Zeier, W. G.; Wilkening, H. M. R. Opening Diffusion Pathways through Site Disorder: The Interplay of Local Structure and Ion Dynamics in the Solid Electrolyte Li_{6+x}P_{1-x}Ge_xS₅I as Probed by Neutron Diffraction and NMR. *J. Am. Chem. Soc.* **2022**, *144* (4), 1795–1812.
- (55) Gautam, A.; Al-Kutubi, H.; Famprakis, T.; Ganapathy, S.; Wagemaker, M. Exploring the Relationship Between Halide Substitution, Structural Disorder, and Lithium Distribution in Lithium Argyrodites (Li_{6-x}PS_{5-x}Br_{1+x}). *Chem. Mater.* **2023**, *35* (19), 8081–8091.
- (56) Perdew, J. P.; Burke, K.; Ernzerhof, M. Generalized Gradient Approximation Made Simple. *Phys. Rev. Lett.* **1996**, *77* (18), 3865.
- (57) Kresse, G.; Furthmüller, J. Efficiency of Ab-Initio Total Energy Calculations for Metals and Semiconductors Using a Plane-Wave Basis Set. *Comput. Mater. Sci.* **1996**, *6* (1), 15–50.
- (58) Blöchl, P. E. Projector Augmented-Wave Method. *Phys. Rev. B* **1994**, *50* (24), 17953.
- (59) Nosé, S. A Unified Formulation of the Constant Temperature Molecular Dynamics Methods. *J.*

- Chem. Phys.* **1984**, *81* (1), 511–519.
- (60) Hoover, W. G. Canonical Dynamics: Equilibrium Phase-Space Distributions. *Phys. Rev. A* **1985**, *31* (3), 1695.
- (61) Tilley, R. J. D. *Defects in Solids*; John Wiley & Sons, 2008.
- (62) Wert, C.; Zener, C. Interstitial Atomic Diffusion Coefficients. *Phys. Rev.* **1949**, *76* (8), 1169–1175.
- (63) Dienes, G. J. Frequency Factor and Activation Energy for the Volume Diffusion of Metals. *J. Appl. Phys.* **1950**, *21* (11), 1189–1192.
- (64) Almond, D. P.; West, A. R. The Activation Entropy for Transport in Ionic Conductors. *Solid State Ionics* **1987**, *23* (1–2), 27–35.
- (65) Gao, Y.; Li, N.; Wu, Y.; Yang, W.; Bo, S. H. Rethinking the Design of Ionic Conductors Using Meyer–Neldel–Conductivity Plot. *Adv. Energy Mater.* **2021**, *11* (13), 1–9.
- (66) Du, P.; Zhu, H.; Braun, A.; Yelon, A.; Chen, Q. Entropy and Isokinetic Temperature in Fast Ion Transport. *Adv. Sci.* **2024**, *11* (2), 1–8.
- (67) Landgraf, V.; Tu, M.; Cheng, Z.; de Leeuw, J.; Ganapathy, S.; Wagemaker, M.; Famprikis, T. Entropy-Induced High Conductivity in Fully-Reduced Electrolytes for Solid-State Batteries with Lithium Metal Anodes. *ChemRxiv* **2023**.
- (68) Yu, P.; Zhang, H.; Hussain, F.; Luo, J.; Tang, W.; Lei, J.; Gao, L.; Butenko, D.; Wang, C.; Zhu, J.; Yin, W.; Zhang, H.; Han, S.; Zou, R.; Chen, W.; Zhao, Y.; Xia, W.; Sun, X. Lithium Metal-Compatible Antifluorite Electrolytes for Solid-State Batteries. *J. Am. Chem. Soc.* **2024**.
- (69) Ji, H.; Urban, A.; Kitchaev, D. A.; Kwon, D. H.; Artrith, N.; Ophus, C.; Huang, W.; Cai, Z.; Shi, T.; Kim, J. C.; Kim, H.; Ceder, G. Hidden Structural and Chemical Order Controls Lithium Transport in Cation-Disordered Oxides for Rechargeable Batteries. *Nat. Commun.* **2019**, *10* (1).

Chapter 4: Compositional flexibility in irreducible antiferroite electrolytes for next-generation battery anodes

Victor Landgraf, Mengfu Tu, Zhu Cheng, Alexandros Vasileiadis, Theodosios Famprikis, Marnix Wagemaker

4.1 Abstract

Solid-state batteries currently receive ample attention due to their potential to outperform lithium-ion batteries in terms of energy density when featuring next-generation anodes such as Li metal or silicon. One key remaining challenge is identifying solid electrolytes that combine high ionic conductivity with stability in contact with the highly reducing potentials of next-generation anodes. *Fully reduced* electrolytes, based on irreducible anions, offer a promising solution by avoiding electrolyte decomposition altogether. In this study, we demonstrate the compositional flexibility of the disordered antiferroite framework accessible by mechanochemical synthesis and leverage it to discover irreducible electrolytes with high ionic conductivities. We show that the recently investigated $\text{Li}_9\text{N}_2\text{Cl}_3$ and Li_5NCl_2 phases are part of the same solid solution of Li-deficient *antiferroite* phases existing on the LiCl-Li₃N tie line with a general chemical formula of $\text{Li}_{1+2x}\text{Cl}_{1-x}\text{N}_x$ ($0.33 < x < 0.5$). Using density functional theory calculations, we identify the origin of the 5-order-of-magnitude conductivity increase of the $\text{Li}_{1+2x}\text{Cl}_{1-x}\text{N}_x$ phases compared to the structurally related *rock-salt* LiCl phase. Finally, we demonstrate that S_{Cl^-} and Br_{Cl^-} -substituted analogues of the $\text{Li}_{1+2x}\text{Cl}_{1-x}\text{N}_x$ phases may be synthesized, enabling significant conductivity improvements by a factor of 10, reaching 0.2 mS cm^{-1} for $\text{Li}_{2.31}\text{S}_{0.41}\text{Br}_{0.14}\text{N}_{0.45}$. This investigation demonstrates for the first time that irreducible antiferroite-like phases are compositionally highly modifiable; this finding lays the ground for discovery of new compositions of irreducible antiferroite-like phases with even further increased conductivities, which could help eliminate solid-electrolyte decomposition and decomposition-induced Li losses on the anode side in high-performance next-generation batteries.

4.2 Introduction

Solid-state batteries have the potential to supersede conventional Li-ion batteries in terms of energy density and safety.^{1,2} Three main advantages of solid electrolytes are as follows. (1) The solid nature of solid electrolytes potentially enables bipolar stacking of individual cells, increasing the overall pack energy density. (2) Solid electrolytes are typically less flammable than liquid equivalents and thus safer. (3) Solid electrolytes are potentially better compatible with high-energy anodes such as Si or Li metal.^{1,2} An initial challenge has been to develop solid electrolytes with sufficiently high ionic conductivities to compete with liquid electrolytes. In recent years, multiple derivatives of the argyrodite and $\text{Li}_{10}\text{GeP}_2\text{S}_{12}$ solid electrolytes have been developed with Li-ion conductivities beyond 10 mS cm^{-1} , thus exceeding the conductivities of their liquid equivalents.³⁻⁶ Nevertheless, the main issue with all known high-conducting ($>1 \text{ mS cm}^{-1}$) solid electrolytes is that they are not (electro)-chemically stable at the high potentials of typical Li-ion battery cathodes nor at low potentials of desirable high-capacity anodes such as Si or Li metal. The electrochemical instability of solid electrolytes with electrodes inevitably leads to electrolyte decomposition at the electrolyte-electrode interfaces.^{1,7} Electrolyte decomposition at the electrode interfaces causes Li loss, formation of resistive interphases and contact loss between solid-electrolyte- and electrode particles, which are all directly linked to battery degradation and failure.^{8,9}

This study aims to design solid electrolytes that are highly conducting and thermodynamically stable against the low potentials of desirable high-capacity anodes such as Li metal and Si. Such electrolytes would eliminate (electro)chemical degradation on the anode side and thus eliminate complications that electrolyte degradation entails. When interested in thermodynamically stable phases at low potentials, *fully reduced* phases become immediately pertinent; i.e. phases in which the only cation present is Li and in which all anions are in their lowest permitted formal oxidation state and thus irreducible.^{10,11} Commonly known examples of such irreducible phases are the lithium binaries LiCl, LiBr, Li_2S , LiI, LiF, Li_3N and Li_3P . While these phases all feature thermodynamic stability at the low potentials ($<0 \text{ V vs. Li}^+/\text{Li}$), they are fraught with low ionic conductivities ($<10^{-6} \text{ mS cm}^{-1}$), except for Li_3N , which is reported to have a conductivity of 0.5 mS cm^{-1} .^{10,12} New irreducible phases were recently discovered by exploring the tie lines between the above-listed binaries using mechanochemical synthesis; one example is the $\text{Li}_{2+x}\text{S}_{1-x}\text{P}_x$ phases discovered by Szcuka et al. reaching high ionic conductivities of 0.2 mS cm^{-1} .¹¹ Another example is the recently discovered $\text{Li}_{2+x}\text{S}_{1-x}\text{N}_x$ phases also reaching high conductivities of 0.2 mS cm^{-1} .¹³ Additionally, the Li_5NCl_2 ¹⁰ and $\text{Li}_9\text{N}_2\text{Cl}_3$ ¹⁴ phases existing on the Li_3N -LiCl tie line were recently investigated. Li et al. demonstrated excellent stability against Li-metal, stability in dry air and high critical-current density for dendrite formation of 10 mA cm^{-2} for the $\text{Li}_9\text{N}_2\text{Cl}_3$ phase.¹⁴ Additionally, excellent performance of $\text{Li}_9\text{N}_2\text{Cl}_3$ in full cells was demonstrated where $\text{Li}_9\text{N}_2\text{Cl}_3$ is used as an anolyte to protect the $\text{Li}_{2.73}\text{Ho}_{1.09}\text{Cl}_6$ halide electrolyte against a Li metal anode.¹⁴ These results are promising, however an essential drawback remains the low room temperature (RT) conductivity of $\text{Li}_9\text{N}_2\text{Cl}_3$ which is reported to be 0.04 mS cm^{-1} .¹⁴ Moreover, the mechanistic origin of the increased conductivity of $\text{Li}_9\text{N}_2\text{Cl}_3$ phases compared to the structurally related rocksalt LiCl phase has not been established.

The present study develops compositional design strategies to improve the conductivity of $\text{Li}_9\text{N}_2\text{Cl}_3$ through the following advances:

- Synthetically, we demonstrate that the antifluorite framework is compositionally flexible; Li-deficient and Li-excess antifluorite phases can be stabilized through mechanochemistry. We find

that Li_5NCl_2 and $\text{Li}_9\text{N}_2\text{Cl}_3$ are both members of the same solid solution of Li-deficient antifluorite phases on the Li_3N - LiCl tie line with the general chemical formula of $\text{Li}_{1+2x}\text{Cl}_{1-x}\text{N}_x$ with $0.33 < x < 0.5$. Additionally, we show that $\text{Li}_{1+2x}\text{Cl}_{1-x}\text{N}_x$ phases are compositionally highly modifiable; we synthesize S_{Cl^-} and Br_{Cl^-} -substituted analogues boosting the ionic conductivities of $\text{Li}_{1+2x}\text{Cl}_{1-x}\text{N}_x$ phases by an order of magnitude enabling conductivity enhancements up to 0.2 mS cm^{-1} for $\text{Li}_{2.31}\text{S}_{0.41}\text{Br}_{0.14}\text{N}_{0.45}$.

- Computationally, we explain how introducing nitrogen into the LiCl anionic-framework brings tetrahedral and octahedral lithium sites closer in energy so that vacant sites become energetically accessible for diffusion. Our analysis of diffusion bottlenecks resolving the effect of the local anion coordination shows that nitrogen widens diffusion bottlenecks further facilitating Li diffusion.
- Finally, we find through both experiments and computations that the oxidation limit of the irreducible antifluorite-like phases is compositionally tunable and generally higher compared to Li_3N which may be a critical advantage to stabilize next-generation anodes.

4.3 Results and Discussion

Our starting point for this work is our previous work on fully reduced electrolytes, showing the conductivity of Li_2S could be highly improved by dissolving Li_3N into the antifluorite Li_2S phase.¹³ Dissolving Li_3N in Li_2S results in a series of phases where N and S share sites (Figure S4.1). A solid solution exists with the general chemical formula $\text{Li}_{2+x}\text{S}_{1-x}\text{N}_x$ ($0 < x < \sim 0.5$), exhibiting an anion-disordered Li-rich antifluorite crystal structure (Figure S4.1) and showing much higher conductivity ($>0.2 \text{ mS cm}^{-1}$ for $x=0.5$) than the Li_2S host phase ($10^{-6} \text{ mS cm}^{-1}$) (see Figure S4.1).¹³ This motivated our investigation of whether a similar solid solution may be found between Li_3N and LiCl (schematically illustrated in Figure 4.1a), and examine their functional solid-electrolyte properties.

A solid solution of Li-deficient antifluorite phases on the Li_3N - LiCl tie line

To answer this question, Li_3N and LiCl were mixed in different ratios, followed by a high-energy mechanochemical treatment (*ball milling*). The resulting products were analyzed using powder X-ray diffraction, the results of which are shown in Figure 4.1b. Attempting to dissolve small quantities of Li_3N into LiCl did not result in a pure phase but a mixture of two cubic phases: LiCl and Li_5NCl_2 . The stoichiometric formula of the latter may alternatively be written as $\text{Li}_{1.66}\text{N}_{0.33}\text{Cl}_{0.66}$ (i.e. $\text{Li}_{1+2x}\text{Cl}_{1-x}\text{N}_x$ with $x=0.33$), and has been previously reported as a stable phase prepared by conventional solid-state synthesis.^{10,15} Only when the $\text{Li}_{1.66}\text{N}_{0.33}\text{Cl}_{0.66}$ stoichiometry is reached, having a 2:1 $\text{LiCl}/\text{Li}_3\text{N}$ ratio, a pure $\text{Li}_{1.66}\text{N}_{0.33}\text{Cl}_{0.66}$ phase is observed (i.e. the LiCl phase is not observed in the X-ray diffraction pattern). The mixtures with a higher nitrogen composition than the $\text{Li}_{1.66}\text{N}_{0.33}\text{Cl}_{0.66}$ phase ($\text{Li}_{1+2x}\text{Cl}_{1-x}\text{N}_x$ with $0.33 < x < 0.5$) show the same cubic $Fm\bar{3}m$ diffraction pattern as the $x=0.33$ phase but with an increasing shift towards larger scattering vector Q indicating a decreasing lattice parameter with increasing nitrogen content. When exceeding an overall stoichiometry of $\text{Li}_2\text{N}_{0.5}\text{Cl}_{0.5}$ (i.e. $x=0.5$) a second phase identified as $\beta\text{-Li}_3\text{N}$ is observed in the diffraction pattern while the lattice parameter of the first phase remains constant. As expected

based on the smaller ionic radius of N^{3-} compared to Cl^- (1.46 vs 1.81 Å),¹⁶ the lattice parameter of the $Li_{1+2x}Cl_{1-x}N_x$ phases decreases with increasing nitrogen content, where the linear shift is in accordance with Vegard's law (Figure 4.1c). A solid-solution region of cubic $Li_{1+2x}Cl_{1-x}N_x$ phases is thus observed on the $x \cdot LiCl - (1-x) \cdot Li_3N$ tie line for compositions between 0.33 < x < 0.5, i.e. between the end members $Li_{1.66}N_{0.33}Cl_{0.66}$ and $Li_2N_{0.5}Cl_{0.5}$.

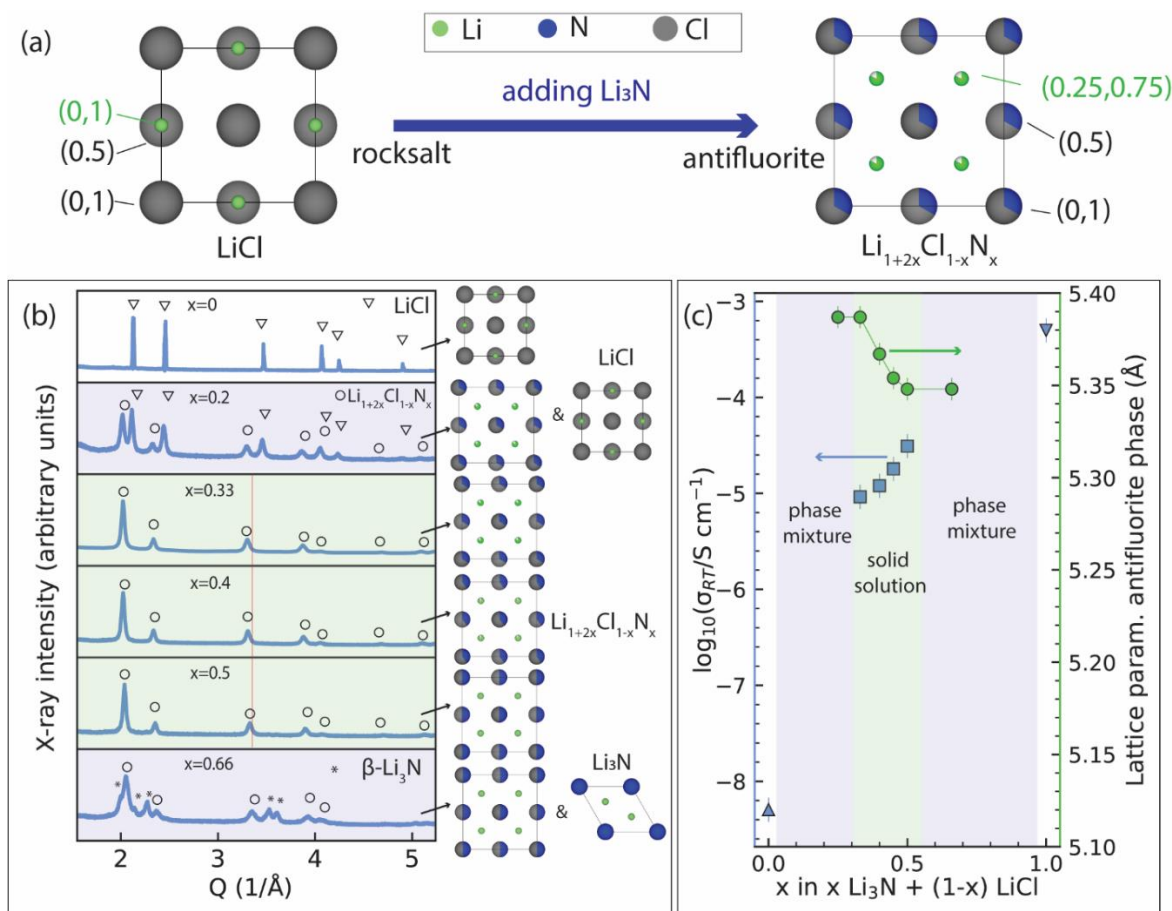


Figure 4.1. (a) View along the [001] of the unit cell of rock-salt LiCl and Li-deficient antifluorite $Li_{1+2x}Cl_{1-x}N_x$ phases (exact example of $x=0.33$ shown). (b) X-ray diffraction pattern of the products of mechanochemically treating $x \text{ Li}_3\text{N} + (1-x) \text{ LiCl}$ mixtures. In the range ($x=0.33$ to $x=0.5$) phase-pure Li-deficient antifluorite structures are obtained. Phases existing at each overall composition are shown next to the diffraction patterns. Red line is guide to the eye to better observe peak shifts. (c) Overall conductivity and the lattice parameter of the antifluorite-like phase for different mixtures of $x \text{ Li}_3\text{N} + (1-x) \text{ LiCl}$. Conductivity of (structurally distinct) Li_3N and $LiCl$ are also shown for reference. Green and purple shading in (b) and (c) indicate solid-solution- and two-phase- regions, respectively.

Rietveld refinements of the x-ray diffractograms (SI Figure S4.2 and Tables S4.1-4.4) show that the crystal structure of the $Li_{1+2x}Cl_{1-x}N_x$ ($x < 0.33 < 0.5$) phases consist in a face-centered-cubic arrangement of the anions where N^{3-} and Cl^- share the same site. At the nitrogen-poor boundary of the solid solution (i.e.

$\text{Li}_{1.66}\text{N}_{0.33}\text{Cl}_{0.66}$) the tetrahedral interstitials are partially occupied by Li ions (83%).² With increasing N content the Li content increases to balance the charge, and the tetrahedral sites become increasingly populated until reaching the N-rich solid-solution boundary (i.e. $\text{Li}_2\text{N}_{0.5}\text{Cl}_{0.5}$). Consequently, where the $\text{Li}_2\text{N}_{0.5}\text{Cl}_{0.5}$ phase can be described as a (stoichiometric) antiferroite phase (with fully occupied tetrahedral sites), the solid-solution members with ($x < 0.5$) may be described as Li-deficient antiferroite phases (having only partially occupied tetrahedral sites). Further lithium insertion ($x > 0.5$) seems to destabilize the antiferroite, leading to decomposition into a mixture of $\text{Li}_2\text{Cl}_{0.5}\text{N}_{0.5}$ and Li_3N (Figure 4.1b). This is in contrast to the lithium-rich antiferroites $\text{Li}_{2+x}\text{S}_{1-x}\text{N}_x$ which exhibit partial occupation of their octahedral sites in addition to full occupation of their tetrahedral sites (*vide infra*). The structural shift that occurs when going from rock-salt LiCl to Li-deficient antiferroite $\text{Li}_{1.66}\text{N}_{0.33}\text{Cl}_{0.66}$ entails a significant increase of the cubic lattice parameter from 5.17 Å to 5.39 Å (Figure 4.1b), which is likely related to the rearrangement of lithium from the octahedral sites (in the former) to tetrahedral sites (in the latter).

Figure 4.1c also shows the ionic conductivity of the mechanochemically prepared samples as quantified by impedance spectroscopy experiments on pelletized samples which could be invariably fitted by a single bulk-diffusion process (SI Figure S4.3). The rock-salt LiCl phase has a conductivity of the order of 10^{-7} mS cm^{-1} (Figure S4.4). The conductivity of Li-deficient antiferroite $\text{Li}_{1.66}\text{N}_{0.33}\text{Cl}_{0.66}$ is significantly higher reaching 0.01 mS cm^{-1} , and introducing more nitrogen into the solid solution further increases the conductivity up to 0.03 mS cm^{-1} for $\text{Li}_2\text{N}_{0.5}\text{Cl}_{0.5}$ as shown in Figure 4.1c.

We have thus discovered a new solid solution on the LiCl- Li_3N tie line with the general formula $\text{Li}_{1+2x}\text{Cl}_{1-x}\text{N}_x$ ($x < 0.33 < 0.5$) accessible by mechanochemistry (in contrast to conventional solid state synthesis previously explored in refs. ^{10,15}). These phases crystallize in an anion disordered Li-deficient antiferroite-like crystal structure and their conductivity is orders of magnitude higher than the conductivity of rock-salt LiCl. In the next section, we will analyze the mechanistic origin of this 5-order-of-magnitude boost in ionic conductivity.

Rock-salt LiCl vs. Li-deficient antiferroite $\text{Li}_{1+2x}\text{Cl}_{1-x}\text{N}_x$ – origin of the improved conductivity

Fast Li diffusion relies on two prerequisites: (1) Li sites connected by low Li-hop activation energies into a percolating network and (2) a sufficient fraction of vacancies among these Li sites. Vacant Li-sites may be introduced by defects (e.g. Frenkel defect pairs) and/or may be synthetically introduced via compositional tuning.

In LiCl, the octahedral interstitials are preferably occupied over the tetrahedral ones (Figure 4.2a), indicating that the former are more stable than the latter. All tetrahedral interstitials in LiCl are vacant thus, in principle, LiCl features a high concentration of vacant interstitials enabling potential diffusion pathways via an octahedral-tetrahedral-octahedral jump sequence. To investigate Li diffusion in (defect-free) LiCl we initiated *ab initio* molecular dynamics (AIMD) simulations of (2x2x2) LiCl supercells. As done in previous studies, we dissected our AIMD simulations into individual jump events. ^{10,17–20} From the frequency of

² A small fraction of the Li ions $\leq 5\%$ may potentially occupy the octahedral sites as detailed in Supplementary Note 1.

jumps between two sites A and B ($\nu_{A \rightarrow B}$), we calculate jump-activation energies (jump- E_a) by using equation (4.1) and assuming a prefactor frequency (ν_0) of 10^{13} Hz: ^{3*}

$$\text{jump } E_{a,A \rightarrow B} = -k_b T \ln \left(\frac{\nu_{A \rightarrow B}}{\nu_0} \right) \quad (4.1)$$

where k_b is the Boltzmann constant, T the temperature in K, $\nu_{A \rightarrow B}$ the observed frequency of jumps between sites A and B and jump- $E_{a,A \rightarrow B}$ the jump-activation energy of a jump event from site A to site B. Details on this methodology may be found in refs. ^{17,21}. We use these jump-activation energies as a proxy for the local energy barriers.

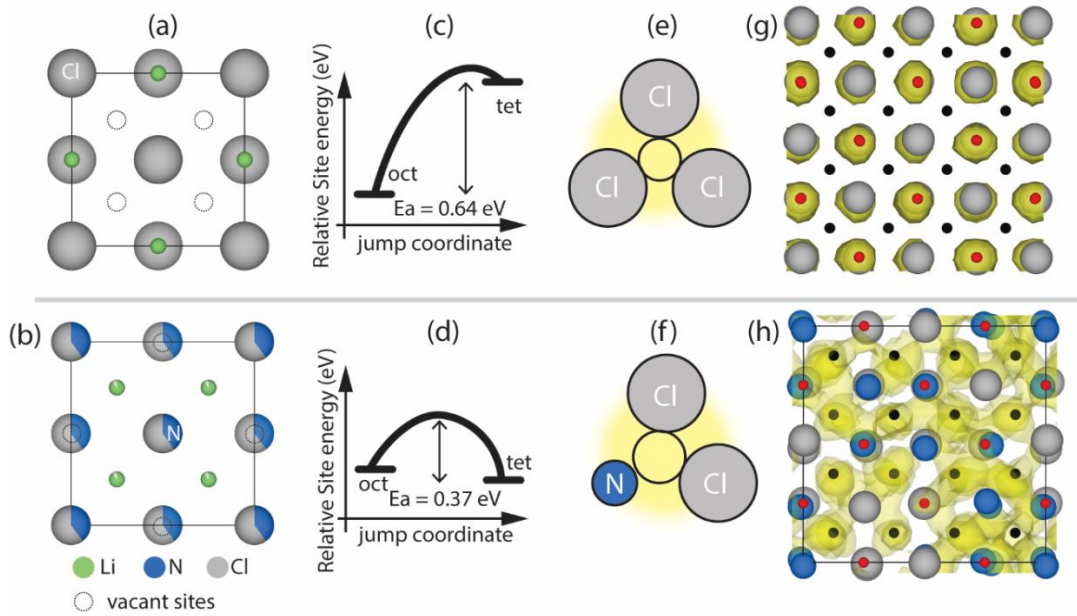


Figure 4.2. (a) and (b) View along the [001] of the unit cell of rock-salt LiCl and Li-deficient antifluorite $\text{Li}_{1+2x}\text{Cl}_{1-x}\text{N}_x$ phases. (c) and (d) Schematic illustration of the energy difference and average jump-activation energy between tetrahedral and octahedral sites in rock-salt LiCl and Li-deficient antifluorite $\text{Li}_{1+2x}\text{Cl}_{1-x}\text{N}_x$ phases. (e) and (f) Schematics of the triangular bottlenecks for oct-tet jumps. (g) and (h) LiCl and $\text{Li}_{1.8}\text{Cl}_{0.6}\text{N}_{0.4}$ supercell with the Li density of a 100 ps AIMD simulation at 1000 K. The Li density cutoff is set to 3% of the maximum value.

From the difference between the activation energies of the forward and backward jump, the energy difference between two crystallographic positions may be approximated as follows (and illustrated in Figure S4.5):

$$\Delta E_{\text{site}}(A, B) = |\text{jump } E_{a,A \rightarrow B} - \text{jump } E_{a,B \rightarrow A}| \quad (4.2)$$

^{3*} Assuming $\nu_0 = 10^{13} \text{ s}^{-1}$ is commonly adopted in the solid electrolyte field. ⁴³⁻⁴⁵ Additionally we justify this choice by calculating the average vibration frequency around the equilibrium Li-sites in our AIMD simulations and find it to be $1.0 \pm 0.2 \cdot 10^{13} \text{ Hz}$ for 5 different $\text{Li}_{1+2x}\text{Cl}_{1-x}\text{N}_x$ supercells (Table S4.5).

$|\Delta E_{\text{site}}(\text{tet, oct})|$ may be approximated from equation 4.2 as the average of $\Delta E_{\text{site}}(\text{A,B})$ for all sites where A and B are tetrahedral and octahedral sites respectively. $|\Delta E_{\text{site}}(\text{tet, oct})|$ is 0.61 ± 0.02 eV in the case of LiCl indicating that tetrahedral sites are on average significantly destabilized by ca. 0.6 eV versus octahedral sites. The jump-activation energy for the tet-oct jumps in LiCl is low (ca. 0.03 eV) suggesting that the tetrahedral site is highly metastable and should arguably more generally be referred to as ‘position’ than ‘site’ as further detailed in Supplementary Note 2. For the remaining discussion of this work however this distinction will not be made and the tetrahedral positions in LiCl will also be referred to as sites. One potential reason for the high metastability of tetrahedral Li sites may be the small void space at the tetrahedral site enabling occupation of an ion with a max radius of 0.38 Å (see Supplementary Note 3) which is smaller than the Li-ion radius (0.59 Å).¹⁶ Additionally, oct-tet transitions are sterically hindered in LiCl due to a highly constrained bottleneck with a diameter of 0.8 Å, which requires energetically unfavorably close Li-Cl ion distances and/or lattice distortion to accommodate the passing of Li ions (Figure 4.2e). To summarize, in rock-salt LiCl, Li is confined to the octahedral sites and low-activation-energy jumps to vacant sites are not available, rationalizing the absence of diffusion during simulations (localized density in Figure 4.2g) and the low RT ion conductivity of LiCl.^{4*}

In contrast, in the Li-deficient antiferroite $\text{Li}_{1.66}\text{N}_{0.33}\text{Cl}_{0.66}$ structure the tetrahedral Li sites are occupied, indicating that they are stabilized with respect to the octahedral sites. $\text{Li}_{1.66}\text{N}_{0.33}\text{Cl}_{0.66}$ features two types of intrinsic vacancies. (1) the tetrahedral sites are partially occupied and (2) the octahedral interstitials are essentially vacant (Figure 4.2b).^{5*} Compared to LiCl the difference in site energy between octahedral and tetrahedral is much smaller, with $|\Delta E_{\text{site}}(\text{tet-oct})| = 0.07 \pm 0.01$ eV as compared to $|\Delta E_{\text{site}}(\text{tet-oct})| = 0.61 \pm 0.02$ eV in LiCl (Figure 4.2c and 4.2d). This flat(ter) energy landscape enables low-activation-energy oct-tet jumps and increased bulk diffusion reflected in the much more diffuse Li-density compared to the LiCl case (Figure 4.2h) and higher experimentally-measured conductivities of $\text{Li}_{1.66}\text{N}_{0.33}\text{Cl}_{0.66}$ (Figure 4.1c).

From our AIMD simulations we observe that diffusion occurs via Li jumps between oct and tet sites through triangular bottlenecks consisting of three anions (Figure 4.3a) as well as between tet sites through linear bottlenecks consisting of two anions (Figure 4.3b). Li diffusion through triangular and linear bottlenecks is facilitated by the presence of N in the anionic lattice. Because N^{3-} (1.46 Å) anions are considerably smaller than Cl^- (1.81 Å) anions, the bottleneck becomes larger, enabling Li diffusion. To quantify this further, we calculated the bottleneck diameters for 5 $\text{Li}_{1.66}\text{N}_{0.33}\text{Cl}_{0.66}$ DFT relaxed (2x2x2) supercells (featuring >500 bottlenecks) to account for local distortions that may not be evident in the average crystallographic unit cell. The bottleneck diameters for different bottlenecks as well as the average jump-Ea for jumps through the respective bottlenecks are shown in Figure 4.3. Comparing the bottleneck diameter to the diameter of Li-ions (1.18 Å) is a good proxy for the constraints on Li diffusion; bottlenecks with significantly smaller diameters than 1.18 Å will constrain Li diffusion more than bottlenecks with diameters > 1.18 Å. Figure 4.3a and 4.3b for instance shows that triangular bottlenecks consisting of three chlorides are considerably smaller (~0.8 Å) than bottlenecks containing one or more nitrogen (>1.25 Å). Figure 4.3c and 4.3d show

^{4*} Due to the high activation energy required for oct-tet jumps in LiCl and the high metastability of tet sites/positions diffusion in LiCl is likely mediated by Schottky defects just as in NaCl. Accordingly, the charge carrier concentration in LiCl at room temperature is extremely low ($\sim 1 \times 10^{-9} c_{\text{Li}}$ where c_{Li} is the Li concentration in LiCl) as the formation energy for Schottky defects is typically ~1 eV. This low charge carrier concentration additionally contributes to the low ionic conductivity in LiCl.

^{5*} Potentially a small fraction of Li ions $\leq 5\%$ on average may occupy the octahedral sites in which case the octahedral sites as detailed in Supplementary Note 1.

that jumps through nitrogen-containing bottlenecks for oct-tet and tet-tet jumps have lower activation energies indicating easier diffusion through N containing bottlenecks. Consequently, increasing the nitrogen content in the $\text{Li}_{1+2x}\text{Cl}_{1-x}\text{N}_x$ phase, results in more nitrogen-rich, low-activation-energy bottlenecks, explaining the increase in conductivity upon increasing the nitrogen content in the $\text{Li}_{1+2x}\text{Cl}_{1-x}\text{N}_x$ solid solution shown in Figure 4.2.

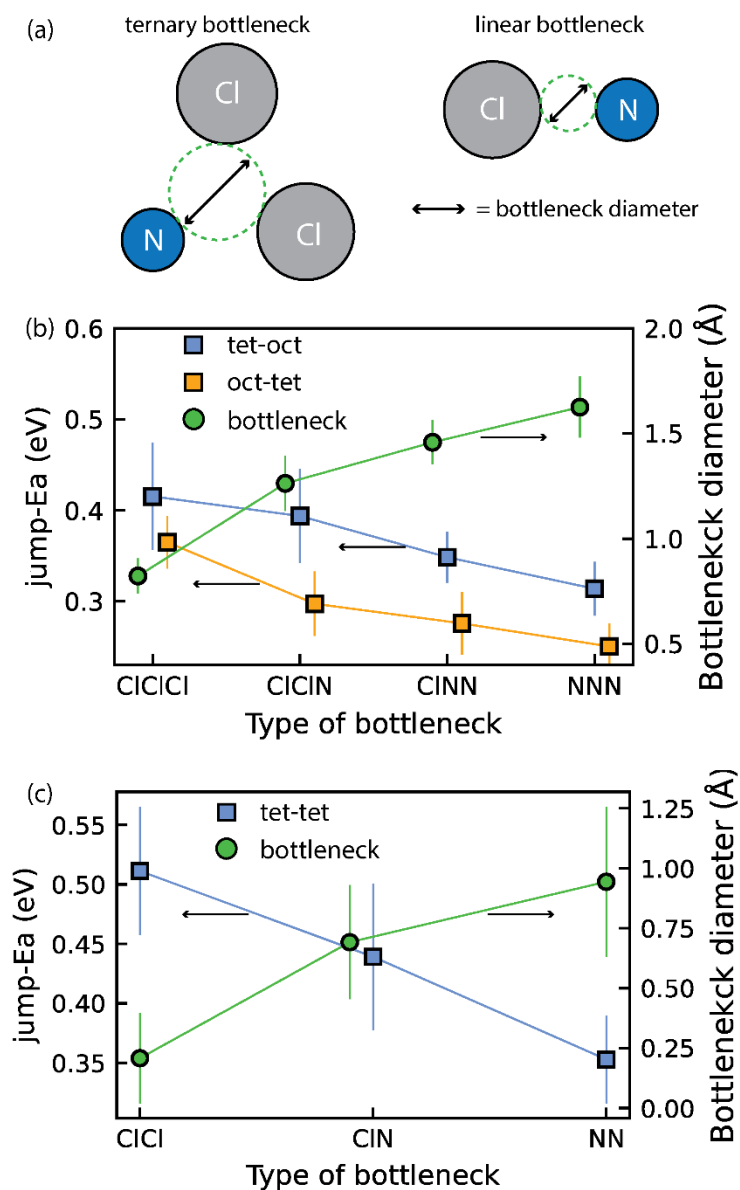


Figure 4.3. (a) Schematic of triangular and linear bottlenecks connecting oct-tet and tet-tet site pairs, respectively. (b) Average activation energy of tet-oct and oct-tet jumps for different bottleneck compositions along with the bottleneck size. Error bars are the standard deviation of the distribution of observed bottleneck sizes and activation energies. (c) Same as (b) for tet-tet jumps.

In conclusion, it is not possible to continuously dissolve Li_3N into rock-salt LiCl to form Li-excess rock-salt phases as the excess Li ions would occupy tetrahedral sites which are sterically too constrained to

accommodate Li ions. However, once a critical amount of Li_3N ($x \geq 0.33$) is mixed with LiCl sufficient Li ions are available to stabilize (Li-deficient) antifluorite phases where Li ions occupy tetrahedral sites. The occupation of tetrahedral sites indicates that the tetrahedral sites are more stable than octahedral sites in Li-deficient antifluorite phases. The vacant octahedral sites and the occupied tetrahedral sites are energetically in close proximity ($|\Delta E_{\text{site}}(\text{tet-oct})| \sim 0.07$ eV) and oct-tet (and tet-tet) transitions are facilitated by the presence of N^{3-} anions in the anionic lattice as the smaller ionic radius of N^{3-} compared to Cl^- increases the bottleneck size (Figure 4.2f and 4.3c). Consequently, the vacant octahedral sites which are innate to Li-deficient antifluorite phases are thermodynamically and kinetically accessible so that tet-oct jumps may be achieved with jump-Ea values of 0.37 ± 0.01 eV on average. In contrast, in LiCl the vacant tetrahedral sites are at much larger energies than the occupied octahedral sites ($|\Delta E_{\text{site}}(\text{tet-oct})| \sim 0.6$ eV). Additionally, the oct-tet transitions are sterically hindered by small bottlenecks consisting of 3 Cl^- ions so that an oct-tet transition has a jump-Ea value of 0.64 ± 0.01 eV on average. Consequently, the vacant tetrahedral sites which are innate to rock-salt LiCl phases are thermodynamically and kinetically inaccessible explaining the absence of diffusion in simulations and the experimentally obtained low ionic conductivity.

Comparison between Li-rich antifluorite $\text{Li}_{2+x}\text{S}_{1-x}\text{N}_x$ and Li-deficient antifluorite $\text{Li}_{1+2x}\text{Cl}_{1-x}\text{N}_x$

The presently discovered $\text{Li}_{1+2x}\text{Cl}_{1-x}\text{N}_x$ ($0.33 < x < 0.5$) solid solution phases are a structural analog of the $\text{Li}_{2+x}\text{S}_{1-x}\text{N}_x$ ($0 < x < \sim 0.5$) system previously discovered.¹³ Comparing the $\text{Li}_{1+2x}\text{Cl}_{1-x}\text{N}_x$ and $\text{Li}_{2+x}\text{S}_{1-x}\text{N}_x$ phases in the ($0.33 < x < 0.5$) range, where both exist as solid solutions, is insightful in understanding the relationship between structure and Li-ion conductivity. For this we consider three phases of each solid solution, $x=0.33$, $x=0.4$ and $x=0.45$, —representing the lower, center and upper limit of the $0.33 < x < 0.5$ range, respectively— and compare their ionic conductivity metrics as quantified by variable-temperature impedance spectroscopy.

A notable difference is that the $\text{Li}_{2+x}\text{S}_{1-x}\text{N}_x$ phases are Li-excess antifluorite structures (more than 2 Li per anion), with partial Li occupancy of the octahedral sites (ref 13) while the $\text{Li}_{1+2x}\text{Cl}_{1-x}\text{N}_x$ phases are Li-deficient antifluorite phases (less than 2 Li per anion) where the tetrahedral sites are partially occupied by Li (Figures S4.1-4.2). Figure 4.4a shows that the Li-excess $\text{Li}_{2+x}\text{S}_{1-x}\text{N}_x$ phases have much higher ($\sim 10x$) conductivity than the Li-deficient $\text{Li}_{1+2x}\text{Cl}_{1-x}\text{N}_x$ phases, whereas the bulk activation energies, determined by EIS, for the $\text{Li}_{2+x}\text{S}_{1-x}\text{N}_x$ and the $\text{Li}_{1+2x}\text{Cl}_{1-x}\text{N}_x$ phases differ by at most 0.03 eV (Figure 4.4b) suggesting that the energy thresholds for diffusion in both systems are similar. However, the difference in the Arrhenius prefactors is large, on average a factor of 7 larger for the phases compared to of the $\text{Li}_{1+2x}\text{Cl}_{1-x}\text{N}_x$ phases (Figure 4.4c). This suggests that the origin of the higher conductivity of $\text{Li}_{2+x}\text{S}_{1-x}\text{N}_x$ phases is largely comprised in the Arrhenius prefactor. The larger charge carrier concentration in $\text{Li}_{2+x}\text{S}_{1-x}\text{N}_x$ (and potentially the inducing of concerted motion though we do not explicitly investigate this here) are likely the origin for the larger Arrhenius prefactor of Li-excess $\text{Li}_{2+x}\text{S}_{1-x}\text{N}_x$ antifluorite phases.

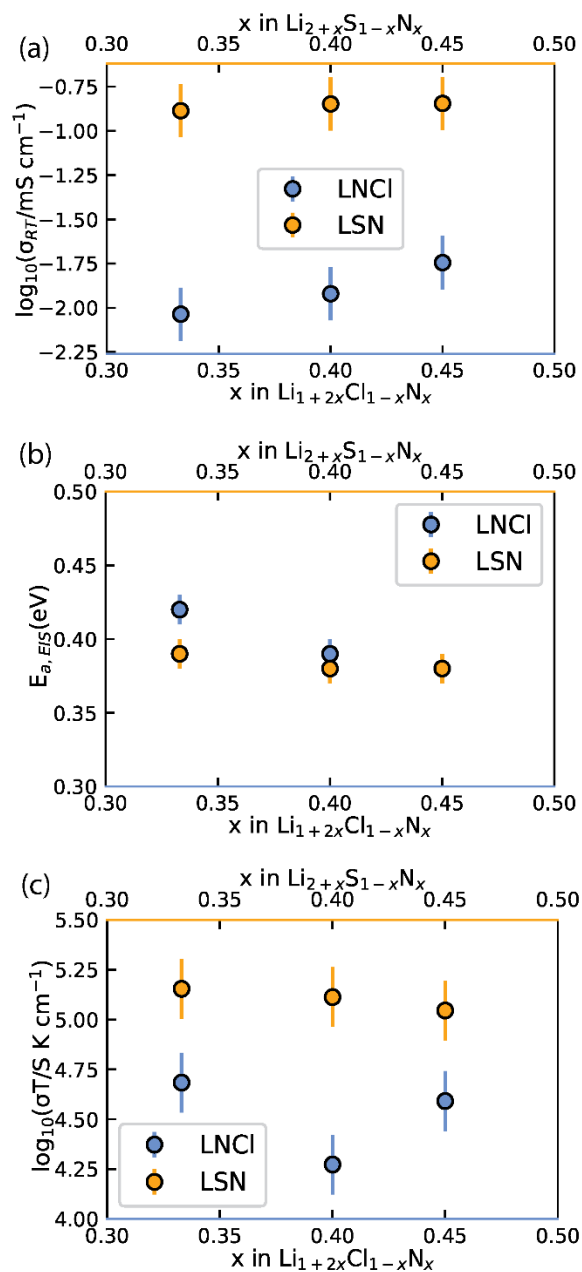


Figure 4.4. Comparison of the experimentally obtained conductivity, activation energy and Arrhenius prefactor of $\text{Li}_{1+2x}\text{Cl}_{1-x}\text{N}_x$ and $\text{Li}_{2+x}\text{S}_{1-x}\text{N}_x$ phases. (a) Comparison of the RT (22 °C in our labs) conductivity determined experimentally via EIS. (b) Comparison of the Arrhenius plot for the activation energy. (c) Comparison of the Arrhenius prefactor. The Arrhenius fits for (b) are shown in Figure S6.

Oxidation limits of Li-rich antifluorite $\text{Li}_{2+x}\text{S}_{1-x}\text{N}_x$ and Li-deficient antifluorite $\text{Li}_{1+2x}\text{Cl}_{1-x}\text{N}_x$ phases

We computationally investigated the metastability of $\text{Li}_{2+x}\text{S}_{1-x}\text{N}_x$ and $\text{Li}_{1+2x}\text{Cl}_{1-x}\text{N}_x$ antifluorite-like phases. For compositions ($x=0.11, 0.17, 0.36, 0.55, 0.72$) we built 10000 random ($2 \times 2 \times 2$) antifluorite-like $\text{Li}_{2+x}\text{S}_{1-x}\text{N}_x$ supercells and calculated their electrostatic energies with the formal oxidation states Li^+ , S^{2-} and N^{3-} assigned to the ions. We took the 30 supercells with the lowest electrostatic energies and relaxed the structures using density functional theory. With the energies obtained, the energy above the hull of these phases was calculated using entries of the materials project database (see also Supplementary Note 4). Figure 4.5a shows the average energy above the hull for the $\text{Li}_{2+x}\text{S}_{1-x}\text{N}_x$ phases and shows that increased nitrogen content and Li stuffing increase metastability (i.e. higher energy above the hull). Note the energy above the hull was calculated for antifluorite-like $\text{Li}_{2+x}\text{S}_{1-x}\text{N}_x$ phases even at nitrogen contents that cannot be stabilized experimentally (i.e. $x > 0.55$) to clearly demonstrate the effect of Li_3N dissolution into Li_2S on phase (meta)stability. The increased metastability of N-rich antifluorite-like $\text{Li}_{2+x}\text{S}_{1-x}\text{N}_x$ phases is reflected in the oxidation stability which decreases the higher the nitrogen content (Figure 4.5c).

Turning to the $\text{Li}_{1+2x}\text{Cl}_{1-x}\text{N}_x$ phases, the metastability of $\text{Li}_{1+2x}\text{Cl}_{1-x}\text{N}_x$ phases was calculated in an analogous manner to the $\text{Li}_{2+x}\text{S}_{1-x}\text{N}_x$ phases and is shown in Figure 4.5b. Note the energy above the hull is calculated for antifluorite-like $\text{Li}_{1+2x}\text{Cl}_{1-x}\text{N}_x$ phases even at nitrogen contents that cannot be stabilized experimentally (i.e. $x < 0.33$ and $x > 0.5$) to clearly demonstrate the effect of nitrogen content on phase (meta)stability. For $\text{Li}_{1+2x}\text{Cl}_{1-x}\text{N}_x$ phases the metastability is high at low and at high nitrogen content. The metastability of $\text{Li}_{1+2x}\text{Cl}_{1-x}\text{N}_x$ phases is lowest around the center of the LiCl - Li_3N tie line. This modulated (i.e. non-monotonic) trend in the metastability is consistent with the experimentally observed low-N-content and high-N-content boundaries of the $\text{Li}_{1+2x}\text{Cl}_{1-x}\text{N}_x$ ($0.33 < x < 0.5$) solid solution. Considering the modulated trend in the metastability of antifluorite-like $\text{Li}_{1+2x}\text{Cl}_{1-x}\text{N}_x$ phases, a modulated trend is expected in the oxidation stability of $\text{Li}_{1+2x}\text{Cl}_{1-x}\text{N}_x$ phases which is indeed experimentally observed (Figure 4.5c).

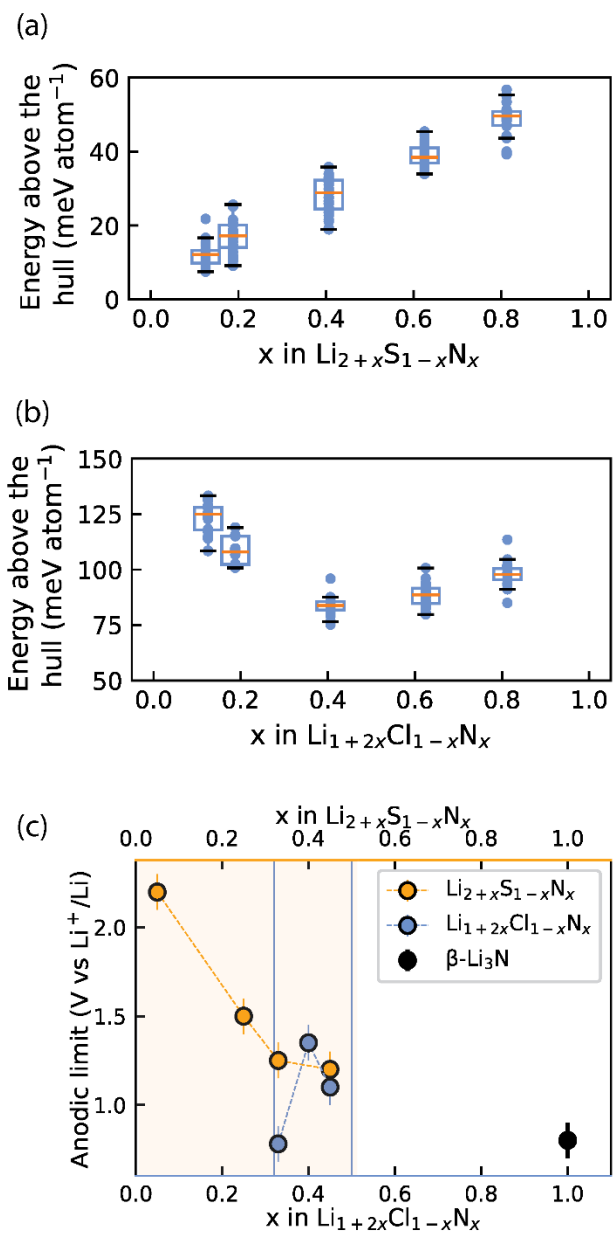


Figure 4.5. (a) and (b) Calculated energy above the hull for 30 Li_{2+x}N_xS_{1-x} and Li_{1+2x}Cl_{1-x}N_x antifluorite supercells at each of the antifluorite compositions. At each composition above the distribution of energies above the hull is shown as a box plot where the orange line indicates the arithmetic mean and the box indicates the first standard deviation. (c) Experimental anodic limits obtained from LSV for Li_{2+x}S_{1-x}N_x, Li_{1+2x}Cl_{1-x}N_x samples and β-Li₃N for reference. Orange shading and blue lines denote the solid-solution range for Li_{2+x}S_{1-x}N_x and Li_{1+2x}Cl_{1-x}N_x respectively.

S_{Cl} and Br_{Cl} substitutions on Li_{1+2x}Cl_{1-x}N_x phases to boost conductivity

S_{Cl} substitutions in Li_{1+2x}Cl_{1-x}N_x may increase the number of charge carriers and Br_{Cl} substitutions could increase the lattice parameter making facilitating Li diffusion. S_{Cl} and Br_{Cl} could thus increase the ionic conductivity and in this section we investigate the effect of S_{Cl} and Br_{Cl} substitutions in Li_{1+2x}Cl_{1-x}N_x phases. To narrow down this vast compositional space, the effect of the S_{Cl}, Br_S and Br_{Cl} substitutions considered at a fixed nitrogen content x=0.45. Thus the phase space we set out to investigate can be expressed by the following solid-solution formula: Li_{1.9+0.55y}Cl_{0.55(1-y-z)}S_{0.55y}Br_{0.55z}N_{0.45} (0<y,z<1), plotted schematically in the quasi-ternary phase diagram of Figure 4.6. We explored the ionic conductivity of this phase space by synthesizing various compositions in the ternary phase diagram and measuring their ionic conductivity using impedance spectroscopy (provided a single antifluorite-like phase was obtained). The results of this investigation are shown in SI Figures S4.8-S4.13 and summarized in Figure 4.6. We find that nearly all compositions in the phase space shown in Figure 4.6 exist as Li-deficient or Li-excess antifluorite structures. Only highly Br-rich samples where the bromine content exceeds 40% of all anions (that is, values of z>0.75 in Li_{1.9+0.55y}Cl_{0.55(1-y-z)}S_{0.55y}Br_{0.55z}N_{0.45}) did not result in phase-pure antifluorite-like phases.

Three main trends may be derived from Figure 4.6. (1) S_{Cl} substitutions entail a continuous increase in ionic conductivity. For instance, when substituting Cl in Li_{1.9}Cl_{0.55}N_{0.45} by S to form Li_{2.45}S_{0.55}N_{0.45} the conductivity increases by an order of magnitude (from 0.02 to 0.15 mS cm⁻¹). We rationalize this trend by the increase in Li concentration through charge compensation of replacing S²⁻ by Cl⁻ ions. This trend can be rationalized based on the increased mobile charge-carrier concentration (2) The second main trend we derive from Figure 4.6 is that Br_{Cl} substitutions entail a continuous increase in ionic conductivity. For instance, substituting all Cl in Li_{2.175}Cl_{0.275}S_{0.275}N_{0.45} by Br to form Li_{2.175}Br_{0.275}S_{0.275}N_{0.45} leads to a conductivity increase by a factor of ca. 2. This trend may be rationalized by the larger ion radius of Br⁻ compared to Cl⁻. Consequently, the presence of Br⁻ increases the lattice parameter, which facilitates diffusion through the sterically constrained diffusion bottlenecks. Additionally, the higher polarizability (*softness*) of Br compared to Cl (ref ²²) may ease diffusion through Br-containing bottlenecks compared to Cl-containing bottlenecks. (3) The third trend we derive from Figure 4.6 is that partial Br_S substitutions increase ionic conductivities. Unlike the two previous trends, this trend is not monotonic. While partial Br_S substitution leads to higher conductivities, carrying the substitution too far leads to decreasing conductivities. This discontinuous trend may be explained as follows. While Br_S substitutions increase the lattice parameter, Br_S substitutions concurrently reduce the Li concentration to compensate for the lower valence of Br⁻ compared to S²⁻ ions.

In agreement with the trends described above we find that the phase with the highest conductivity is a moderately Br-substituted Li_{2.45}S_{0.55}N_{0.45} phase – that is a phase with a stoichiometry of Li_{2.31}S_{0.41}Br_{0.14}N_{0.45} reaching a RT conductivity of ca. 0.2 mS cm⁻¹. Overall this investigation demonstrates the high structural and compositional flexibility of the antifluorite framework; Li-deficient and Li-rich antifluorite phases may be stabilized and may feature numerous elements on the anion site.

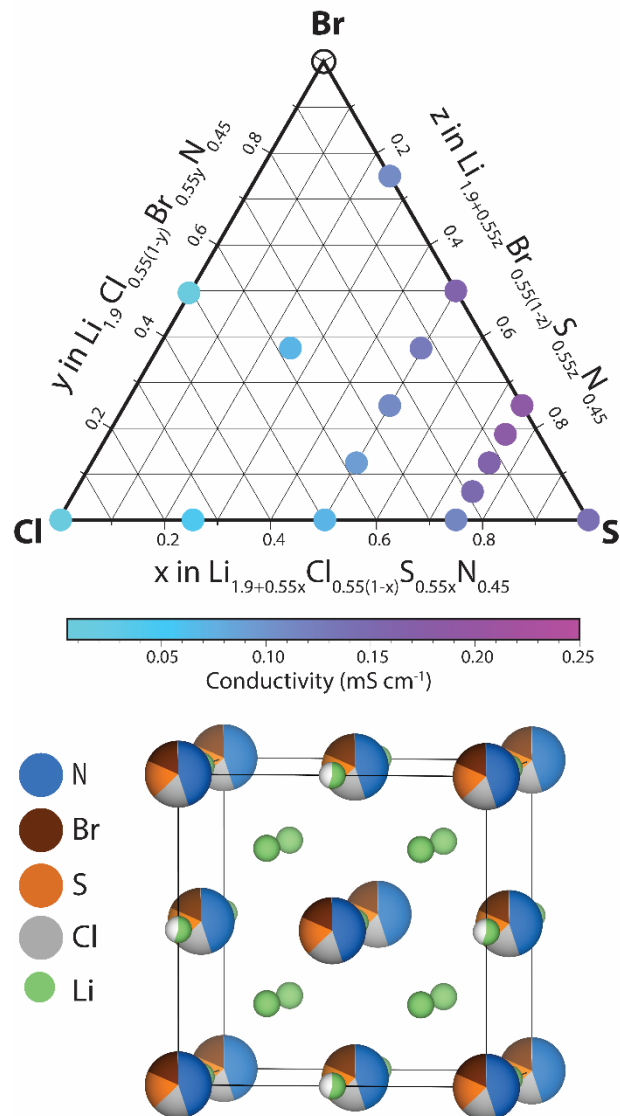


Figure 4.6. Quasi-ternary phase diagram with the $\text{Li}_{1.9}\text{Cl}_{0.55}\text{N}_{0.45}$, $\text{Li}_{1.9}\text{Br}_{0.55}\text{N}_{0.45}$ and the $\text{Li}_{2.45}\text{S}_{0.55}\text{N}_{0.45}$ compositions at its vertices. The circles represent the phase-compositions that were synthesized as part of this work. Coloured circles signify pure-phase antifluorite-like products. Hollow circles signify no pure-phase antifluorite-like phase product. The colors correspond to measured ionic conductivities. A schematic unit cell of the phase space investigated is also shown.

Perspectives of irreducible antifluorite-like electrolytes for batteries

SSB need high-energy, low-voltage anodes such as Li metal (or potentially Li_xSi) to supersede conventional Li-ion batteries.^{8,23} However, the best ion conductors known to date -reaching $>0.1 \text{ mS cm}^{-1}$ in conductivity and comprising oxide, sulfide and halide chemistries- suffer from electrochemical decomposition $<1\text{V vs (Li}^+)$ ^{7,24–26} –with the exception of garnet oxides which are compatible with Li metal.²⁷ Electrochemical decomposition on the anode side is associated with increased cell resistance, capacity loss, dendrite

formation and short circuiting.^{28,29} A promising strategy to avoid reductive decomposition are bilayer separators comprising a catholyte facing the cathode and an anolyte facing the anode.¹ Even oxide garnet electrolytes may potentially benefit from protection layers against Li metal.^{30,31} Anolytes should be highly-conducting and electrochemically stable at the low potentials of Li metal anodes. Highly conducting fully-reduced phases are thus inherently promising anolyte candidates which has also been demonstrated experimentally.^{13,14,32}

High conductivity and stability, however, are not the only suitability criteria of anolytes. Mechanical and microstructural properties of solid electrolytes play a key role, for instance in dendrite formation.^{33,34} Chemical compatibilities of anolytes with the paired catholytes also need to be considered.¹⁰ Additionally, the oxidation limit of anolytes needs to be considered; for example, the operation window of Li_xSi anodes ranges from 0.01 V to 1.1 V.⁸ Due to the low oxidation limit of Li_3N (0.8 V), Li_3N would be inert to reduction but not inert to oxidation when in contact with Li_xSi anodes. In contrast, some compositions of the antifluorite-like phases have oxidation limits exceeding 1.1 V (see Figure 4.5) and would be suitable anolytes for Li_xSi anodes as they would be inert to reduction and oxidation against Li_xSi anodes. In summary, irreducible electrolytes are promising anolyte candidates. The suitability of anolyte layers is system-dependent and multiple factors need to be considered. The high compositional and structural flexibility of fully-reduced antifluorite-like phases we demonstrate in this study will enable the further tunability of ionic conductivity, electrochemical stability, mechanical and microstructural properties – essential for functional electrode/electrolyte interfaces in batteries.³³

4.4 Conclusion

Fully reduced electrolytes based on the antifluorite framework recently received ample attention as their stability against low potentials eliminates performance degradation due to reductive decomposition.³⁵ In this study we demonstrated that the mechanism underlying the increased conductivity in herein discovered irreducible antifluorite-like $\text{Li}_{1+2x}\text{Cl}_{1-x}\text{N}_x$ phases (which includes $\text{Li}_9\text{N}_2\text{Cl}_3$ ref³⁵ and Li_5NCl_2 ref^{10,15} phases) compared to the structurally similar LiCl phase. Computationally, we find that introducing nitrogen into the LiCl anionic framework brings tetrahedral and octahedral Li sites closer in energy so that vacant sites become energetically accessible for diffusion. Analyzing local diffusion bottlenecks we further showed that nitrogen opens diffusion bottlenecks further facilitating Li diffusion. Experimentally we demonstrated that the antifluorite framework is structurally flexible; Li-deficient and Li-excess antifluorite phases can be stabilized. Additionally, we showed that $\text{Li}_{1+2x}\text{Cl}_{1-x}\text{N}_x$ phases are compositionally highly modifiable. S_{Cl} - and Br_{Cl} -substituted analogues were synthesized, boosting the ionic conductivities of $\text{Li}_{1+2x}\text{Cl}_{1-x}\text{N}_x$ phases by an order of magnitude. We further found that fully reduced antifluorite-like phases have an increased oxidation limit compared to Li_3N (0.8 V vs Li) which may be critical advantage over Li_3N (the archetypical fully-reduced electrolyte) to stabilize next-generation anodes.

4.5 Methodology

Synthesis. All preparation steps were performed in an argon atmosphere ($\text{H}_2\text{O} < 1$ ppm, $\text{O}_2 < 1$ ppm). *$\text{Li}_{1+2x}\text{Cl}_{1-x}\text{N}_x$ phases:* The synthesis precursors were LiCl (Sigma-Aldrich, 99%) and Li_3N (Sigma-Aldrich, >99.5%). Stoichiometric amounts of the precursors were milled in a planetary ball mill (Jar: ZrO_2 , 45 mL) with 10 mm ZrO_2 balls and a ball:powder mass ratio of 30 at 550 rpm for 99 (5-min milling-5 min-pause) cycles. *$\text{Li}_{2+x}\text{S}_{1-x}\text{N}_x$ phases:* The synthesis precursors were Li_2S (Sigma-Aldrich, 99%) and Li_3N (Sigma-Aldrich, >99.5%). Stoichiometric amounts of the precursors were milled in a planetary ball mill (Jar: ZrO_2 , 45 mL) with 10 mm ZrO_2 balls and a ball:powder mass ratio of 30 at 550 rpm for 99 (5-min milling-5 min-pause) cycles.

Electrochemical Characterization. the same procedure was applied to all solid electrolytes (SE) investigated in this work: $\text{Li}_{1+2x}\text{Cl}_{1-x}\text{N}_x$ and $\text{Li}_{2+x}\text{S}_{1-x}\text{N}_x$ and $\text{Li}_{1.9+0.55y}\text{Cl}_{0.55(1-y-z)}\text{S}_{0.55y}\text{Br}_{0.55z}\text{N}_{0.45}$. *Electrochemical Impedance Spectroscopy (EIS):* Pellets (diameter=10 mm) of the SE powder samples were pressed (3.2 tons) in custom-made cells. These lab cells consist of an alumina tube and two stainless steel (SS) plungers and an airtight seal. The stainless steel plungers act as current collectors. Solid electrolyte powder is filled in the alumina tube and compressed on both sides with the stainless steel plungers. The cell configuration used was SS|SE|SS. AC impedance was performed with a Metrohm Autolab (AUT86298) in the frequency range 10 MHz to 0.1 Hz with a voltage amplitude of 10 mV. EIS spectra were fitted with a resistor in parallel with a constant phase element (CPE) representing the solid electrolyte and a CPE representing the solid electrolyte-SS interface. *Linear sweep voltammetry (LSV):* LSV measurements were also performed with an Metrohm Autolab (AUT86298). To measure the anodic limit of SE phases, Li|SE|SE-C cells were used. To make the SE-C composite cathode a mixture of SE:Super P with a weight ratio of 0.7:0.3 was milled in a planetary ball mill (Jar: ZrO_2 , 45 mL) with 10 mm ZrO_2 balls and a ball/powder ratio of 30 at 400 rpm for 2 h (5 min milling; 5 min pause). Li|SE|SE-C cells were assembled by pressing a SE pellet (130 mg, 3.2 tons) and subsequently the SE-C composite (15 mg, 3.2 tons) on top. Finally, a Li disk was placed on the opposite side of the SE pellet. The LSV scanning rate was 0.01 mV s^{-1} .

X-ray diffraction. Powder diffraction patterns were collected using $\text{Cu K}\alpha$ X-rays (1.54 \AA) on a PANalytical X'Pert Pro X-ray diffractometer. The air sensitive SE probes were loaded into air-tight holders in an Ar-filled glovebox prior to the measurements. GSAS-II³⁶ and FullProf³⁷ used for LeBail and Rietveld refinements. As a starting point the structure solution of Li_5NCl_2 (i.e. $\text{Li}_{1.66}\text{Cl}_{0.66}\text{N}_{0.33}$) was taken. ¹⁵For $\text{Li}_{1+2x}\text{Cl}_{1-x}\text{N}_x$ phases with higher nitrogen content the nitrogen amount was increased, the chlorine amount reduced and the Li fraction of occupied tetrahedral sites increased according to the synthesized stoichiometry. Based on the initial structure solution of $\text{Li}_{1.66}\text{Cl}_{0.66}\text{N}_{0.33}$ [ref. ¹⁵] all Li ions were assumed in tetrahedral sites though we note that generally a small occupation of the octahedral sites ($\leq 5\%$) may potentially exist (see Supplementary Note 1).

Computational details. All DFT calculations were performed with the Vienna ab initio simulation package VASP with computational settings consistent with those used in the Materials Project database. ³⁸ *Obtaining jump-activation energies for $\text{Li}_{1+2x}\text{Cl}_{1-x}\text{N}_x$ and LiCl.* For the generation and analysis of supercells the calculations were done on $2 \times 2 \times 2$ $\text{Li}_{1+2x}\text{Cl}_{1-x}\text{N}_x$ or $2 \times 2 \times 2$ LiCl supercells. Because of the shared site occupations and partial occupancies in $\text{Li}_{1+2x}\text{Cl}_{1-x}\text{N}_x$ phases, different atomic arrangements were generated by random decoration of the Wyckoff 4a (0,0,0) position with nitrogen and chlorine and the 8c (0.25,0.25,0.25) positions were randomly decorated with Li and vacancies. For the generation and analysis

of supercells the pymatgen package was used.³⁹ For the AIMD simulations the Li pseudopotential was changed from one considering the semicore s electrons as valence (i.e. $1s^22s^1$ “Li_sv”, which was used for relaxations) to one considering the 2s electrons (i.e. $2s^1$ “Li”) as this enables the use of a lower energy cutoff and vastly improves computational speed. The simulation time was 200 ps for every AIMD simulation. The AIMD simulations were executed at 1000 K. The dissection of AIMD simulations into individual jump events and subsequent analysis of jump frequencies and individual $E_{a, \text{jump}}$ values was done as first described by de Klerk and Wagemaker¹⁷ and currently developed as a python package in our group.⁴⁰ A comprehensive account can be found in ref¹⁷ but crucial aspects for the understanding of the reported data is presented here. *Calculation of $E_{a, \text{jump}}$ values between two sites:* The sites are defined around the 0 K equilibrium positions of the Li ions. At every simulation step it is recorded in which site each Li ion is located or whether it is currently between two sites. From this information the jump frequency between two sites $v_{A \rightarrow B}$ can be calculated according to equation 4.3:

$$v_{A \rightarrow B} = \frac{N_{A \rightarrow B}}{\tau_A} \quad (4.3)$$

where $v_{A \rightarrow B}$ is the jump frequency for jumps from site A to site B, $N_{A \rightarrow B}$ is the number of recorded jumps from A to B, and τ_A is the time of occupation of site A. $E_{a, \text{jump}}$ is then obtained from equation (4.1). This analysis can be done with the *gemdat ref* (⁴⁰) python package currently developed in our group. To obtain a picture as complete as possible for the jump processes in the disordered $\text{Li}_{1+2x}\text{Cl}_{1-x}\text{N}_x$ phases we executed the AIMD simulations on 5 supercells that together feature all of the possible site-bottleneck-site permutations in $\text{Li}_{1+2x}\text{Cl}_{1-x}\text{N}_x$ phases. A table with jump E_a values is provided Table S4.7.

Stability calculations for $\text{Li}_{1+2x}\text{Cl}_{1-x}\text{N}_x$ and for $\text{Li}_{2+x}\text{S}_{1-x}\text{N}_x$. 10,000 $2 \times 2 \times 2$ supercells were generated by randomly decorating the Wyckoff 4a (0,0,0) position with nitrogen and chlorine. The 8c (0.25,0.25,0.25) positions were also randomly decorated with Li and vacancies according to the targeted stoichiometry. Then formal charges of -3, -1, and +1 were assigned to nitrogen, chlorine and Li, respectively and the electrostatic energy (‘Ewald energy’) was calculated via *pymatgen*. Subsequently, out of the $\text{Li}_{1+2x}\text{Cl}_{1-x}\text{N}_x$ structures, 30 with the lowest Ewald energy were taken and relaxed by DFT. The energies obtained from DFT were used to calculate the energy of the hull of the $\text{Li}_{1+2x}\text{Cl}_{1-x}\text{N}_x$ phases, energetic corrections from the materials project data base were applied and the energies for the end-member phases (Li_3N and Li_2S) were also obtained from the materials project data base (see Supplementary Note 4 also).³⁸

4.6 References

The following references used in the Supplementary Information: 13,15,38,41,42

- (1) Famprikis, T.; Canepa, P.; Dawson, J. A.; Islam, M. S.; Masquelier, C. Fundamentals of Inorganic Solid-State Electrolytes for Batteries. *Nat. Mater.* **2019**, *18*, 1278–1291.
- (2) Janek, J.; Zeier, W. G. Challenges in Speeding up Solid-State Battery Development. *Nat. Energy* **2023**, *8* (3), 230–240.
- (3) Kato, Y.; Hori, S.; Saito, T.; Suzuki, K.; Hirayama, M.; Mitsui, A.; Yonemura, M.; Iba, H.; Kanno, R. High-Power All-Solid-State Batteries Using Sulfide Superionic Conductors. *Nat. Energy* **2016**, *1* (4), 1–7.
- (4) Zhou, L.; Assoud, A.; Zhang, Q.; Wu, X.; Nazar, L. F. New Family of Argyrodite Thioantimonate Lithium Superionic Conductors. *J. Am. Chem. Soc.* **2019**, *141* (48), 19002–19013.
- (5) Kraft, M. A.; Ohno, S.; Zinkevich, T.; Koerver, R.; Culver, S. P.; Fuchs, T.; Senyshyn, A.; Indris, S.; Morgan, B. J.; Zeier, W. G. Inducing High Ionic Conductivity in the Lithium Superionic Argyrodites $\text{Li}_{6+x}\text{P}_{1-x}\text{Ge}_x\text{S}_{51}$ for All-Solid-State Batteries. *J. Am. Chem. Soc.* **2018**, *140* (47), 16330–16339.
- (6) Kamaya, N.; Homma, K.; Yamakawa, Y.; Hirayama, M.; Kanno, R.; Yonemura, M.; Kamiyama, T.; Kato, Y.; Hama, S.; Kawamoto, K. A Lithium Superionic Conductor. *Nat. Mater.* **2011**, *10* (9), 682–686.
- (7) Zhu, Y.; He, X.; Mo, Y. First Principles Study on Electrochemical and Chemical Stability of Solid Electrolyte-Electrode Interfaces in All-Solid-State Li-Ion Batteries. *J. Mater. Chem. A* **2016**, *4* (9), 3253–3266.
- (8) Huo, H.; Janek, J. Silicon as Emerging Anode in Solid-State Batteries. *ACS Energy Lett.* **2022**, *7* (11), 4005–4016.
- (9) Zaman, W.; Hatzell, K. B. Processing and Manufacturing of next Generation Lithium-Based All Solid-State Batteries. *Curr. Opin. Solid State Mater. Sci.* **2022**, *26* (4), 101003.
- (10) Landgraf, V.; Famprikis, T.; de Leeuw, J.; Bannenberg, L. J.; Ganapathy, S.; Wagemaker, M. Li_5NCl_2 : A Fully-Reduced, Highly-Disordered Nitride-Halide Electrolyte for Solid-State Batteries with Lithium-Metal Anodes. *ACS Appl. Energy Mater.* **2023**, *6* (3), 1661–1672.
- (11) Szczuka, C.; Karasulu, B.; Groh, M. F.; Sayed, F. N.; Sherman, T. J.; Bocarsly, J. D.; Vema, S.; Menkin, S.; Emge, S. P.; Morris, A. J.; Grey, C. P. Forced Disorder in the Solid Solution $\text{Li}_3\text{P-Li}_2\text{S}$: A New Class of Fully Reduced Solid Electrolytes for Lithium Metal Anodes. *J. Am. Chem. Soc.* **2022**, *144* (36), 16350–16365.
- (12) Xu, X.; Du, G.; Cui, C.; Liang, J.; Zeng, C.; Wang, S.; Ma, Y.; Li, H. Stabilizing the Halide Solid Electrolyte to Lithium by a $\beta\text{-Li}_3\text{N}$ Interfacial Layer. *ACS Appl. Mater. Interfaces* **2022**, *14* (35), 39951–39958.
- (13) Landgraf, V.; Tu, M.; Cheng, Z.; de Leeuw, J.; Ganapathy, S.; Wagemaker, M.; Famprikis, T. Entropy-Induced High Conductivity in Fully-Reduced Electrolytes for Solid-State Batteries with Lithium Metal Anodes. *ChemRxiv* **2023**.
- (14) Li, W.; Li, M.; Chien, P.-H.; Wang, S.; Yu, C.; King, G.; Hu, Y.; Xiao, Q.; Shakouri, M.; Feng, R. Lithium-Compatible and Air-Stable Vacancy-Rich $\text{Li}_9\text{N}_2\text{Cl}_3$ for High-Areal Capacity, Long-Cycling All-Solid-State Lithium Metal Batteries. *Sci. Adv.* **2023**, *9* (42), eadh4626.
- (15) Marx, R.; Mayer, H. M. Preparation and Crystal Structure of Ordered and Disordered Lithium Nitride Dichloride, Li_5NCl_2 . *J. Solid State Chem.* **1997**, *130* (1), 90–96.
- (16) Shannon, R. D. Revised Effective Ionic Radii and Systematic Studies of Interatomic Distances in Halides and Chalcogenides. *Acta Crystallogr. Sect. A Cryst. physics, diffraction, Theor. Gen. Crystallogr.* **1976**, *32* (5), 751–767.
- (17) De Klerk, N. J. J.; Van Der Maas, E.; Wagemaker, M. Analysis of Diffusion in Solid-State Electrolytes through MD Simulations, Improvement of the Li-Ion Conductivity in $\beta\text{-Li}_3\text{PS}_4$ as an Example. *ACS Appl. Energy Mater.* **2018**, *1* (7), 3230–3242.

- (18) Yu, C.; Ganapathy, S.; De Klerk, N. J. J.; Roslon, I.; Van Eck, E. R. H.; Kentgens, A. P. M.; Wagemaker, M. Unravelling Li-Ion Transport from Picoseconds to Seconds: Bulk versus Interfaces in an Argyrodite $\text{Li}_6\text{PS}_5\text{Cl-Li}_2\text{S}$ All-Solid-State Li-Ion Battery. *J. Am. Chem. Soc.* **2016**, *138* (35), 11192–11201.
- (19) De Klerk, N. J. J.; Rosłoń, I.; Wagemaker, M. Diffusion Mechanism of Li Argyrodite Solid Electrolytes for Li-Ion Batteries and Prediction of Optimized Halogen Doping: The Effect of Li Vacancies, Halogens, and Halogen Disorder. *Chem. Mater.* **2016**, *28* (21), 7955–7963.
- (20) De Klerk, N. J. J.; Wagemaker, M. Diffusion Mechanism of the Sodium-Ion Solid Electrolyte Na_3PS_4 and Potential Improvements of Halogen Doping. *Chem. Mater.* **2016**, *28* (9), 3122–3130.
- (21) Li, X.; Liu, H.; Zhao, C.; Kim, J. T.; Fu, J.; Hao, X.; Li, W.; Li, R.; Chen, N.; Cao, D.; Wu, Z.; Su, Y.; Liang, J.; Sun, X. Hopping Rate and Migration Entropy as the Origin of Superionic Conduction within Solid-State Electrolytes. *J. Am. Chem. Soc.* **2023**.
- (22) Flores-González, N.; Minafra, N.; Dewald, G.; Reardon, H.; Smith, R. I.; Adams, S.; Zeier, W. G.; Gregory, D. H. Mechanochemical Synthesis and Structure of Lithium Tetrahaloaluminates, LiAlX_4 (X = Cl, Br, I): A Family of Li-Ion Conducting Ternary Halides. *ACS Mater. Lett.* **2021**, *3* (5), 652–657.
- (23) Janek, J.; Zeier, W. G. A Solid Future for Battery Development. *Nat. Energy* **2016**, *1* (9), 1–4.
- (24) Zhu, Y.; He, X.; Mo, Y. Origin of Outstanding Stability in the Lithium Solid Electrolyte Materials: Insights from Thermodynamic Analyses Based on First-Principles Calculations. *ACS Appl. Mater. Interfaces* **2015**, *7* (42), 23685–23693.
- (25) Schwietert, T. K.; Arszewska, V. A.; Wang, C.; Yu, C.; Vasileiadis, A.; de Klerk, N. J. J.; Hageman, J.; Hupfer, T.; Kerkamm, I.; Xu, Y. Clarifying the Relationship between Redox Activity and Electrochemical Stability in Solid Electrolytes. *Nat. Mater.* **2020**, *19* (4), 428–435.
- (26) Wang, S.; Bai, Q.; Nolan, A. M.; Liu, Y.; Gong, S.; Sun, Q.; Mo, Y. Lithium Chlorides and Bromides as Promising Solid-State Chemistries for Fast Ion Conductors with Good Electrochemical Stability. *Angew. Chemie - Int. Ed.* **2019**, *58* (24), 8039–8043.
- (27) Subramanian, K.; Alexander, G. V.; Karthik, K.; Patra, S.; Indu, M. S.; Sreejith, O. V.; Viswanathan, R.; Narayanasamy, J.; Murugan, R. A Brief Review of Recent Advances in Garnet Structured Solid Electrolyte Based Lithium Metal Batteries. *J. Energy Storage* **2021**, *33*, 102157.
- (28) Riegger, L. M.; Schlem, R.; Sann, J.; Zeier, W. G.; Janek, J. Lithium-Metal Anode Instability of the Superionic Halide Solid Electrolytes and the Implications for Solid-State Batteries. *Angew. Chemie* **2021**, *133* (12), 6792–6797.
- (29) Du, M.; Liao, K.; Lu, Q.; Shao, Z. Recent Advances in the Interface Engineering of Solid-State Li-Ion Batteries with Artificial Buffer Layers: Challenges, Materials, Construction, and Characterization. *Energy Environ. Sci.* **2019**, *12* (6), 1780–1804.
- (30) Xu, H.; Li, Y.; Zhou, A.; Wu, N.; Xin, S.; Li, Z.; Goodenough, J. B. Li₃N-Modified Garnet Electrolyte for All-Solid-State Lithium Metal Batteries Operated at 40 °C. *Nano Lett.* **2018**, *18* (11), 7414–7418.
- (31) Zhu, C.; Fuchs, T.; Weber, S. A. L.; Richter, F. H.; Glasser, G.; Weber, F.; Butt, H. J.; Janek, J.; Berger, R. Understanding the Evolution of Lithium Dendrites at $\text{Li}_{6.25}\text{Al}_{0.25}\text{La}_3\text{Zr}_2\text{O}_{12}$ Grain Boundaries via Operando Microscopy Techniques. *Nat. Commun.* **2023**, *14* (1), 1300.
- (32) Yu, P.; Zhang, H.; Hussain, F.; Luo, J.; Tang, W.; Lei, J.; Gao, L.; Butenko, D.; Wang, C.; Zhu, J.; Yin, W.; Zhang, H.; Han, S.; Zou, R.; Chen, W.; Zhao, Y.; Xia, W.; Sun, X. Lithium Metal-Compatible Antifluorite Electrolytes for Solid-State Batteries. *J. Am. Chem. Soc.* **2024**.
- (33) Krauskopf, T.; Richter, F. H.; Zeier, W. G.; Janek, J. Physicochemical Concepts of the Lithium Metal Anode in Solid-State Batteries. *Chem. Rev.* **2020**, *120* (15), 7745–7794.
- (34) Hatzell, K. B.; Chen, X. C.; Cobb, C. L.; Dasgupta, N. P.; Dixit, M. B.; Marbella, L. E.; Mcdowell, M. T.; Mukherjee, P. P.; Verma, A.; Viswanathan, V.; Westover, A. S.; Zeier, W. G. Challenges in Lithium Metal Anodes for Solid-State Batteries. **2020**.
- (35) Li, W.; Li, M.; Chien, P.; Wang, S.; Yu, C.; King, G.; Hu, Y.; Xiao, Q.; Shakouri, M.; Feng, R.; Fu, B.; Abdolvand, H.; Fraser, A.;

- Li, R.; Huang, Y.; Liu, J.; Mo, Y.; Sham, T.; Sun, X. Lithium-Compatible and Air-Stable Vacancy-Rich $\text{Li}_9\text{N}_2\text{Cl}_3$ for High – Areal Capacity , Long-Cycling All – Solid-State Lithium Metal Batteries. **2023**.
- (36) Toby, B. H.; Von Dreele, R. B. GSAS-II: The Genesis of a Modern Open-Source All Purpose Crystallography Software Package. *J. Appl. Crystallogr.* **2013**, *46* (2), 544–549.
- (37) Rodriguez-Carvajal, J. In Satellite Meeting on Powder Diffraction of the XV Congress of the IUCr, 1990, 127. *Toulouse, Fr.*
- (38) Jain, A.; Ong, S. P.; Hautier, G.; Chen, W.; Richards, W. D.; Dacek, S.; Cholia, S.; Gunter, D.; Skinner, D.; Ceder, G.; Persson, K. A. Commentary: The Materials Project: A Materials Genome Approach to Accelerating Materials Innovation. *APL Mater.* **2013**, *1* (1), 001002.
- (39) Ong, S. P.; Richards, W. D.; Jain, A.; Hautier, G.; Kocher, M.; Cholia, S.; Gunter, D.; Chevrier, V. L.; Persson, K. A.; Ceder, G. Python Materials Genomics (Pymatgen): A Robust, Open-Source Python Library for Materials Analysis. *Comput. Mater. Sci.* **2013**, *68*, 314–319.
- (40) Azizi, V.; Smeets, S.; Lavrinenko, A. K.; Ciarella, S.; Famprikis, T. GEMDAT. Zenodo July 2024.
- (41) Catlow, C. R. A. Static Lattice Simulation of Structure and Transport in Superionic Conductors. *Solid State Ionics* **1983**, *8* (SUPPL. 3), 89–107.
- (42) Marx, R.; Lissner, F.; Schleid, T. $\text{Li}_9\text{N}_2\text{S}_3$: Das Erste Nitridsulfid Der Alkalimetalle in Einer Li_2O -Typ-Variante. *Zeitschrift für Anorg. und Allg. Chemie* **2006**, *632* (12-13), 2151.
- (43) Yu, C.; Ganapathy, S.; De Klerk, N. J. J.; Roslon, I.; Van Eck, E. R. H.; Kentgens, A. P. M.; Wagemaker, M. Unravelling Li-Ion Transport from Picoseconds to Seconds: Bulk versus Interfaces in an Argyrodite $\text{Li}_6\text{PS}_5\text{Cl-Li}_2\text{S}$ All-Solid-State Li-Ion Battery. *J. Am. Chem. Soc.* **2016**, *138* (35), 11192–11201.
- (44) Deng, Z.; Mishra, T. P.; Mahayoni, E.; Ma, Q.; Tieu, A. J. K.; Guillon, O.; Chotard, J.-N.; Seznec, V.; Cheetham, A. K.; Masquelier, C. Fundamental Investigations on the Sodium-Ion Transport Properties of Mixed Polyanion Solid-State Battery Electrolytes. *Nat. Commun.* **2022**, *13* (1), 4470.
- (45) Wilkening, M.; Gebauer, D.; Heitjans, P. Diffusion Parameters in Single-Crystalline Li_3N as Probed by 6Li and 7Li Spin-Alignment Echo NMR Spectroscopy in Comparison with Results from 8Li β -Radiation Detected NMR. *J. Phys. Condens. Matter* **2007**, *20* (2), 22201.

Chapter 5: High conductivity in irreducible nitridophosphide solid electrolytes

5.1 Summary of chapter

In this chapter we experimentally demonstrate that N_p substitutions can be obtained on irreducible antiferite $Li_{2+x}S_{1-x}P_x$ phases: we successfully synthesized antiferite $Li_{2.6}S_{0.4}P_{0.6}$, $Li_{2.6}S_{0.4}P_{0.35}N_{0.15}$ and $Li_{2.6}S_{0.4}P_{0.35}N_{0.25}$. $Li_{2.6}S_{0.4}P_{0.35}N_{0.25}$ has a conductivity of ~ 0.75 mS and is thus, at the time of writing, the highest-conducting irreducible solid electrolyte reported. Computationally we demonstrate that N_p substitutions increase the void space in steric diffusion bottlenecks due to the smaller ionic radius of N^{3-} compared to P^{3-} ions which correlates with facilitated Li diffusion.

5.2 Introduction

Solid-state batteries currently receive ample attention due to their potential to outperform lithium-ion batteries in terms of energy density when featuring next-generation anodes such as Li metal or silicon.^{1,2} One key remaining challenge is identifying solid electrolytes that combine high ionic conductivity with stability in contact with the highly reducing potentials of next-generation anodes.³ Fully reduced electrolytes have all anions in their lowest permitted oxidation state and are thus *irreducible*, that is they are resistant to reductive decomposition in contact with low-voltage anodes. Li_3N was for a long time the only fully reduced phase exhibiting an ionic conductivity exceeding 0.1 mS cm^{-1} .⁴⁻⁷ Recently however, significant advances have been made in developing highly-conducting irreducible antiferite electrolytes.⁸⁻¹¹ The best conducting irreducible antiferite phases known at the time of writing are the $Li_{2.5}S_{0.5}N_{0.5}$ and the $Li_{2.75}S_{0.25}P_{0.75}$ phases (part of the antiferite $Li_{2+x}S_{1-x}P_x$ and $Li_{2+x}S_{1-x}N_x$ solid solutions) reaching ~ 0.2 mS cm^{-1} .⁸⁻¹⁰ The conductivity of these phases, however, are still superseded by Li_3N with an ionic conductivity of 0.5 mS cm^{-1} .⁴⁻⁷ The $Li_{2+x}S_{1-x}P_x$ and $Li_{2+x}S_{1-x}N_x$ phases are structurally analogous suggesting that P_N or N_p substituted phases could potentially exist but this has so far not been investigated. This chapter aims to answer the following two questions: (1) Can partially N_p -substituted $Li_{2+x}S_{1-x}P_x$ phases — that is $Li_{2+x+y}S_{1-x-y}P_xN_y$ phases—be stabilized? And (2), is N_p substitution in $Li_{2+x}S_{1-x}P_x$ phases a viable strategy to improve conductivity and potentially supersede the ionic conductivity of Li_3N ?

We found computationally that N_p substitution increases the conductivity of antiferite $Li_{2+x}S_{1-x}P_x$ phases as the small ionic radius of N^{3-} ions increases the void space of steric diffusion bottlenecks facilitating Li diffusion. Experimentally we verified that N_p substituted antiferite $Li_{2+x}S_{1-x}P_x$ (that is $Li_{2+x+y}S_{1-x-y}P_xN_y$) phases can be synthesized and that N_p substitutions indeed increase ionic conductivity. The synthesized $Li_{2.6}S_{0.4}P_{0.35}N_{0.25}$ phase has an ionic conductivity of 0.75 mS cm^{-1} while the equivalent phase without N_p substitution ($Li_{2.6}S_{0.4}P_{0.6}$) has a conductivity of ~ 0.1 mS cm^{-1} . At the time of writing the $Li_{2+x+y}S_{1-x-y}P_xN_y$ phases synthesized in this work for the first time, are the best conducting irreducible solid electrolytes known.

5.3 Results and Discussion

Structural description

The Li-excess antiferite $\text{Li}_{2+x}\text{S}_{1-x}\text{P}_x$ phases crystallize in the $Fm\bar{3}m$ space group.⁸ The anions on the Wyckoff 4a position are partially occupied by S and P, the tetrahedral Li sites on the Wyckoff 8c position are fully occupied and the octahedral Li sites on the Wyckoff 4b position are partially occupied.⁸ The Li-excess $\text{Li}_{2+x}\text{S}_{1-x}\text{N}_x$ phases have an analogous structure with N substituted for P.^{9,10} Partially N-substituted $\text{Li}_{2+x}\text{S}_{1-x}\text{P}_x$ phases, that is $\text{Li}_{2+x+y}\text{S}_{1-x-y}\text{P}_x\text{N}_y$ phases – if existing– would have equivalent crystal structures with three anions sharing the Wyckoff 4a site (S, N and P, Figure 5.1a).⁶ We begin our investigation with ab initio molecular dynamic (AIMD) simulations of Li-diffusivity in antiferite $\text{Li}_{2+x+y}\text{S}_{1-x-y}\text{P}_x\text{N}_y$ phases.

Chemical compositions that maximize Li diffusivity

To investigate Li diffusion in partially N_p substituted antiferite $\text{Li}_{2+x}\text{S}_{1-x}\text{P}_x$ phases we performed AIMD simulations on 8 (2x2x2) $\text{Li}_{2+x+y}\text{S}_{1-x-y}\text{P}_x\text{N}_y$ supercells; to obtain these supercells the anion Wyckoff 4a positions were randomly decorated with N, S and P respecting the overall desired stoichiometry. The AIMD simulations show that –just as is the case for $\text{Li}_{1+2x}\text{Cl}_{1-x}\text{N}_x$ and $\text{Li}_{2+x}\text{S}_{1-x}\text{N}_x$ phases (refs^{9,11})– Li-ions hop between tetrahedral sites (tet \leftrightarrow tet) and between octahedral and tetrahedral sites (oct \leftrightarrow tet). Tet \leftrightarrow tet jumps occur through linear bottlenecks consisting of two anions and oct \leftrightarrow tet jumps occur through triangular bottlenecks consisting of three anions which is illustrated in Figures 5.1a and 5.1b. As done previously (ref 9), we defined jump types by the anion at the corners of the Li-site-polyhedra and the anion-composition of the diffusion-bottleneck. For example, a Li-ion jump departing from a tetrahedral Li-site with one N^{3-} and three S^{2-} at its corners (N_1S_3) through a bottleneck consisting of three S^{2-} anions (SSS) ending in an octahedral Li site with three S^{2-} and three N^{3-} at its corners (N_3S_3) is a jump of type $\text{N}_1\text{S}_3\text{-N}_3\text{S}_3(\text{SSS})$. AIMD simulations allow to determine the jump rate ($v_{A\rightarrow B}$) between two sites (A and B) which can be rescaled to yield a jump activation energy as shown in equation 5.1 (ref.¹²):

$$E_{a,A\rightarrow B} = -k_b T \ln \left(\frac{v_{A\rightarrow B}}{v_0} \right) \quad (5.1)$$

where k_b is Boltzmann's constant, T the temperature in Kelvin and v_0 the attempt frequency assumed to be 10^{13} s^{-1} which is a common assumption (refs¹³⁻¹⁶) that we further validated for our system by analysing the frequency of the Li oscillations around Li sites which has also been done in previous investigations (refs^{9,12}, Table S5.1).

⁶ We note that $\text{Li}_{2+x}\text{S}_{1-x}\text{P}_x$, $\text{Li}_{2+x}\text{S}_{1-x}\text{N}_x$ and $\text{Li}_{2+x+y}\text{S}_{1-x-y}\text{P}_x\text{N}_y$ phases are strictly speaking Li-excess antiferite phases (that is the Li/anion ratio is >2) which means that these are not *antiferite* but *antiferite-like* phases. This distinction, however, is not always made and these *antiferite-like* phases are referred to simply as *antiferite* phases (see refs 8, 10).

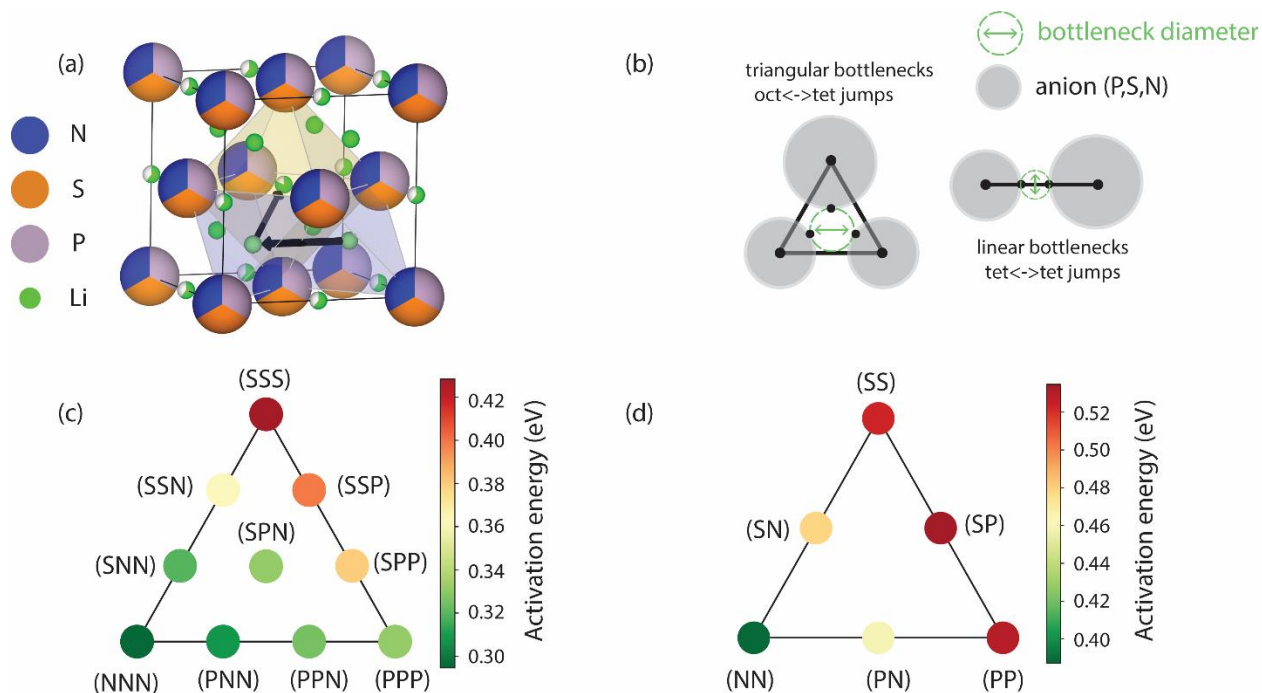


Figure 5.1. Diffusion in $\text{Li}_{2+x+y}\text{S}_{1-x-y}\text{P}_x\text{N}_y$ phases. (a) Schematic unit cell of $\text{Li}_{2+x+y}\text{S}_{1-x-y}\text{P}_x\text{N}_y$ phases crystallising in the $Fm\bar{3}m$ space group. The blue shadings highlight two tetrahedral Li sites, the yellow shading highlights one octahedral Li-site. The arrows indicate the path of tet \leftrightarrow tet jumps and tet \rightarrow oct jumps. (b) Schematic representation of the steric diffusion bottlenecks in $\text{Li}_{2+x+y}\text{S}_{1-x-y}\text{P}_x\text{N}_y$ phases. The triangular bottleneck for oct \leftrightarrow tet and the linear bottleneck for tet \leftrightarrow tet jumps are shown. Figure 5.1b also schematically shows how the bottleneck diameter is obtained by taking into account the anion radii of the bottleneck. (c) Average Li-hop activation energy through triangular steric bottlenecks of oct \leftrightarrow tet hops. (d) Average Li-hop activation energy through linear steric bottlenecks of tet \leftrightarrow tet hops.

The 8 supercells we used for AIMD simulations in total contain 92% of the 816 jump types present in $\text{Li}_{2+x+y}\text{S}_{1-x-y}\text{P}_x\text{N}_y$ phases so that hop activation energies for 92% of all jumps in $\text{Li}_{2+x+y}\text{S}_{1-x-y}\text{P}_x\text{N}_y$ could be identified.

In Figures 5.1c and 5.1d the average activation energy for diffusion through all bottleneck-types is shown. Three trends can be seen in Figures 5.1c and 5.1d: (1) P_s substitutions in bottlenecks monotonically lower the jump activation energy. (2) N_s substitutions in bottlenecks monotonically lower the jump activation energy. (3) N_p substitutions in bottlenecks monotonically lower the activation energy. Figure 5.1d shows similar trends for the linear bottleneck of tet-tet jumps. In the next section we will investigate potential mechanisms by which the above trends may be explained.

Origin of enhanced Li-diffusion through P_s, N_s and N_P-substituted bottlenecks

In the Li_{2+x}S_{1-x}P_x solid solution of antiferroite-like phases the lattice parameter increases with increasing P-content suggesting that the ionic radius of P³⁻ is larger than the ionic radius of S²⁻.⁸ However, the ionic radius of P³⁻ anions is reported to be similar to that of the S²⁻ anions (1.85 Å vs 1.84 Å).^{17,18} That the ionic radii of P³⁻ and S²⁻ are very similar is further supported by the radial distribution functions (rdf) in our AIMD simulations; Figure 5.3 and Figure S5.1 show that the Li-N rdf has its first peak at smaller radii (~0.5 Å) than the Li-S rdf reflecting the smaller ionic radius of N³⁻ compared to S²⁻; in contrast the Li-P rdf is congruent with the Li-S rdf suggesting similar ionic radii for P³⁻ and S²⁻. The experimentally-observed increasing lattice parameter for P-rich Li_{2+x}S_{1-x}P_x phases (ref⁸) thus likely originates from increased electrostatic repulsion between anions because of the higher- valence P³⁻ ions (vide infra).

Most importantly, P^{3-} and S^{2-} have very similar ionic radii and we will use the reported ionic radii for P^{3-} , S^{2-} and N^{3-} (1.85 Å, 1.84 Å, 1.49 Å, refs^{17,18}) in the following sections where we calculate bottleneck diameters as a proxy for the void space in steric diffusion bottlenecks.

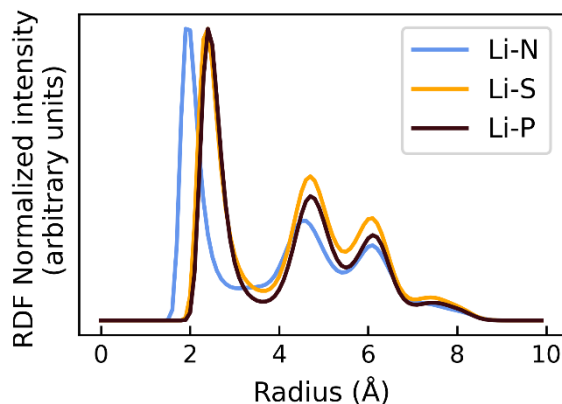


Figure 5.2. Radial distribution functions obtained from an AIMD simulation of a (2x2x2) supercell with $Li_{2.625}S_{0.375}N_{0.31}P_{0.31}$ stoichiometry. Radial distribution functions for the other AIMD simulation executed are shown in Figures S5.1a-h.

It was previously shown for the $Li_{2+x}S_{1-x}N_x$ solid solution that N-containing steric-bottlenecks have larger void spaces due to the considerably smaller ionic radius of N^{3-} anions (1.49 Å) compared to S^{2-} (1.84 Å).⁹ This increased void space facilitates Li diffusion through N-containing bottlenecks. A proxy for the void space in bottlenecks is the bottleneck diameter which is calculated as shown in Figure 5.1b (and described in the methodology), taking into account the ionic radii for the surrounding anions. As done previously (ref⁹), we calculated the average jump activation energy of oct→tet, tet→oct and tet↔tet jumps through all possible bottlenecks as well as the respective average bottleneck diameters. This analysis is shown in Figure 5.3 for tet↔oct jumps and in Figure S5.2 for tet↔tet jumps. Figure 5.3a shows that N_S substitutions in SSS bottlenecks lower the average jump activation energy due to the strongly increasing bottleneck diameter. By the same token, Figure 5.3b shows that N_P substitutions in PPP bottlenecks also lower the jump activation energy. Figure 5.3c shows that P_S substitutions in SSS bonds also lower the jump activation energy which also correlate with increasing bottleneck diameters —despite P^{3-} and S^{2-} having similar ionic radii.

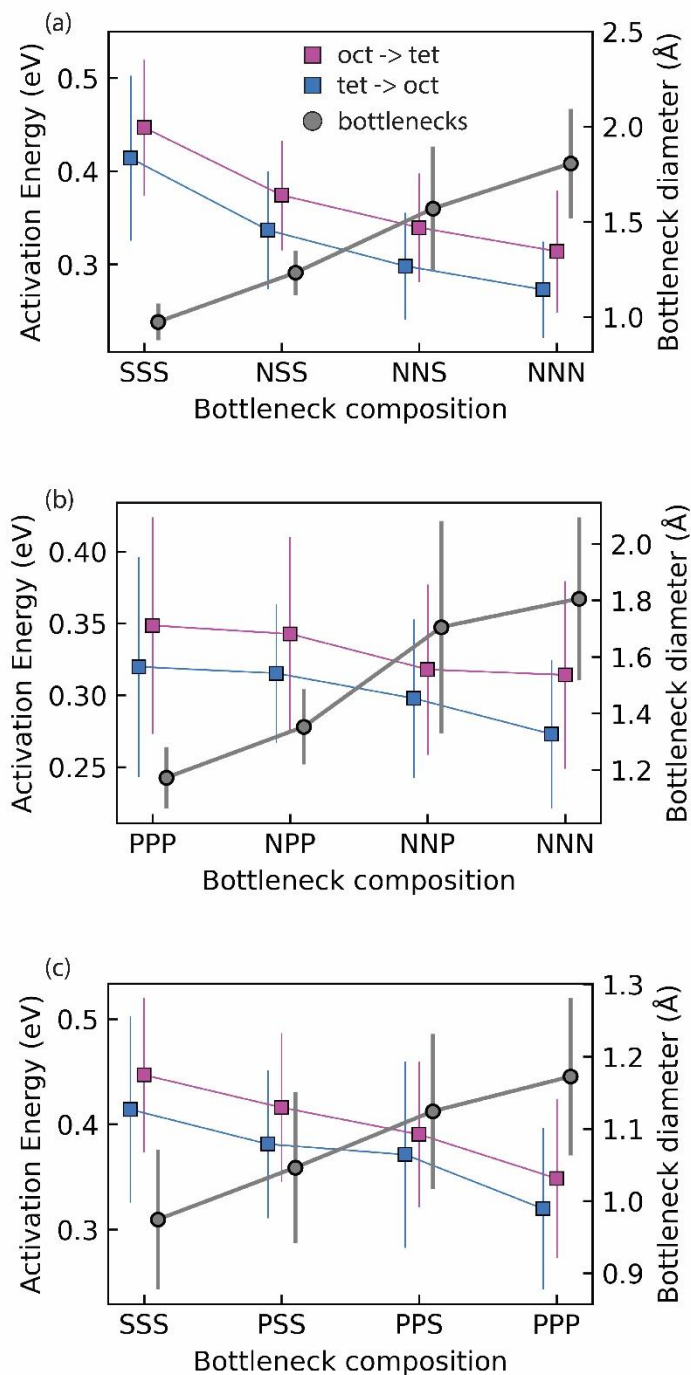


Figure 5.3. Correlation between Li-hop activation energy and bottleneck diameter as a proxy for the void size of the steric bottlenecks. (a) Effect of NS substitution in SSS bottlenecks on bottleneck diameter and Li-hop activation energies. (b) Effect of NP substitution in PPP bottlenecks on bottleneck diameter and Li-hop activation energies. (c) Effect of PS substitution in SSS bottlenecks on bottleneck diameter and Li-hop activation energies.

Since P^{3-} and S^{2-} have almost identical ionic radii (1.84 Å, 1.85 Å) the increased bottleneck diameters of P_S substituted SSS bottlenecks have to originate from an increased distance between the anions. Figure 5.4a shows the area of the triangle defined by the positions of the bottleneck-anions of P_S substituted SSS bottlenecks. Indeed, the triangle area (and hence the distance between the anions) monotonously increases from SSS to PPP bottlenecks likely due to the higher valence of P^{3-} anions and thus increases electrostatic repulsions. The increased distance between the bottleneck anions enables the larger bottleneck diameter despite P^{3-} and S^{2-} having similar ionic radii. In conclusion, N_S and P_S substitutions in SSS bottlenecks increase bottleneck diameters in two different ways. P_S substitution forces the bottleneck anions further apart due to increased electrostatic repulsions. In the case of N_S substitutions, the bottleneck enlargement majorly originates from the smaller ion size of N^{3-} compared to S^{2-} . These two mechanisms of bottleneck enlargements are summarized in Figures 5.4b and 5.4c. We note that increased electrostatic repulsions could in principle also increase the distance between anions in N_S substituted SSS bottleneck since N^{3-} —just like P^{3-} — has a larger valence than S^{2-} . However, a monotonously increasing distance between the anions is not observed for N_S substituted SSS bottlenecks (Figure S5.3) suggesting that the increased inter-anion repulsions of P_S substitutions are mitigated by the smaller ion size of N^{3-} ions. Finally, we note that while the increased bottleneck diameter contributes to the decreasing jump activation energies in P_S substituted SSS bottlenecks, the different polarizability of the anions should also be considered. According to Fajan's rules (ref ¹⁹), P^{3-} is likely more polarizable than S^{2-} since it has higher charge while having a similar ionic radius. This increased polarizability of P^{3-} may additionally contribute to facilitated Li-diffusion through P-containing bottlenecks.

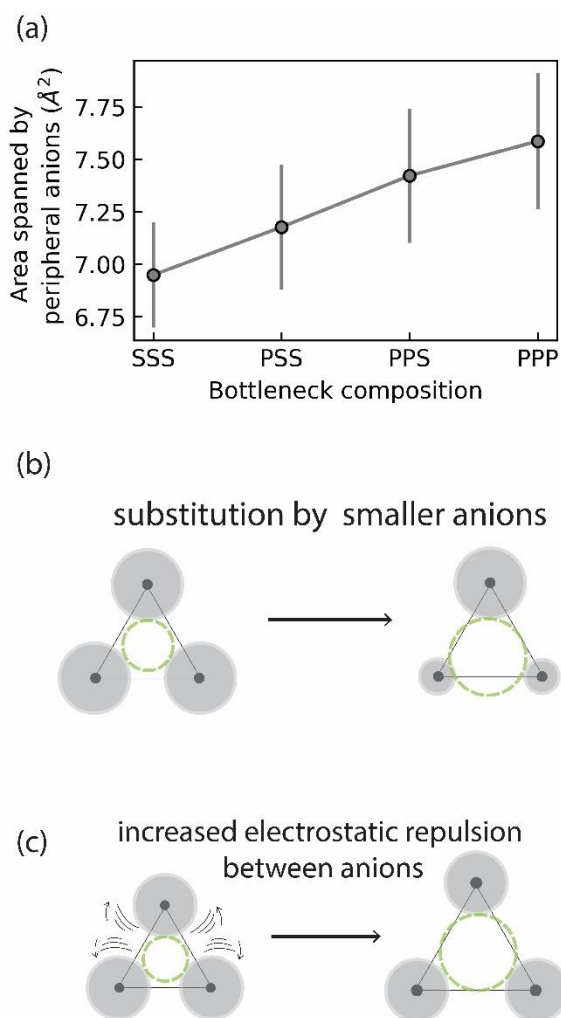


Figure 5.4. Mechanism of bottleneck-diameter enhancements. (a) Area of the triangle spanned by the three bottleneck anions for increased PS substitution in SSS bottlenecks. Triangle area increases showing that the anion distance increases with increased P content in the bottleneck. (b) Schematic of how the bottleneck diameter may be increased by substitution of a smaller anion. (c) Schematic of how the bottleneck diameter may be increased by substitution with an ion of equal size but higher valence inducing increased electrostatic repulsion between the anions.

So far we identified that P_S and N_S and N_P substitutions in bottlenecks facilitate Li diffusion likely because of increased bottleneck diameters. These results suggest that N_P substitutions in $Li_{2+x}S_{1-x}P_x$ phases —if such phases can be synthesized— should increase the conductivity which will be investigated in the next section.

N_P substitution in Li_{2+x}S_{1-x}P_x phases – proof of concept

We synthesized three phases with nominal composition Li_{2.6}S_{0.4}P_{0.6}, Li_{2.6}S_{0.4}P_{0.45}N_{0.15}, Li_{2.6}S_{0.4}P_{0.35}N_{0.25} via mechanical milling of the precursors Li₃N, Li₃P and Li₂S. The X-ray diffraction patterns of all three phases clearly show the characteristic $Fm\bar{3}m$ peaks (Figure 5.5a). From Rietveld refinements we find that the lattice parameter decreases with increasing nitrogen content as expected since N³⁻ has a smaller ionic radius than P³⁻ (Tables S5.2-S5.4). As suggested by the DFT calculations N_P substitutions in Li_{2.6}S_{0.4}P_{0.6} phases enhance conductivity, which is measured to increase from 0.1 mS cm⁻¹ for Li_{2.6}S_{0.4}P_{0.6} to >0.7 mS cm⁻¹ for Li_{2.6}S_{0.4}P_{0.35}N_{0.25} as may be seen from EIS spectra of the three synthesized phases in Figure 5.5b.

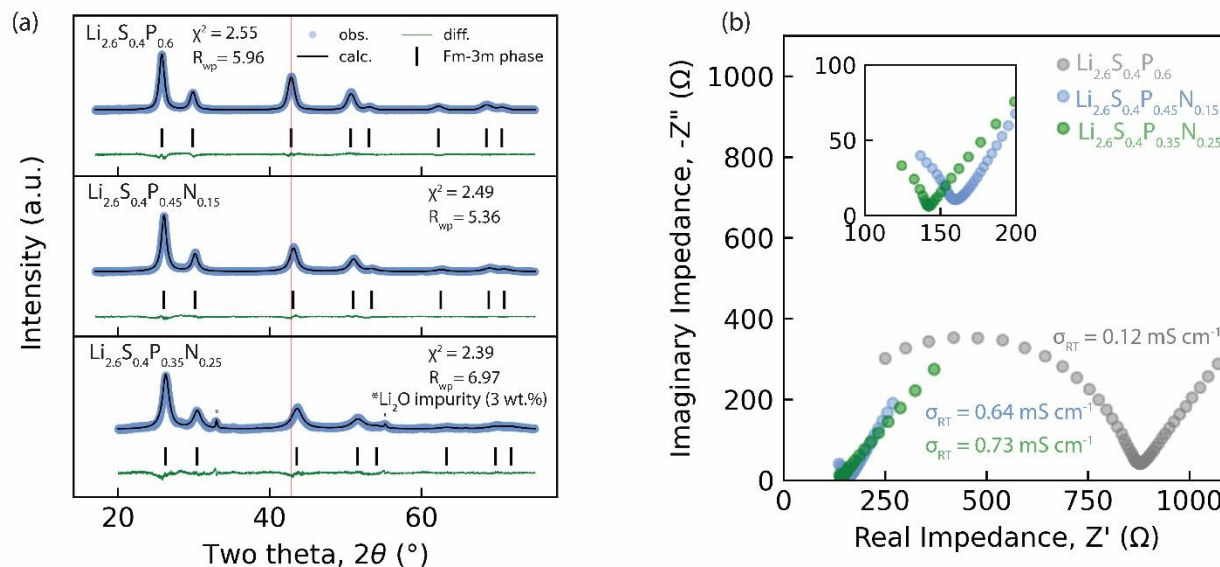


Figure 5.5. (a) XRD patterns and Rietveld refinements of Li_{2.6}S_{0.4}P_{0.6}, Li_{2.6}S_{0.4}P_{0.45}N_{0.15} and Li_{2.6}S_{0.4}P_{0.35}N_{0.25} phases. Red line is a guide to the eye for better visibility of peak shifts. (b) EIS measurements of the phases in (a).

In this final section we place the newly synthesized irreducible phases and their conductivities in the context of known fully-reduced/irreducible phases. Irreducible (lithium) phases may be classified into binary halides (e.g. LiCl), chalcogenides (e.g. Li₂S), pnictides (e.g. Li₃N), antiperovskites (e.g. Li₃OCl) and mixed-anion antiferrofluorites (e.g. Li_{2.6}S_{0.4}P_{0.35}N_{0.25}). These phases and their respective conductivities are shown in Figure 5.6 (Table S5.5). Conductivities of > 1 mS cm⁻¹ have been reported for Li₃N but these were obtained on single crystals and along specific orientations.²⁰ It was shown that these highly-conducting Li₃N samples were likely to be contaminated with hydrogen.²¹ Polycrystalline (β)-Li₃N and (α)-Li₃N samples pressed to pellets reproducibly yield conductivities of ~0.5 mS cm⁻¹.⁴⁻⁷ High conductivities (~1 mS cm⁻¹) have also been reported for Li₃OCl (ref²²) also but could not be substantiated.²³ In light of the above, the mixed-anion antiferrofluorite phases developed in this work can be considered the highest conducting irreducible phases known, almost on par with the conductivity of garnet oxide electrolytes (~1 mS cm⁻¹ refs^{1,24}) at the time of writing. Further conductivity optimizations will likely be possible given the large compositional flexibility of the irreducible antiferrofluorite phases demonstrated in Chapter 3 of this thesis.¹¹

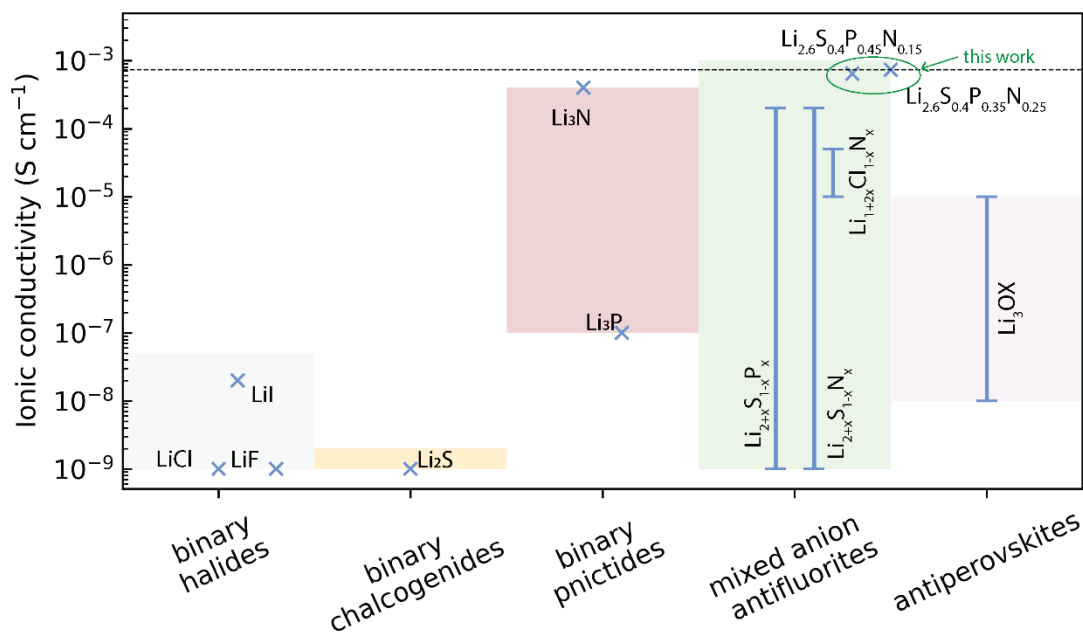


Figure 5.6. Conductivities of all fully-reduced electrolytes known to date. Data collected from refs: (7–11,23,25–32) (See Table S5.6 for more details)

5.4 Conclusions and outlook

In this chapter we showed for the first time that N_P substituted $Li_{2+x}S_{1-x}P_x$ (i.e. $Li_{2+x+y}S_{1-x-y}P_xN_y$) antiferrofluorite phases can be synthesized. Computationally we demonstrate that the lower Li-hop activation energy through N_P , N_S and N_P substituted bottlenecks correlates with an increased bottleneck diameter due to the smaller ion radius of N^{3-} compared to P^{3-} and S^{2-} . N_P substitutions in $Li_{2.6}S_{0.4}P_{0.6}$ phases significantly increases conductivity from 0.1 mS cm^{-1} for $Li_{2.6}S_{0.4}P_{0.6}$ to $>0.7 \text{ mS cm}^{-1}$ for $Li_{2.6}S_{0.4}P_{0.35}N_{0.25}$ which makes $Li_{2.6}S_{0.4}P_{0.35}N_{0.25}$ the highest conducting irreducible solid electrolyte at the time of writing.

Overall this topic, however, requires further work:

- The present study presents a proof of concept and shows that partial N_P substitutions in $Li_{2+x}S_{1-x}P_x$ phases can increase their conductivity. The $Li_{2+x+y}S_{1-x-y}P_xN_y$ phase space, however, has not been systematically explored in this study and better-conducting phases than the ones reported may yet to be discovered. The N content could potentially be further increased beyond the $Li_{2.6}S_{0.4}P_{0.35}N_{0.25}$ phase synthesized in this work. Moreover, the overall pnictide content could be increased or decreased. An increased overall pnictide content is generally beneficial (refs ^{8,9,11}) but it is likely that the obtainable degree of N_P substitution is higher at lower overall pnictide content; this may be deduced since $Li_{2.5}S_{0.5}N_{0.5}$ phases exists but $Li_{2.75}S_{0.25}N_{0.75}$ phase cannot be stabilized, indicating that at an overall pnictide content of 50%, complete N_P substitution can be achieved

which is not possible at an overall pnictide content of 75%. Moreover the possibility of introducing Br⁻ and Cl⁻ into the anionic sublattice and the effects on ionic conductivity should be explored.

- Systematic evaluation of the relationship between the oxidation limit and phase composition is needed for irreducible antifluorite phases. It was shown for Li_{2+x}S_{1-x}N_x phases that their oxidation limit exceeds the oxidation limit of Li₃N (0.8 V) posing a potential advantage when, for example, combined with Si anodes which operate in a voltage range from 0.01 to 1.1 V exceeding the stability window of Li₃N. The oxidation limit of Li_{2+x}S_{1-x}P_x phases should be determined and the effect of N_p substitutions on the oxidation limit should also be investigated.
- Finally, the irreducible antifluorite electrolytes should be extensively studied in full cells (potentially as anolytes of bilayer separators) to test their functionality. This includes investigation of the compatibility of irreducible antifluorite phases with potential catholyte partners in the context of bilayer separators.

The author of this thesis wishes exciting scientific endeavors to anyone deciding to continue this subject.

5.5 Methodology

Synthesis Li_{2+x+y}S_{1-x-y}P_xN_y phases: The synthesis precursors were Li₂S (Sigma-Aldrich, 99%) and Li₃N (Sigma-Aldrich, >99.5%) and Li₃P (synthesized in house vide infra). Stoichiometric amounts of the precursors were milled in a planetary ball mill (Jar: ZrO₂, 45 mL) with 10 mm ZrO₂ balls and a ball:powder mass ratio of 30 at 550 rpm for 99 (5-min milling-5 min-pause) cycles. *Li₃P precursor:* Red P (Sigma-Aldrich, 99%) was slowly added to molten Li metal (Sigma Aldrich 99.5%) in a tungsten crucible with constant stirring at ca. 250 ° C. Red-brown powder is obtained and left in in the crucible at ~250 ° C for ca. 2-4 h. Subsequently, the Li₃P powder was ball milled at 300 rpm with 10 mm ZrO₂ balls and a ball:powder mass ratio of 20 at 300 rpm for 40 (5-min milling-5 min-pause) cycles (Figure S5.6). All preparation steps were performed in an argon atmosphere (H₂O < 1 ppm, O₂ < 1 ppm).

Electrochemical Characterization. Electrochemical Impedance Spectroscopy (EIS): Pellets (diameter=10 mm) of the Li_{2+x+y}S_{1-x-y}P_xN_y probes were pressed (3.2 tons) in custom-made solid-state lab cells. These lab cells consist of an alumina tube and two stainless steel plungers. Solid electrolyte powder is filled in the alumina tube and compressed on both sides with the stainless steel plungers. The cell configuration used was SS| Li_{2+x+y}S_{1-x-y}P_xN_y |SS (SS=stainless steel). AC impedance was performed with a Metrohm Autolab (AUT86298) in the frequency range 10 MHz to 0.1 Hz with a voltage amplitude of 10 mV.

X-ray diffraction. Powder diffraction patterns were collected using Cu K α X-rays (1.54 Å) on a PANalytical X'Pert Pro X-ray diffractometer in Bragg-Brenano (*reflection*) geometry up to a 2 θ _{max}≈80°. The air sensitive

$\text{Li}_{2+x+y}\text{S}_{1-x-y}\text{P}_x\text{N}_y$ probes were loaded into air-tight holders in an Ar-filled glovebox prior to the measurements. GSAS-II³³ was used for Rietveld refinements.

Computational details. All DFT calculations were performed with the Vienna ab-initio simulation package VASP with computational settings consistent with those used in the Materials Project database.³⁴ For the generation and analysis of supercells the calculations were done on $2 \times 2 \times 2$ $\text{Li}_{2+x+y}\text{S}_{1-x-y}\text{P}_x\text{N}_y$ supercells with an overall stoichiometry $\text{Li}_{2.625}\text{S}_{0.375}\text{P}_{0.3125}\text{N}_{0.3125}$. Because of the shared site occupations and partial occupancies in $\text{Li}_{2+x+y}\text{S}_{1-x-y}\text{P}_x\text{N}_y$ phases different atomic arrangements were generated by random decoration of the Wyckoff 4a (0,0,0) position with nitrogen, sulfur, and phosphorus and the 4b (0.5,0.5,0.5) positions were randomly decorated with Li and vacancies. The Wyckoff 8c (0.25,0.25,0.25) position was fully occupied with Li. For the generation and analysis of supercells the pymatgen package was used.³⁵ For the AIMD simulations the Li pseudopotential was changed from Li_sv (which was used for relaxations) to Li as this enables the use of a lower energy cutoff. The simulation time was 200 ps for every AIMD simulation. The AIMD simulations were executed at 900 K. The dissection of AIMD simulations into individual jump events and subsequent analysis of jump frequencies and individual $E_{a, \text{Jump}}$ values was done as first described by de Klerk and Wagemaker;³⁶ a comprehensive account can be found in ref³⁶ but crucial aspects for the understanding of the reported data is presented here: *Partitioning of the supercell volume into site and non-site voxels*: The site centers are obtained from crystallography. The site radii are set to the average vibrational amplitude of the Li-ions determined from the distribution of distances $r(\Delta t)$ where no change in the sign of distance derivative occurs during Δt . The distance derivative is defined as:

$$\Delta r(t) = r(t) - r(t - 1) \quad (5.2)$$

Given the site center and site radius, spherical sites are defined around the site-center. *Calculation of $E_{a, \text{jump}}$ values between two sites*: The sites are defined around the 0 K equilibrium positions of the Li ions. At every simulation step it is recorded in which site each Li ion is located or whether it is currently between two sites. From this information the jump frequency between two site $v_{A \rightarrow B}$ can be calculated according to equation 5.3:

$$v_{A \rightarrow B} = \frac{N_{A \rightarrow B}}{\tau_A} \quad (5.3)$$

where $v_{A \rightarrow B}$ is the jump frequency for jumps from site A to site B, $N_{A \rightarrow B}$ is the number of recorded jumps from A to B, and τ_A is the time of occupation of site A. $E_{a, \text{jump}}$ is then obtained from equation (5.1). This whole analysis is strongly supported by the gemdat (ref³⁷) python package currently developed in our group.

Bottleneck size calculations: The DFT-relaxed structures of the 8 $\text{Li}_{2.625}\text{S}_{0.375}\text{P}_{0.3125}\text{N}_{0.3125}$ investigated supercells were used to account for local distortions which may not be present in long-range averaged crystallographic unit cells. The three atoms at the vertices of triangular bottlenecks connecting sites were identified. For the calculation of bottleneck diameters the biangle line (line that “cuts an angle in half”) was followed by the distance of the ion-radius of the ion located at the vertex. This was done at all three vertices so that a new triangle is formed. The outer-circle diameter of this new triangle is determined by the sympy (ref³⁸) Triangle package and is the bottleneck diameter. For each type of bottleneck (i.e. NSS, NPS...) the average diameter is determined and the standard deviation of the distribution of diameters is taken as the error bar.

5.6 References

- (1) Janek, J.; Zeier, W. G. Challenges in Speeding up Solid-State Battery Development. *Nat. Energy* **2023**, *8* (3), 230–240.
- (2) Huo, H.; Janek, J. Silicon as Emerging Anode in Solid-State Batteries. *ACS Energy Lett.* **2022**, *7* (11), 4005–4016.
- (3) Zhu, Y.; He, X.; Mo, Y. First Principles Study on Electrochemical and Chemical Stability of Solid Electrolyte-Electrode Interfaces in All-Solid-State Li-Ion Batteries. *J. Mater. Chem. A* **2016**, *4* (9), 3253–3266.
- (4) Rea, J. R.; Foster, D. L.; Mallory, P. R.; Co. Inc. High Ionic Conductivity in Densified Polycrystalline Lithium Nitride. *Mater. Res. Bull.* **1979**, *14* (6), 841–846.
- (5) Xu, X.; Du, G.; Cui, C.; Liang, J.; Zeng, C.; Wang, S.; Ma, Y.; Li, H. Stabilizing the Halide Solid Electrolyte to Lithium by a β -Li₃N Interfacial Layer. *ACS Appl. Mater. Interfaces* **2022**, *14* (35), 39951–39958.
- (6) Boukamp, B. A.; Huggins, R. A. Fast Ionic Conductivity in Lithium Nitride. *Mater. Res. Bull.* **1978**, *13* (1), 23–32.
- (7) Li, W.; Wu, G.; Araújo, C. M.; Scheicher, R. H.; Blomqvist, A.; Ahuja, R.; Xiong, Z.; Feng, Y.; Chen, P. Li⁺ Ion Conductivity and Diffusion Mechanism in α -Li₃N and β -Li₃N. *Energy Environ. Sci.* **2010**, *3* (10), 1524–1530.
- (8) Szczuka, C.; Karasulu, B.; Groh, M. F.; Sayed, F. N.; Sherman, T. J.; Bocarsly, J. D.; Vema, S.; Menkin, S.; Emge, S. P.; Morris, A. J.; Grey, C. P. Forced Disorder in the Solid Solution Li₃P–Li₂S: A New Class of Fully Reduced Solid Electrolytes for Lithium Metal Anodes. *J. Am. Chem. Soc.* **2022**, *144* (36), 16350–16365.
- (9) Landgraf, V.; Tu, M.; Zhao, W.; Lavrinenko, A.; Cheng, Z.; Canals, J.; de Leeuw, J.; Ganapathy, S.; Vasileiadis, A.; Wagemaker, M. Disorder-Mediated Ionic Conductivity in Irreducible Solid Electrolytes. **2024**.
- (10) Yu, P.; Zhang, H.; Hussain, F.; Luo, J.; Tang, W.; Lei, J.; Gao, L.; Butenko, D.; Wang, C.; Zhu, J.; Yin, W.; Zhang, H.; Han, S.; Zou, R.; Chen, W.; Zhao, Y.; Xia, W.; Sun, X. Lithium Metal-Compatible Antifluorite Electrolytes for Solid-State Batteries. *J. Am. Chem. Soc.* **2024**.
- (11) Landgraf, V.; Tu, M.; Cheng, Z.; Vasileiadis, A.; Wagemaker, M.; Famprakis, T. Compositional Flexibility in Irreducible Antifluorite Electrolytes for Next-Generation Battery Anodes. **2024**.
- (12) De Klerk, N. J. J.; Van Der Maas, E.; Wagemaker, M. Analysis of Diffusion in Solid-State Electrolytes through MD Simulations, Improvement of the Li-Ion Conductivity in β -Li₃PS₄ as an Example. *ACS Appl. Energy Mater.* **2018**, *1* (7), 3230–3242.
- (13) Van der Ven, A.; Ceder, G.; Asta, M.; Tepsch, P. D. First-Principles Theory of Ionic Diffusion with Nondilute Carriers. *Phys. Rev. B - Condens. Matter Mater. Phys.* **2001**, *64* (18), 1–17.
- (14) Almond, D. P.; Duncan, G. K.; West, A. R. The Determination of Hopping Rates and Carrier Concentrations in Ionic Conductors by a New Analysis of Ac Conductivity. *Solid State Ionics* **1983**, *8* (2), 159–164.
- (15) Wang, Z.; Mishra, T. P.; Xie, W.; Deng, Z.; Gautam, G. S.; Cheetham, A. K.; Canepa, P. Kinetic Monte Carlo Simulations of Sodium Ion Transport in NaSICON Electrodes. *ACS Mater. Lett.* **2023**, *5* (9), 2499–2507.
- (16) Deng, Z.; Mishra, T. P.; Mahayoni, E.; Ma, Q.; Tieu, A. J. K.; Guillon, O.; Chotard, J.-N.; Seznec, V.; Cheetham, A. K.; Masquelier, C. Fundamental Investigations on the Sodium-Ion Transport Properties of Mixed Polyanion Solid-State Battery Electrolytes. *Nat. Commun.* **2022**, *13* (1), 4470.
- (17) Shannon, R. D. Revised Effective Ionic Radii and Systematic Studies of Interatomic Distances in Halides and Chalcogenides. *Acta Crystallogr. Sect. A Cryst. physics, diffraction, Theor. Gen. Crystallogr.* **1976**, *32* (5), 751–767.
- (18) Nazri, G. Preparation, Characterization and Conductivity of Li₃N, Li₃P and Li₃As. *MRS Online Proc. Libr.* **1988**, *135*, 117.
- (19) Fajans, K. Struktur Und Deformation Der Elektronenhüllen in Ihrer Bedeutung Für Die Chemischen Und Optischen

- Eigenschaften Anorganischer Verbindungen. *Naturwissenschaften* **1923**, *11* (10), 165–172.
- (20) Alpen, Rabenau, Talat, Ionic Conductivity in Li₃N Single Crystals. **1977**, 621–623.
- (21) Lapp, T.; Skaarup, S.; Hooper, A. Ionic Conductivity of Pure and Doped Li₃N. *Solid State Ionics* **1983**, *11* (2), 97–103.
- (22) Braga, M. H.; Ferreira, J. A.; Stockhausen, V.; Oliveira, J. E.; El-Azab, A. Novel Li₃ClO Based Glasses with Superionic Properties for Lithium Batteries. *J. Mater. Chem. A* **2014**, *2* (15), 5470–5480.
- (23) Zheng, J.; Perry, B.; Wu, Y. Antiperovskite Superionic Conductors: A Critical Review. *ACS Mater. Au* **2021**, *1* (2), 92–106.
- (24) Kim, A.; Woo, S.; Kang, M.; Park, H.; Kang, B. Research Progresses of Garnet-Type Solid Electrolytes for Developing All-Solid-State Li Batteries. *Front. Chem.* **2020**, *8* (June), 1–13.
- (25) Landgraf, V.; Famprikis, T.; de Leeuw, J.; Bannenberg, L. J.; Ganapathy, S.; Wagemaker, M. Li₅NCl₂: A Fully-Reduced, Highly-Disordered Nitride-Halide Electrolyte for Solid-State Batteries with Lithium-Metal Anodes. *ACS Appl. Energy Mater.* **2023**, *6* (3), 1661–1672.
- (26) Li, W.; Li, M.; Chien, P.-H.; Wang, S.; Yu, C.; King, G.; Hu, Y.; Xiao, Q.; Shakouri, M.; Feng, R. Lithium-Compatible and Air-Stable Vacancy-Rich Li₉N₂Cl₃ for High-Areal Capacity, Long-Cycling All-Solid-State Lithium Metal Batteries. *Sci. Adv.* **2023**, *9* (42), eadh4626.
- (27) Wang, Z.; Xia, J.; Ji, X.; Liu, Y.; Zhang, J.; He, X.; Zhang, W.; Wan, H.; Wang, C. Lithium Anode Interlayer Design for All-Solid-State Lithium-Metal Batteries. *Nat. Energy* **2024**, *9* (3), 251–262.
- (28) Miara, L. J.; Suzuki, N.; Richards, W. D.; Wang, Y.; Kim, J. C.; Ceder, G. Li-Ion Conductivity in Li₉S₃N. *J. Mater. Chem. A* **2015**, *3* (40), 20338–20344.
- (29) Park, S.; Chaudhary, R.; Han, S. A.; Qutaish, H.; Moon, J.; Park, M.-S.; Kim, J. H. Ionic Conductivity and Mechanical Properties of the Solid Electrolyte Interphase in Lithium Metal Batteries. *ENERGY Mater.* **2023**, *3* (1).
- (30) Poulsen, F. W. Ionic Conductivity of Solid Lithium Iodide and Its Monohydrate. *Solid State Ionics* **1981**, *2* (1), 53–57.
- (31) Yang, W.; Tang, S.; Yang, X.; Zheng, X.; Wu, Y.; Zheng, C.; Chen, G.; Gong, Z.; Yang, Y. Li₂Se: A High Ionic Conductivity Interface to Inhibit the Growth of Lithium Dendrites in Garnet Solid Electrolytes. *ACS Appl. Mater. Interfaces* **2022**, *14* (45), 50710–50717.
- (32) Nazri, G. Preparation, Structure and Ionic Conductivity of Lithium Phosphide. *Solid State Ionics* **1989**, *34* (1–2), 97–102.
- (33) Toby, B. H.; Von Dreele, R. B. GSAS-II: The Genesis of a Modern Open-Source All Purpose Crystallography Software Package. *J. Appl. Crystallogr.* **2013**, *46* (2), 544–549.
- (34) Jain, A.; Ong, S. P.; Hautier, G.; Chen, W.; Richards, W. D.; Dacek, S.; Cholia, S.; Gunter, D.; Skinner, D.; Ceder, G.; Persson, K. A. Commentary: The Materials Project: A Materials Genome Approach to Accelerating Materials Innovation. *APL Mater.* **2013**, *1* (1), 001002.
- (35) Ong, S. P.; Richards, W. D.; Jain, A.; Hautier, G.; Kocher, M.; Cholia, S.; Gunter, D.; Chevrier, V. L.; Persson, K. A.; Ceder, G. Python Materials Genomics (Pymatgen): A Robust, Open-Source Python Library for Materials Analysis. *Comput. Mater. Sci.* **2013**, *68*, 314–319.
- (36) De Klerk, N. J. J.; Van Der Maas, E.; Wagemaker, M. Analysis of Diffusion in Solid-State Electrolytes through MD Simulations, Improvement of the Li-Ion Conductivity in β-Li₃PS₄ as an Example. *ACS Appl. Energy Mater.* **2018**, *1* (7), 3230–3242.
- (37) Azizi, V.; Smeets, S.; Lavrinenko, A. K.; Ciarella, S.; Famprikis, T. GEMDAT. Zenodo July 2024.
- (38) Meurer, A.; Smith, C. P.; Paprocki, M.; Čertík, O.; Kirpichev, S. B.; Rocklin, M.; Kumar, Am.; Ivanov, S.; Moore, J. K.; Singh, S. SymPy: Symbolic Computing in Python. *PeerJ Comput. Sci.* **2017**, *3*, e103.

Appendix 1: Supporting information for chapter 2

Table S2.1. Comparison between experimental lattice parameters and the model supercell employed in this investigation. Note of caution, the experimental lattice parameters reported in previous work and the one obtained in our XRD measurements are multiplied by two here, to be comparable with the lattice parameter of the 2x2x2 LNCl supercells employed in computational work. We would also like to mention that in references 1,2 and 3 the authors assumed a $\text{Li}_9\text{N}_2\text{Cl}_3$ stoichiometry which affects their reported densities.

	a [Å]	b [Å]	c [Å]	Volume [Å ³]	Density [g cm ⁻³]
Previous experimental reports ^{1 2 4}	10.772	10.772	10.772	1249.94	1.67
	10.814	10.814	10.814	1264.617	1.65
	10.832	10.832	10.832	1270	1.67
Previous computational report (DFT) ³	10.205	11.406	10.296	1198	1.74
From our XRD experiments	10.792	10.792	10.792	1256.915	1.69
Model supercell employed in this work (DFT)	10.858	10.556	10.913	1250.727	1.68*
Difference between our experiments and our model supercell [%]	-0.61	+2.23	-1.10	+0.49	+0.59
*The actual supercell stoichiometry, $\text{Li}_{4.82}\text{NCl}_{1.91}$ ($\text{Li}_{53}\text{N}_{11}\text{C}_{21}$), was used to calculate this density.					

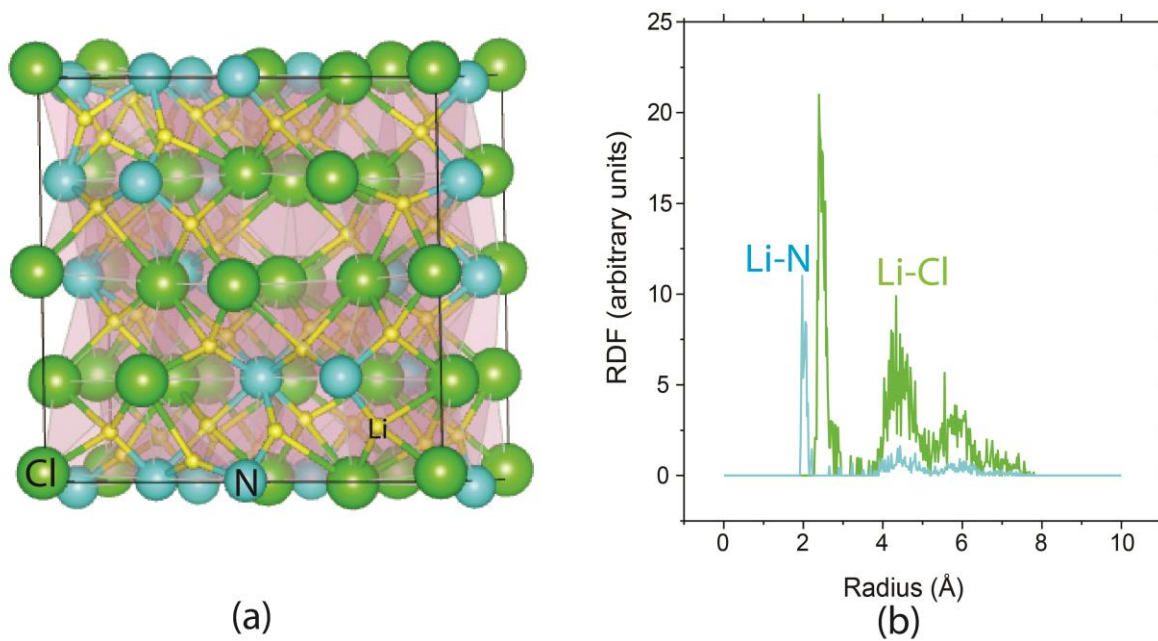


Figure S2.1. a) LNCl model supercell. Li displacement from the ideal tetrahedral position can be well observed. b) RDF of Li-Cl and Li-N for the stationary LNCl supercell shown in a. The peak at lower radii in the Li-N RDF indicates the displacement of Li site position towards N within the tetrahedra.

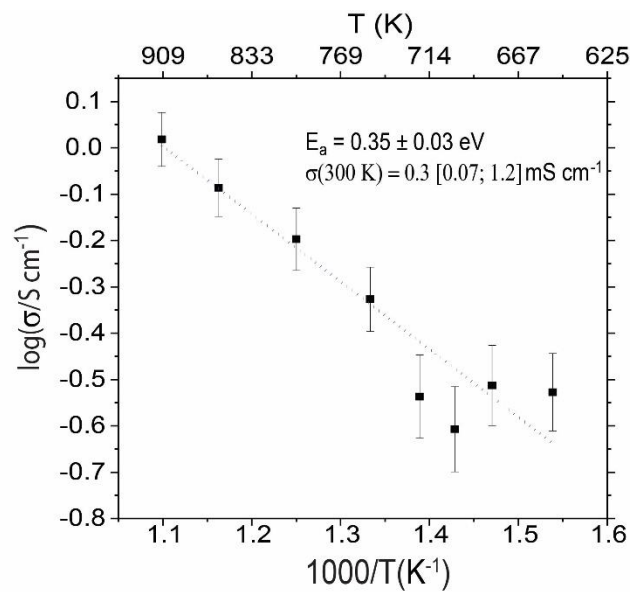


Figure S2.2. Arrhenius plot obtained from the tracer diffusivities D_{tr} calculated with AIMD simulations. The error on the diffusivities were calculated as done by He and Mo.⁵

Table S2.2. This table lists the tracer and jump diffusivities obtained from AIMD simulations at different temperatures. The correlation factor at different temperatures is also listed.

Temperature	650 K	680 K	700 K	720 K	800 K	860 K	910 K	Average
$10^{-10} * D_{tr} [m^2 s^{-1}]$	2.40	2.64	2.19	2.65	6.40	8.94	12.0	-
$10^{-10} * D_j [m^2 s^{-1}]$	6.26	7.54	7.45	8.58	13.60	17.20	24.0	-
$f = D_{tr} / D_j$	0.38	0.35	0.29	0.31	0.47	0.52	0.50	0.4 ± 0.1

Table S2.3. This table contains the data obtained from the pseudo-binaries between LNCl and common SE.

SEE	Molar fraction of Li ₅ NCl ₂ in Li ₅ NCl ₂ - SEE	Phase equilibria	$\Delta E_{D, mutual}$ (eV/atom)
Li₆PS₅Cl	1	Li ₅ NCl ₂	0
	0.711111111	Li ₇ PN ₄ , LiCl, Li ₂ S	-0.251
	0.551724138	LiPN ₂ , LiCl, Li ₂ S	-0.302
	0	Li ₆ PS ₅ Cl	0
LIPON Li _{2.88} N _{0.14} O _{3.73}	1	Li ₅ NCl ₂	0
	0.799	Li ₇ PN ₄ , Li ₂ O, LiCl	-0.137
	0.657	Li ₂ O, LiPN ₂ , LiCl	-0.200
	0.470	Li ₂ PNO ₂ , Li ₂ O, LiCl	-0.088
	0	Li _{2.88} N _{0.14} O _{3.73}	0
Li₃PS₄	1	Li ₅ NCl ₂	0
	0.2	Li ₇ PN ₄ , LiCl, Li ₂ S	-0.267
	0.3	LiPN ₂ , LiCl, Li ₂ S	-0.338
	1	Li ₃ PS ₄	0
Li₃ScCl₆	1	Li ₅ NCl ₂	0
	0.385	Li ₃ ScN ₂ , LiCl	-0.195
	0.444	ScN, LiCl	-0.268
	0	Li ₃ ScCl ₆	0
Li₃YCl₆	1	Li ₅ NCl ₂	0
	0.385	Li ₃ YN ₂ , LiCl	-0.145
	0.556	YN, LiCl	-0.206
	0.714	Y ₂ NCl ₃ , LiCl	-0.138
	0	Li ₃ YCl ₆	0
LLZO (Li ₇ La ₃ Zr ₂ O ₁₂)	1	Li ₅ NCl ₂	0
	0.7	Li ₂ O, Li ₂ ZrN ₂ , LiCl, LaN	-0.093
	0.571	Li ₂ O, La ₂ O ₃ , Li ₂ ZrN ₂ , LiCl	-0.094
	0	Li ₇ La ₃ Zr ₂ O ₁₂	0

Table S2.4. This table contains the data obtained from the pseudo-binaries between Li₃N and common SE.

SEE	Molar fraction of Li ₃ N in Li ₃ N-SEE	Phase equilibria	$\Delta E_{D, mutual}$ (eV/atom)
Li₆PS₅Cl	1	Li ₃ N	0
	0.606	Li ₇ PN ₄ , Li ₄ NCl, Li ₂ S	-0.350
	0.552	Li ₇ PN ₄ , LiCl, Li ₂ S	-0.396
	0.380	LiPN ₂ , LiCl, Li ₂ S	-0.421
	0	Li ₆ PS ₅ Cl	0
LIPON Li _{2.88} N _{0.14} O _{3.73}	1	Li ₃ N	0
	0.666	Li ₇ PN ₄ , Li ₂ O	-0.235
	0.490	Li ₂ O, LiPN ₂	-0.184
	0.307	Li ₂ PNO ₂ , Li ₂ O	-0.119
	0	Li _{2.88} N _{0.14} O _{3.73}	0
Li₃PS₄	1	Li ₃ N	0
	0.667	Li ₇ PN ₄ , Li ₂ S	-0.267
	0.5	LiPN ₂ , Li ₂ S	-0.338
	1	Li ₃ PS ₄	0
Li₃ScCl₆	1	Li ₃ N	0
	0.761	Li ₃ ScN ₂ , Li ₄ NCl	-0.129
	0.444	Li ₃ ScN ₂ , LiCl	-0.286
	0.286	ScN, LiCl	-0.348
	0	Li ₃ ScCl ₆	0
Li₃YCl₆	1	Li ₃ N	0
	0.238	Li ₃ YN ₂ , Li ₄ NCl	-0.098
	0.556	Li ₃ YN ₂ , LiCl	-0.216
	0.714	YN, LiCl	-0.268
	0.833	Y ₂ NCl ₃ , LiCl	-0.162
	0	Li ₃ YCl ₆	0
LLZO (Li ₇ La ₃ Zr ₂ O ₁₂)	1	Li ₃ N	0
	0.538	Li ₂ O, Li ₂ ZrN ₂ , LaN	-0.149
	0.400	Li ₂ O, La ₂ O ₃ , Li ₂ ZrN ₂	-0.136
	0	Li ₇ La ₃ Zr ₂ O ₁₂	0

Statistical details on the model LNCl supercell employed in this study

A jump- E_a value for a jump from A to B is obtained by counting the jumps from A to B. The number of jumps $N_{A \rightarrow B}$ is then divided by the occupation time of site A τ_A . Using the equations S2.1 and S2.2 below, the jump- E_a values are obtained:

$$v_{A \rightarrow B} = \frac{N_{A \rightarrow B}}{\tau_A} \quad (\text{S2.1})$$

$$E_{a, A \rightarrow B} = -k_b T \ln \left(\frac{v_{A \rightarrow B}}{v^*} \right) \quad (\text{S2.2})$$

More than one A-B pair is required to determine the uncertainty on the average $E_{a, A \rightarrow B}$ value. Table S2.5 below shows the occurrence of A-B pairs in the model supercell.

Table S2.5. From this table one obtains how many neighbouring A-B sites are ‘connected’ by Cl-Cl, Cl-N, and N-N bottlenecks respectively, and how many A-B pairs can be found in the model supercell.

Site pairs	Bottleneck that connects the pair			Sum of pairs
	Cl-Cl	Cl-N	N-N	
Cl ₄ - Cl ₄	5	/	/	5
Cl ₄ - Cl ₃ N ₁	31	/	/	31
Cl ₄ - Cl ₂ N ₂	7	/	/	7
Cl ₄ - Cl ₁ N ₃	/	/	/	/
Cl ₃ N ₁ - Cl ₃ N ₁	25	17	/	42
Cl ₃ N ₁ - Cl ₂ N ₂	9	43	/	52
Cl ₃ N ₁ - Cl ₁ N ₃	/	13	/	13
Cl ₂ N ₂ - Cl ₂ N ₂	2	16	6	24
Cl ₂ N ₂ - Cl ₁ N ₃	/	5	8	13
Cl ₁ N ₃ - Cl ₁ N ₃	/	0	5	5
SUM	79	94	19	192

Note: “/” means that such sites cannot be neighbouring. For example, because the tetrahedra in LNCl are edge-sharing, two neighbouring Cl₄ sites cannot be “connected” by a Cl-N or N-N bottleneck. “0” means that the sites could in principle be connected by the bottleneck in question but that such a case is not represented in the model supercell. $E_{a, \text{jump}}$ values are obtained for every individual pair of sites and the ones reported are averaged over all pairs of sites.

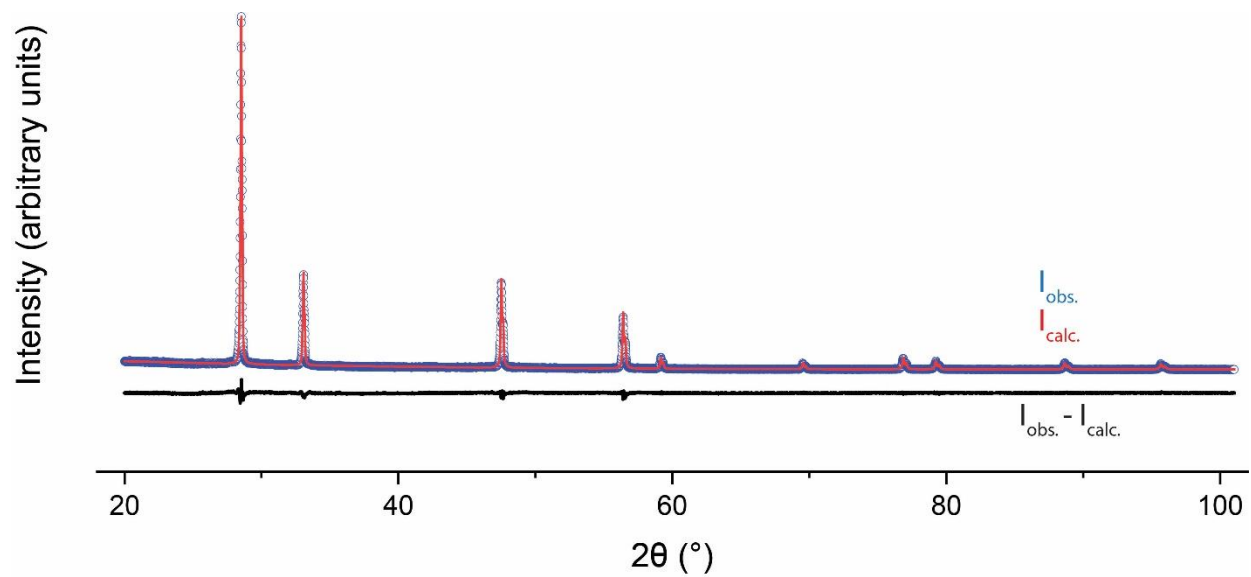


Figure S2.3. XRD of LNCl-I. This is also shown in Figure 2.3 of the main text. $a = 5.39(6)$ Å. X-ray reliability parameters: $R_p = 5.69$, $R_{wp} = 7.39$, $\chi^2 = 2.3$

Table S2.6. Structural parameters from the Rietveld refinement of LNCl-I.

Atom	x	y	z	Wyckoff	Occupancy	U_{iso}
Li	0.25	0.25	0.25	8c	5/6	0.14(0)
N	0	0	0	4a	1/3	0.18(0)
Cl	0	0	0	4a	2/3	0.02(5)

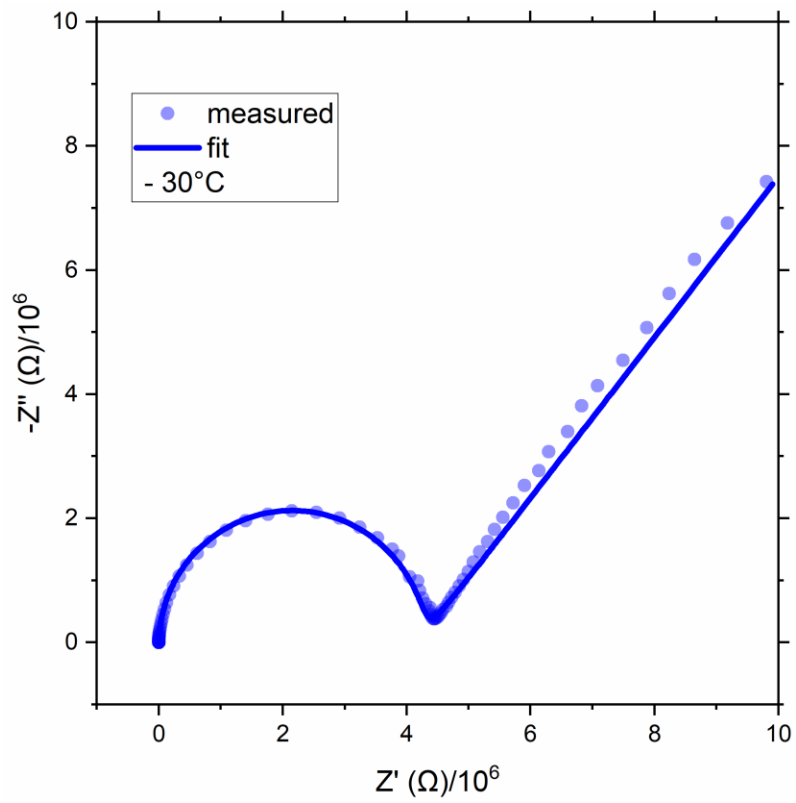


Figure S2.4. EIS of LNCI-I at $-30\text{ }^\circ\text{C}$ fitted to a p(R-CPE)-CPE circuit.

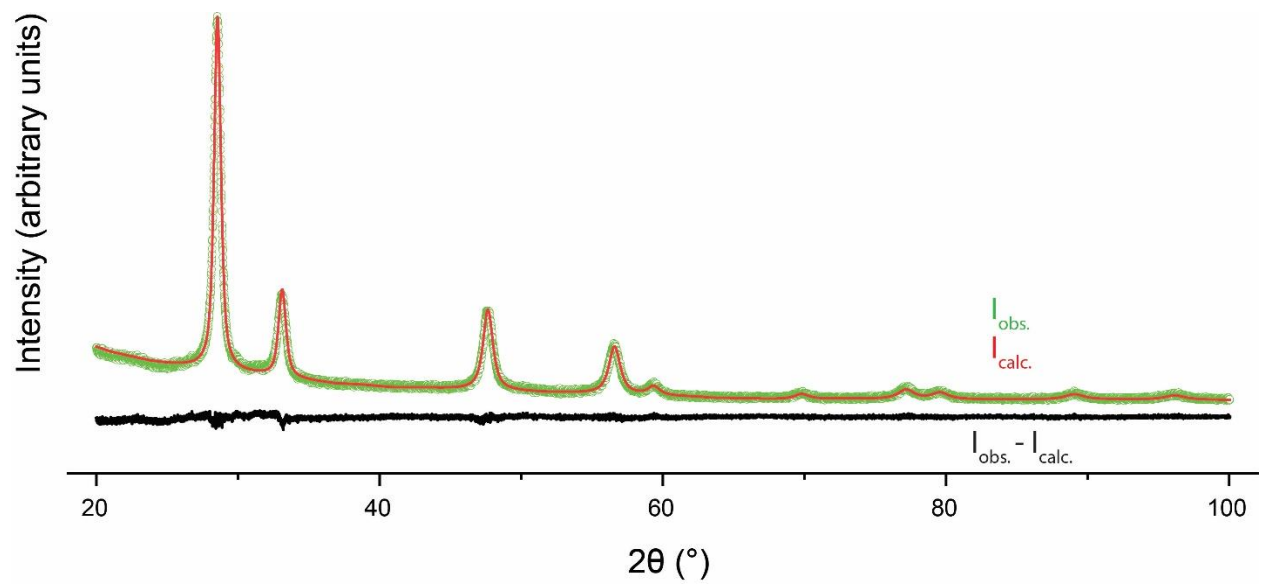


Figure S2.5. XRD of LNCl-I-BM. This is also shown in Figure 2.3 of the main text. $a = 5.37(6)$ Å. X-ray reliability parameters: $R_p = 5.08$, $R_{wp} = 6.46$, $\chi^2 = 3.57$

Table S2.7. Structural parameters from the Rietveld refinement of LNCl-I-BM.

Atom	x	y	z	Wyckoff	Occupancy	U_{iso}
Li	0.25	0.25	0.25	8c	5/6	0.12(1)
N	0	0	0	4a	1/3	0.14(0)
Cl	0	0	0	4a	2/3	0.02(4)

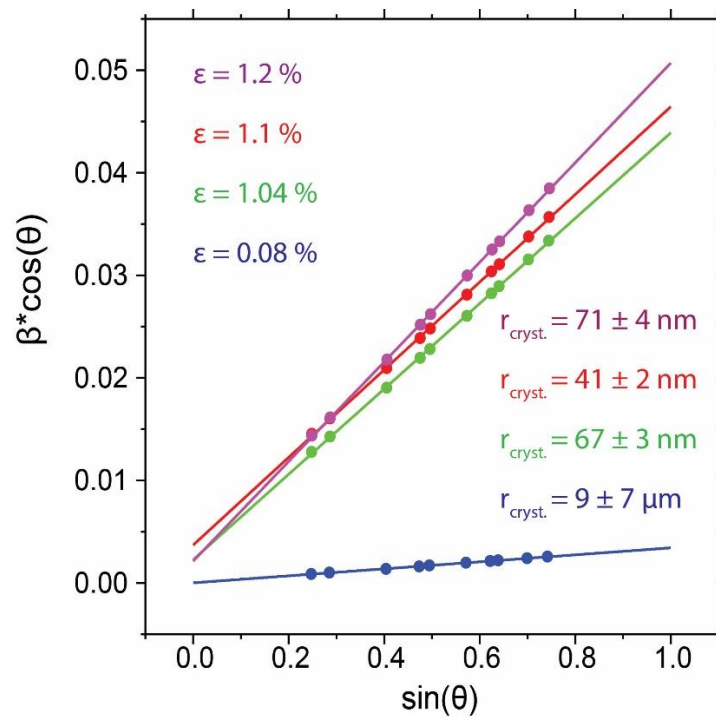


Figure S2.6. Williamson-Hall analysis of the diffractograms of (blue) LNCl-I, (green) LNCl-I-BM, (red) LNCl-I-BM-8h, (violet) LNCl-I-BM-12h. β here is the peak-width in the diffractograms. These were obtained with the Jana2006 software. ⁶

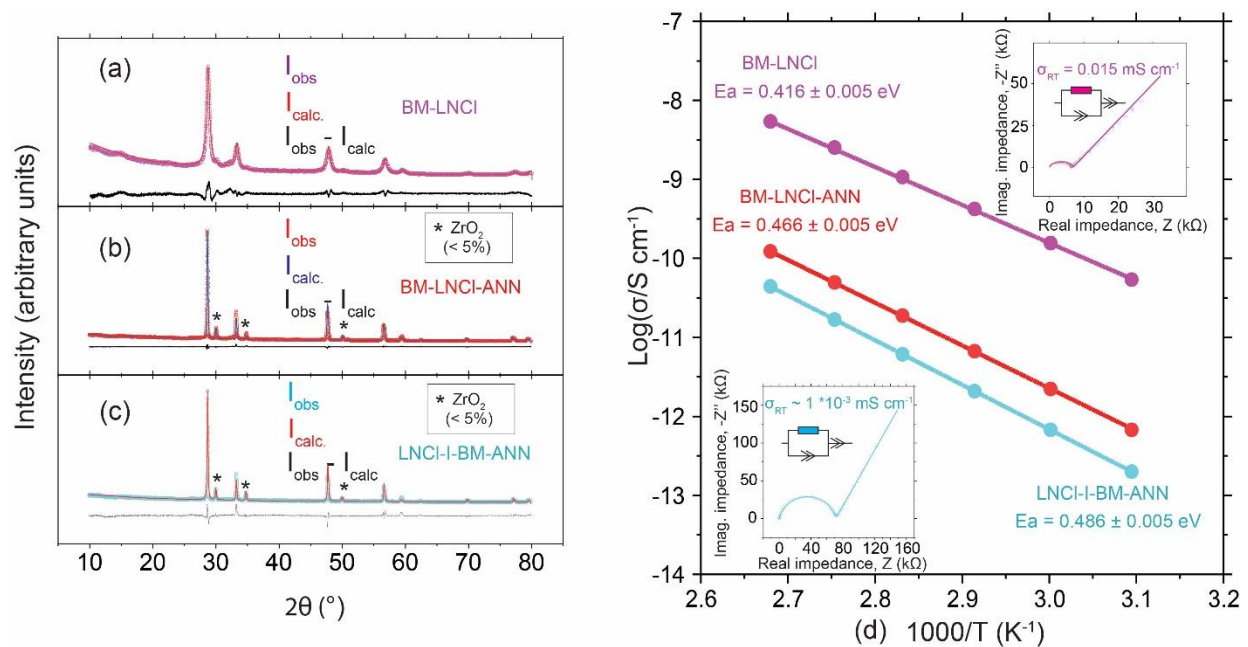


Figure S2.7. (a) , (b), (c) are X-ray diffractograms of BM-LNCl, BM-LNCl-ANN, LNCl-I-BM-ANN. A small ZrO_2 impurity likely coming from the milling medium is marked with * (d) Arrhenius plots for BM-LNCl, BM-LNCl-ANN, LNCl-I-BM-ANN. The inset at the lower left shows the EIS of LNCl-I-BM-ANN and the one at the top right shows the EIS of BM-LNCl. (ANN is an abbreviation for annealed. E.g. BM-LNCl-ANN refers to the BM-LNCl sample that is annealed at 600 $^{\circ}\text{C}$ for 3 h and then air quenched as described in the main text).

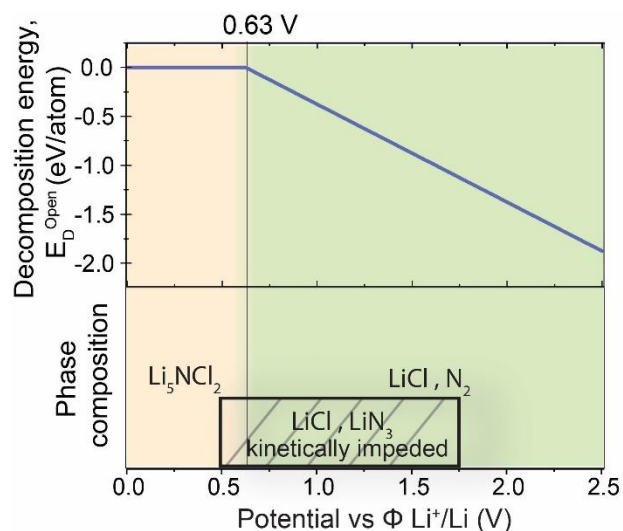


Figure S2.8. Phase equilibria of the Li_xNCl_2 $\{x \in \mathbb{R} | x \geq 0\}$ phase space at different potentials ϕ vs Li^+/Li . Additionally this figure shows the decomposition energy $E_{D,open}$ as defined by Zhu and Mo⁷ of LNCl at different ϕ . The difference here to figure 2.4a is that LiN_3 was removed from the phase space obtained from the materials project.⁸ As a consequence the stability window is shifted up slightly from 0.50 V to 0.63 V. Investigating this was motivated by the following reasoning. Decomposition of LNCl to LiN_3 necessitates a complex rearrangement of the anionic framework to from the $[\text{N}_3]^-$ moieties present in LiN_3 . Given the complexity of this rearrangement and the likely limited RT diffusivity of N^{3-} and Cl^- in LNCl, it is conceivable that the formation of LiN_3 may be kinetically impeded even at very low current densities and that LNCl “directly” decomposes to LiCl and N_2 .

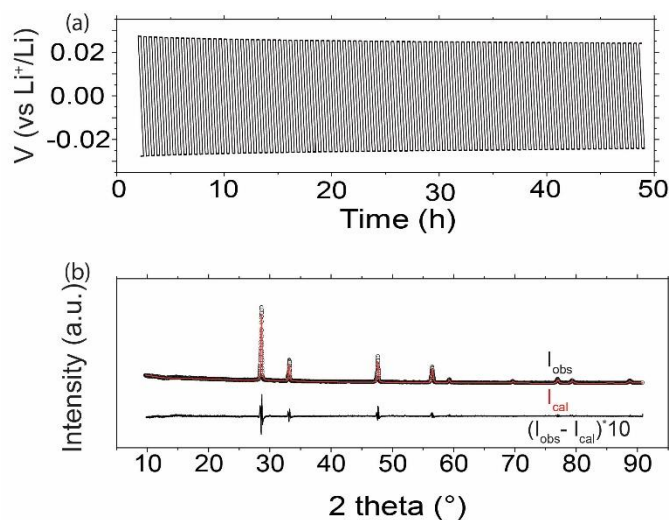


Figure S2.9. (a) Example of the cycling of a Li|LNCl-I-BM|Li cell. Applied current density: 0.01 mA cm^{-2} . Time for one cycle: 30 min. This cell was cycled at $50 \text{ }^\circ\text{C}$ to better control temperature. No increase in the cell voltage is observed over time which indicates excellent compatibility of LNCl and Li-metal (LM). A small decrease (from 26 to 24 mV) in the cell voltage is observed at the early stages of cycling which may be a consequence of improved contact between LM and LNCl establishing during the first cycles. (b) X-ray diffractogram of LNCl-I after in contact with molten LM at $210 \text{ }^\circ\text{C}$ for 2h. No other phases besides LNCl are observed that would indicate decomposition of LNCl in contact with LM. The difference plot was multiplied by 10 to make better visible the differences between I_{obs} and I_{calc} .

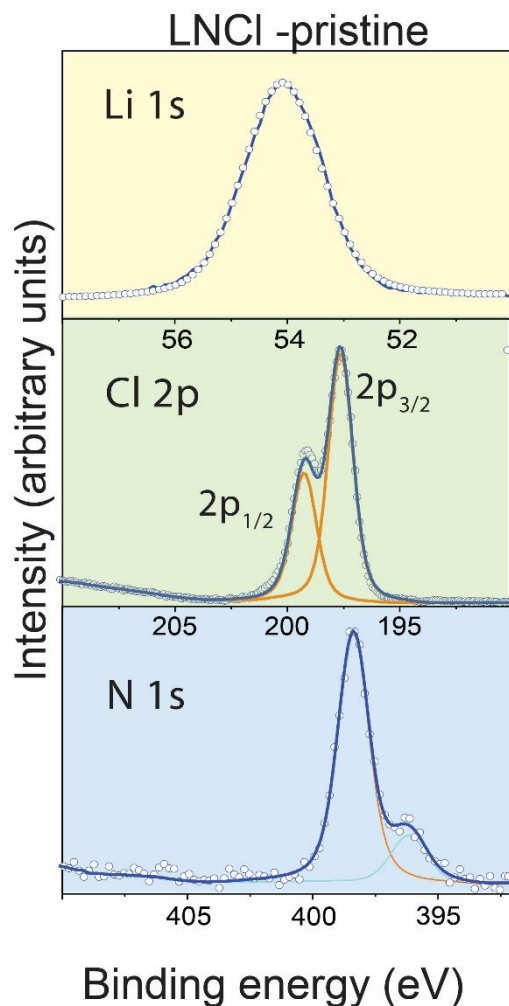


Figure S2.10. Li1s Cl2p and N1s XPS spectra of LNCl. A second peak is observed in the N1s spectrum (small blue peak). Comparison with the XPS NIST database⁹ the binding energies of this peak match different chemical compositions that can be summarized by the general formula $(C_xH_yN_z)_n$. The presence of this second small contribution in the XPS spectrum suggests an impurity on the surface of the LNCl particles. This impurity may have been introduced during the transfer from the glovebox to the XPS machine inside the vacuum transfer unit.

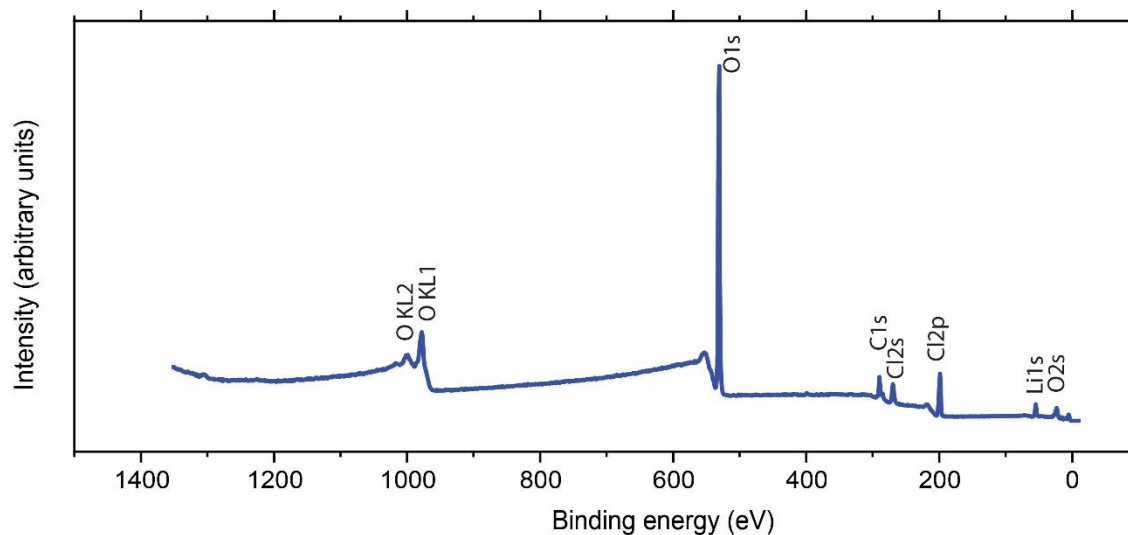


Figure S2.11. XPS survey scan of LNCl.

Experimental details of X-ray photon spectroscopy. XPS measurements were performed with a ThermoFisher K-Alpha spectrometer to investigate the chemical state of the elements present. The spectrometer is equipped with a focused monochromatic Al $\kappa\alpha$ source (1486.6 eV) anode operating at 36 W (12 kV, 3mA), a flood gun operating at 1V, 100 μ A, and the base pressure in the analysis chamber is approximately $2 \cdot 10^{-9}$ mbar. The spot-size is approximately $800 \times 400 \mu\text{m}^2$. The pass energy of the analyzer was set to 50 eV. The samples were transferred from the glove box to the spectrometer inside a dedicated ThermoFisher vacuum transfer module to avoid air-exposure. In the analysis, the binding energy was corrected for the 0.5 eV charge shift by taking the primary C1s hydrocarbon peak at $BE = 284.8$ eV as a reference. The peaks were fitted using 70% Gaussian and 30% Lorentzian line shapes (weighted least-squares fitting method) and nonlinear Shirley-type background using the ThermoFisher Avantage software.

References for Appendix 1

- (1) Hartwig, P.; Rabenau, A.; Weppner, W. Phase Equilibria and Thermodynamic Properties of the Li-N-Cl, Li-N-Br and Li-N-I Systems. **1981**, *80*, 81–90.
- (2) Sattlegger, H.; Hahn, H. Uber Das System Li , N / LiCl. **1964**, *173*, 1–7.
- (3) Galvez-Aranda, D. E.; Seminario, J. M. Ab Initio Study of the Interface of the Solid-State Electrolyte Li₉N₂Cl₃ with a Li-Metal Electrode. *J. Electrochem. Soc.* **2019**, *166* (10), A2048–A2057.
- (4) Marx, R.; Mayer, H. M. Preparation and Crystal Structure of Ordered and Disordered Lithium Nitride Dichloride, Li₅NCl₂. *J. Solid State Chem.* **1997**, *130* (1), 90–96.
- (5) He, X.; Zhu, Y.; Epstein, A.; Mo, Y. Statistical Variances of Diffusional Properties from Ab Initio Molecular Dynamics Simulations. *npj Comput. Mater.* **2018**, *4* (1), 1–9.
- (6) Petříček, V.; Dušek, M.; Palatinus, L. Crystallographic Computing System JANA2006: General Features. *Zeitschrift für Krist. - Cryst. Mater.* **2014**, *229* (5), 345–352.
- (7) Zhu, Y.; He, X.; Mo, Y. First Principles Study on Electrochemical and Chemical Stability of Solid Electrolyte-Electrode Interfaces in All-Solid-State Li-Ion Batteries. *J. Mater. Chem. A* **2016**, *4* (9), 3253–3266.
- (8) Jain, A.; Ong, S. P.; Hautier, G.; Chen, W.; Richards, W. D.; Dacek, S.; Cholia, S.; Gunter, D.; Skinner, D.; Ceder, G.; Persson, K. A. Commentary: The Materials Project: A Materials Genome Approach to Accelerating Materials Innovation. *APL Mater.* **2013**, *1* (1), 001002.
- (9) *NIST X-ray Photoelectron Spectroscopy Database, NIST Standard Reference Database Number 20.*

Appendix 2: Supporting Information for Chapter 3

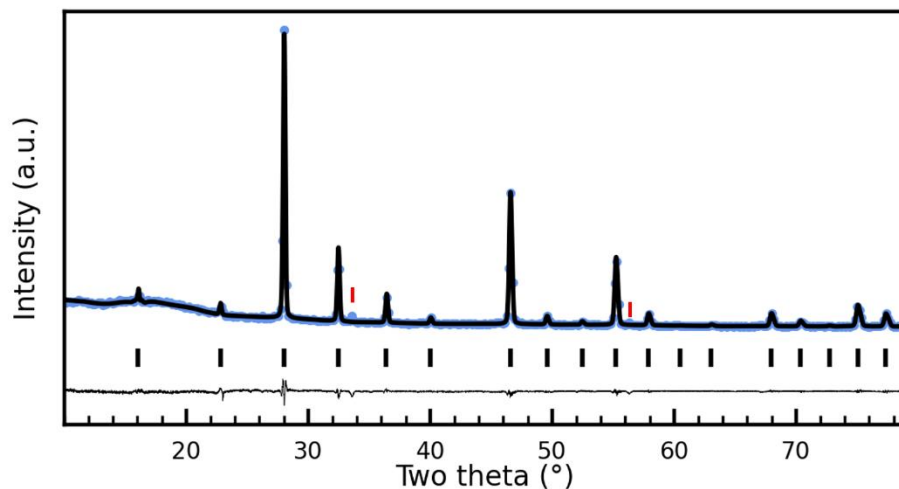


Figure S3.1. X-ray diffraction pattern of ordered- $\text{Li}_9\text{S}_3\text{N}$ with a simulation of the structure solution proposed in ref. ¹ and shown in Table S3.1. A small Li_2O impurity is present (~ 3 wt. %) indicated by red lines.

Table S3.1: Structure solution for $Pm\bar{3}m$ - $\text{Li}_9\text{S}_3\text{N}$ proposed by Marx et al.¹ for ampoule-synthesized $\text{Li}_9\text{S}_3\text{N}$. Our diffraction measurement with the Rietveld simulation superimposed is shown in Figure S3.1.

Atom	x	y	z	Wyckoff	Occupancy	U_{iso}
Li	0.2191	0.2191	0.2191	8g	1	0.0263
Li	$\frac{1}{2}$	$\frac{1}{2}$	$\frac{1}{2}$	1b	1	0.0376
N	0	0	0	1a	1	0.0101
S	0	0	0	3c	1	0.0092

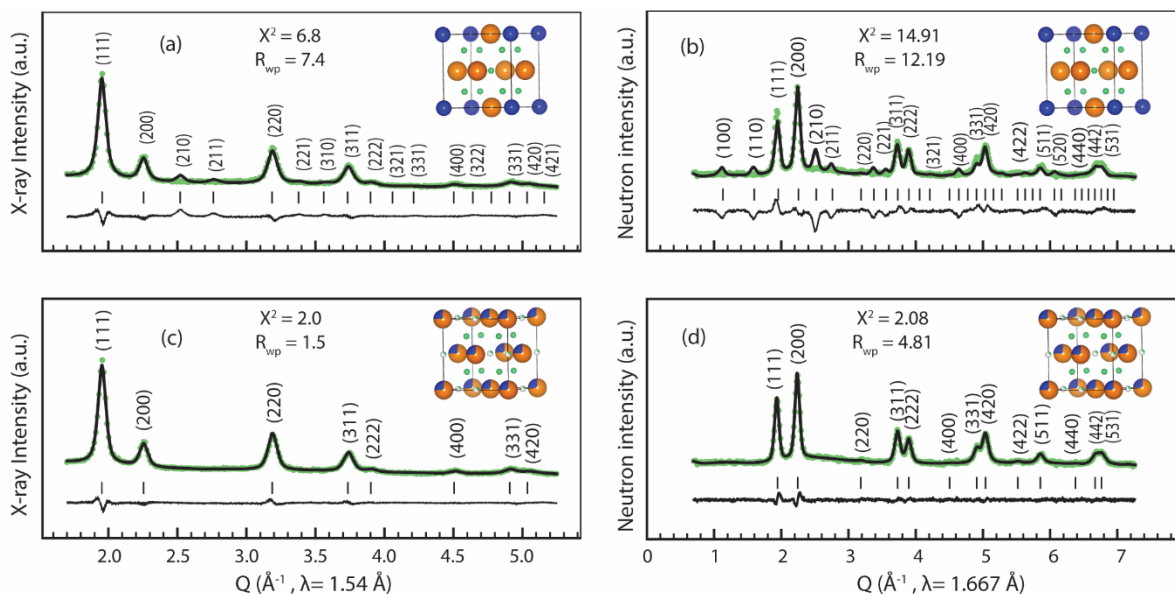


Figure S3.2. Powder diffraction on mechanochemically prepared $\text{Li}_9\text{S}_3\text{N}$. (a) X-ray diffraction pattern of mechanochemically prepared $\text{Li}_9\text{S}_3\text{N}$ with an attempt to fit the $Pm\bar{3}m$ - $\text{Li}_9\text{S}_3\text{N}$ crystal solution proposed by Marx et al.¹ (b) Neutron diffraction pattern of mechanochemically prepared $\text{Li}_9\text{S}_3\text{N}$ with an attempt to fit the $Pm\bar{3}m$ - $\text{Li}_9\text{S}_3\text{N}$ crystal solution proposed by Marx et al.¹ (c) Same X-ray diffraction pattern as in (a) but now with the Rietveld fit of an improved structure solution with the higher-symmetry $Fm\bar{3}m$ space group (d) Same Neutron diffraction pattern as in (b) but now with the Rietveld fit of an improved structure solution with the higher-symmetry $Fm\bar{3}m$ space group. The vertical lines indicate the position of the Bragg reflections. Inset structural models with Li, S, N in green, orange, blue, respectively.

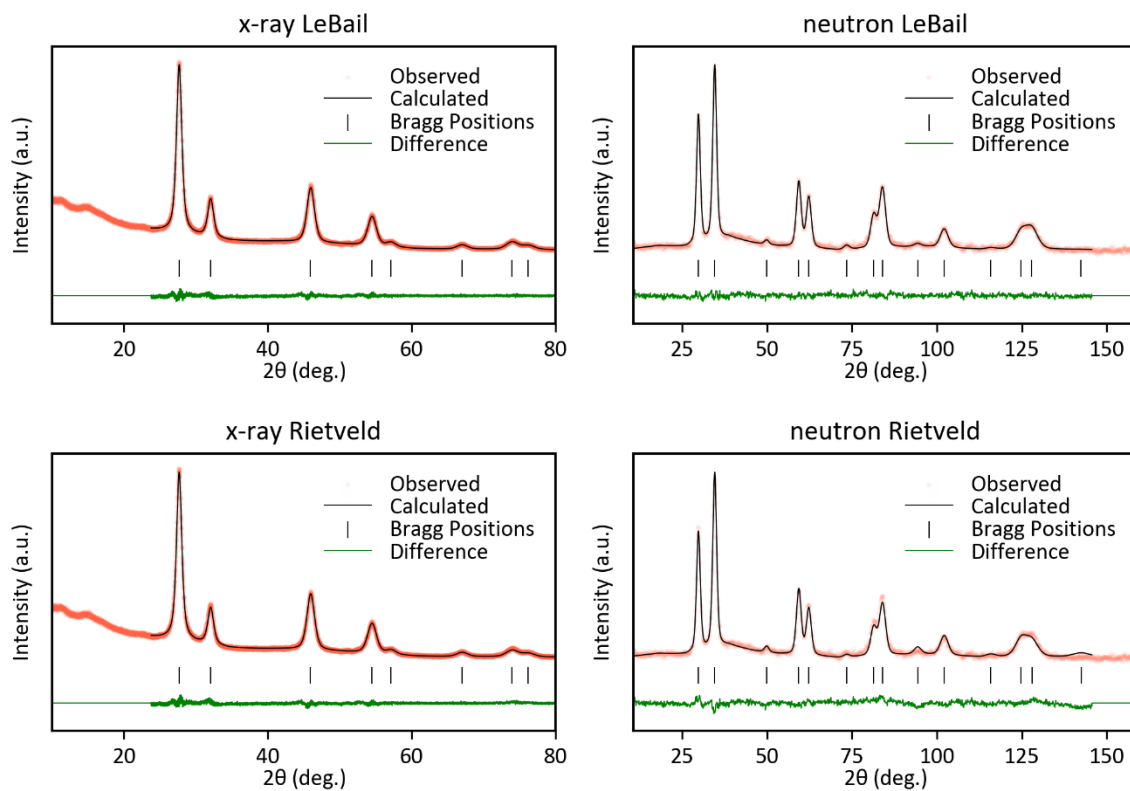


Figure S3.3. Combined fits of x-ray (Cu K α) and neutron ($\lambda=1.667$ Å) diffractogram of disordered Li₉S₃N. LeBail x-rays $wR_p = 4.70$, GoF= 1.26 — LeBail neutron $wR_p = 3.99$, GoF= 1.25 — Rietveld x-ray $wR_p = 4.91$, GoF= 1.32 — Rietveld neutron $wR_p = 5.19$, GoF= 1.62. Associated structural model in Table S3.2.

Table S3.2: Refined structure solution for $Fm\bar{3}m$ -Li₉S₃N obtained from the combined Rietveld refinement of neutron and X-ray diffraction patterns shown in Figure S3.3. Fitted parameters in **bold**. Lattice parameter **$a = 5.5846(4)$ Å**

Atom	x	y	z	Wyckoff	Occupancy	U_{iso} (Å ²)
S	0	0	0	4a	$\frac{3}{4}$	0.0331(3)
N	0	0	0	4a	$\frac{1}{4}$	0.0132(5)
Li-tet	$\frac{1}{4}$	$\frac{1}{4}$	$\frac{1}{4}$	8c	1	0.0760 (7)
Li-oct	$\frac{1}{2}$	$\frac{1}{2}$	$\frac{1}{2}$	4b	$\frac{1}{4}$	0.55(2)

Table S3.3. Average jump-Ea values used for anion-disordered $\text{Li}_{2+x}\text{S}_{1-x}\text{N}_x$ phases and their uncertainty ($\epsilon_{\text{jump-Ea}}$) and the ϵ_{mean} and $\epsilon_{\text{convergence}}$ values which are comprised in $\epsilon_{\text{jump-Ea}}$.

Jump type	Average jump-Ea (eV)	ϵ_{mean} (eV)	$\epsilon_{\text{convergence}}$ (eV)	$\epsilon_{\text{jump-Ea}}$ (eV)
S ₆ -N ₁ S ₃ (SSS)	0.409	0.004	0.007	0.011
N ₄ S ₂ -N ₄ (NNN)	0.225	0.004	0.005	0.009
N ₃ S ₁ -N ₅ S ₁ (NNS)	0.317	0.006	0.004	0.01
N ₃ S ₁ -N ₁ S ₃ (NS)	0.465	0.008	0.005	0.013
N ₄ -N ₃ S ₁ (NN)	0.349	0.007	0.007	0.013
N ₁ S ₃ -N ₁ S ₃ (SS)	0.488	0.004	0.004	0.008
N ₅ S ₁ -N ₃ S ₁ (NNN)	0.285	0.006	0.002	0.008
N ₁ S ₃ -N ₃ S ₁ (NS)	0.469	0.008	0.009	0.017
N ₂ S ₂ -N ₄ (NN)	0.428	0.02	0.01	0.03
N ₃ S ₃ -N ₄ (NNN)	0.128	0.001	0.01	0.011
S ₄ -N ₁ S ₃ (SS)	0.535	0.004	0.005	0.01
N ₃ S ₁ -N ₄ (NN)	0.356	0.005	0.006	0.011
N ₃ S ₁ -N ₂ S ₄ (NNS)	0.329	0.004	0.003	0.007
N ₂ S ₄ -N ₂ S ₂ (NSS)	0.294	0.003	0.001	0.004
N ₄ S ₂ -N ₂ S ₂ (NSS)	0.27	0.005	0.004	0.009
S ₄ -S ₆ (SSS)	0.488	0.004	0.012	0.016
N ₃ S ₁ -N ₃ S ₁ (NN)	0.376	0.003	0.001	0.004
N ₁ S ₃ -N ₄ S ₂ (NSS)	0.355	0.008	0.004	0.012
N ₂ S ₂ -N ₃ S ₃ (NNS)	0.376	0.003	0.003	0.006
S ₄ -S ₄ (SS)	0.529	0.005	0.009	0.014
N ₁ S ₃ -N ₁ S ₅ (NSS)	0.429	0.003	0.001	0.004
S ₆ -S ₄ (SSS)	0.411	0.009	0.005	0.014
N ₁ S ₃ -N ₂ S ₄ (NSS)	0.402	0.002	0.002	0.004
N ₃ S ₁ -N ₃ S ₁ (NS)	0.413	0.005	0.006	0.011
N ₂ S ₂ -N ₂ S ₄ (NSS)	0.339	0.003	0.002	0.004
N ₄ S ₂ -N ₃ S ₁ (NNN)	0.286	0.004	0.001	0.005
N ₃ S ₁ -N ₄ S ₂ (NNS)	0.307	0.003	0.001	0.004
N ₄ -N ₆ (NNN)	0.334	0.005	0.008	0.013
N ₃ S ₁ -N ₆ (NNN)	0.334	0.011	0.006	0.018
N ₃ S ₁ -N ₃ S ₃ (NNN)	0.428	0.01	0.004	0.013
N ₃ S ₃ -N ₂ S ₂ (NSS)	0.292	0.002	0.001	0.003
N ₂ S ₂ -N ₂ S ₄ (NNS)	0.373	0.004	0.002	0.006
N ₂ S ₂ -N ₃ S ₃ (NSS)	0.343	0.003	0.004	0.007
N ₂ S ₂ -N ₂ S ₂ (NS)	0.459	0.002	0.006	0.008
N ₂ S ₄ -N ₁ S ₃ (SSS)	0.41	0.007	0.009	0.016

N ₁ S ₃ -N ₂ S ₂ (SS)	0.515	0.008	0.005	0.013
N ₅ S ₁ -N ₃ S ₁ (NNS)	0.29	0.005	0.007	0.012
N ₂ S ₂ -N ₁ S ₃ (NS)	0.453	0.004	0.01	0.014
N ₂ S ₂ -N ₂ S ₂ (SS)	0.456	0.013	0.022	0.035
N ₃ S ₁ -N ₅ S ₁ (NNN)	0.344	0.008	0.006	0.014
N ₁ S ₃ -S ₆ (SSS)	0.414	0.005	0.009	0.014
N ₃ S ₃ -N ₂ S ₂ (NNS)	0.308	0.003	0.003	0.006
N ₁ S ₃ -N ₃ S ₃ (SSS)	0.455	0.011	0.015	0.026
N ₄ -N ₄ (NN)	0.329	0.003	0.006	0.008
N ₂ S ₂ -S ₄ (SS)	0.517	0.011	0.013	0.024
S ₄ -N ₂ S ₄ (SSS)	0.488	0.004	0.007	0.011
N ₅ S ₁ -N ₂ S ₂ (NNS)	0.321	0.008	0.005	0.013
N ₃ S ₃ -N ₃ S ₁ (NNS)	0.277	0.003	0.001	0.004
N ₄ S ₂ -N ₃ S ₁ (NNS)	0.254	0.002	0.001	0.003
N ₁ S ₅ -N ₁ S ₃ (NSS)	0.329	0.003	0.001	0.005
N ₃ S ₃ -N ₁ S ₃ (NSS)	0.274	0.003	0	0.003
N ₄ S ₂ -N ₁ S ₃ (NSS)	0.291	0.009	0.001	0.01
N ₃ S ₃ -N ₁ S ₃ (SSS)	0.391	0.005	0.003	0.008
N ₄ -N ₅ S ₁ (NNN)	0.301	0.005	0.005	0.011
N ₄ -N ₂ S ₂ (NN)	0.344	0.005	0.006	0.012
N ₂ S ₂ -N ₅ S ₁ (NNS)	0.299	0.013	0.009	0.022
N ₄ -N ₃ S ₃ (NNN)	0.237	0.004	0.003	0.007
N ₂ S ₄ -N ₂ S ₂ (NNS)	0.286	0.007	0.003	0.01
N ₁ S ₃ -N ₂ S ₄ (SSS)	0.452	0.007	0.008	0.015
N ₁ S ₃ -N ₃ S ₃ (NSS)	0.366	0.003	0.001	0.004
N ₁ S ₃ -N ₁ S ₅ (SSS)	0.422	0.004	0.003	0.007
N ₁ S ₃ -N ₂ S ₂ (NS)	0.454	0.003	0.009	0.012
N ₂ S ₂ -N ₄ S ₂ (NSS)	0.339	0.006	0.003	0.01
N ₂ S ₂ -N ₄ S ₂ (NNS)	0.349	0.004	0.001	0.005
N ₁ S ₅ -N ₁ S ₃ (SSS)	0.36	0.003	0.002	0.005
N ₆ -N ₄ (NNN)	0.267	0.003	0.006	0.009
N ₂ S ₄ -N ₁ S ₃ (NSS)	0.297	0.003	0.005	0.008
N ₄ -N ₄ S ₂ (NNN)	0.318	0.008	0.004	0.012
S ₄ -N ₂ S ₂ (SS)	0.567	0.003	0.011	0.014
N ₁ S ₅ -N ₂ S ₂ (NSS)	0.319	0.005	0.002	0.007
N ₂ S ₄ -S ₄ (SSS)	0.328	0.007	0.004	0.011
N ₄ S ₂ -N ₂ S ₂ (NNS)	0.272	0.003	0.001	0.004
N ₃ S ₃ -N ₃ S ₁ (NNN)	0.349	0.007	0.004	0.011
N ₁ S ₅ -S ₄ (SSS)	0.324	0.005	0.001	0.006
N ₃ S ₁ -N ₂ S ₂ (NS)	0.443	0.003	0.01	0.013
N ₃ S ₁ -N ₂ S ₂ (NN)	0.392	0.006	0.006	0.012

N ₂ S ₂ -N ₂ S ₂ (NN)	0.374	0.003	0.006	0.01
N ₃ S ₁ -N ₄ S ₂ (NNN)	0.347	0.006	0.001	0.007
N ₆ -N ₃ S ₁ (NNN)	0.294	0.007	0.002	0.01
S ₄ -N ₁ S ₅ (SSS)	0.463	0.004	0.015	0.019
N ₂ S ₂ -N ₃ S ₁ (NN)	0.396	0.006	0.006	0.012
N ₅ S ₁ -N ₄ (NNN)	0.294	0.005	0.004	0.009
N ₂ S ₄ -N ₃ S ₁ (NNS)	0.286	0.004	0.001	0.005
N ₁ S ₃ -N ₁ S ₃ (NS)	0.477	0.002	0.009	0.011
N ₂ S ₂ -N ₁ S ₅ (NSS)	0.324	0.004	0.003	0.007
S ₄ -N ₃ S ₃ (SSS)	0.487	0.013	0.004	0.017
N ₁ S ₃ -S ₄ (SS)	0.503	0.006	0.011	0.017
N ₃ S ₁ -N ₃ S ₃ (NNS)	0.322	0.004	0.004	0.008
N ₃ S ₃ -S ₄ (SSS)	0.419	0.007	0.007	0.014
N ₂ S ₂ -N ₁ S ₃ (SS)	0.509	0.01	0.011	0.021
N ₂ S ₂ -N ₃ S ₁ (NS)	0.442	0.004	0.011	0.015

Table S3.4. Average jump-Ea values used for anion-ordered Li₉S₃N phases and their uncertainty ($\epsilon_{\text{jump-Ea}}$) and the ϵ_{mean} and $\epsilon_{\text{convergence}}$ values which are comprised in $\epsilon_{\text{jump-Ea}}$.

Jump type	Average jump-Ea (eV)	ϵ_{mean} (eV)	$\epsilon_{\text{convergence}}$ (eV)	$\epsilon_{\text{jump-Ea}}$ (eV)
N ₁ S ₃ -N ₂ S ₄ (NSS)	0.431	0.002	0.003	0.005
N ₂ S ₄ -N ₁ S ₃ (NSS)	0.245	0.002	0.002	0.004
N ₁ S ₃ -S ₆ (SSS)	0.482	0.003	0.009	0.011
S ₆ -N ₁ S ₃ (SSS)	0.483	0.003	0.008	0.010
N ₁ S ₃ -N ₁ S ₃ (SS)	0.590*	n/a	n/a	0.015
N ₁ S ₃ -N ₁ S ₃ (NS)	0.472	0.002	0.009	0.011

* For N₁S₃-N₁S₃(SS) jump-type no jump was observed in the AIMD of ordered-Li₉S₃N. If one jump had occurred the jump-Ea would be 0.575 eV so that we know jump-Ea >0.575. We set the jump-Ea to 0.59 and accord an uncertainty of 0.015 which regarding the magnitude of uncertainties of the other jump-types is a cautious estimate.

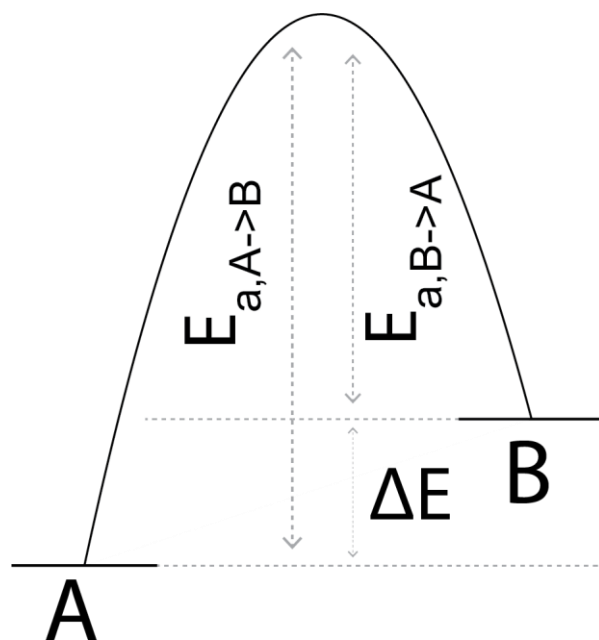


Figure S3.4. Schematic of the energy profile for a Li ion jump from site A to site B. This figure demonstrates that if $E_{a,A \rightarrow B} > E_{a,B \rightarrow A}$ then site A is more stable than site B by ΔE .

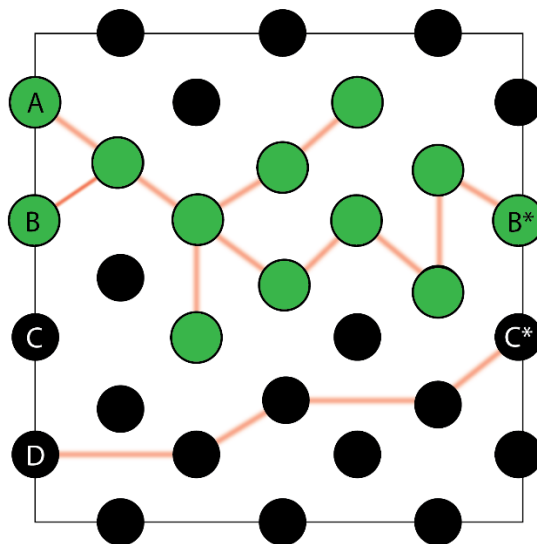


Figure S3.5. Schematic illustrating the percolation model used in this study. We define a path as percolating if it connects sites throughout one full side length of the (5x5x5) supercells and provided that the end-point of percolation is also the starting point of a percolating path. For example, in the schematic above the path leading from site A to site B* is percolating because site B is a starting point of a percolating path. In contrast, the path from D to C* is not percolating because C is not starting point of a percolating path. In this way periodic boundary conditions are respected. The green highlighting shows all sites which are connected to percolation paths.

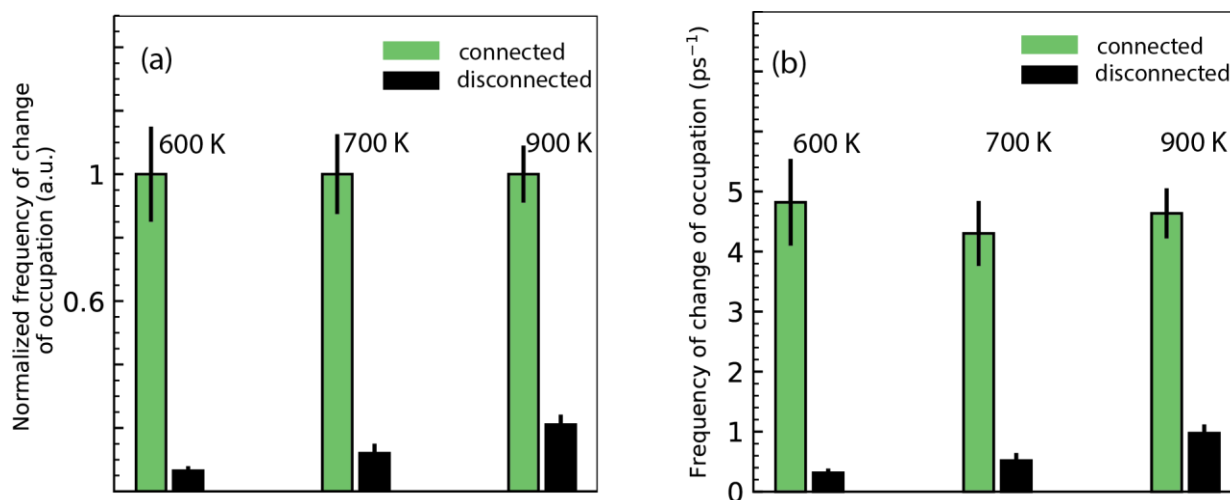


Figure S3.6. (a) Normalized frequency of occupation change for AIMD simulations at different temperatures for the same disordered-Li₉S₃N supercell. The connected sites were obtained with a jump-E_a cutoff of 0.4 eV. It becomes apparent that the frequency of occupation-change is much larger for connected sites than for disconnected sites. This discrepancy is more prominent at lower temperatures and at 300K likely even more pronounced than at 600 K. (b) Same as in (a) but not normalized. The frequency of occupation-change is obtained by tracking the occupation of sites throughout the AIMD simulation and the number of changes (i.e. change from one Li to another Li or from Li to vacancy) of occupation for individual sites.

Table S3.5. Ionic Radii used in this investigation for example for the calculations for Figure 3.5. All ionic radii are taken from ref ³ except for the ionic radius of phosphide ions P(-III) which was estimated to be ~1.89 Å from the average Li-P distance in Li₃P taken from the structure proposed in ref ⁴.

Atom	Oxidation state	Coordination number	Ionic Radius (Å)
Li	1	4	0.59
N	-3	4	1.46
S	-2	6	1.84
P	-3	5	~1.89

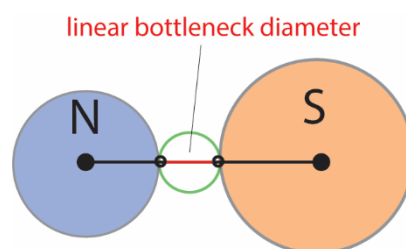


Figure S3.7. Illustration of the geometrical consideration to calculate the bottleneck diameter for linear bottlenecks between tet-tet jumps.

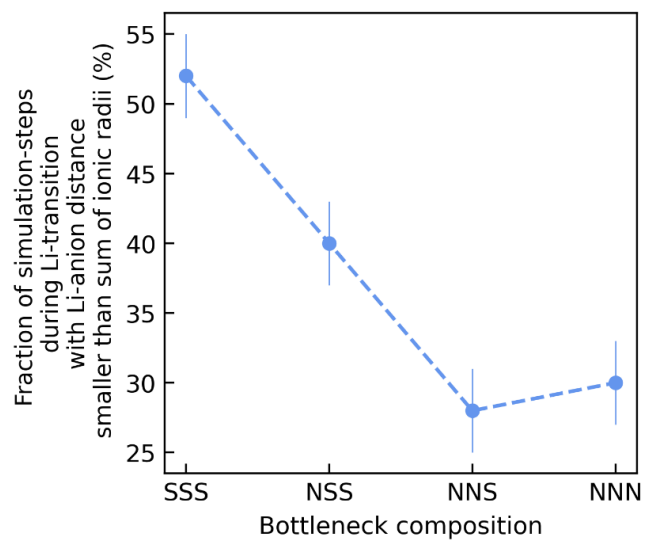


Figure S3.8. Correlation between bottleneck composition and the time spent during ion jumps (ion-“transitions”) at distances short of the sum of the ionic radii which are energetically unfavourable, obtained from an AIMD simulation of a $\text{Li}_{2.25}\text{S}_{0.75}\text{N}_{0.25}$ supercell. The dotted line is a guide to the eye.

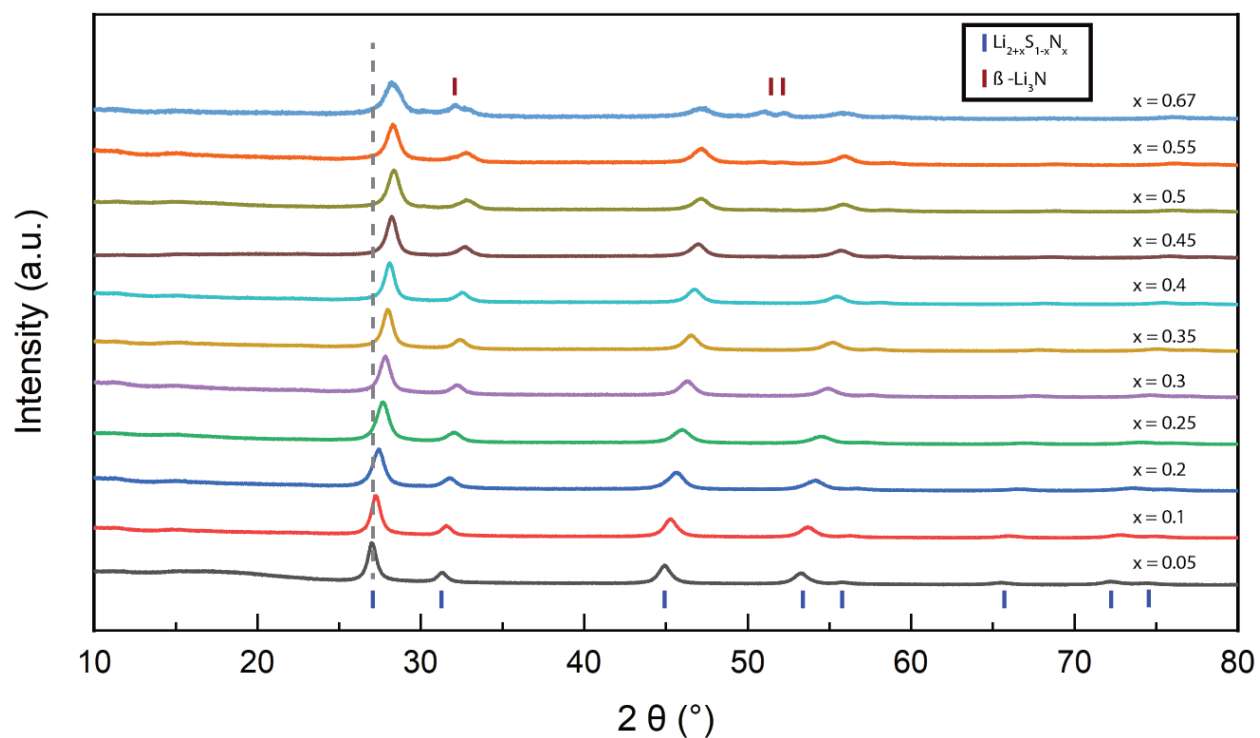


Figure S3.9. X-ray diffraction patterns of mechanochemically treated $(1-x)\text{Li}_2\text{S}-x\text{Li}_3\text{N}$ samples for $0.05 < x < 0.67$. Diffraction peaks for Fm-3m antiferite-like $\text{Li}_{2+x}\text{S}_{1-x}\text{N}_x$ observed throughout. The grey vertical line is a guide to the eye to better visualize the peak shifts due to a decreasing lattice parameter with increasing nitrogen content. A synthesis attempted with the formal composition $\text{Li}_{2.67}\text{S}_{0.33}\text{N}_{0.67}$ resulted in a phase mixture of $\beta\text{-Li}_3\text{N}$ and an $\text{Li}_{2+x}\text{S}_{1-x}\text{N}_x$ with the same lattice parameter as $\text{Li}_{2.55}\text{S}_{0.45}\text{N}_{0.55}$ indicating that $x=0.55$ is the solubility limit of nitrogen in in the $\text{Li}_{2+x}\text{S}_{1-x}\text{N}_x$ phases.

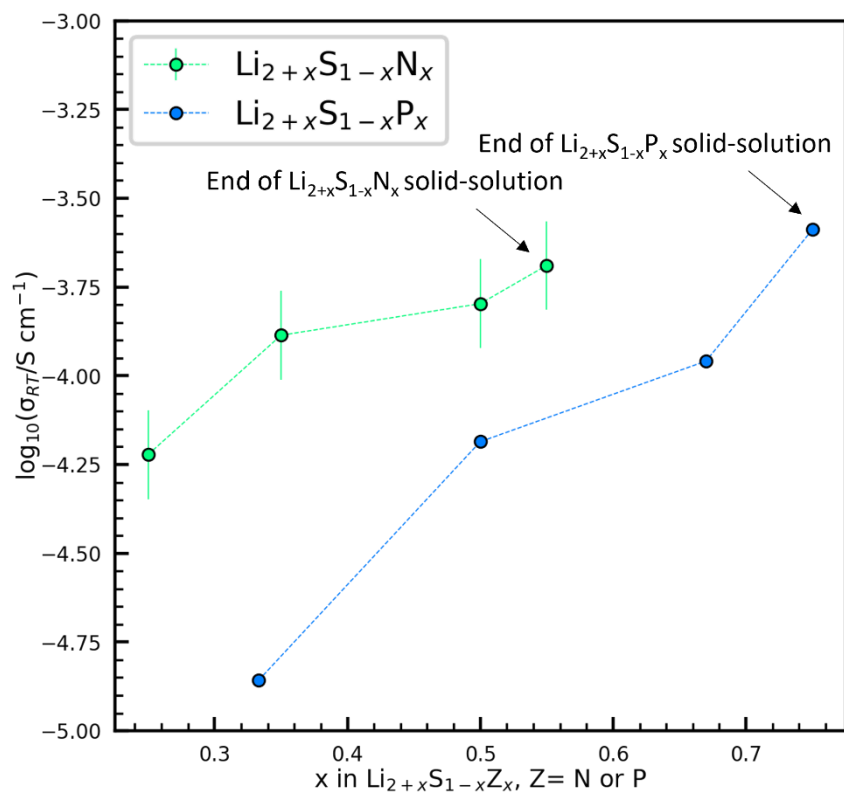


Figure S3.10. Comparison of the $\text{Li}_{2+x}\text{S}_{1-x}\text{N}_x$ and $\text{Li}_{2+x}\text{S}_{1-x}\text{P}_x$ solid-solutions. Data for the latter from Sczuka and coworkers.² For a given pnictide content x the $\text{Li}_{2+x}\text{S}_{1-x}\text{N}_x$ phases shows higher conductivities by factor ~ 3 . The $\text{Li}_{2+x}\text{S}_{1-x}\text{P}_x$ solid solution extends to higher pnictide content likely because of the better ion-size match between P ($\sim 1.89 \text{ \AA}$) and S (1.84 \AA) than between S and N (1.46 \AA).³

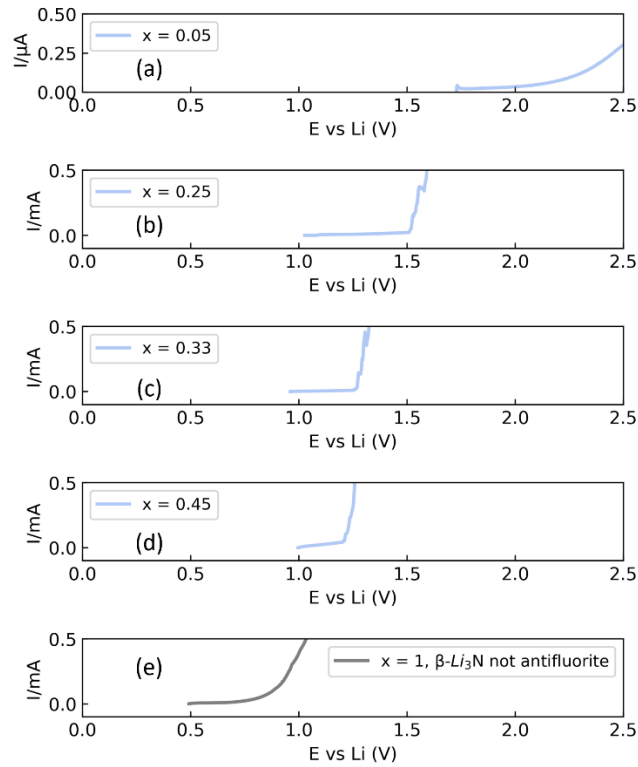


Figure S3.11. (a-d) Oxidative LSV sweeps of Li|LSN|LSN-C cells for LSN phases with different N content. (LSN: $\text{Li}_{2+x}\text{S}_{1-x}\text{N}_x$) (e) oxidative LSV sweep of a Li| Li_3N | Li_3N -C cell. It can be seen that the anodic limit of LSN phases decreases with increasing N content. For comparison the anodic limit of Li_3N was also measured. It can be seen that the oxidation limit of LSN phases is higher than that of Li_3N by more than 0.4 V.

Supplementary Note 1: Estimation of amorphous fraction in mechanochemically-synthesized $\text{Li}_{2+x}\text{S}_{1-x}\text{N}_x$ phases

High-energy ball milled samples inherently result in products with small particle sizes which results in diffraction peak broadening and potential amorphization. This may result in obscured impurities in high-energy ball-milled samples. This section aims to estimate the fraction of amorphous phases and impurities by (1) using a crystalline Si standard and (2) annealing the samples so that they become fully crystalline. To investigate the amorphous fraction introduced by synthesis approach used for the $\text{Li}_{2+x}\text{S}_{1-x}\text{N}_x$ phases we further investigated the $\text{Li}_{2.2}\text{S}_{0.8}\text{N}_{0.2}$ as a representative of these phases.

The amorphous fraction was estimated as follows. 320 mg of mechanochemically-synthesized $\text{Li}_{2.2}\text{S}_{0.8}\text{N}_{0.2}$ and 42 mg of crystalline Si powder (Sigma 7440-21-3) were thoroughly hand-ground together. Rietveld refinements of the diffraction pattern (Figure S3.12) enable to estimate the weight ratio of crystalline $\text{Li}_{2.2}\text{S}_{0.8}\text{N}_{0.2}$ and crystalline Si.

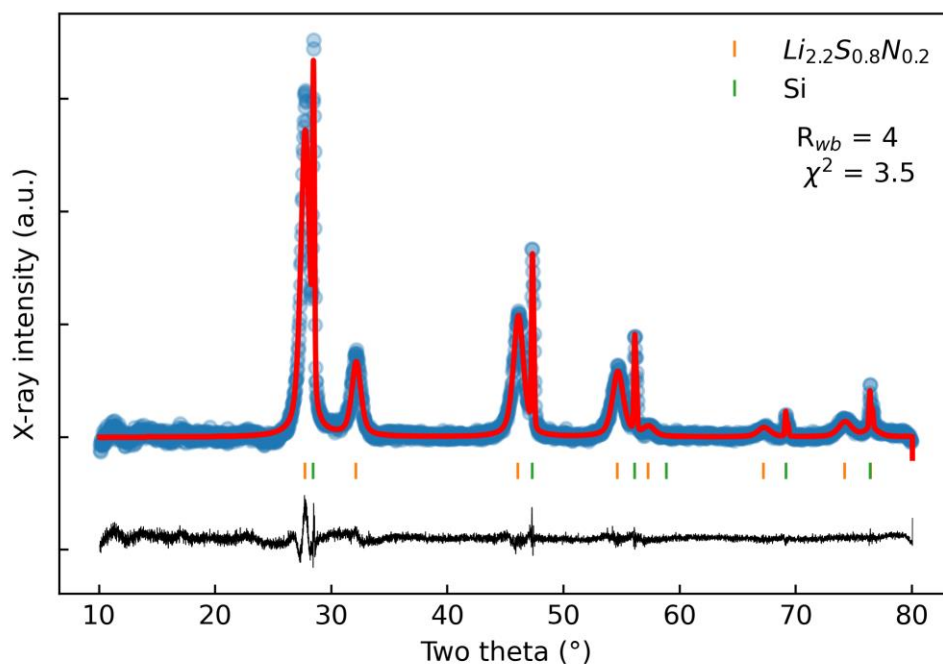


Figure S3.12. Rietveld refinement of mechanochemically-synthesized $\text{Li}_{2.2}\text{S}_{0.8}\text{N}_{0.2}$ with a crystalline Si standard. The $w_{\text{Li}_{2.2}\text{S}_{0.8}\text{N}_{0.2}}/w_{\text{Si}}$ ratio is 7.62.

Since the amount of crystalline Si is known, the amorphous fraction of $\text{Li}_{2.2}\text{S}_{0.8}\text{N}_{0.2}$ may be determined. From the refined weight ratio of crystalline $\text{Li}_{2.2}\text{S}_{0.8}\text{N}_{0.2}$ and crystalline Si powder a table of the elemental composition can be obtained (Table S3.6)

$$\kappa = \frac{w_{S,sample}M_{Si}}{w_{Si,sample}M_S} \quad (S3.1)$$

$$a_f = \left(\kappa - \frac{w_{S,refinement}M_{Si}}{w_{Si,refinement}M_S} \right) * \frac{1}{\kappa} \quad (S3.2)$$

In the equations above a_f is the amorphous fraction, w_S and w_{Si} are the weight fractions of S and Si respectively (shown in the Table S3.6) and M_{Si} and M_S are the molar weights of S and Si respectively.

Table S3.6. Elemental composition obtained from Rietveld refinement with crystalline Si standard

	Wt % Li	Wt % S	Wt % N	Wt % Si
Nominal	0.320	0.492	0.072	0.116
Calculated from refinement	0.318	0.490	0.071	0.120

Based on the above assumption a maximum amorphous fraction of the order of 4.3 wt% is determined.

To investigate whether amorphous impurities are present we heated the $Li_{2.2}S_{0.8}N_{0.2}$ samples to 600 °C for 48 h and cooled them slowly ($20 \text{ }^\circ\text{C h}^{-1}$) to room temperature. The resulting phases are the thermodynamically stable ordered- Li_9S_3N (which can also be written as ordered- $Li_{2.25}S_{0.75}N_{0.25}$) and Li_2S . This partial decomposition of the $Li_{2.2}S_{0.8}N_{0.2}$ into these two thermodynamic products is coherent with our understanding that the $Li_{2+x}S_{1-x}N_x$ phases are metastable. A small Li_2O impurity is also found (~3 wt. %). Besides no impurity could be identified. The Rietveld refinement of the diffraction pattern of the mechanochemically synthesized and annealed $Li_{2.2}S_{0.8}N_{0.2}$ is shown in Figure S3.13.

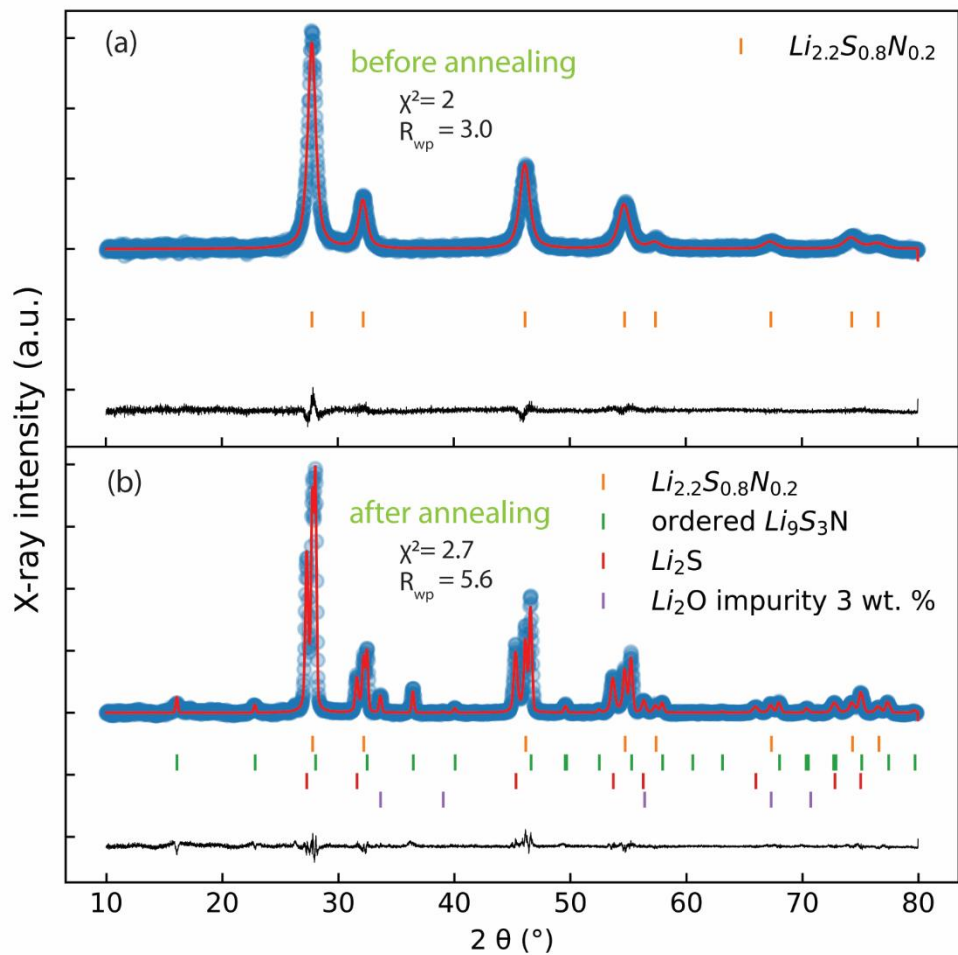


Figure S3.13. a) Rietveld refinement of pure $\text{Li}_{2.2}\text{S}_{0.8}\text{N}_{0.2}$ b) Rietveld refinement of mechanochemically-synthesized $\text{Li}_{2.2}\text{S}_{0.8}\text{N}_{0.2}$ heated to 600 $^{\circ}\text{C}$ for 2 h and cooled down slowly (20 $^{\circ}\text{C h}^{-1}$)

Supplementary Note 2: Analysis of the lithium distribution in disordered-Li₉S₃N

The structure solution that we propose for disordered-Li₉S₃N feature large thermal parameters (see Table S3.2 with $U_{\text{iso}} > 0.5 \text{ \AA}^2$ and $> 0.07 \text{ \AA}^2$ for octahedral and tetrahedral sites). These U_{iso} values are larger than the ones for the Pm-3m ordered-Li₉S₃N phase which has U_{iso} values $< 0.04 \text{ \AA}^2$ for tetrahedral and octahedral sites (see Table S3.1).

In the following we address why such large thermal parameters were necessary to obtain good Rietveld refinements for the disordered Li₉S₃N phase and we demonstrate that good Rietveld fits may be obtained with split-sites for the disordered Li₉S₃N phase which does not necessitate large thermal parameters and where the split-site coordinates are coherent with observations from molecular dynamics trajectories (vide infra).

Large U_{iso} values may either capture the large thermal displacements within a site (*dynamic disorder*) or a displacive relaxation away from the crystallographic centre due to local ordering (*static disorder*). To establish whether the large U_{iso} originate from large thermal displacements around the sites we studied the thermal motion of Li around its sites with AIMD. To study the thermal displacements of Li-ions around their equilibrium site positions we performed AIMD simulations at 300 K on two disordered-Li₉S₃N (2x2x2) supercells. We performed the simulations at 300 K to eliminate jump-events during simulations. The average square displacement of Li ions from their equilibrium site position may be used to estimate the U_{iso} value of sites. Figure S3.14 shows U_{iso} values estimated in this way for different tetrahedral and octahedral sites.

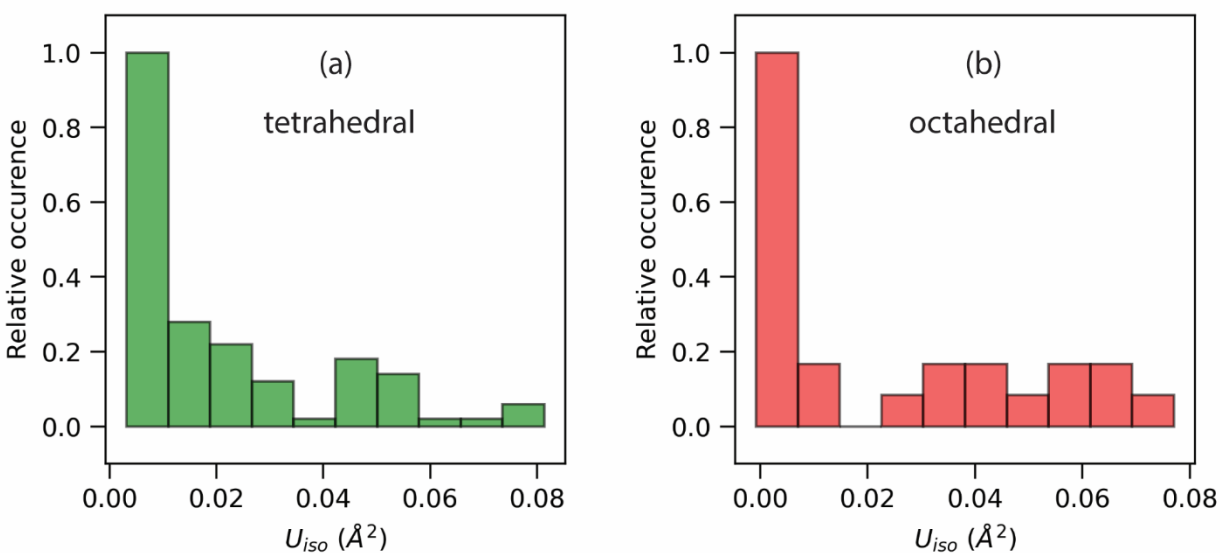


Figure S3.14. (a) U_{iso} values calculated from AIMD simulations at 300 K for different tetrahedral sites in disordered Li₉S₃N supercells. (b) U_{iso} values calculated from AIMD simulations for different octahedral sites in disordered Li₉S₃N supercells.

Figure S3.14 shows that if the U_{iso} values in the Rietveld refinements only captured thermal displacements, they should be significantly smaller than the values which were necessary for good Rietveld refinements with the structure solution proposed in Table S3.2.

The above argument suggests that the large U_{iso} values capture static disorder of the Li sites. We study the exact Li positions by analysing radial distribution functions of our AIMD simulations. The Li-anion radial distribution function of Figure S3.15 shows that Li is on average closer to N^{3-} than to S^{2-} anions. The closer proximity of Li ions and N^{3-} anions suggests that Li sites may be displaced from the centre of coordination polyhedra (i.e. tetrahedra and octahedra) towards N^{3-} anions. The N-N, S-S and S-N RDFs overlay entirely which underpins that it is clearly Li sites displaced from the centre of polyhedra towards N^{3-} rather than N^{3-} displaced from the Wyckoff (0,0,0) positions.

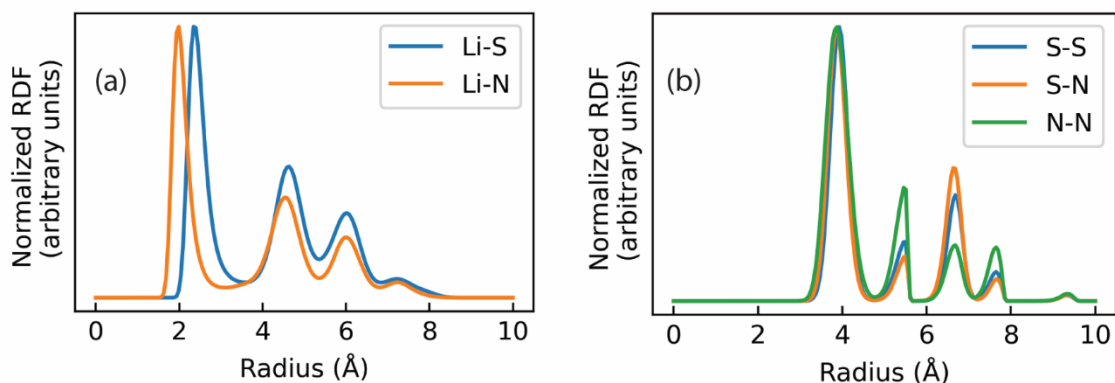


Figure S3.15. Radial distribution function (RDF) from an AIMD of a $\text{Li}_{2.25}\text{N}_{0.25}\text{S}_{0.75}$ supercell at 300 K. (a) Li-N and Li-S RDF. (b) N-N, N-S, S-S RDF.

Based on the above findings the large U_{iso} values needed for good Rietveld refinements may be explained as follows. The presence of different polyhedra in disordered $\text{Li}_9\text{S}_3\text{N}$ cause displacements of the Li-sites away from the centre of polyhedra towards the surrounding N^{3-} anions. Good Rietveld refinements were obtained for disordered- $\text{Li}_9\text{S}_3\text{N}$ with Li-sites at the centre of polyhedra and large U_{iso} values.

Based on the above observations, an alternative model is proposed, based on refinement against the neutron diffractogram which entails a 6-fold splitting of the octahedral site (Wyckoff 4b, $(\frac{1}{2}, \frac{1}{2}, \frac{1}{2})$) in the [100] direction, i.e. Wyckoff 24e ($x, \frac{1}{2}, \frac{1}{2}$). This model, presented in Figures S3.16 and Table S3.7, results in a slightly better fit of the neutron diffractogram and a lower value of U_{iso} for the lithium sites, namely 0.0420 \AA^2 which is altogether reasonable for the mobile ion in an ion conductor. The shift along the [100] is consistent with the observation from MD of the tendency of Li to displace towards the nitride ions, and the resulting Li-N distance of ca. 2 Å is reasonable considering the ionic radii of N^{3-} and Li^+ .

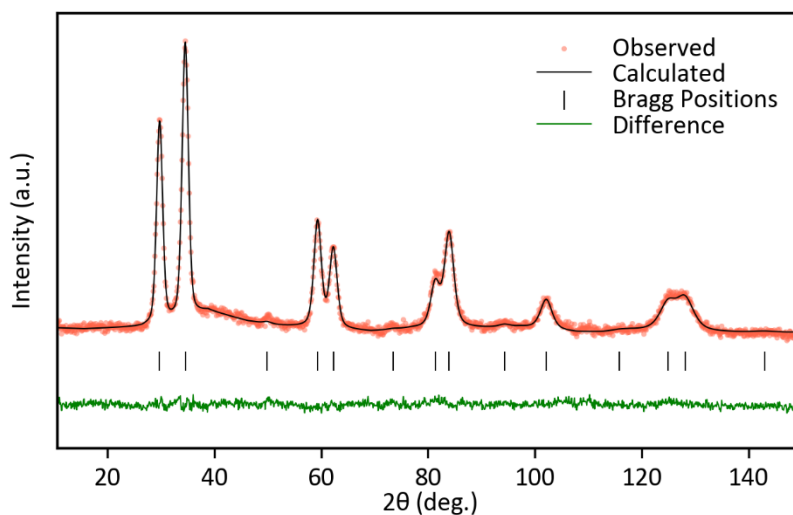


Figure S3.16: Rietveld fit of neutron diffractogram of disordered $\text{Li}_9\text{S}_3\text{N}$. $\lambda=1.667 \text{ \AA}$, $wRp = 4.46$, $GoF=1.36$

Table S3.7: Refined structure solution for $Fm\bar{3}m$ - $\text{Li}_9\text{S}_3\text{N}$ obtained from the Rietveld refinement of neutron pattern shown in Figure S3.3. Fitted parameters in **bold**. Lattice parameter $a = 5.5846(4) \text{ \AA}$

Atom	x	y	z	Wyckoff	Occupancy	U_{iso}
S	0	0	0	4a	0.762(4)	0.0232(5)
N	0	0	0	4a	0.238(4)	0.0232(5)
Li-tet	$\frac{1}{4}$	$\frac{1}{4}$	$\frac{1}{4}$	8c	1	0.0420(17)
Li-oct	$\frac{1}{2}$	$\frac{1}{2}$	$\frac{1}{2}$	4b	0.163(19)	0.0420(17)
Li-oct-split	0.65(3)	$\frac{1}{2}$	$\frac{1}{2}$	24e	0.012(4)	0.0420(17)

Constraints (occ: occupancy, U: U_{iso} , mult:multiplicity)

- $occ[N] + occ[S] = 1$
- $occ[\text{Li-tet}] = 1$ (*freely fitting led to values slightly >1*)
- $U[N] = U[S]$
- $U[\text{Li-tet}] = U[\text{Li-oct}] = U[\text{Li-oct-split}]$
- $2*occ[N]*mult[N] + 3*occ[S]*mult[S] = occ[\text{Li-tet}]*mult[\text{Li-tet}] + occ[\text{Li-oct}]*mult[\text{Li-oct}] + occ[\text{Li-oct-split}]*mult[\text{Li-oct-split}]$ (*electroneutrality*)

Supplementary Note 3: Correlation of ion hops in disordered-Li₉S₃N

It was shown for some high-conductivity ion conductors, such as Li₆PS₅Cl (ref.¹³) and Li₁₀GeP₂S₁₂ (ref.¹⁴), that lithium hops do not occur independently but in a correlated fashion. Additionally, some ion conductors such as Li₆PS₅Cl feature flat energy landscapes with a lack of well-defined energy minima that make it difficult to well define Li-ion sites. In this section we set out to investigate how *well-defined* sites are in disordered-Li₉S₃N and to what extent Li jumps are correlated in disordered-Li₉S₃N and ordered-Li₉S₃N.

Particle motion may be described in terms of hopping when diffusion through the solid occurs as a series of distinct events. One may test for this by verifying whether the conditions listed in Table S3.8 are met for the material of interest. We find the conditions to describe diffusion in terms of hopping met for disordered-Li₉S₃N (Table S3.9).

Table S3.8. Requirements to describe diffusion processes as “hops” adapted from ¹⁵

$\tau_r \gg \tau_h$	The hopping time, τ_h , associated with the event when compared with the residence time, τ_r , spent by a given particle between hops (i.e. in sites).
$\tau_r \gg \nu_0^{-1}$	For ν_0 the mean thermal vibrational frequency, i.e. the attempt frequency
$d \gg a$	For d the hopping distance (i.e. distance between sites) and a the mean amplitude of thermal motions
$E_a \gg kT$	For E_a the maximum change in potential energy during a hopping even

Table S3.9. Verifying the conditions for describing ion diffusion as hopping in disordered Li₉S₃N. τ_r residence time, τ_h , the time during the hop, ν_0 attempt frequency ($\approx 10^{13}$ Hz), a , vibration amplitude, d distance between sites, E_a/kT assuming $E_a = 0.2$ eV which is on the order of the lowest jump-activation energies in Li_{2+x}S_{1-x}N_x phases.

τ_r/τ_h	τ_r/ν_0^{-1}	d/a	E_a/kT (T=900K)	E_a/kT (T=300K)	Condition met
5.35	1684.98	5.26	2.67	8	yes

In addition to the above criteria Catlow et al (ref.¹⁵) described 2 exact criteria to validate whether the hopping model applies:

The 1st criterion requires a highly structured pair correlation function of the mobile species. The 2nd criterion requires a non-gaussian self-correlation function of the mobile species. Figure S3.17a and b show the pair correlation functions and the self-correlation of the Li ions. The pair Li-Li correlation function is highly structured and the self-correlation functions is non-Gaussian as may be quantitatively determined from evaluating $3 \langle r^4(t) \rangle / 5 \langle r^2(t) \rangle$ which is of the order of 30 (unity would indicate liquid-like diffusion). $\langle r^n(t) \rangle$ is defined in equation S3.3 as :

$$\langle r^n(t) \rangle = \int dr r^n G^S(r, t) \quad (S3.3).$$

Additionally, the clearly visible gap in Li-population visible in Figure S3.17b between $\sim 0 \text{ \AA}$ and $\sim 3 \text{ \AA}$ shows that Li ions favorably reside in their initial site (0 \AA) or in a neighboring site (3 \AA) which is approximately the distance between octahedral and tetrahedral sites. At higher radii such clear gaps are not visible as jumps do not occur in a straight line i.e. the distance from the second site to the initial site is not necessarily twice the distance from the first site to the initial site.

We now concern ourselves with the extent to which motion is *correlated* in disordered-Li₉S₃N. Previously correlated motion has been detected by two means: (i) by demonstrating *bundling in time* of jump events and (ii) by identifying a distribution of *strings of jumps* that does not follow a Poisson distribution. A string consists of at least two jumps where the second jump departs from the end-site of the first jump. The start-time of this second jump needs to be after the start time of the first jump and before the end-time of the first jump. Generally a string of length n is given if all the below conditions are met where i represents jump-event indices of jumps that are part of the string; $t_{i,start}$ and $t_{i,end}$ relate to the time in the simulation where event i starts and ends, respectively. $\text{Site}_{i,start} / \text{Site}_{i,end}$ stand for start-site and end-site of jump event i, respectively:

$$t_{i-1,start} \leq t_{i,start} \cap \text{site}_{i-1,end} = \text{site}_{i,start} \cap t_{i-1,end} \geq t_{i,start} \text{ for } i \text{ in } [2,3,4,5 \dots, n] \quad (S4)$$

In Figure S3.17c we show that no bundling in time of the hop events as observed by Mo et al.¹⁴ and Morgan¹³ is observed for AIMD simulations of the Li_{2+x}S_{1-x}N_x phases suggesting that the mechanism described by Mo et al.¹⁴ is not dominant in disordered-Li₉S₃N phases.

To analyse the *poissonicity* of the probability distribution of string lengths for each AIMD simulation we performed the following analyses.

- 1) We compared the probability distribution of string lengths obtained in one AIMD simulation and the probability distribution of an *ideal* Poisson distribution with λ =average-string-length of the AIMD simulation (*ideal* meaning a Poisson distribution with a very large distribution size, $>10^6$ samples). Figure S3.17d shows that the distribution of string lengths follows a Poisson distribution.
- 2) While the distribution of string lengths closely follows a Poisson distribution deviations can still be made out. Such deviations may represent a deviation from Poisson behaviour or be a consequence of a limited size of distributions. In order to quantify the magnitude of the deviations caused by limited distribution size we calculated the Cramer-von-Mises statistic for the distribution of string lengths in different AIMD simulations vis-à-vis an *ideal* Poisson distribution. Additionally we calculated the Cramer-von-Mises statistic for 100 control Poisson distribution with λ =average-string-length, each of these control Poisson distributions had the same distribution-size as the distribution of string lengths obtained from the AIMD simulations. We find that the deviations from an *ideal* Poisson distributions that we observe can be accounted for by the limited AIMD-string-length distribution's size because similar Cramer-von-Mises statistics are obtained for the string-length distributions obtained from AIMD and the 100 control Poisson distributions of equivalent size vis-à-vis an *ideal* Poisson distribution with distribution size $>10^6$ (Table S3.10).

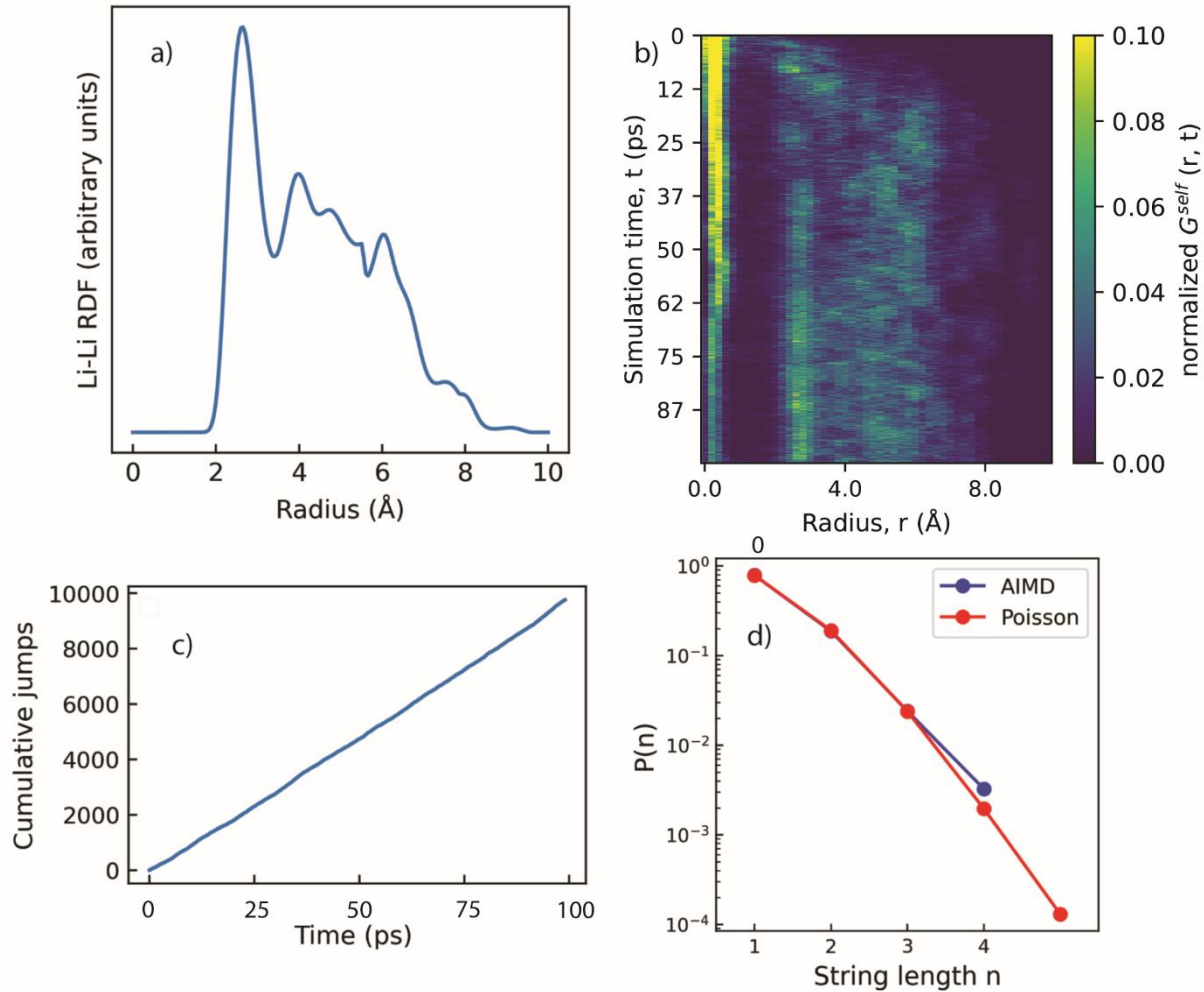


Figure S3.17. Validity of the hopping model and the correlation of hops in disordered-Li₉S₃N. (a) Li-Li RDF of the AIMD of disordered Li₉S₃N at 900K. The RDF is *well-structured* suggesting well-defined sites. (b) Self correlation function of the Li-ions in the AIMD. (c) Cumulative jumps over the AIMD simulation time. No *cascades* of jumps are observable the number of jumps increases continuously. (d) Distribution of the string lengths together with an *ideal* Poisson distribution with λ = average-string-length from AIMD.

In conclusion, the diffusion in disordered-Li₉S₃N clearly occurs via hops between well-defined sites and in an uncorrelated fashion.

The same investigation of the Li-diffusion was performed for ordered-Li₉S₃N and we equally find that diffusion in ordered Li₉S₃N occurs via hops between well-defined sites in an uncorrelated fashion Figure S3.18.

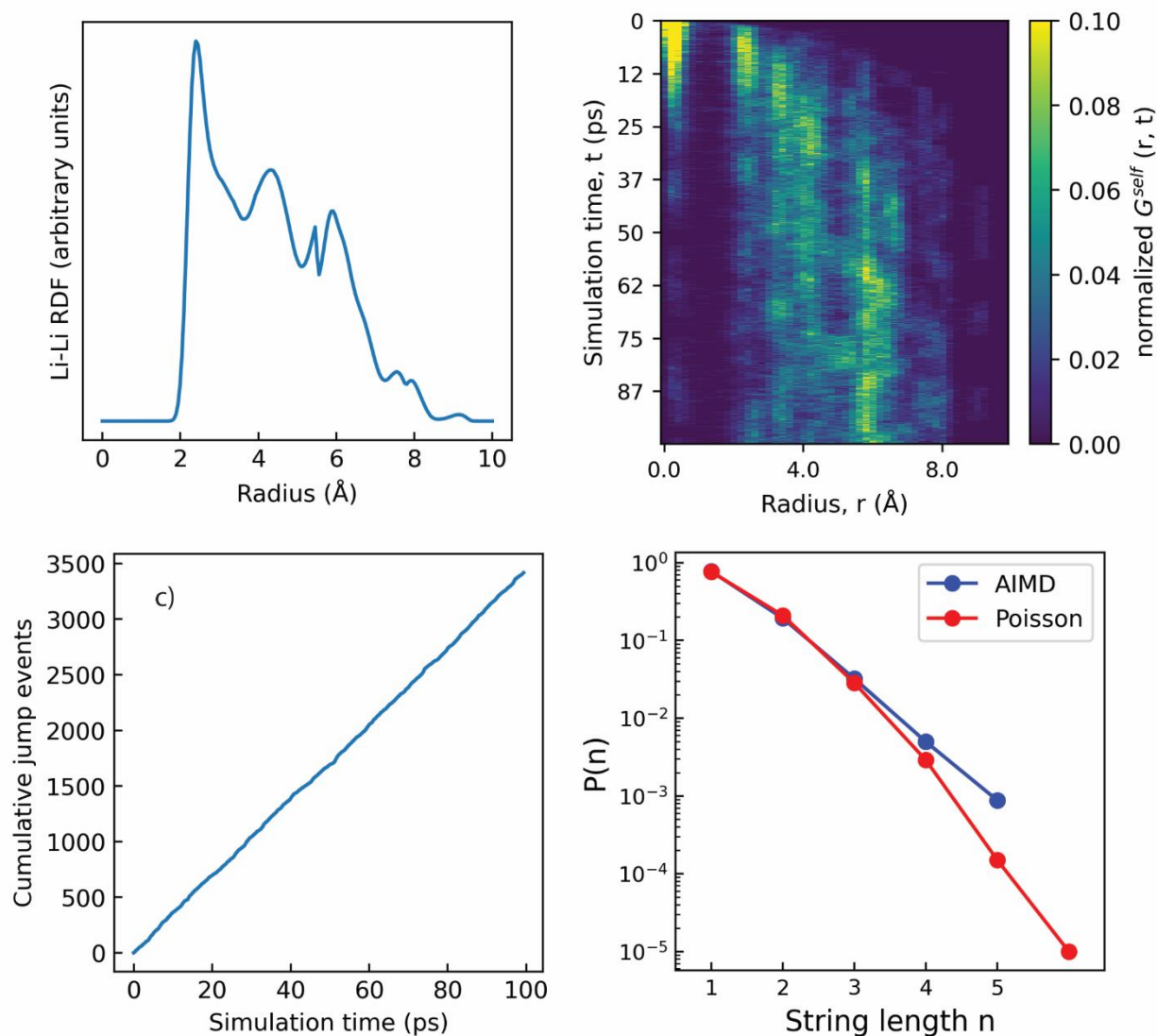


Figure S3.18. This Figure addresses the validity of the hopping model and the correlation of hops in ordered-Li₉S₃N. (a) Li-Li RDF of the AIMD of ordered Li₉S₃N at 900K. The RDF is *well-structured* suggesting well-defined sites. (b) Self correlation function of the Li-ions in the AIMD. (c) Cumulative jumps over the AIMD simulation time. No *cascades* of jumps are observable the number of jumps increases continuously. (d) Distribution of the string lengths together with an *ideal* Poisson distribution with λ = average-string-length from AIMD.

Table S3.10: Results of Cramér-von Mises analysis for the data in Figures S3.17d and S3.18d

Phase	Cramér-von Mises statistic for string length distribution obtained from AIMD simulations	Average Cramér-von Mises statistic of 100 Poisson distributions of equivalent length as the string length distribution obtained from AIMD
Disordered-Li ₉ S ₃ N	946.245	946 ± 1
Ordered-Li ₉ S ₃ N	508.001	509 ± 1

Supplementary Note 4: Estimation of the *attempt* frequency ν_0

In the field of solid-state ionics it is commonly accepted that 10^{13} Hz is a reasonable *a priori* assumption for the attempt frequency ν_0 as explored e.g. in references ⁵⁻⁸.

We support our assumption of $\nu_0 = 10^{13}$ Hz for the $\text{Li}_{2+x}\text{S}_{1-x}\text{N}_x$ phases by computationally estimating ν_0 using a previously published approach ^{9,10} briefly described as follows: The oscillations of the Li-ions around the site centers are obtained from AIMD simulations. A Fourier transform of this oscillatory signal in time yields a distribution of the frequencies of the underlying oscillations. The average oscillatory frequency serves as an estimate for the attempt frequency ν_0 . ^{9,10} The average oscillatory frequencies for different $\text{Li}_{2+x}\text{S}_{1-x}\text{N}_x$ phases obtained in this way are shown in Table S3.11. Clearly the estimates for the attempt frequency ν_0 obtained from this method are on the order of $1 \cdot 10^{13} \text{ s}^{-1}$.

Table S3.11. Average frequency of oscillatory motion in Li sites obtained from 900K AIMD simulations of different $\text{Li}_{2+x}\text{S}_{1-x}\text{N}_x$ supercells.

Supercell composition x in $\text{Li}_{2+x}\text{S}_{1-x}\text{N}_x$	Average frequency of oscillatory motion in Li sites (10^{13} Hz). Error bar is the standard deviation
0.25 (i.e. disordered- $\text{Li}_9\text{S}_3\text{N}$)	1.09 ± 0.04
0.34	1.09 ± 0.05
0.44	1.11 ± 0.03
0.5	1.12 ± 0.02

Additionally, Equation S3.5 derived from transition theory allows to estimate the average attempt frequency from the experimental activation energy as done in ref. ¹¹:

$$\nu_0 = \frac{1}{a_0} \sqrt{\frac{2 E_a}{M_{\text{Li}}}} \quad (\text{S5})$$

where ν_0 is the attempt frequency a_0 the average (jump) distance between sites, E_a the activation energy for a jump between sites and M_{Li} the mass of a Li-ion. This approach is approximate as Equation S3.5 is derived for a parabolic potential-well (ref. ¹²) but serves to estimate the order of magnitude of the average attempt frequency. Table S3.12 shows the attempt frequencies calculated in this way for different $\text{Li}_{2+x}\text{S}_{1-x}\text{N}_x$ phases. (2.5 Å was used as an average distance between jumps i.e. average of the 2.7 Å tet-tet distance and the average oct-tet 2.3 Å distance.) This second approach based on experimental conductivity-activation energies also yields estimates for $\nu_0 \approx 1 \cdot 10^{13}$ Hz

Table S3.12. Attempt frequency obtained by applying Equation S3.5 to different $\text{Li}_{2+x}\text{S}_{1-x}\text{N}_x$ phases using the experimental conductivity- E_a .

Composition, x in $\text{Li}_{2+x}\text{S}_{1-x}\text{N}_x$	Experimental E_a (eV)	Attempt frequency $\nu_0/10^{13}$ Hz
0.05	0.47 ± 0.01	1.02 ± 0.011
0.1	0.45 ± 0.01	1.00 ± 0.010
0.2	0.40 ± 0.01	0.94 ± 0.012
0.25	0.39 ± 0.01	0.93 ± 0.012
0.45	0.38 ± 0.01	0.91 ± 0.012

The two independent approaches to estimate the order of the attempt frequencies yield values of the order of 10^{13} Hz justifying the order of magnitude of the assumed $\nu_0=10^{13}$ Hz.

Small deviations of the attempt frequency about this order of magnitude would cause a small systematic shift of the individual jump- E_a values and so of the percolation-energy curves. We demonstrate this in SI Figure S3.19 by recalculating the percolation-energy diagram for three values of $0.9 \cdot 10^{13}$ Hz $\leq \nu_0 \leq 1.1 \cdot 10^{13}$ Hz resulting in deviations of < 0.01 eV. The shape of the percolation diagram is not affected and so we conclude that the exact value of ν_0 would not affect any of the conclusions in our study.

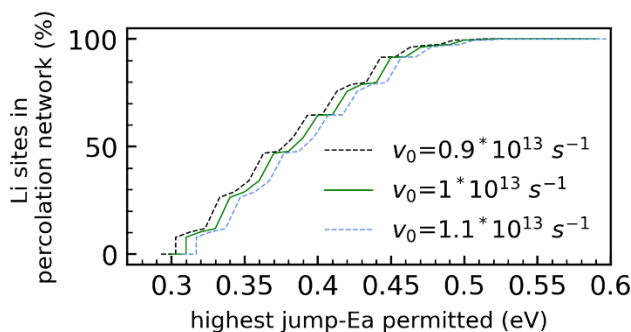


Figure S3.19. Percolation energy diagram for disordered- $\text{Li}_9\text{S}_3\text{N}$ with jump- E_a values calculated with $\nu_0=0.9 \cdot 10^{13}$ Hz, $\nu_0=1 \cdot 10^{13}$ Hz, $\nu_0=1.1 \cdot 10^{13}$ Hz

To the best of our knowledge, it is typically assumed that the attempt frequency is a material property, constant in all sites.⁵⁻⁸ It is however, conceivable that the difference in coordination environment in disordered materials and/or materials with multiple distinct sites effects a significant difference in effective attempt frequency per site in a given material.

We performed model AIMD simulations at 300 K on one $\text{Li}_{2.25}\text{S}_{0.75}\text{N}_{0.25}$ supercell and one $\text{Li}_{2.5}\text{S}_{0.5}\text{N}_{0.5}$ supercell (respectively representative of the $\text{Li}_{2+x}\text{S}_{1-x}\text{N}_x$ solid solution to study the thermal motions around the Li-ion equilibrium positions (i.e. the sites) as a function of coordination environment. Applying the above described method we derived the oscillatory frequency in $\text{Li}_{2+x}\text{S}_{1-x}\text{N}_x$ phases for different site types.

The average oscillatory frequencies in SI Table S3.13 suggest that the oscillatory frequencies do not vary significantly with site type and no monotonic relation with local S/N coordination is observed.

Table S3.13. Oscillatory frequency of individual sites obtained from the analysis of 300K AIMD simulations of two different $\text{Li}_{2+x}\text{S}_{1-x}\text{N}_x$ supercells. The values shown are the averages and their standard deviation obtained for different occurrences of the same type of site. Some oct sites not represented in the supercells studied.

Type of site	Average oscillatory frequency in site / (10^{13} Hz)	
tet	N_4	1.34 ± 0.05
	N_3S_1	1.15 ± 0.06
	N_2S_2	1.37 ± 0.08
	N_1S_3	1.32 ± 0.04
	S_4	1.41 ± 0.04
oct	N_6	
	N_5S_1	1.21 ± 0.06
	N_4S_2	1.13 ± 0.05
	N_3S_3	1.0 ± 0.13
	N_2S_4	1.43 ± 0.06
	N_1S_5	
	S_6	

Finally, to investigate the effect on our conclusions of hypothetical variations of the attempt frequency in different sites in $\text{Li}_{2+x}\text{S}_{1-x}\text{N}_x$ we recalculate the jump-Ea values using ν_0 with a 30% uncertainty that is $(1 \pm 0.3) \cdot 10^{13}$ Hz instead of $\nu_0 = 1 \cdot 10^{13}$ Hz. The corresponding uncertainty on the jump-Ea values amounts to 40-50 meV (rather than 10-20 meV). Key figures of the main text are reproduced in Figure S3.20 below with the increased uncertainty in the attempt frequency. Small shifts of the percolation onsets are observed and the distribution of possible fraction of sites in percolation network is increased as would be expected. Overall, however, none of the conclusions of our study are affected.

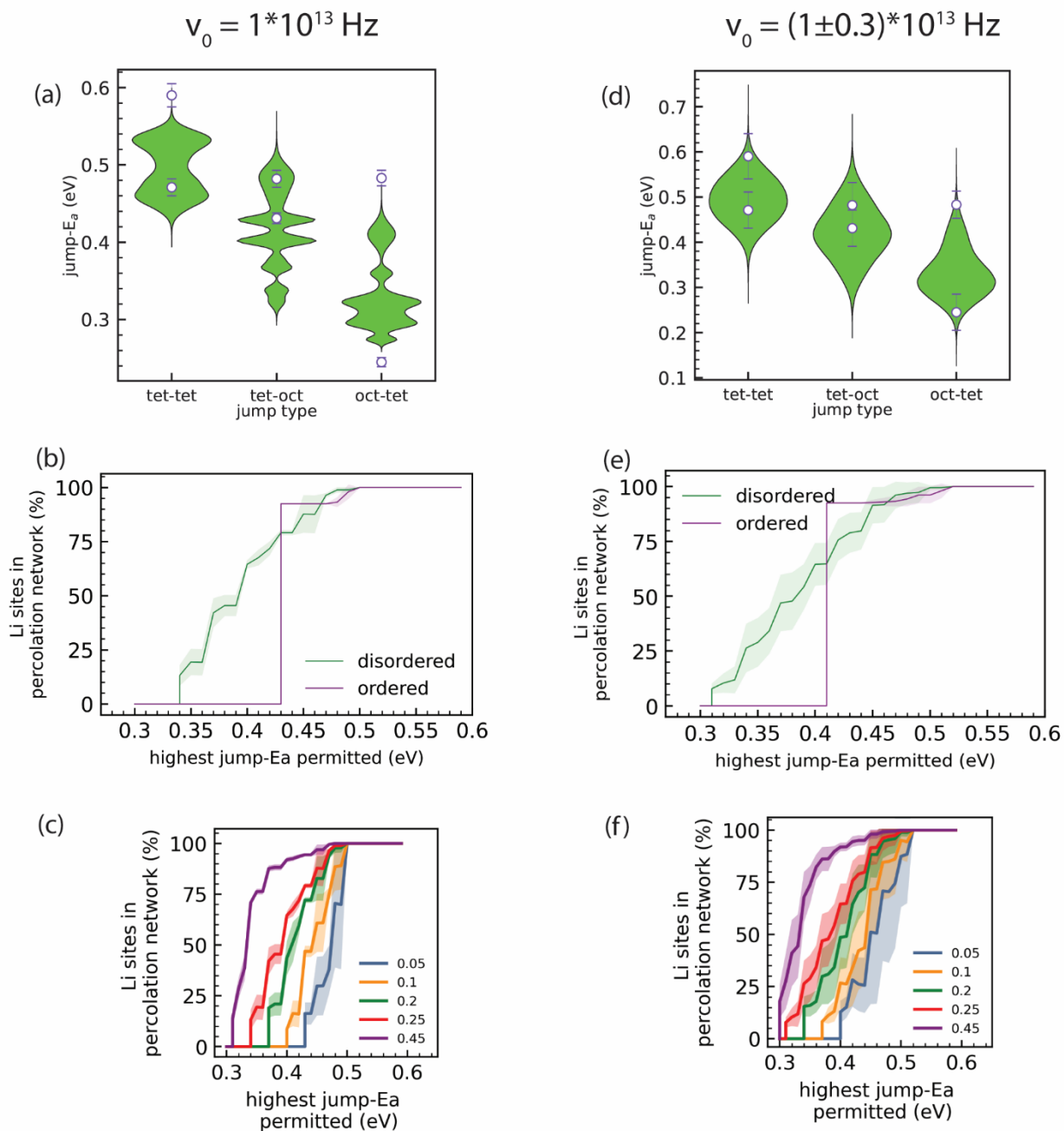


Figure S3.20. Key figures from the main text reproduced with $\nu_0=(1\pm 0.3)\cdot 10^{13}$ Hz to account for hypothetical 30% variations in the attempt frequency between sites, resulting in larger uncertainty on the jump- E_a (a) Figure 3.4a from main text. (b) Figure 3.4b from main text. (c) Figure 3.7b from main text

Supplementary Note 5: Conceptual differences between the jump activation energies from AIMD and the energy barriers obtained from NEB

Migration barriers obtained by the Nudged-elastic band approach (NEB) require an a priori knowledge or intuition of the jump event. The researcher will have to make a choice on whether the ion to be investigated takes part in an independent jump or a correlated jump and, in the latter case, how many ions will be involved. Structural disorder —whether compositional, occupational, displacive, rotational etc.— needs to be defined explicitly. For example, in the case of $\text{Li}_{2+x}\text{S}_{1-x}\text{N}_x$, the local coordination by S/N and the occupation or not of adjacent tetrahedral and octahedral sites (i.e. *defect/charge-carrier* concentration and distribution) needs to be explicitly defined. Finally, by the nature of the NEB methodology, the quantitative barrier can only be determined statically (i.e. at 0 K), that is any contribution from any thermally activated dynamics is normally excluded.

In contrast, jump activation energies are obtained from AIMD simulations at finite temperatures by determining the jump frequency $\nu_{A \rightarrow B}$ for jumps going from site A to site B (count of jumps divided by the time of site occupation of site A). Provided that the jump frequency exhibits Arrhenius behavior and that the attempt frequency ν_0 is known (or an appropriate estimate used), a jump activation energy can be calculated as shown in equation (3.1) from the main text:

$$\text{jump-} E_{a,A \rightarrow B} = -k_b T * \ln \left(\frac{\nu_{A \rightarrow B}}{\nu_0} \right) \quad (3.1)$$

where k_b is the Boltzmann constant, T the temperature in K, $\nu_{A \rightarrow B}$ the observed frequency of jumps between sites A and B and $\text{jump-} E_{a,A \rightarrow B}$ the jump-activation energy of a jump event from site A to site B. Across the simulation time different jumps between the sites of interest occur, certain jump events may be part of correlated “strings” and other jump-events may be “independent”. Additionally these jump-events occur with different arrangements of the surrounding mobile species which inherently changes during the AIMD simulations. In contrast to NEB migration barriers, jump- E_a values from AIMD can thus be interpreted as *time-averaged* migration barriers associated with all occurring types of jump events (i.e. independent and correlated) and associated with a *time-averaged* occupation of the surrounding mobile-species sites rather than a specific arrangement of the mobile species. In case no appropriate ν_0 value can be identified and/or jumps between sites do not exhibit Arrhenius behavior, the jump- E_a values can still be interpreted as rescaled jump-frequencies which are still highly informative and enable to identify diffusion-promoting and diffusion-hampering local environments.

Supplementary Note 6: Uncertainty on jump-Ea values

Jump-Ea values are calculated between a pair of sites (i.e. two neighbouring sites) A and B via equation 3.1 of the main text:

$$\text{jump-} E_{a,A \rightarrow B} = -k_b T * \ln \left(\frac{v_{A \rightarrow B}}{v_0} \right)$$

where k_b is the Boltzmann constant, T the temperature in K, $v_{A \rightarrow B}$ the observed frequency of jumps between sites A and B and $\text{jump-} E_{a,A \rightarrow B}$ the average jump-activation energy of a jump event from site A to site B. Jump types are defined based on the composition of site A and site B, as well as the bottleneck connecting the two sites. Specific jump types, for instance $N_3S_1-N_3S_3$ (NNN), are represented by numerous pairs of sites through the multiple supercells simulated. The average jump-Ea of a jump type is the arithmetic mean of the jump-Ea values of all pairs of sites representing that jump type and its standard deviation as the uncertainty on the mean (ϵ_{mean}). An additional uncertainty on the average jump-Ea values arises from convergence. To estimate the uncertainty arising from convergence we evaluate the average jump-Ea value over different stretches of the AIMD simulation time i.e. from 20 ps to 200 ps in steps of 20 ps as demonstrated for the example of $N_3S_1-N_3S_3$ (NNN) jump-type in SI Figure 3.21. The uncertainty on the average-jump-Ea arising from convergence ($\epsilon_{\text{convergence}}$) is estimated as the largest difference between jump-Ea values existing between 140 ps and 200 ps simulation time:

$$\epsilon_{\text{convergence}} = \max (|E_{200ps} - E_{180ps}|, |E_{200ps} - E_{160ps}|, |E_{200ps} - E_{140ps}|, |E_{180ps} - E_{160ps}|, |E_{180ps} - E_{140ps}|, |E_{160ps} - E_{140ps}|)$$

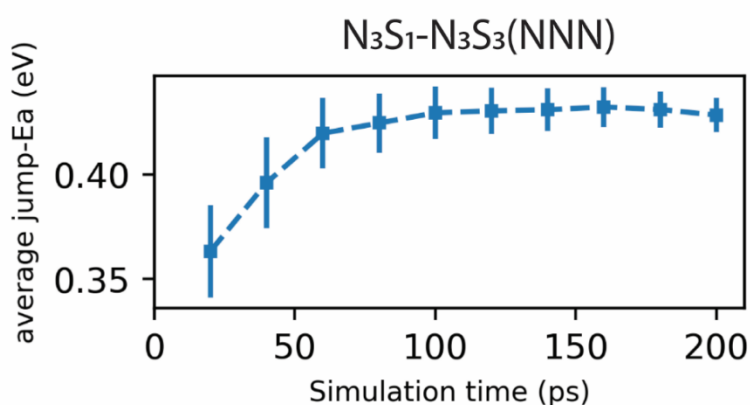


Figure S3.21. Average jump-Ea of the $N_3S_1-N_3S_3$ (NNN) jump evaluated for different AIMD simulation times.

The uncertainty on the average jump-Ea value for a jump type $\epsilon_{\text{jump-Ea}}$ is defined as:

$$\epsilon_{\text{jump-Ea}} = \epsilon_{\text{convergence}} + \epsilon_{\text{mean}}$$

and is typically of the order of 10-20 meV. The $\epsilon_{\text{jump-Ea}}$ and its components ϵ_{mean} and $\epsilon_{\text{convergence}}$ are tabulated for every jump type SI Table S3.3. The exact same procedure was applied to extract the jump-Ea values for ordered-Li₉S₃N from an AIMD simulation of an ordered-Li₉S₃N supercell (SI Table S3.4).

Supplementary Note 7: Jump-Ea values in ordered- versus disordered-Li₉S₃N

Differences in the jump activation energies for the same jump types in ordered and disordered Li₉S₃N suggest that the long-range anion-ordering in ordered-Li₉S₃N has an effect on the jump activation energy values in addition to the local N/S occupation of polyhedra and bottlenecks.

Table S3.14. Comparison of the jump-Ea values obtained for the jump types observable in ordered-Li₉S₃N from AIMD on ordered-Li₉S₃N and disordered-Li_{2+x}S_{1-x}N_x supercells.

Jump type	ordered		disordered	
	Average jump-Ea (eV)	$\epsilon_{\text{jump-Ea}}$ (eV)	Average jump-Ea (eV)	$\epsilon_{\text{jump-Ea}}$ (eV)
N ₁ S ₃ -N ₂ S ₄ (NSS)	0.431	0.005	0.402	0.004
N ₂ S ₄ -N ₁ S ₃ (NSS)	0.245	0.004	0.297	0.008
N ₁ S ₃ -S ₆ (SSS)	0.482	0.011	0.414	0.014
S ₆ -N ₁ S ₃ (SSS)	0.483	0.010	0.409	0.011
N ₁ S ₃ -N ₁ S ₃ (SS)	0.59*	0.015	0.488	0.01
N ₁ S ₃ -N ₁ S ₃ (NS)	0.472	0.011	0.477	0.011

Jump-Ea values depend on the occupancy of the ‘start’ and ‘end’ sites. Ordered-Li₉S₃N features 3 Li sites S₆, N₁S₃, N₂S₄. The former two sites are highly occupied, the latter N₂S₄ site is highest in energy and essentially unoccupied. The effect of long-range anion ordering on jump-Ea values will be discussed on the example of S₆ - N₁S₃(SSS) and N₁S₃-S₆(SSS) jumps.

The jump frequency for S₆ - N₁S₃(SSS) jumps depends on the low probability of N₁S₃ sites being vacant. In ordered Li₉S₃N vacant N₁S₃ sites may only be obtained by the unfavourable occupation of N₂S₄ sites⁷ and this effect increases the jump-Ea values of S₆ - N₁S₃(SSS) jumps —and by the same token increases jump-Ea values of N₁S₃-S₆(SSS) jumps since vacancies on S₆ may also only be obtained by N₂S₄ site occupation. In contrast in disordered Li₉S₃N supercells N₁S₃ sites are more likely to be vacant due to the presence of lower-energy octahedra that are more favourably occupied than N₂S₄ sites. This increased likelihood of a vacancy on a N₁S₃ site is reflected in higher S₆ - N₁S₃(SSS) jump-frequencies and thus lower jump-Ea values.

The diffusion-hampering effect of long-range anion-ordering on jump-Ea values may be observed by performing percolation analysis for ordered-Li₉S₃N with the jump-Ea values from disordered-Li₉S₃N. In Figure S3.22 the results from the main text (where the effect of long-range anion ordering is taken into account) are compared with the same analysis but applying the jump-Ea values from disordered-Li₉S₃N to ordered-Li₉S₃N. As shown in Figure S322d the onset is shifted up by 0.03 eV when considering the effect of long-range anion-ordering on jump-Ea values highlighting a Li-diffusion hampering effect of the anion-ordering in ordered-Li₉S₃N.

⁷ That is, essentially an energetically costly Frenkel-defect formation.

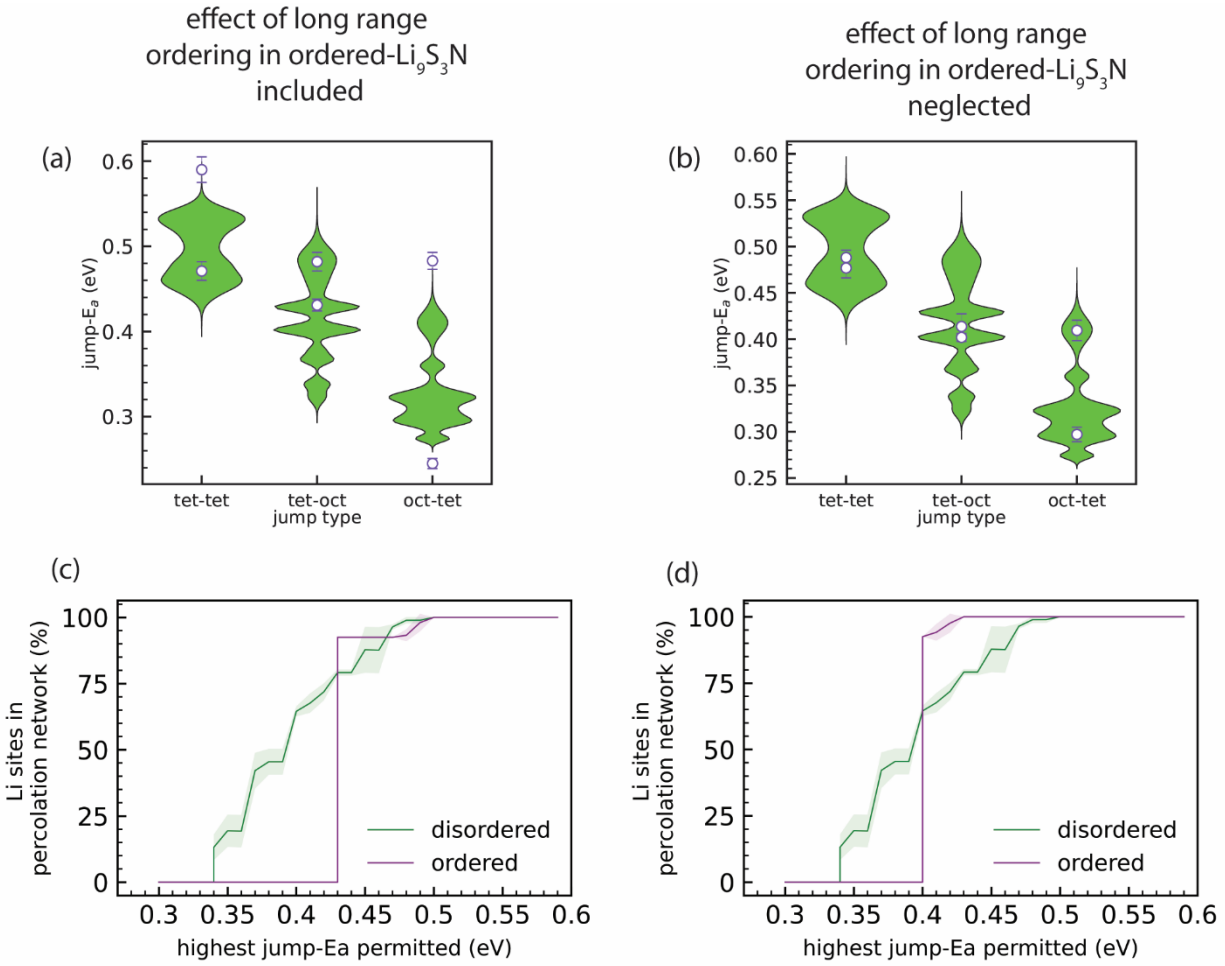


Figure S3.22. Effect of different jump-types existing in ordered and disordered $\text{Li}_9\text{S}_3\text{N}$. (a) and (b) Comparison of the observable jump-activation energies in ordered and disordered- $\text{Li}_9\text{S}_3\text{N}$. Purple markers indicate jump- E_a of six distinct jump types possible in ordered- $\text{Li}_9\text{S}_3\text{N}$, labelled with the *start-end(bottleneck)* notation explained in the main text. In disordered- $\text{Li}_9\text{S}_3\text{N}$ 91 different jumps are observable, listed in SI Table S3.3 and shown here as density plots (*violins*). The horizontal scale of the violins represent the relative occurrence of jump types at that energy. In (b) the jump- E_a values obtained for disordered- $\text{Li}_9\text{S}_3\text{N}$ were used. (c) and (d) Percolation-energy diagram showing the fraction of Li sites that are connected to percolating networks (averaged over 50 disordered $5 \times 5 \times 5$ supercells) for ordered- and disordered- $\text{Li}_9\text{S}_3\text{N}$. Shading is the standard deviation over 50 supercells. The vertical lines indicate the experimental activation energy $\text{E}_{a,\text{EIS}}$ obtained experimentally from EIS for ordered- and disordered- $\text{Li}_9\text{S}_3\text{N}$ (see Figure 3.2). In (d) the jump- E_a values obtained for disordered- $\text{Li}_9\text{S}_3\text{N}$ were used.

Supplementary Note 8: Additional details on the interpretation of percolation-energy diagrams

Energy-percolation diagrams enable to estimate a range within which the bulk-activation energy of a solid-electrolyte will lie provided two conditions are given:

- (1) The jump frequency between sites A and B exhibits Arrhenius behaviour to ensure validity of equation 1 from the main text
- (2) An accurate estimate of the ν_0 value is employed in equation 1 from the main text, and it should be estimated to what extent ν_0 varies across different sites in the phase.

If the above conditions are fulfilled the range of the bulk activation energy may be obtained as follows:

The experimental activation energy will be at the percolation-onset or above since the percolation onset presents the minimum energy threshold to be overcome for percolation. So far we can thus say that energy-percolation diagrams predict that the bulk activation energy will lie in the range [percolation-onset, ∞]. But the upper limit for the predicted bulk activation energy may potentially be further reined in as follows:

Diffusion through sites connected by 0.55 eV is negligible compared to diffusion through sites connected by 0.35 eV as diffusion through the latter is $>10^3$ times faster. However, diffusion through sites connected by jump-activation energies of 0.35 eV is only twice as fast as through sites connected by 0.36 eV. In case a percolation onset was at 0.35 eV, diffusion through sites connected by 0.36 eV would not be negligible and may contribute to the overall diffusion which in turn may increase the overall activation energy (i.e. the experimental activation energy) beyond the percolation onset. Accordingly the experimental activation energy may be above the percolation onset. However, contribution of sites diffusing 1 order of magnitude slower than the sites at the percolation-onset is likely negligible. At 300 K it takes an activation energy increase of 0.06 eV before the jump-frequency reduces by a factor 10 (this is independent of the attempt frequency ν_0 used, see Figure S3.23). Based on this analysis we propose that the experimental activation energy will likely be in the range [percolation-onset, percolation-onset+0.06 eV]. We highlight that this is only rough approach to obtain an estimate of the upper limit. However, the experimental activation energies obtained with EIS for different $\text{Li}_{2+x}\text{S}_{1-x}\text{N}_x$ phases fall well into the ranges that may be gauged from percolation-energy diagrams in this way:

Table S3.15. Predicted range of activation energy by percolation-energy analysis. The experimentally measured activation energies from EIS are in the said ranges.

x in $\text{Li}_{2+x}\text{S}_{1-x}\text{N}_x$	Experimental activation-energy-range predicted from percolation-energy diagrams (eV)	Measured activation energy (eV)
0.05	[0.43, 0.49]	0.47 ± 0.01
0.1	[0.40, 0.46]	0.45 ± 0.01
0.2	[0.37, 0.43]	0.40 ± 0.01
0.25	[0.34, 0.4]	0.39 ± 0.01
0.45	[0.31, 0.37]	0.38 ± 0.01

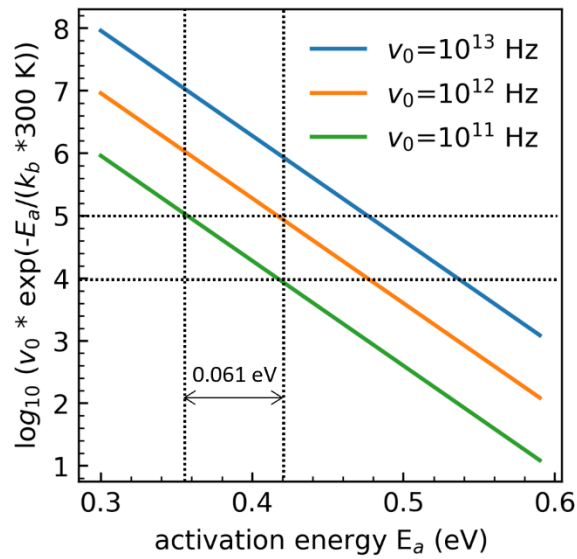


Figure S3.23. Evaluation of jump frequencies at different activation energies for different attempt frequencies v_0 . The point of this figure is to illustrate that the jump-frequency drops by a factor 10 if the activation energy is increased by 0.061 independent of the choice of the attempt frequency.

Supplementary Note 9: Application of MD-percolation methodology on $\text{Li}_6\text{PS}_5\text{Br}$

To establish the wide applicability of the methodology developed to analyse disordered solid electrolytes, we investigate the $\text{Li}_6\text{PS}_5\text{Br}$ argyrodite system. $\text{Li}_6\text{PS}_5\text{Br}$ crystallizes in the cubic $F\bar{4}3m$ space group (216), as depicted in Figure S3.24. In this structure, lithium ions typically occupy the T5 (Wyckoff 48h), T2 (Wyckoff 48h), and T4 (Wyckoff 16e) ref(16–21) sites. Here, for the sake of simplicity, only the T5 (Wyckoff 48h) and T4 (Wyckoff 16e) sites were considered.

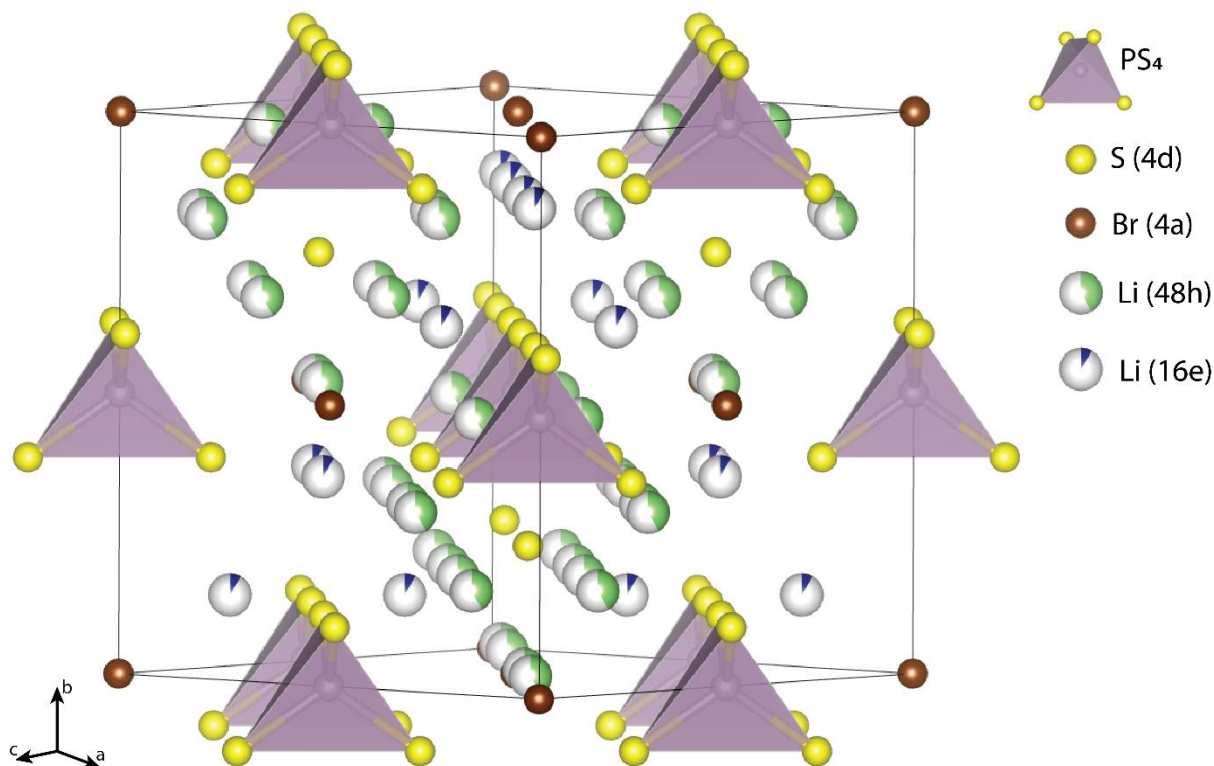


Figure S24. Ordered crystal structure of $\text{Li}_6\text{PS}_5\text{Br}$ (0% S/Br-site inversion), where Br^- ions are located at the Wyckoff 4a positions and S^{2-} ions (not bonded to P^{5+}) occupy the Wyckoff 4d positions. The anion framework forms 136 interstitial tetrahedral voids per unit cell, suitable for cation occupancy. Four of these voids are filled by P^{5+} cations at the Wyckoff 4b site, forming PS_4^{3-} tetrahedra. The remaining 132 tetrahedral voids can accommodate lithium⁹. Lithium sites Wyckoff 48h and Wyckoff 16e, which are considered in the current study, are presented.

Lithium ions distributed across the Wyckoff 48h positions form a cage-like substructure encircling the 4d site, while the Wyckoff 16e positions are located between these cages (Figure S3.24). This configuration defines three types of Li-ion movements: doublet, intracage, and intercage jumps.¹⁹ Doublet jumps occur between paired 48h sites (distance 1.9 Å), and intracage jumps occur between pairs of 48h sites (distance 2.25 Å) within a cage. The intercage jumps, which are essential for long-range lithium-ion diffusion, occur between the cages via the 48h–16e–48h pathways.

The coordination of 48h and 16e tetrahedra for each jump type is depicted in Figure S3.25a. The 48h tetrahedra (in green) are formed by two S^{2-} ions (corner-shared with PS_4 tetrahedra in violet) and two anions at the 4a and 4d sites, respectively. 16e sites (in blue) are coordinated by three S^{2-} ions (also corner-shared with PS_4 tetrahedra in violet) and one anion at the 4a site. Due to the similar ionic radii of bromine

and sulfur ions, they can exchange positions and occupy both 4a and 4d sites (Figure S3.25a). This introduces site disorder in the structure and creates different local environments that affect lithium mobility.

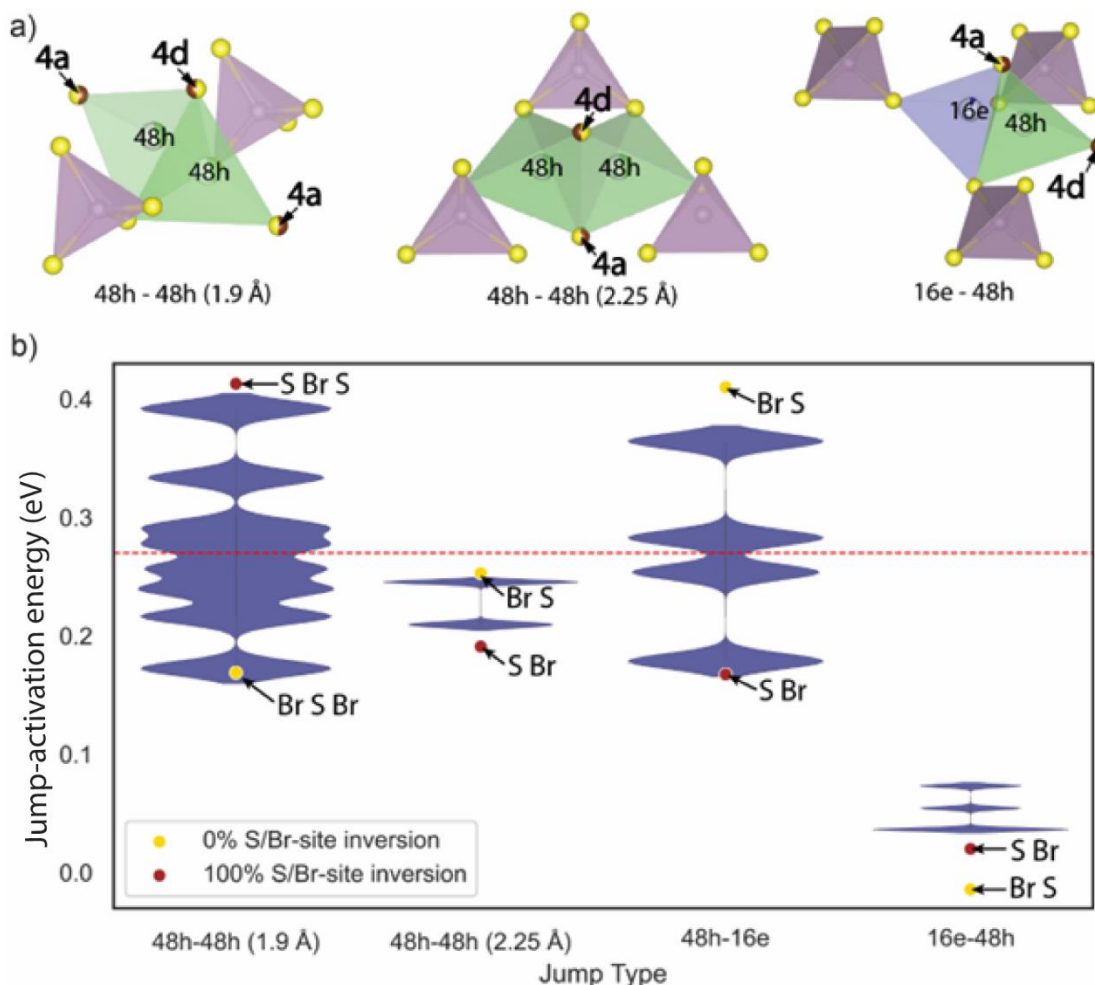


Figure S3.25. Impact of sulfur/bromine local environments on jump activation energy. a) Illustration of the coordination of 48h and 16e tetrahedra for each jump type, where the 4a and 4d sites used for jump environment nomenclature are shown as partially occupied by sulfur and bromine (half-yellow, half-red dots) and highlighted by arrows. b) Comparison of jump activation energies per possible jump environment within $\text{Li}_6\text{PS}_5\text{Br}$ composition, calculated from AIMD at 900 K. Yellow and red solid dot markers indicate the jump activation energies for $\text{Li}_6\text{PS}_5\text{Br}$ (0% S/Br-site inversion) and $\text{Li}_6\text{PS}_5\text{Br}$ (100% S/Br-site inversion), respectively. Jump local environments are labelled with the “4a 4d 4a” notation for 48h–48h (1.9 Å) doublet jumps and “4a 4d” notation for 48h–48h (2.25 Å) intracage, 48h–16e, and 16e–48h jumps, as explained in the main text. The average jump activation energy, calculated across eight $\text{Li}_6\text{PS}_5\text{Br}$ 2x1x1 supercells with different site disorder (Table S3.16), is shown in blue as “violins”. The width of the violins represents the relative occurrence of each jump local environment at that energy in $\text{Li}_6\text{PS}_5\text{Br}$ (50% S/Br-site inversion) structure.

In analogy to the study of $\text{Li}_{2+x}\text{S}_{1-x}\text{N}_x$, we calculate jump- E_a from the jump-frequency $\nu_{A \rightarrow B}$ between sites, segregated by local environment:

$$\text{jump } E_{a,A \rightarrow B} = -k_b T \ln \left(\frac{\nu_{A \rightarrow B}}{\nu_0} \right) \quad (\text{S6})$$

where k_b is the Boltzmann constant, T the temperature in K, $\nu_{A \rightarrow B}$ the observed frequency of jumps between sites A and B, jump- $E_{a,A \rightarrow B}$ the jump-activation energy⁸ of a jump event from site A to site B and ν_0 the attempt frequency.

We investigated the impact of the local jump environment created by the distribution of bromine and sulfur across the 4a and 4d sites on the Li-ion transport and jump activation energy by examining AIMD simulations of eight configurations of the $\text{Li}_6\text{PS}_5\text{Br}$ composition, each having different S and Br distributions on these sublattices (Table S3.16). The structure set was chosen to ensure multiple repetitions of each possible anionic environment and to obtain reliable statistics. The average activation energy for each type of jump across the different local environments is depicted in Figure S3.25b. To characterize a local jump environment, we label the anions occupying the 4a and 4d positions of the start site and the 4a position of the end site in 48h–48h (1.9 Å) doublet jumps, as both 48h sites share the same 4d position but differ in 4a positions (Figure S3.25a). For 48h–48h (2.25 Å) intracage, 48h–16e, and 16e–48h jumps, the labels include the anions occupying the 4a and 4d positions since both the start and the end sites share the same environment (Figure S3.25a).

In the ordered configurations of $\text{Li}_6\text{PS}_5\text{Br}$ (0% and 100% S/Br-site inversion), distinct jump activation energies were observed, with only one possible jump local environment per jump type. Similar to the ordered- $\text{Li}_9\text{S}_3\text{N}$ structure, both ordered configurations of $\text{Li}_6\text{PS}_5\text{Br}$ do not exhibit low-energy percolating paths⁹. To illustrate this, we take the example of a jump activation energy of 0.3 eV (Figure S3.25b). $\text{Li}_6\text{PS}_5\text{Br}$ with 0% S/Br-site inversion does not feature 48h-16e jump with activation energy < 0.3 eV, while $\text{Li}_6\text{PS}_5\text{Br}$ with 100% S/Br-site inversion does not feature 48h-48h (1.9 Å) jump with activation energy < 0.3 eV. The

⁸ Note: Care needs to be taken on how to interpret the jump- E_a . If the jump frequency exhibits Arrhenius behavior and if the exact attempt frequency is known then the jump- E_a represents the ‘time-averaged’ energy-barrier for the transitions between sites A and B. If the jump frequencies do not follow an Arrhenius law and/or a good estimate of ν_0 cannot be obtained then the jump- E_a is “merely” an arbitrary rescaling of the jump-frequency. In such cases jump- E_a values are not time-average energy barriers but still allow to identify diffusion-promoting and diffusion-hampering local environments. In both cases, percolation-energy diagrams may be calculated. In both cases percolation onsets at lower energies indicate the possibility of a phase to feature faster Li-diffusion typically correlated with higher Li-conductivities. In $\text{Li}_6\text{PS}_5\text{Br}$, the jump-frequencies in Li-argyrodites are likely governed by an Arrhenius law since the experimental bulk conductivity (which consists of individual Li-transitions/“jumps”) follows an Arrhenius law.²² For the present example we will assume $\nu_0 = 1 \cdot 10^{13}$ Hz in all sites and will not further investigate possibly existing variations of ν_0 in different sites. We will interpret the jump- E_a values in this study as “rescaled jump-frequencies” which enable to identify diffusion-promoting and diffusion-hampering local environments and are thus not concerned with the exact value of ν_0 . Nonetheless we would like to highlight that the choice of $\nu_0 = 1 \cdot 10^{13}$ Hz is not unreasonable and may be a good approximation: The attempt frequency for a material may be estimated from the oscillations of the Li-ions and for the 8 $\text{Li}_6\text{PS}_5\text{Br}$ supercells on which we performed AIMD simulations ν_0 values of 8.67, 8.63, 8.4, 8.23, 8.39, 8.29, 8.39 and 7.96 GHz were obtained.

⁹ Note: **Figure S3.21** contains negative jump- E_a values which may at first be perplexing but we would like to highlight again that for this study we interpret the jump- E_a “merely” as rescaled jump-frequencies. A negative jump- E_a thus signifies a high jump-frequency for the 16e-48h jump. As a general note, such high jump-frequencies between positions may occur if the start position is not a site (i.e. not a minimum on the energy landscape). For the present study this would suggest that the 16e position is not a site for the cases of 100% and 0% inversion of occupation between 4a and 4d sites.

inability to perform either a 48h–16e or a 48h–48h (1.9 Å) jump prevents macroscopic diffusion of lithium. Thus, in both cases, no percolating path exists with an activation energy below 0.3 eV.

In contrast to ordered configurations, the disordered arrangement of S/Br creates a variation of jump local environments, enabling low-energy pathways. To investigate the effect of S/Br-site disorder on lithium percolation network, we generated $\text{Li}_6\text{PS}_5\text{Br}$ with 50% S/Br-site inversion which encounters every possible jump local environment with equal probability, as depicted by the width of the violin plot in Figure S3.25b. $\text{Li}_6\text{PS}_5\text{Br}$ with 50% S/Br-site inversion exhibits local environments with jump activation energy < 0.3 eV for each jump type. Thus, similar to disordered- $\text{Li}_9\text{S}_3\text{N}$, in disordered $\text{Li}_6\text{PS}_5\text{Br}$ with 50% S/Br-site inversion, percolating paths with jump activation energy < 0.3 eV may exist.

To further investigate the role of S/Br local arrangements in the macroscopic diffusion of lithium, we employed a percolation model as was done in the main text for disordered- $\text{Li}_9\text{S}_3\text{N}$. We created structures of $\text{Li}_6\text{PS}_5\text{Br}$ with 0% S/Br-site inversion and $\text{Li}_6\text{PS}_5\text{Br}$ with 100% S/Br-site inversion, both without site disorder, as well as $\text{Li}_6\text{PS}_5\text{Br}$ with 50% S/Br-site inversion, with bromine equally distributed across the 4a and 4d sites, in a 5x5x5 supercell. The results of our percolation analysis are demonstrated in Figure S3.26.

Figures S3.26a and b show that for $\text{Li}_6\text{PS}_5\text{Br}$ with 0% and 100% S/Br-site inversion, respectively, no percolating path exists when the cutoff jump energy is set to 0.3 eV. Connections are formed only within the isolated cages with no possibility of long-range lithium diffusion. In contrast, in the case of $\text{Li}_6\text{PS}_5\text{Br}$ with 50% S/Br-site inversion, a percolation network is observed with the same cutoff jump energy of 0.3 eV (Figure S3.26c). Approximately 70% of sites participate in percolation, while some sites remain disconnected from the percolation network and require higher energy to become accessible.

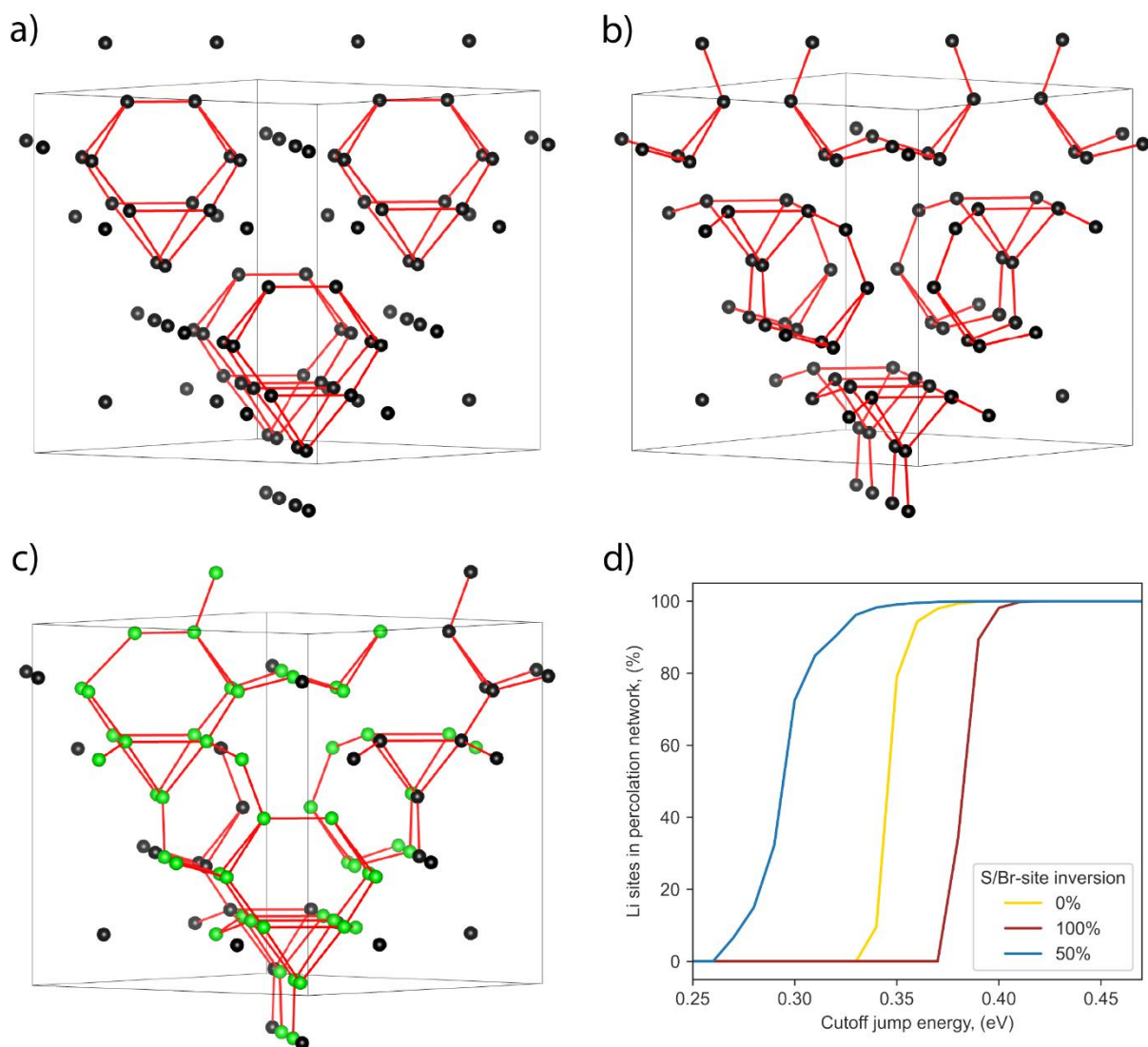


Figure S3.26. Analysis of percolation network in $\text{Li}_6\text{PS}_5\text{Br}$. Connected sites within the 0.3 eV cutoff jump energy (in the forward and backward direction) are indicated in red. The sites highlighted in green participate in percolation, while the sites highlighted in black are not connected to the percolation network. a) Every possible lithium jump in $\text{Li}_6\text{PS}_5\text{Br}$ (0% S/Br-site inversion) with a cutoff jump energy of 0.3 eV. No percolation observed. b) Every possible lithium jump in $\text{Li}_6\text{PS}_5\text{Br}$ (100% S/Br-site inversion) with a cutoff jump energy of 0.3 eV. No percolation observed. c) Every possible lithium jump in $\text{Li}_6\text{PS}_5\text{Br}$ (50% S/Br-site inversion) with a cutoff jump energy of 0.3 eV. Around 70% of sites are connected to the percolation network. d) Energy-percolation diagram showing the fraction of Li sites connected to a percolating network for $\text{Li}_6\text{PS}_5\text{Br}$ (0% S/Br-site inversion) in yellow, $\text{Li}_6\text{PS}_5\text{Br}$ (100% S/Br-site inversion) in red, and $\text{Li}_6\text{PS}_5\text{Br}$ (50% S/Br-site inversion) in blue (averaged over twenty $5 \times 5 \times 5$ supercells with sulfur and bromine randomly distributed), as detailed in the Computational Details section.

Figure S3.26d shows the fraction of lithium sites connected to a percolating network as a function of cutoff energy value. For both ordered structures $\text{Li}_6\text{PS}_5\text{Br}$ (0% S/Br-site inversion) and $\text{Li}_6\text{PS}_5\text{Br}$ (100% S/Br-site inversion), percolation becomes possible only with cutoff energy values higher than the corresponding average activation energy of the rate-limiting jumps: 48h–16e at 0.36 ± 0.04 eV and 48h–48h (1.9 Å) at 0.39 ± 0.04 eV, respectively (**Table S3.15**). In contrast, for the $\text{Li}_6\text{PS}_5\text{Br}$ (50% S/Br-site inversion) structure, percolation is possible with a cutoff energy of 0.27 eV, where all types of jumps (48h–48h, 1.9 Å; 48h–48h, 2.25 Å; 48h–16e; and 16e–48h) are available according to local environment-specific jump activation energies (Figure 3.25b, highlighted by the red dashed line).

The findings from the percolation model suggest that while both low-energy and high-energy local environments appear in the ordered variants, $\text{S}^{2-}/\text{Br}^-$ disorder across both sublattices enables percolation through $\text{Li}_6\text{PS}_5\text{Br}$ by striking a balance between the three jump-types needed for percolation. This disorder introduces a range of activation energies, thereby facilitating the formation of percolating pathways at lower energy thresholds. This investigation thus reveals what local environments enable fast Li-diffusion and how these local environments need to be connected to enable long-scale fast diffusivity. The lower onset for 50% site-inversion suggests that faster Li-diffusivity is possible compared to 0% site-inversion which correlates with the larger conductivity of $\text{Li}_6\text{PS}_5\text{Br}$ phases with increasing site-inversion (i.e. increasing Br occupation on 4d sites) shown e.g. in ref.²². The percolation energy diagrams however suggest, that this trend is not monotonous, the percolation-energy diagrams predict that in the case of 100% sites inversion the ability of $\text{Li}_6\text{PS}_5\text{Br}$ is similar to 0% site-inversion (this may however not be verified experimentally as samples with 100% site-inversion cannot be synthesized).

Table S3.16. The activation energies associated with different lithium ion jump types and environments within Li₆PS₅Br structures, showcasing variations across samples with different degrees of site disorder and ordering. These values are calculated from AIMD simulations conducted at 900 K.

Jump Type	Jump Environment			0% S/Br-site inversion	12% S/Br-site inversion		38% S/Br-site inversion				100% S/Br-site inversion	Average	Standard Deviation
	4a	4d	4a	(1)	(1)	(2)	(1)	(2)	(3)	(4)	(1)		
48h–48h (1.9 Å)	Br	S	Br	0.169	0.176	0.172	0.167	0.176	0.171	0.176		0.172	0.003
	Br	S	S		0.214	0.219	0.203	0.215	0.218	0.216		0.214	0.005
	S	S	Br		0.238	0.241	0.230	0.237	0.240	0.239		0.237	0.004
	Br	Br	Br		0.282	0.244	0.245	0.261	0.247	0.263		0.257	0.013
	S	S	S				0.278	0.279	0.252	0.284		0.274	0.012
	Br	Br	S		0.284		0.311	0.293	0.282	0.274		0.289	0.013
	S	Br	Br		0.334		0.347	0.336	0.321	0.321		0.332	0.010
	S	Br	S				0.383	0.411	0.367	0.390	0.413	0.393	0.018
48h–48h (2.25 Å)	Br	Br			0.199	0.217	0.202	0.206	0.216	0.209		0.208	0.007
	S	Br			0.211		0.205	0.213	0.221	0.219	0.191	0.210	0.010
	Br	S		0.253	0.257	0.253	0.238	0.244	0.243	0.245		0.247	0.007
	S	S			0.251	0.247	0.251	0.252	0.241	0.245		0.248	0.004
48h–16e	S	Br			0.181		0.181	0.178	0.191	0.176	0.167	0.179	0.007
	Br	Br			0.278	0.263	0.242	0.268	0.245	0.256		0.259	0.013
	S	S			0.300	0.302	0.257	0.275	0.277	0.289		0.283	0.016
	Br	S		0.410	0.400	0.383	0.342	0.346	0.342	0.360		0.369	0.026
16e–48h	S	Br			0.041		0.048	0.042	0.048	0.027	0.020	0.038	0.010
	Br	Br			0.059	0.042	0.022	0.047	0.032	0.030		0.039	0.012
	Br	S		-0.014	0.033	0.030	0.058	0.056	0.084	0.059		0.044	0.029
	S	S			0.065	0.005	0.074	0.092	0.068	0.083		0.064	0.028

Computational details for the $\text{Li}_6\text{PS}_5\text{Br}$ example

Density functional theory (DFT) calculations based on the Perdew–Burke–Ernzerhof functional for solid-state systems (PBEsol)²³ within the Vienna Ab initio Software Package (VASP 6.3.2)²⁴ were utilized. Projector augmented wave (PAW)²⁵ potentials were used with cores of [He] for Li, [Ne] for P and S, and [Ar] for Br. Structure optimizations were conducted with an energy cutoff of 340 eV in 2x1x1 argyrodite supercells.

Ab initio molecular dynamics (AIMD) simulations in the canonical (NVT) ensemble using the Nosé-Hoover thermostat^{26,27} were performed at 900 K. The energy cutoff was reduced to 300 eV, and gamma-only k-point mesh was used. The selected time step was 2 fs for a total computational time of 150 ps. Site-sensitive properties such as site-specific jump frequencies, and energy barriers were obtained using the analysis tools developed in our group.^{28,29} To analyze the individual jumps, we defined two types of Li positions in the crystal lattice, namely, Wyckoff 48h and Wyckoff 16e (ref.³⁰), counting the times Li resides in these positions throughout the simulation as well as the number of hops between these positions.

Four argyrodite structures $\text{Li}_6\text{PS}_5\text{Br}$ were generated labelled by percentage of site inversion. Among these, $\text{Li}_6\text{PS}_5\text{Br}$ (12% S/Br-site inversion) and $\text{Li}_6\text{PS}_5\text{Br}$ (38% S/Br-site inversion) structures reflect the sublattice disorder, corresponding to experimentally determined site occupancies of sulfur and bromine²². These specific structures were selected to validate computational results by published experimental data. Since multiple orderings of S and Br in the sublattices can result in the same site occupancy, several unique configurations with random distribution of sulfur and bromine across 4a and 4d were optimized for both structures. Additionally, two configurations of $\text{Li}_6\text{PS}_5\text{Br}$ exhibiting perfect order in the anionic sublattice, where bromine fully occupies 4a (0% S/Br-site inversion) or 4d (100% S/Br-site inversion) sites, were studied.

To analyze Li-ion jump activation energy specific to the local environments of sulfur and bromine, we examined AIMD simulations at 900 K for eight selected supercells: $\text{Li}_6\text{PS}_5\text{Br}$ (0% S/Br-site inversion), two configurations of $\text{Li}_6\text{PS}_5\text{Br}$ (12% S/Br-site inversion), four configurations of $\text{Li}_6\text{PS}_5\text{Br}$ (38% S/Br-site inversion), and $\text{Li}_6\text{PS}_5\text{Br}$ (100% S/Br-site inversion). These configurations had different S and Br distributions on the 4a and 4d sublattices, encompassing every possible local environment for each type of jump. Local environment-specific activation energies for all eight configurations are presented in Table S3.16.

For percolation analysis, we generated structures of $\text{Li}_6\text{PS}_5\text{Br}$ (0% S/Br-site inversion), $\text{Li}_6\text{PS}_5\text{Br}$ (100% S/Br-site inversion), and $\text{Li}_6\text{PS}_5\text{Br}$ (50% S/Br-site inversion) in a 5x5x5 supercell using the pymatgen library³¹ (version 2023.11.12). For $\text{Li}_6\text{PS}_5\text{Br}$ (50% S/Br-site inversion), twenty configurations with random arrangements of sulfur and bromine across the 4a and 4d sublattices were generated. For each configuration, the percolation model was applied with twenty iterations. In each iteration, an environment-specific activation energy was randomly selected within ± 0.04 eV from the average values listed in Table S3.16. This random selection accounts for the uncertainty in the activation energy values. The average results across all iterations and configurations per structure are analysed.

Supplementary Note 10: Discussions on the Arrhenius prefactor of $\text{Li}_{2+x}\text{S}_{1-x}\text{N}_x$ phases

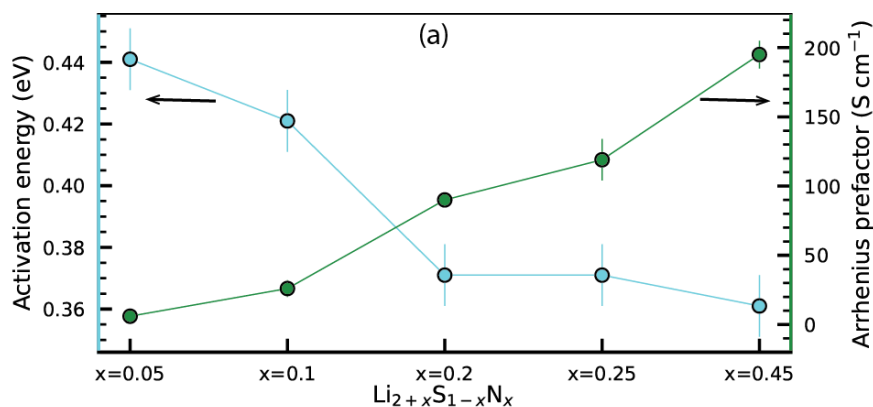


Figure S3.27 . Evolution of the Arrhenius prefactor and the activation energy obtained from EIS at variable temperatures for $\text{Li}_{2+x}\text{S}_{1-x}\text{N}_x$ phases.

With increasing Nitrogen content the experimental activation energy decreases in $\text{Li}_{2+x}\text{S}_{1-x}\text{N}_x$ phases but the Arrhenius prefactor increases. In the following we will discuss the possible origin of this observation

Based on the Nernst-Einstein relation and the definition of hop diffusivity, the Arrhenius prefactor (σ_0) can be written as shown in Equation S3.6³².

$$\sigma_0 = \frac{\gamma a_0^2 v_0 (Ze)^2}{k} c_{ion} \exp\left(\frac{-\Delta S_m}{k}\right) \quad (\text{S3.6})$$

where γ is a geometrical factor, a_0 the average jump distance between sites, (Ze) the charge of the diffusing ion, v_0 the attempt frequency, k the Boltzmann constant, ΔS_m the entropy of migration and c_{ion} the charge-carrier concentration.

Our analysis reported in Supplementary Note 4 indicate that changes in the attempt are unlikely to explain the **18-fold** increase in σ_0 that we observe experimentally. Similarly a_0 which only changes slightly with nitrogen content.

Different physical expressions have been proposed for ΔS_m .^{33–35} While ΔS_m remains ill-defined and no consensus is established on which relation is correct, the **existing** expressions for ΔS_m **unanimously** suggest that ΔS_m decreases with decreasing activation energy (ΔH_m), which amount to the enthalpy-entropy *compensation rule*, aka the *Meyer-Neldel rule* in the context of ion conduction.^{35–37} The latter is typically demonstrated as a linear correlation between the measured (logarithm of the) conductivity prefactor ($\ln(\sigma_0) \propto \Delta S_m$) and activation energy ($E_a \propto \Delta H_m$) in a given structural framework; which is exactly the opposite of the trend we are observing in $\text{Li}_{2+x}\text{S}_{1-x}\text{N}_x$.

Thus, either the Meyer-Neldel rule does not hold in the $\text{Li}_{2+x}\text{S}_{1-x}\text{N}_x$ sample series, or there are differences in the mobile charge-carrier concentration that could explain the evolution of the prefactor with nitrogen content (x). The latter could be linked to the idea of active (percolating) versus inactive (non-percolating) lithium sites, explored in the manuscript.

Supplementary Note 11: Chemical and Electrochemical Characterization of $\text{Li}_{2+x}\text{S}_{1-x}\text{N}_x$

To prove the stability of $\text{Li}_{2+x}\text{S}_{1-x}\text{N}_x$ against Li metal, we added Li metal to an excess of $\text{Li}_{2.3}\text{S}_{0.7}\text{N}_{0.3}$ and ground both substances together vigorously for 20 minutes. We use $\text{Li}_{2.3}\text{S}_{0.7}\text{N}_{0.3}$ as a representative of the antifluorite-like $\text{Li}_{2+x}\text{S}_{1-x}\text{N}_x$ solid solution. Figure S3.28a shows the X-ray diffraction pattern of $\text{Li}_{2.3}\text{S}_{0.7}\text{N}_{0.3}$ and Figure S3.28b shows the X-ray diffraction pattern of the $\text{Li}_{2.3}\text{S}_{0.7}\text{N}_{0.3}$ -Li- metal mixture. $\text{Li}_{2.3}\text{S}_{0.7}\text{N}_{0.3}$ was chosen as a representative of the antifluorite-like $\text{Li}_{2+x}\text{S}_{1-x}\text{N}_x$ ($0 < x < 0.55$) solid solution. No change in the diffraction pattern indicative of reductive decomposition of $\text{Li}_{2.3}\text{S}_{0.7}\text{N}_{0.3}$ may be observed in the $\text{Li}_{2.3}\text{S}_{0.7}\text{N}_{0.3}$ -Li metal mixture. Diffraction peaks attributable to Li metal are observed in the diffraction pattern of the $\text{Li}_{2.3}\text{S}_{0.7}\text{N}_{0.3}$ -Li metal mixture indicating that that Li metal does not chemically react with $\text{Li}_{2.3}\text{S}_{0.7}\text{N}_{0.3}$.

To exclude the presence of amorphous decomposition products, we measured XPS (Figure S3.28c, d) of $\text{Li}_{2.3}\text{S}_{0.7}\text{N}_{0.3}$ and of the $\text{Li}_{2.3}\text{S}_{0.7}\text{N}_{0.3}$ -Li metal mixture. No new peaks or peak-shifts to lower energies (as would be expected for a reductive decomposition of $\text{Li}_{2.3}\text{S}_{0.7}\text{N}_{0.3}$) can be observed in the S 2p and N 1s XPS spectra of the $\text{Li}_{2.3}\text{S}_{0.7}\text{N}_{0.3}$ -Li metal mixture again indicating the stability of $\text{Li}_{2.3}\text{S}_{0.7}\text{N}_{0.3}$ against Li metal. These experiments prove the stability of $\text{Li}_{2+x}\text{S}_{1-x}\text{N}_x$ phases against Li metal.

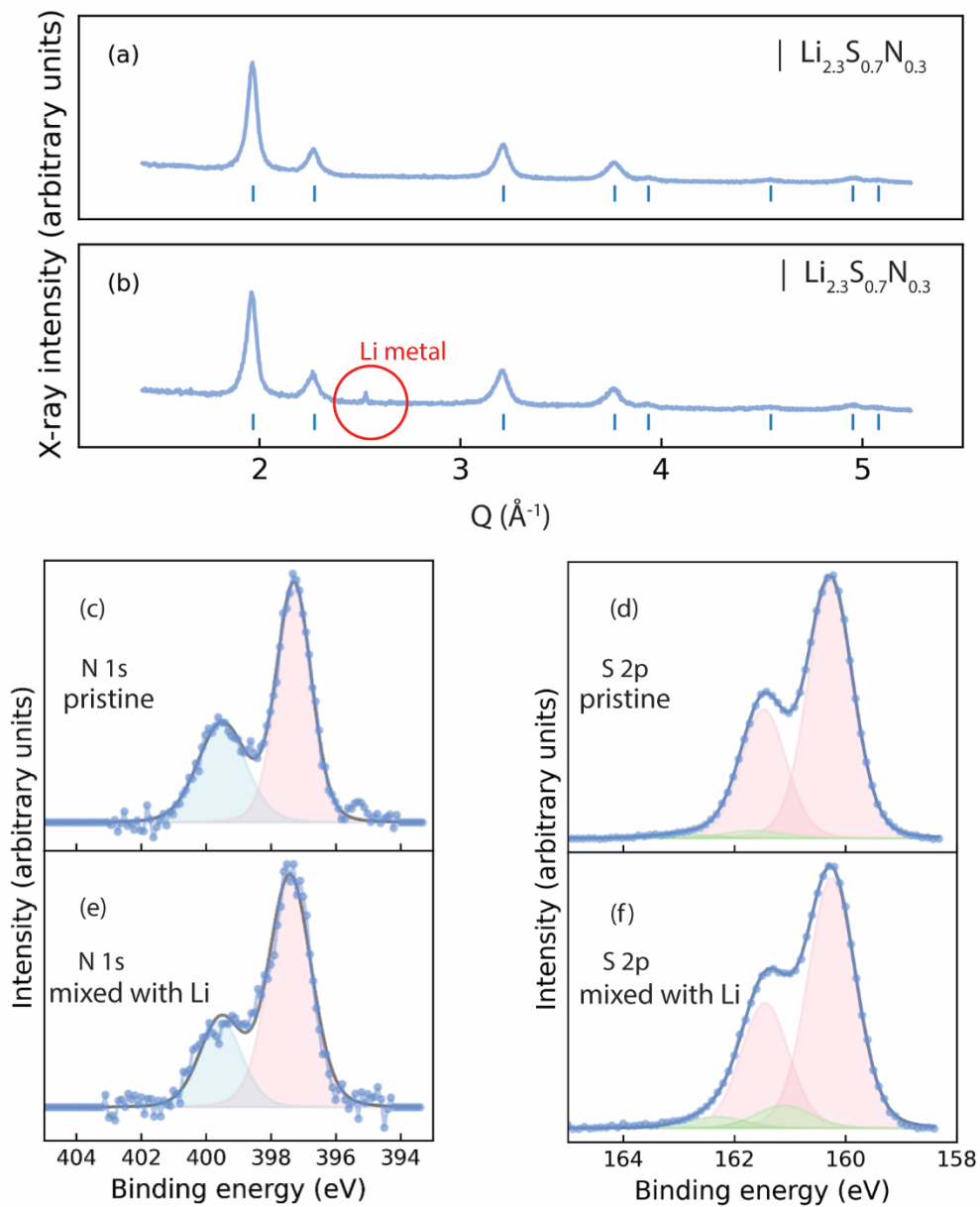


Figure S3.28. Investigation of chemical stability of the $\text{Li}_{2.3}\text{S}_{0.7}\text{N}_{0.3}$ phases against Li metal as a representative of the $\text{Li}_{2+x}\text{S}_{1-x}\text{N}_x$ phases. (a) X-ray diffraction pattern of $\text{Li}_{2.3}\text{S}_{0.7}\text{N}_{0.3}$ phases. (b) X-ray diffraction pattern of $\text{Li}_{2.3}\text{S}_{0.7}\text{N}_{0.3}$ vigorously mixed with Li metal. No decomposition product visible. Red circle indicates the strongest peak of the Li-metal diffraction pattern and thus indicates the presence of Li-metal. (c) N 1s XPS of $\text{Li}_{2.3}\text{S}_{0.7}\text{N}_{0.3}$. (d) N 1s XPS of $\text{Li}_{2.3}\text{S}_{0.7}\text{N}_{0.3}$ vigorously mixed with Li metal. No new peak or increase in relative peak intensities at lower energies which would be indicative of reductive decomposition. (e) S 2p XPS of $\text{Li}_{2.3}\text{S}_{0.7}\text{N}_{0.3}$. (f) S 2p XPS of $\text{Li}_{2.3}\text{S}_{0.7}\text{N}_{0.3}$ vigorously mixed with Li metal. No new peak or increase in relative peak intensities at lower energies which would be indicative of reductive decomposition.

We repeated the same experiments with $\text{Li}_6\text{PS}_5\text{Cl}$ instead of $\text{Li}_{2.3}\text{S}_{0.7}\text{N}_{0.3}$, to highlight the contrast between the intrinsic stability of fully reduced (irreducible) $\text{Li}_{2+x}\text{S}_{1-x}\text{N}_x$ phases and state of the art argyrodites solid electrolytes Figure S3.29. During grinding of $\text{Li}_6\text{PS}_5\text{Cl}$ with Li-metal a vigorous reaction occurred, including observations of a flame (in the glovebox). The XRD of the $\text{Li}_6\text{PS}_5\text{Cl}$ -lithium mixture clearly shows reduction products of $\text{Li}_6\text{PS}_5\text{Cl}$ (LiCl , Li_2S) and the XPS of the $\text{Li}_6\text{PS}_5\text{Cl}$ -lithium mixture shows clear reduction peaks.

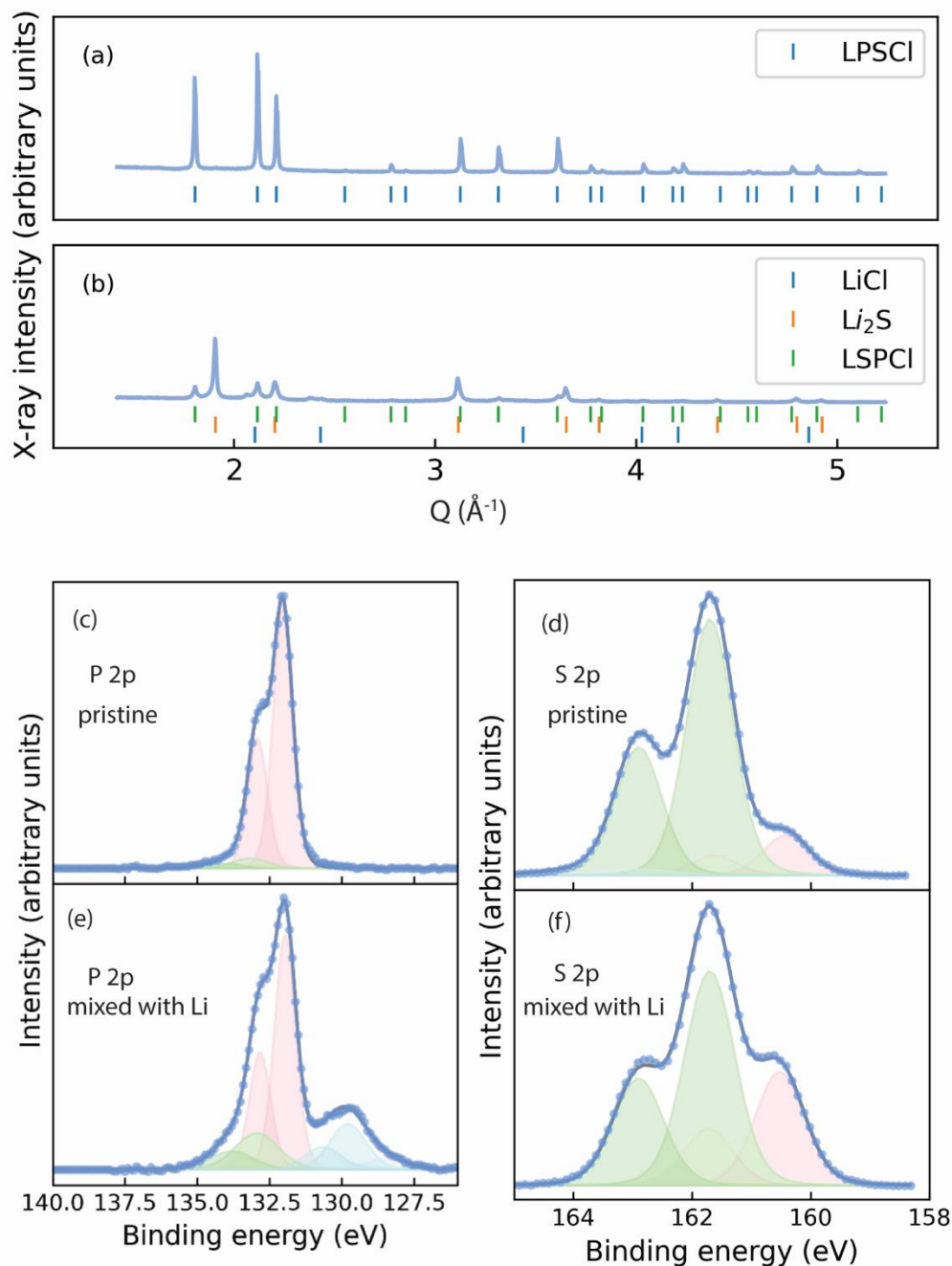


Figure S3.29. (a) Investigation of chemical stability of the LPSCl phases against Li metal to prove effectiveness of the approach to detect decomposition against Li metal. (a) X-ray diffraction pattern of LPSCl phases. (b) X-ray diffraction pattern of LPSCl vigorously mixed with Li metal. No decomposition product visible. Red signal indicates the strongest peak of the Li-metal diffraction pattern. (c) P2p XPS of LPSCl. (d) P2p XPS of LPSCl vigorously mixed with Li metal. Clear reductive peaks at low energies can be observed. (e) S2p XPS of LPSCl (f) S2p XPS of LPSCl vigorously mixed with Li metal. Clear reductive peaks at low energies can be observed.

So far we proved chemical stability of the $\text{Li}_{2+x}\text{S}_{1-x}\text{N}_x$ phases against metallic Li. Chemical stability against Li metal is equivalent to electrochemical stability at 0V (i.e. electrochemical stability against Li-metal) for the following reason based on ref³⁸:

Chemical stability means that no reaction exists where

$$a * \Delta G_{f,LSN} + n * \mu_{\text{Li,Li-metal}} = \sum c_i \Delta G_{f,i} \quad \Delta_r G < 0 \quad (\text{S3.7})$$

In equation (S3.7) $\Delta G_{f,LSN}$ stands for the Gibbs free energy of formation of an arbitrary $\text{Li}_{2+x}\text{S}_{1-x}\text{N}_x$ ($0 < x < 0.55$) phase, $\mu_{\text{Li,Li-metal}}$ is the chemical potential of Li in Li metal, a , n and c_i are arbitrary stoichiometric factors and i is a possible reaction product between an arbitrary $\text{Li}_{2+x}\text{S}_{1-x}\text{N}_x$ ($0 < x < 0.55$) phase and Li metal.

Electrochemical stability means that no reaction exists between the material of interest and a lithium repository where lithium is at a chemical potential of

$$\mu_{\text{Li,repository}} = \mu_{\text{Li,Li-metal}} - \Phi e \quad (\text{S3.8})$$

where Φ is an arbitrary potential (vs Li/Li⁺). In other words electrochemical stability at a potential Φ (vs Li/Li⁺) means that no reaction exists where

$$a * \Delta G_{f,LSN} + n * (\mu_{\text{Li,Li-metal}} - \Phi e) = \sum c_i \Delta G_{f,i} \quad \Delta_r G < 0 \quad (\text{S3.9})$$

It can be seen that equation S3.7 and equation S3.9 are the same at a potential $\Phi = 0$ V vs Li/Li⁺. It follows from this that electrochemical stability at 0 V vs Li is equivalent to chemical stability against Li-metal and *vice versa*.

Moreover we proved the stability of $\text{Li}_{2+x}\text{S}_{1-x}\text{N}_x$ ($0 < x < 0.55$) against Li metal by cycling $\text{Li} | \text{Li}_{2.25}\text{S}_{0.75}\text{N}_{0.25} | \text{Li}$ symmetric cells showing no voltage increase that would suggest decomposition for 1000 h of cycling (Figure S3.30a). Additionally, we show that $\text{Li}_{2+x}\text{S}_{1-x}\text{N}_x$ ($0 < x < 0.55$) phases may be used to protect solid-electrolytes such as the Li_2ZrCl_6 electrolyte for example against Li-metal (Figure S3.30b). Figure S3.30b shows a rapid increase of the voltage in $\text{Li} | \text{Li}_2\text{ZrCl}_6 | \text{Li}$ cells indicative of solid-electrolyte decomposition against lithium. No such increase is seen when the Li_2ZrCl_6 is protected with $\text{Li}_{2.25}\text{S}_{0.75}\text{N}_{0.25}$.

While relatively stable over time (compared to the decomposing Li_2ZrCl_6 case) the voltage profile of the $\text{Li} | \text{Li}_{2.25}\text{S}_{0.75}\text{N}_{0.25} | \text{Li}$ cell (Figure S3.30) still shows an evolution. At the beginning the overpotential decreased and then slightly increases over time. Without further investigations, the reasons for this evolution of the voltage profile remain speculative. But the following hypothesis can be made. The reduction in the overpotential may come from Li-metal protruding into the pellet because of inhomogeneous plating; this could lower the overpotential in two ways. (1) Protruding Li-metal would result in an increased electrochemically active area which (at a constant applied current) would result in a lower current density and hence result in a lower overpotential. (2) Protruding Li-metal would effectively reduce the pellet thickness and hence contribute to a lower pellet-resistance. The subsequent increase in the overpotential could be due to small leakages in our solid-state cells enabling partial decomposition of the materials in the cell-interior by atmospheric moisture which in turn could increase the overall cell resistance.

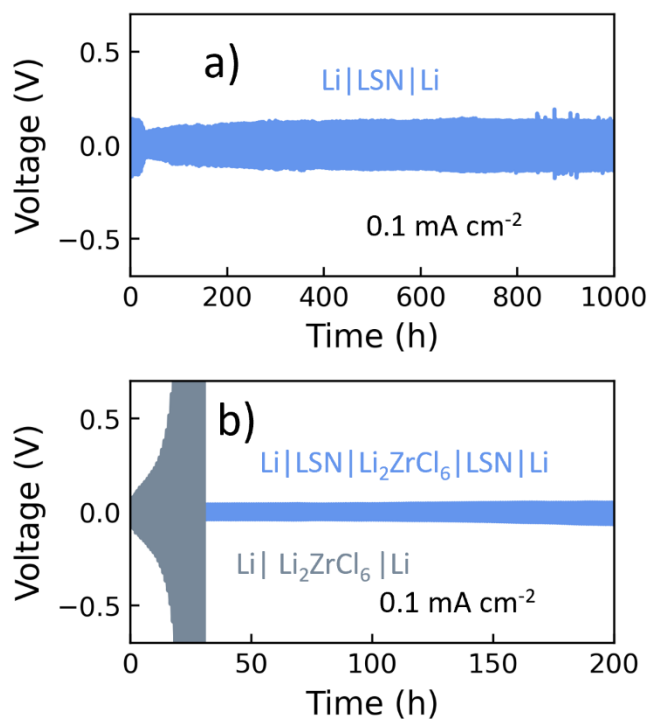


Figure S3.30. Cycling profiles of symmetric cells. (a) $\text{Li}|\text{Li}_{2.25}\text{S}_{0.75}\text{N}_{0.25}|\text{Li}$ symmetric cell 0.1 mA cm^{-2} for $0.05 \text{ mA h cm}^{-2}$. (b) A protected cell $\text{Li}|\text{Li}_{2.25}\text{S}_{0.75}\text{N}_{0.25}|\text{Li}_2\text{ZrCl}_6|\text{Li}_{2.25}\text{S}_{0.75}\text{N}_{0.25}|\text{Li}$ cell and an unprotected cell (grey trace) $\text{Li}|\text{Li}_2\text{ZrCl}_6|\text{Li}$ cell 0.1 mA cm^{-2} for $0.05 \text{ mA h cm}^{-2}$. Protecting Li_2ZrCl_6 against Li with $\text{Li}_{2.25}\text{S}_{0.75}\text{N}_{0.25}$ highly improves the cycling performance and eliminates the catastrophic voltage increase caused by the decomposition of Li_2ZrCl_6 . LSN in the legend stands for $\text{Li}_{2.25}\text{S}_{0.75}\text{N}_{0.25}$.

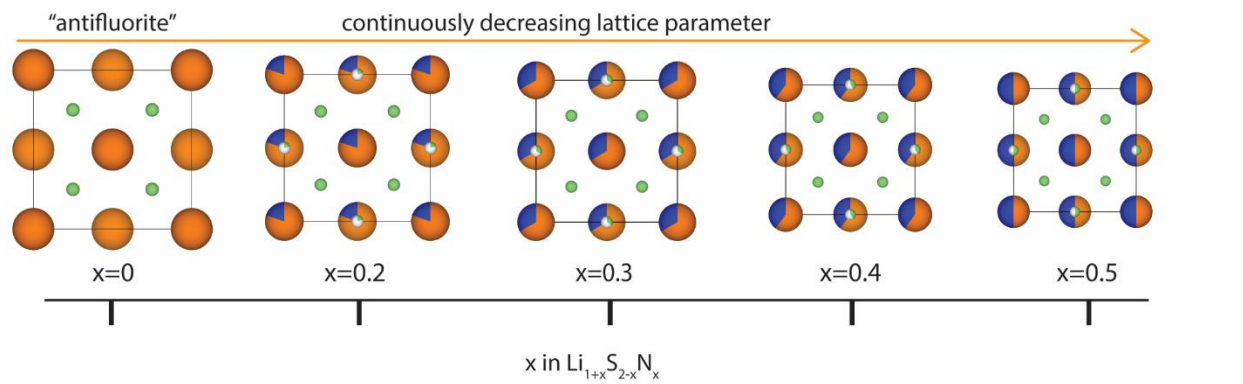
Methodology for Supplementary Note 11: XPS: Measurements were performed with a ThermoFisher K-Alpha spectrometer to investigate the chemical state of the elements present. The spectrometer is equipped with a focused monochromatic Al $\text{K}\alpha$ source (1486.6 eV) anode operating at 36W (12 kV, 3mA), a flood gun operating at 1V, 100 μA , and the base pressure in the analysis chamber is approximately 2×10^{-9} mbar. The spot-size is approximately $800 \times 400 \mu\text{m}^2$. The pass energy of the analyzer was set to 50 eV. In the analysis, the binding energy was corrected for the charge shift by taking the done relative to the primary C1s hydrocarbon peak at $BE = 284.8 \text{ eV}$ as a reference. The peaks were fitted using 70% Gaussian and 30% Lorentzian line shapes (weighted least-squares fitting method) and nonlinear Shirley-type background using the ThermoFisher Avantage software. *Cell assembly symmetric cells:* Symmetric cells were assembled custom-made slid state cells by pressing 60 mg of Li_2ZrCl_6 at 1 ton (on 10 mm diameter). Subsequently 20 mg LSN were added on each side and pressed at 2.7 tons. Subsequently 100 μm Li disks were placed on each side. The custom made solid state cells were then tightened by hand which applies $\sim 5 \text{ MPa}$ of pressure during cycling. *X-ray Diffraction:* Powder diffraction patterns were collected using Cu $\text{K}\alpha$ X-rays (1.54 \AA) on a PANalytical X'Pert Pro X-ray diffractometer. The air sensitive $\text{Li}_{2+x}\text{S}_{1-x}\text{N}_x$ probes were loaded into air-tight holders in an Ar-filled glovebox prior to the measurements.

References Appendix 2

- (1) Marx, R.; Lissner, F.; Schleid, T. $\text{Li}_9\text{N}_2\text{S}_3$: Das Erste Nitridsulfid Der Alkalimetalle in Einer Li_2O -Typ-Variante. *Zeitschrift für Anorg. und Allg. Chemie* **2006**, *632* (12-13), 2151.
- (2) Szczuka, C.; Karasulu, B.; Groh, M. F.; Sayed, F. N.; Sherman, T. J.; Bocarsly, J. D.; Vema, S.; Menkin, S.; Emge, S. P.; Morris, A. J.; Grey, C. P. Forced Disorder in the Solid Solution $\text{Li}_3\text{P-Li}_2\text{S}$: A New Class of Fully Reduced Solid Electrolytes for Lithium Metal Anodes. *J. Am. Chem. Soc.* **2022**, *144* (36), 16350–16365.
- (3) Shannon, R. D. Revised Effective Ionic Radii and Systematic Studies of Interatomic Distances in Halides and Chalcogenides. *Acta Crystallogr. Sect. A Cryst. physics, diffraction, Theor. Gen. Crystallogr.* **1976**, *32* (5), 751–767.
- (4) Dong, Y.; DiSalvo, F. J. Reinvestigation of Trilithium Phosphide, Li_3P . *Acta Crystallogr. Sect. E Struct. Reports Online* **2007**, *63* (4), i97–i98.
- (5) Van der Ven, A.; Ceder, G.; Asta, M.; Tepesch, P. D. First-Principles Theory of Ionic Diffusion with Nondilute Carriers. *Phys. Rev. B* **2001**, *64* (18), 184307.
- (6) Almond, D. P.; Duncan, G. K.; West, A. R. The Determination of Hopping Rates and Carrier Concentrations in Ionic Conductors by a New Analysis of Ac Conductivity. *Solid State Ionics* **1983**, *8* (2), 159–164.
- (7) Wang, Z.; Mishra, T. P.; Xie, W.; Deng, Z.; Gautam, G. S.; Cheetham, A. K.; Canepa, P. Kinetic Monte Carlo Simulations of Sodium Ion Transport in NaSICON Electrodes. *ACS Mater. Lett.* **2023**, *5* (9), 2499–2507.
- (8) Deng, Z.; Mishra, T. P.; Mahayoni, E.; Ma, Q.; Tieu, A. J. K.; Guillon, O.; Chotard, J.-N.; Seznec, V.; Cheetham, A. K.; Masquelier, C. Fundamental Investigations on the Sodium-Ion Transport Properties of Mixed Polyanion Solid-State Battery Electrolytes. *Nat. Commun.* **2022**, *13* (1), 4470.
- (9) De Klerk, N. J. J.; Van Der Maas, E.; Wagemaker, M. Analysis of Diffusion in Solid-State Electrolytes through MD Simulations, Improvement of the Li-Ion Conductivity in $\beta\text{-Li}_3\text{PS}_4$ as an Example. *ACS Appl. Energy Mater.* **2018**, *1* (7), 3230–3242.
- (10) Li, X.; Liu, H.; Zhao, C.; Kim, J. T.; Fu, J.; Hao, X.; Li, W.; Li, R.; Chen, N.; Cao, D.; Wu, Z.; Su, Y.; Liang, J.; Sun, X. Hopping Rate and Migration Entropy as the Origin of Superionic Conduction within Solid-State Electrolytes. *J. Am. Chem. Soc.* **2023**, *145* (21), 11701–11709.
- (11) Kraft, M. A.; Culver, S. P.; Calderon, M.; Böcher, F.; Krauskopf, T.; Senyshyn, A.; Dietrich, C.; Zevalkink, A.; Janek, J.; Zeier, W. G. Influence of Lattice Polarizability on the Ionic Conductivity in the Lithium Superionic Argyrodites $\text{Li}_6\text{PS}_5\text{X}$ (X= Cl, Br, I). *J. Am. Chem. Soc.* **2017**, *139* (31), 10909–10918.
- (12) Rice, M. J.; Roth, W. L. Ionic Transport in Super Ionic Conductors: A Theoretical Model. *J. Solid State Chem.* **1972**, *4* (2), 294–310.
- (13) Morgan, B. J. Mechanistic Origin of Superionic Lithium Diffusion in Anion-Disordered $\text{Li}_6\text{PS}_5\text{X}$ Argyrodites. *Chem. Mater.* **2021**, *33* (6), 2004–2018.
- (14) He, X.; Zhu, Y.; Mo, Y. Origin of Fast Ion Diffusion in Super-Ionic Conductors. *Nat. Commun.* **2017**, *8* (May), 1–7.
- (15) Catlow, C. R. A. STATIC LATTICE SIMULATION OF STRUCTURE AND TRANSPORT IN SUPERIONIC CONDUCTORS. *Solid State Ionics* **1983**, *8* (SUPPL. 3), 89–107.
- (16) Gautam, A.; Sadowski, M.; Ghidui, M.; Minafra, N.; Senyshyn, A.; Albe, K.; Zeier, W. G. Engineering the Site-Disorder and Lithium Distribution in the Lithium Superionic Argyrodite $\text{Li}_6\text{PS}_5\text{Br}$. *Adv. Energy Mater.* **2021**, *11* (5).
- (17) Zhao, E.; He, L.; Zhang, Z.; Doux, J.-M.; Tan, D. H. S.; Wu, E. A.; Deysher, G.; Chen, Y.-T.; Zhao, J.; Wang, F. New Insights into Li Distribution in the Superionic Argyrodite $\text{Li}_6\text{PS}_5\text{Cl}$. *Chem. Commun.* **2021**, *57* (82), 10787–10790.
- (18) Zhou, L.; Minafra, N.; Zeier, W. G.; Nazar, L. F. Innovative Approaches to Li-Argyrodite Solid Electrolytes for All-Solid-State Lithium Batteries. *Acc. Chem. Res.* **2021**, *54* (12), 2717–2728.
- (19) De Klerk, N. J. J.; Rostół, I.; Wagemaker, M. Diffusion Mechanism of Li Argyrodite Solid Electrolytes for Li-Ion Batteries and Prediction of Optimized Halogen Doping: The Effect of Li Vacancies, Halogens, and Halogen Disorder. *Chem. Mater.*

- 2016, 28 (21), 7955–7963.
- (20) Zhou, L.; Zhang, Q.; Nazar, L. F. Li-Rich and Halide-Deficient Argyrodite Fast Ion Conductors. *Chem. Mater.* **2022**, 34 (21), 9634–9643.
- (21) Hogrefe, K.; Minafra, N.; Hanghofer, I.; Banik, A.; Zeier, W. G.; Wilkening, H. M. R. Opening Diffusion Pathways through Site Disorder: The Interplay of Local Structure and Ion Dynamics in the Solid Electrolyte $\text{Li}_{6+x}\text{P}_{1-x}\text{Ge}_x\text{S}_{51}$ as Probed by Neutron Diffraction and NMR. *J. Am. Chem. Soc.* **2022**, 144 (4), 1795–1812.
- (22) Gautam, A.; Al-Kutubi, H.; Famprikis, T.; Ganapathy, S.; Wagemaker, M. Exploring the Relationship Between Halide Substitution, Structural Disorder, and Lithium Distribution in Lithium Argyrodites ($\text{Li}_6\text{-XPS}_5\text{-XBr}_{1+x}$). *Chem. Mater.* **2023**, 35 (19), 8081–8091.
- (23) Perdew, J. P.; Burke, K.; Ernzerhof, M. Generalized Gradient Approximation Made Simple. *Phys. Rev. Lett.* **1996**, 77 (18), 3865.
- (24) Kresse, G.; Furthmüller, J. Efficiency of Ab-Initio Total Energy Calculations for Metals and Semiconductors Using a Plane-Wave Basis Set. *Comput. Mater. Sci.* **1996**, 6 (1), 15–50.
- (25) Blöchl, P. E. Projector Augmented-Wave Method. *Phys. Rev. B* **1994**, 50 (24), 17953.
- (26) Nosé, S. A Unified Formulation of the Constant Temperature Molecular Dynamics Methods. *J. Chem. Phys.* **1984**, 81 (1), 511–519.
- (27) Hoover, W. G. Canonical Dynamics: Equilibrium Phase-Space Distributions. *Phys. Rev. A* **1985**, 31 (3), 1695.
- (28) De Klerk, N. J. J.; Van Der Maas, E.; Wagemaker, M. Analysis of Diffusion in Solid-State Electrolytes through MD Simulations, Improvement of the Li-Ion Conductivity in $\beta\text{-Li}_3\text{PS}_4$ as an Example. *ACS Appl. Energy Mater.* **2018**, 1 (7), 3230–3242.
- (29) Azizi, V.; Smeets, S.; Lavrinenko, A. K.; Ciarella, S.; Famprikis, T. GEMDAT. Zenodo July 2024.
- (30) Kong, S.; Deiseroth, H.; Reiner, C.; Gün, Ö.; Neumann, E.; Ritter, C.; Zahn, D. Lithium Argyrodites with Phosphorus and Arsenic: Order and Disorder of Lithium Atoms, Crystal Chemistry, and Phase Transitions. *Chem. Eur. J.* **2010**, 16 (7), 2198–2206.
- (31) Ong, S. P.; Richards, W. D.; Jain, A.; Hautier, G.; Kocher, M.; Cholia, S.; Gunter, D.; Chevrier, V. L.; Persson, K. A.; Ceder, G. Python Materials Genomics (Pymatgen): A Robust, Open-Source Python Library for Materials Analysis. *Comput. Mater. Sci.* **2013**, 68, 314–319.
- (32) Tilley, R. J. D. *Defects in Solids*; John Wiley & Sons, 2008.
- (33) Wert, C.; Zener, C. Interstitial Atomic Diffusion Coefficients. *Phys. Rev.* **1949**, 76 (8), 1169–1175.
- (34) Dienes, G. J. Frequency Factor and Activation Energy for the Volume Diffusion of Metals. *J. Appl. Phys.* **1950**, 21 (11), 1189–1192.
- (35) Almond, D. P.; West, A. R. The Activation Entropy for Transport in Ionic Conductors. *Solid State Ionics* **1987**, 23 (1–2), 27–35.
- (36) Gao, Y.; Li, N.; Wu, Y.; Yang, W.; Bo, S. H. Rethinking the Design of Ionic Conductors Using Meyer–Neldel–Conductivity Plot. *Adv. Energy Mater.* **2021**, 11 (13), 1–9.
- (37) Du, P.; Zhu, H.; Braun, A.; Yelon, A.; Chen, Q. Entropy and Isokinetic Temperature in Fast Ion Transport. *Adv. Sci.* **2024**, 11 (2), 1–8.
- (38) Zhu, Y.; He, X.; Mo, Y. First Principles Study on Electrochemical and Chemical Stability of Solid Electrolyte-Electrode Interfaces in All-Solid-State Li-Ion Batteries. *J. Mater. Chem. A* **2016**, 4 (9), 3253–3266.

Appendix 3: Supporting information for chapter 4



T S4.1. Schematic illustration of the solid solution existing on the $\text{Li}_2\text{S}-\text{Li}_3\text{N}$ tie line, that is the $\text{Li}_{2+x}\text{S}_{1-x}\text{N}_x$ phases reported in ref ¹.

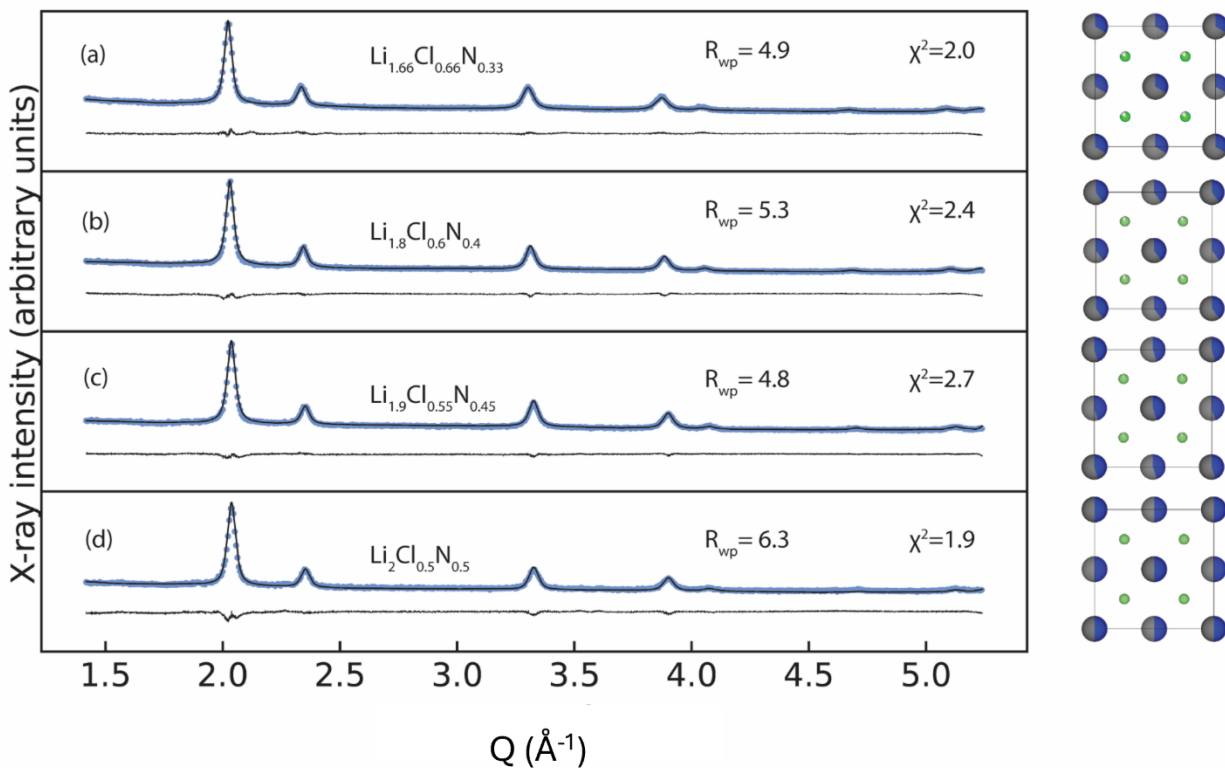


Figure S4.2. Rietveld refinements of the X-ray diffraction patterns of different $\text{Li}_{1+2x}\text{S}_{1-x}\text{N}_x$ phases along with an illustration of the respective structure solutions on the right. (a) $x=0.33$, (b) $x=0.4$, (c) $x=0.45$, (d) $x=0.5$.

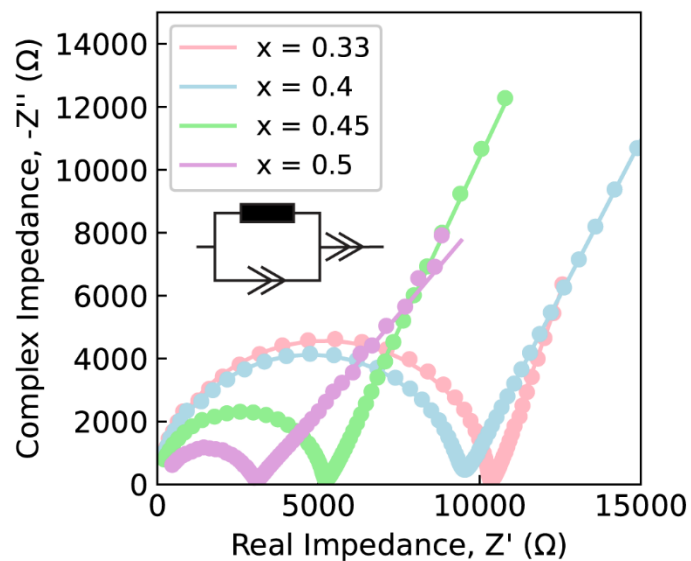


Figure S4.3. Room temperature electrochemical impedance spectroscopy (EIS) of different $\text{Li}_{1+2x}\text{Cl}_{1-x}\text{N}_x$ phases. The equivalent circuit fitted is shown in the inset of the figure.

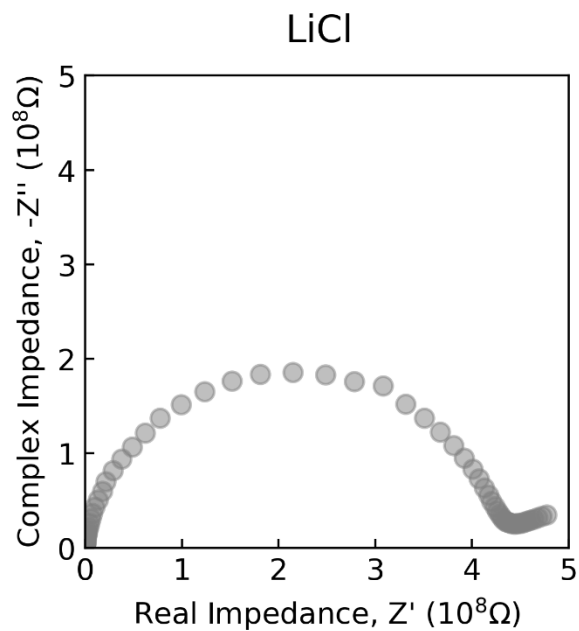


Figure S4.4. Room temperature electrochemical impedance spectroscopy (EIS) of different LiCl phase. For 1 mm thick pellet this corresponds to a conductivity on the order of $1 \cdot 10^{-10} \text{ S cm}^{-1}$.

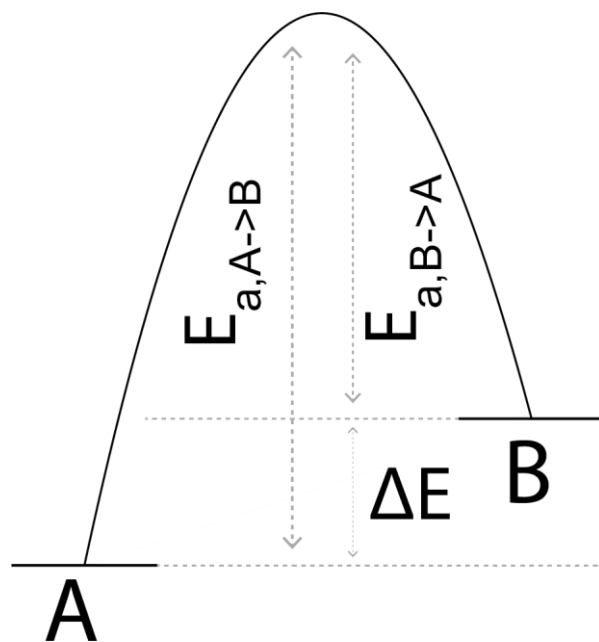


Figure S4.5. Schematic of the energy profile for a Li ion jump from site A to site B. This figure demonstrates that if $E_{a,A \rightarrow B} > E_{a,B \rightarrow A}$ then site A is more stable than site B by ΔE .

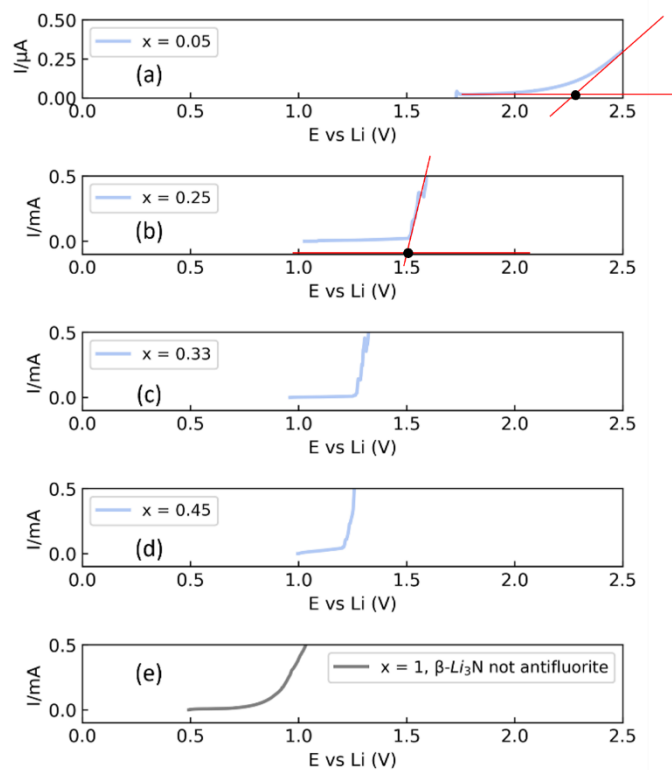


Figure S4.6. LSV of $\text{Li}/\text{Li}_{2+x}\text{S}_{1-x}\text{N}_x/\text{Li}_{2+x}\text{S}_{1-x}\text{N}_x\text{-C}$ cells and of a $\text{Li}/\text{Li}_3\text{N}/\text{Li}_3\text{N-C}$ cell. We show that increasing the nitrogen content progressively decreases the oxidation limit. Scan rate 0.01 mV s^{-1} . The red lines in (a) and (b) show how the oxidation onset is obtained from the LSV measurements. We accord an uncertainty of $\pm 0.1 \text{ V}$ to the onsets determined in this way. The red lines are only shown for (a) and (b) but this approach was adopted to all LSV measurements.

Oxidation window of $Li_{1+2x}Cl_{1-x}N_x$ phases

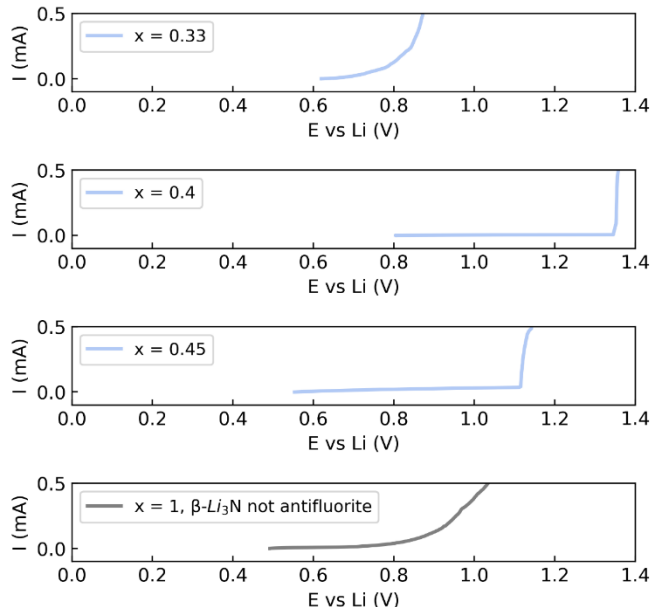


Figure S4.7. LSV of $Li/Li_{1+2x}Cl_{1-x}N_x/ Li_{1+2x}Cl_{1-x}N_x-C$ cells and of a $Li/Li_3N/ Li_3N-C$ cell. We show that there is a discontinuous trend. Increasing the nitrogen content from $x=0.33$ to $x=0.4$ increases the oxidation limit. Further increasing the N content decreases the oxidation limit increasing the nitrogen content progressively decreases the oxidation limit. This may be explained by the increasing metastability of the Li-deficient antifluorite $Li_{1+2x}Cl_{1-x}N_x$ phases at both the upper-N and lower-N boundary of the solid solution. Scan rate 0.01 mV s^{-1} . The oxidation onsets were determined following the approach shown in Figure S4.6 (a) and (b).

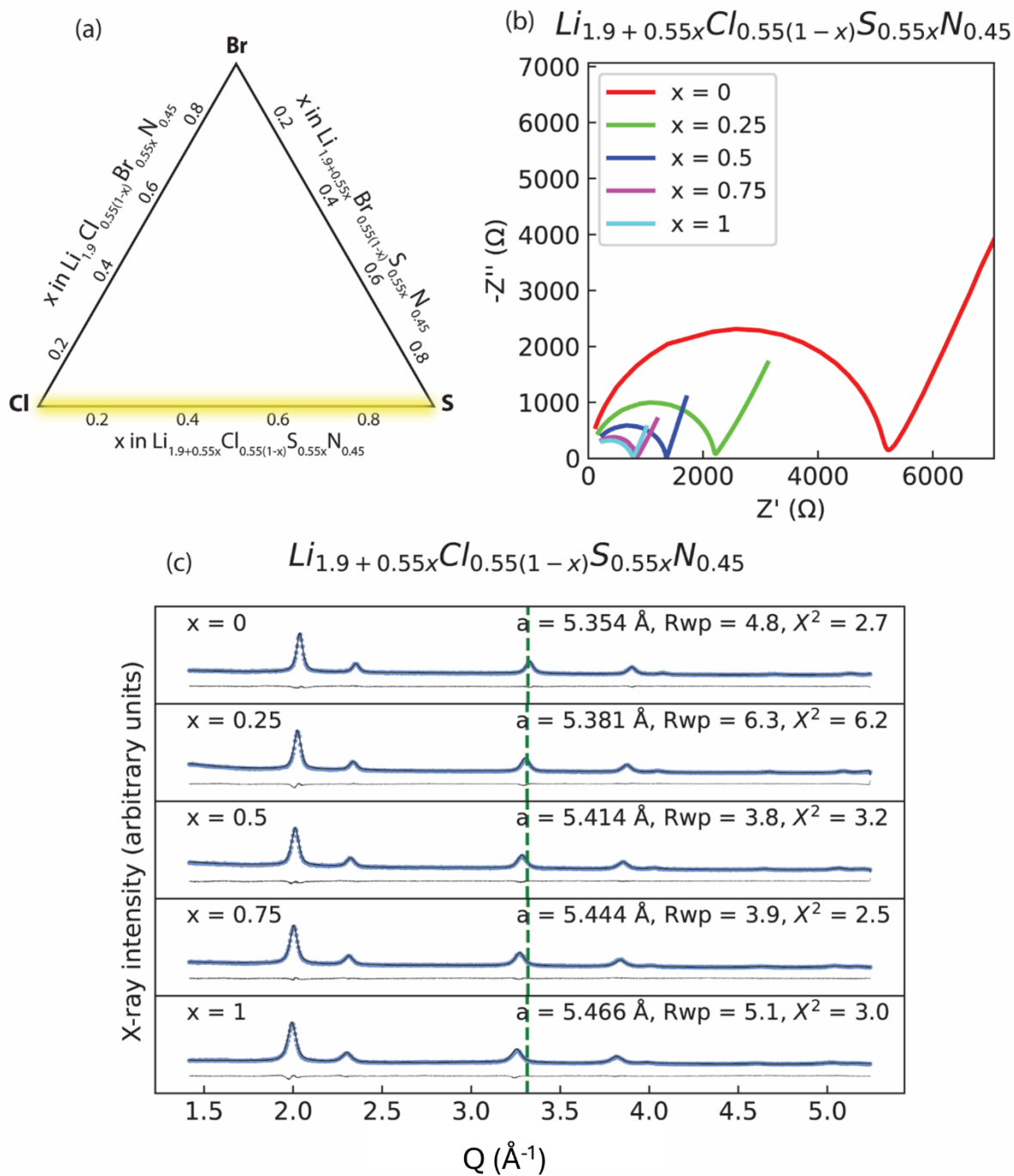


Figure S4.8. (a) highlighting which phases are shown in “b” and “c”. (b) Room temperature electrochemical impedance spectroscopy (EIS) of different $\text{Li}_{1.9+0.55x}\text{Cl}_{0.55(1-x)}\text{S}_{0.55x}\text{N}_{0.45}$ phases. (c) X-ray diffraction pattern and Rietveld refinements of the different phases $\text{Li}_{1.9+0.55x}\text{Cl}_{0.55(1-x)}\text{N}_{0.45}$. Dotted green line is guide to the eye to easily see the peak shift originating from different lattice parameters.

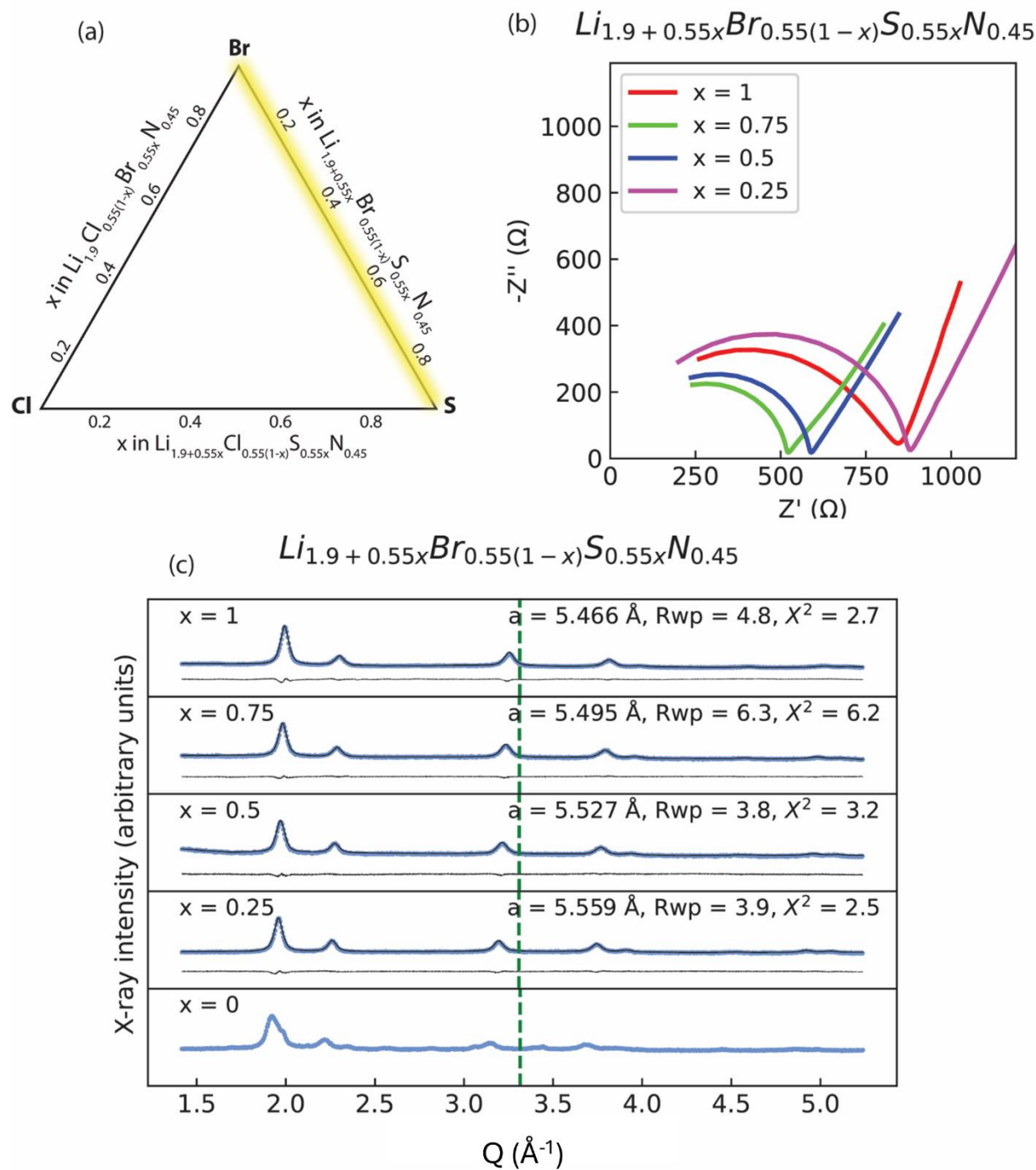


Figure S4.9. (a) highlighting which phases are shown in “b” and “c”. (b) Room temperature electrochemical impedance spectroscopy (EIS) of different $Li_{1.9+0.55x}Br_{0.55(1-x)}S_{0.55x}N_{0.45}$ phases. (c) X-ray diffraction pattern and Rietveld refinements of the different phases $Li_{1.9+0.55x}Br_{0.55(1-x)}N_{0.45}$. At $x=0$ an impure phase was obtained. The antifluorite structure can thus not be stabilized at this composition. Dotted green line is guide to the eye to easily see the peak shift originating from different lattice parameters.

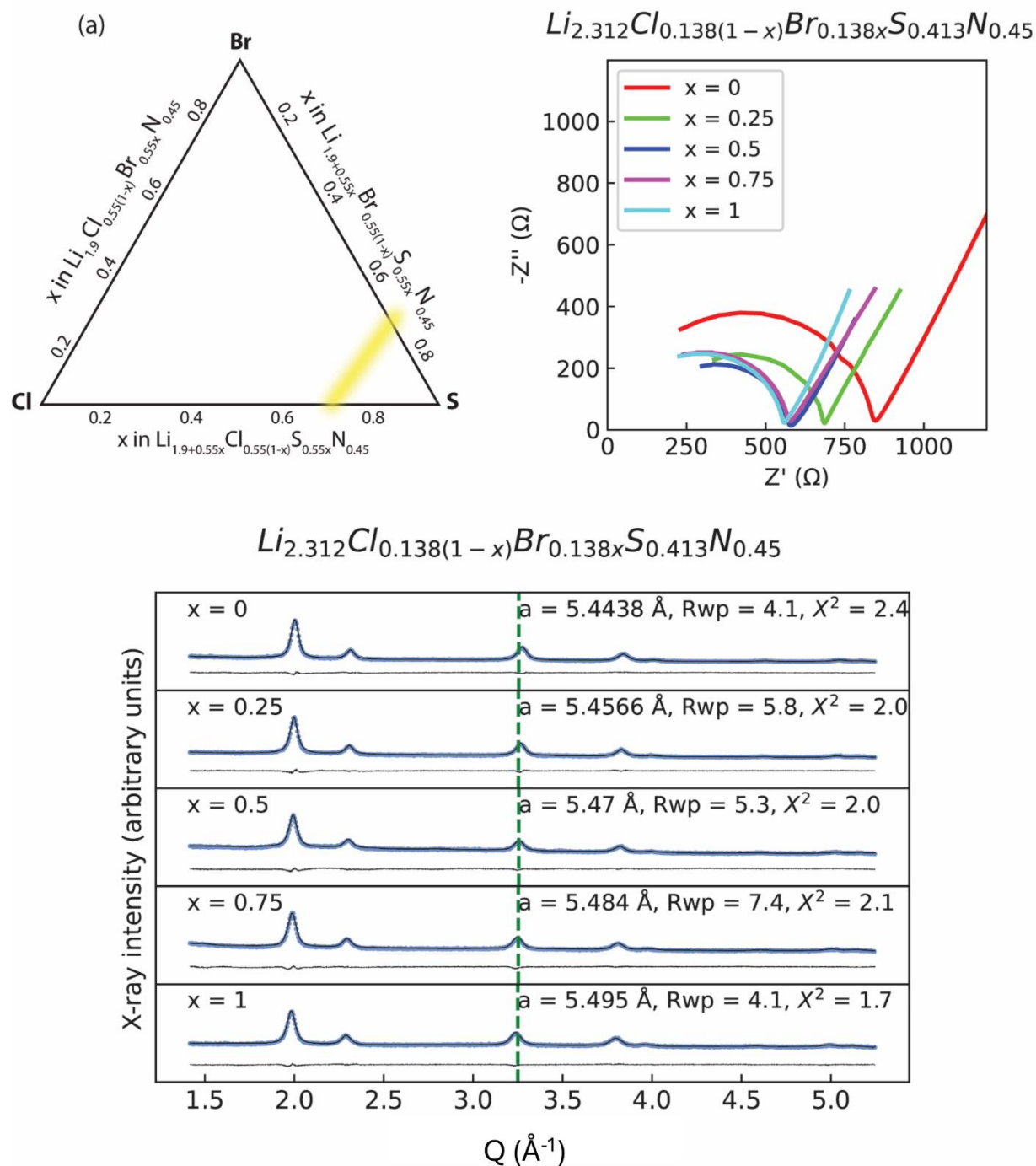


Figure S4.10. (a) highlighting which phases are shown in “b” and “c”. (b) Room temperature electrochemical impedance spectroscopy (EIS) of different $Li_{2.31}Br_{0.138x}Cl_{0.138(1-x)}S_{0.55x}N_{0.45}$ phases. (c) X-ray diffraction pattern and Rietveld refinements of the different $Li_{2.31}Br_{0.138x}Cl_{0.138(1-x)}S_{0.55x}N_{0.45}$ phases. Dotted green line is guide to the eye to easily see the peak shift originating from different lattice parameters.

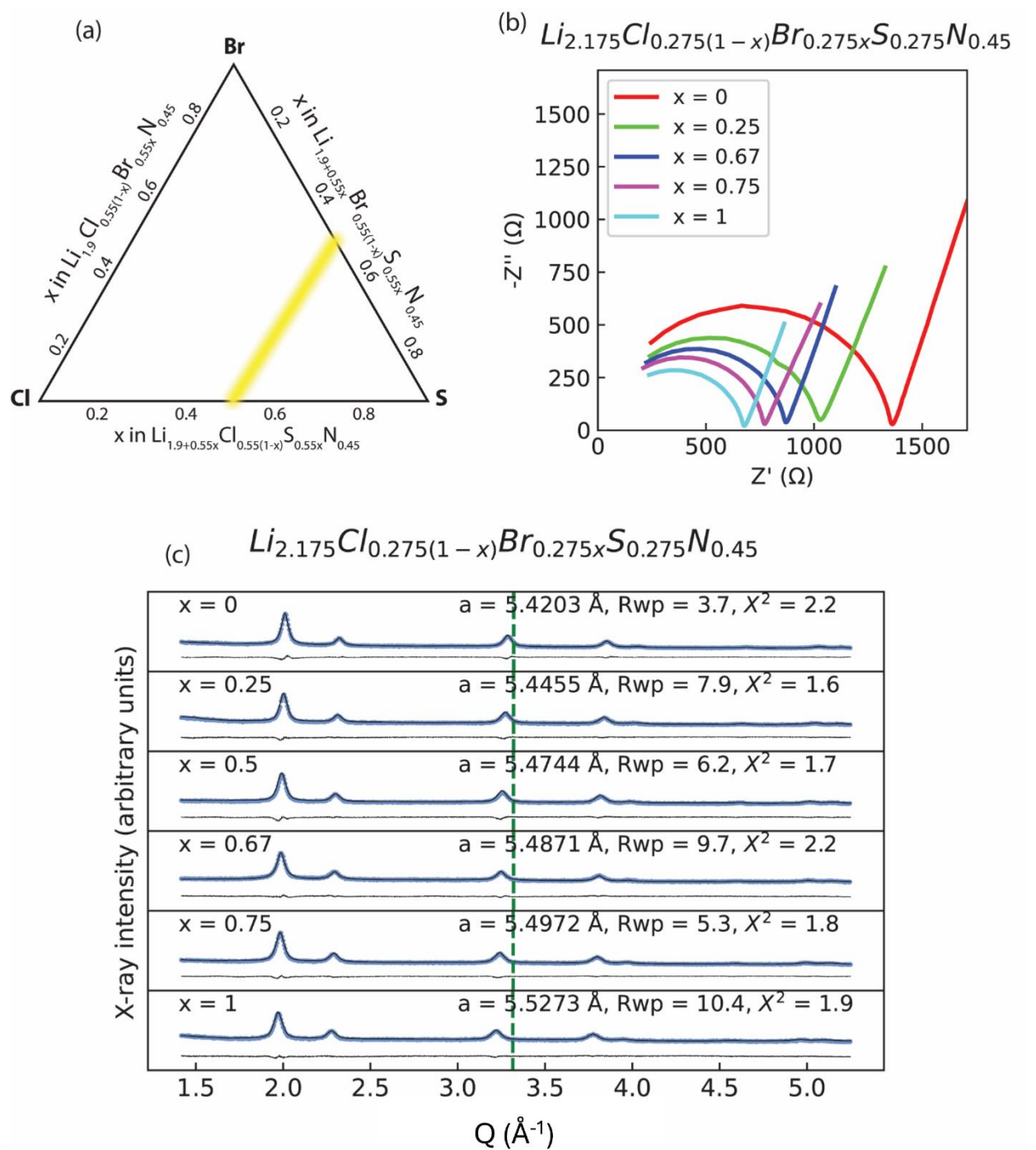


Figure S4.11. (a) highlighting which phases are shown in “b” and “c”. (b) Room temperature electrochemical impedance spectroscopy (EIS) of different $\text{Li}_{2.175}\text{Br}_{0.275x}\text{Cl}_{0.275(1-x)}\text{S}_{0.275}\text{N}_{0.45}$ phases. (c) X-ray diffraction pattern and Rietveld refinements of the different $\text{Li}_{2.31+0.55x}\text{Br}_{0.275x}\text{Cl}_{0.275(1-x)}\text{S}_{0.55x}\text{N}_{0.45}$ phases. Dotted green line is guide to the eye to easily see the peak shift originating from different lattice parameters.

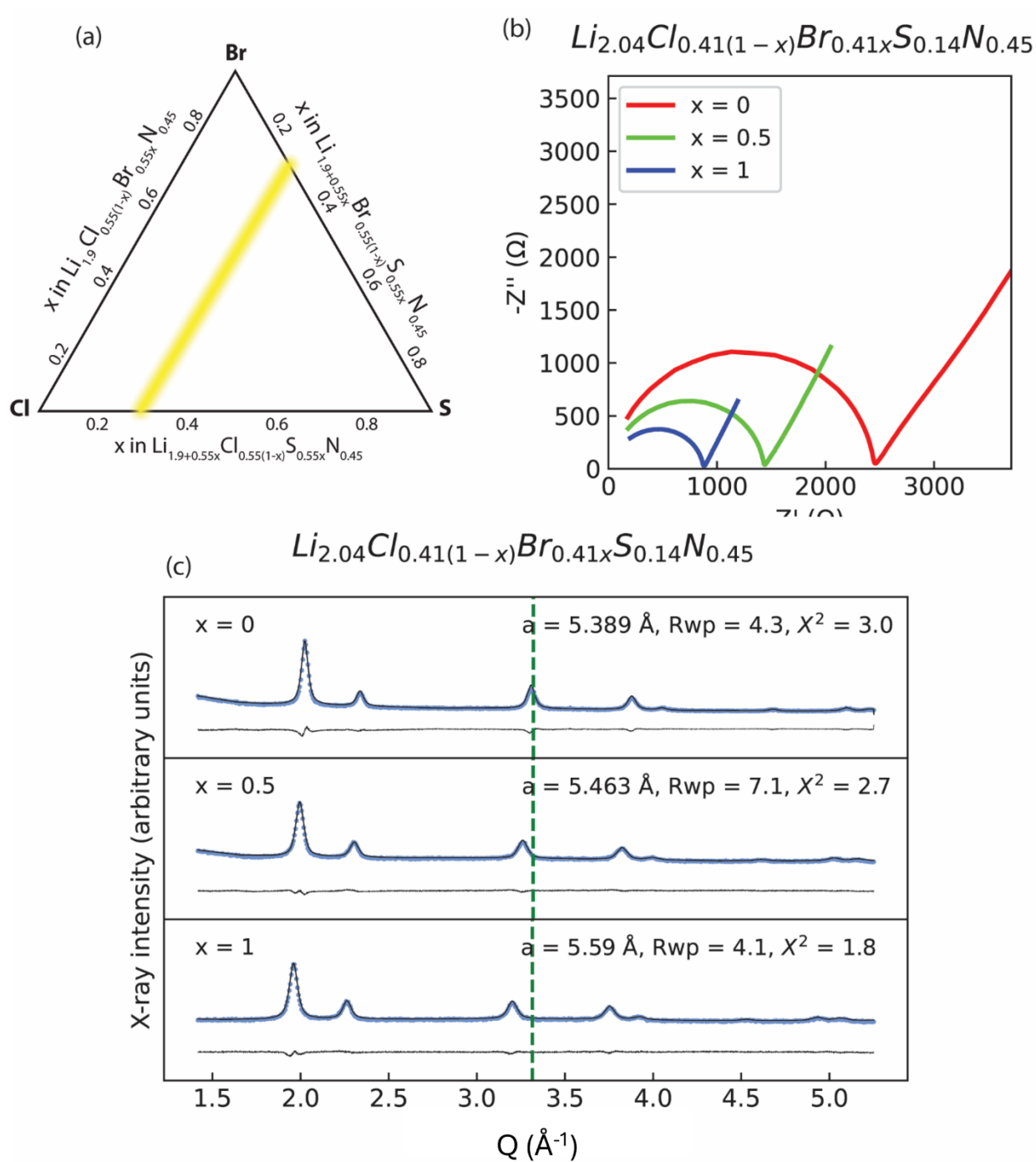


Figure S4.12. (a) highlighting which phases are shown in “b” and “c”. (b) Room temperature electrochemical impedance spectroscopy (EIS) of different $\text{Li}_{2.04}\text{Br}_{0.41x}\text{Cl}_{0.41(1-x)}\text{S}_{0.14}\text{N}_{0.45}$ phases. (c) X-ray diffraction pattern and Rietveld refinements of the different $\text{Li}_{2.04}\text{Br}_{0.41x}\text{Cl}_{0.41(1-x)}\text{S}_{0.14}\text{N}_{0.45}$ phases. Dotted green line is guide to the eye to easily see the peak shift originating from different lattice parameters.

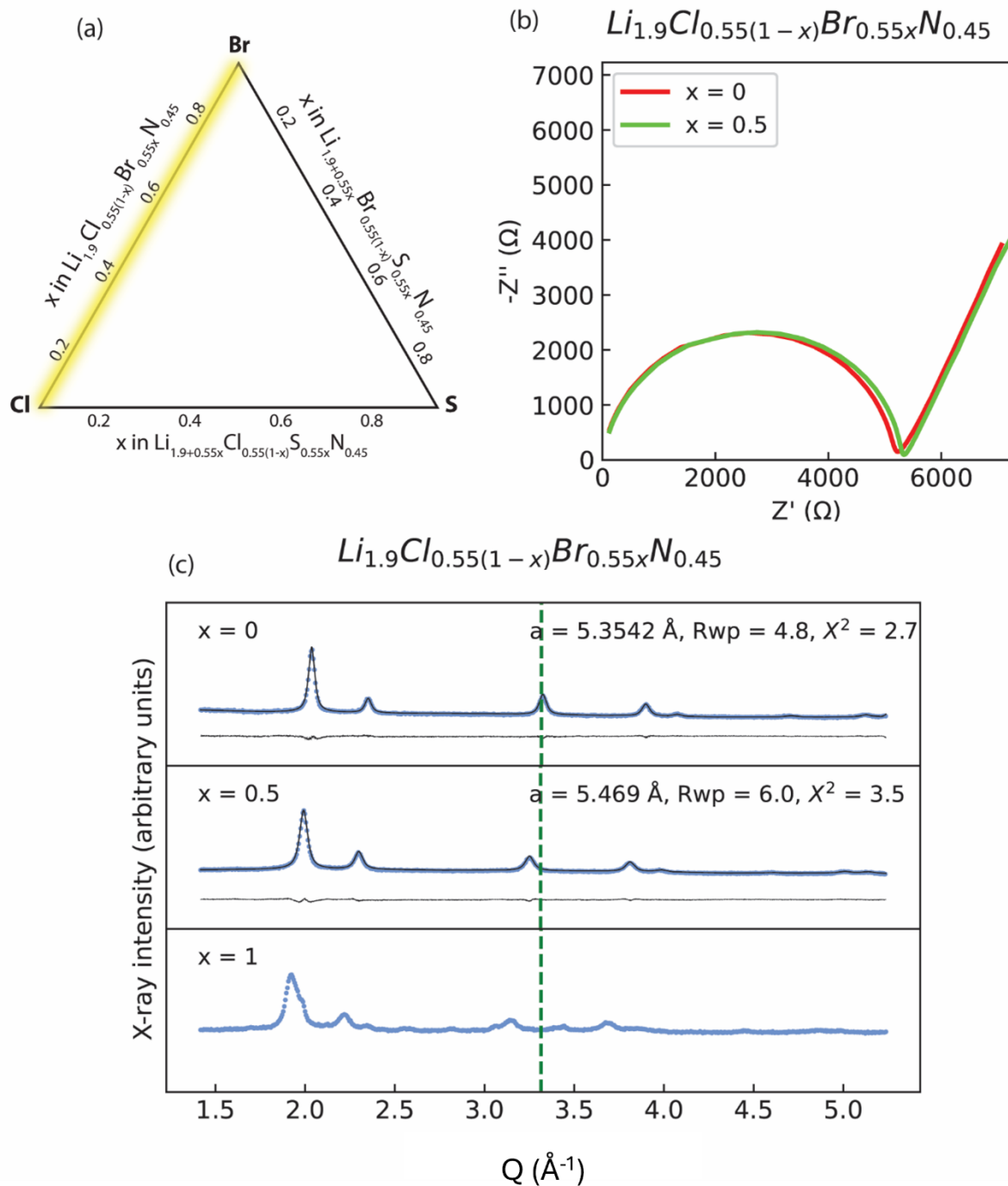


Figure S4.13. (a) highlighting which phases are shown in “b” and “c”. (b) Room temperature electrochemical impedance spectroscopy (EIS) of different $\text{Li}_{1.9}\text{Br}_{0.55x}\text{Cl}_{0.55(1-x)}\text{S}_{0.55x}\text{N}_{0.45}$ phases. (c) X-ray diffraction pattern and Rietveld refinements of the different $\text{Li}_{2.04}\text{Br}_{0.41x}\text{Cl}_{0.41(1-x)}\text{S}_{0.55x}\text{N}_{0.45}$ phases. At $x=1$ an impure phase was obtained. The antifluorite structure can thus not be stabilized at this composition. Dotted green line is guide to the eye to easily see the peak shift originating from different lattice parameters.

Table S4.1. Structure solution of the $\text{Li}_{1.66}\text{Cl}_{0.66}\text{N}_{0.33}$ structure. $R_{\text{wp}} = 4.9$, $\chi^2 = 2.0$, Lattice parameter: $a = 5.387(1)$ Å. The rather large B_{iso} values originate from displacive relaxations off the centre of tetrahedral Li sites with a mix of N and Cl at their corners. ²

Atom	x	y	z	Wyckoff	Occupancy	B_{iso}
Li	0.25	0.25	0.25	8c	0.833	4.41183(7)
N	0	0	0	4a	0.333	0.99577(8)
Cl	0	0	0	4a	0.666	0.99577(8)

Table S4.2. Structure solution of the $\text{Li}_{1.8}\text{Cl}_{0.6}\text{N}_{0.4}$ structure. $R_{\text{wp}} = 5.3$, $\chi^2 = 2.4$. Lattice parameter: $a = 5.368(1)$ Å. The rather large B_{iso} values originate from displacive relaxations off the centre of tetrahedral Li sites with a mix of N and Cl at their corners. ²

Atom	x	y	z	Wyckoff	Occupancy	B_{iso}
Li	0.25	0.25	0.25	8c	0.9	7.72856(7)
N	0	0	0	4a	0.4	0.77151(9)
Cl	0	0	0	4a	0.6	0.77151(9)

Table S4.3. Structure solution of the $\text{Li}_{1.9}\text{Cl}_{0.55}\text{N}_{0.45}$ structure. $R_{\text{wp}} = 4.8$, $\chi^2 = 2.7$ Lattice parameter: $a = 5.354(1)$ Å. The rather large B_{iso} values originate from displacive relaxations off the center of tetrahedral Li sites with a mix of N and Cl at their corners. ²

Atom	x	y	z	Wyckoff	Occupancy	B_{iso}
Li	0.25	0.25	0.25	8c	0.95	8.45905(7)
N	0	0	0	4a	0.45	0.99576(6)
Cl	0	0	0	4a	0.55	0.99576(6)

Table S4.4. Structure solution of the $\text{Li}_2\text{Cl}_{0.5}\text{N}_{0.5}$ structure. $R_{\text{wp}} = 6.5$, $\chi^2 = 1.8$ Lattice parameter: $a = 5.348(1)$ Å. The rather large B_{iso} values originate from displacive relaxations off the center of tetrahedral Li sites with a mix of N and Cl at their corners. ²

Atom	x	y	z	Wyckoff	Occupancy	B_{iso}
Li	0.25	0.25	0.25	8c	1.00	11.69183(6)
N	0	0	0	4a	0.50	1.37784(8)
Cl	0	0	0	4a	0.50	1.37784(8)

Table S4.5. Attempt frequency obtained from 5 $\text{Li}_{1+2x}\text{N}_x\text{Cl}_{1-x}$ ($2 \times 2 \times 2$) supercells at 1000 K.

Supercell Supercell	Attempt frequency (10^{13} Hz)	Standard deviation (10^{13} Hz)
1	1.0	0.21
2	1.0	0.22
3	1.0	0.22
4	1.0	0.23
5	1.0	0.24

Table S4.6. Lattice parameter (experimental obtained from refinements) of different antifluorite-like phases. The lattice parameters for $\text{Li}_{2+x}\text{S}_{1-x}\text{N}_x$ phases are obtained from previous work (ref 1).

x	Lattice params of antifluorite-like structure (\AA)	
	$\text{Li}_{1+2x}\text{N}_x\text{Cl}_{1-x}$	$\text{Li}_{2+x}\text{N}_x\text{S}_{1-x}$
0.33	5.387	5.521
0.4	5.367	5.491
0.45	5.354	5.471

Table S4.7. Table with the average jump-Ea values for each jump type existing in $\text{Li}_{1+2x}\text{N}_x\text{Cl}_{1-x}$ phases obtained from AIMD simulations of $\text{Li}_{1+2x}\text{N}_x\text{Cl}_{1-x}$ supercells. The total uncertainty on the individual jump-Ea values comprises uncertainty from convergence and uncertainty on the mean value.

Jump type	Average jump-Ea (eV)	Uncertainty on Mean (eV)	Uncertainty from convergence (eV)	Total uncertainty (eV)
$\text{N}_1\text{Cl}_5\text{-Cl}_4(\text{CICICI})$	0.282	0.004	0.004	0.008
$\text{N}_1\text{Cl}_5\text{-N}_1\text{Cl}_3(\text{CICIN})$	0.249	0.003	0.001	0.005
$\text{N}_5\text{Cl}_1\text{-N}_3\text{Cl}_1(\text{NNN})$	0.289	0.006	0.001	0.008
$\text{N}_5\text{Cl}_1\text{-N}_2\text{Cl}_2(\text{CINN})$	0.291	0.006	0.007	0.013
$\text{N}_1\text{Cl}_5\text{-N}_1\text{Cl}_3(\text{CICICI})$	0.363	0.007	0.014	0.021
$\text{N}_4\text{Cl}_2\text{-N}_2\text{Cl}_2(\text{CINN})$	0.288	0.004	0	0.004
$\text{N}_4\text{Cl}_2\text{-N}_1\text{Cl}_3(\text{CICIN})$	0.315	0.012	0.014	0.026
$\text{N}_4\text{Cl}_2\text{-N}_2\text{Cl}_2(\text{CICIN})$	0.336	0.007	0.005	0.012
$\text{N}_6\text{-N}_3\text{Cl}_1(\text{NNN})$	0.243	0.003	0.004	0.007
$\text{N}_2\text{Cl}_4\text{-N}_1\text{Cl}_3(\text{CICIN})$	0.268	0.003	0.001	0.004
$\text{N}_2\text{Cl}_4\text{-N}_2\text{Cl}_2(\text{CICIN})$	0.281	0.004	0.001	0.004
$\text{N}_3\text{Cl}_3\text{-N}_2\text{Cl}_2(\text{CICIN})$	0.327	0.004	0.003	0.007
$\text{N}_3\text{Cl}_3\text{-N}_1\text{Cl}_3(\text{CICIN})$	0.287	0.004	0.006	0.009
$\text{N}_3\text{Cl}_3\text{-N}_2\text{Cl}_2(\text{CINN})$	0.264	0.003	0.001	0.004
$\text{N}_3\text{Cl}_3\text{-N}_3\text{Cl}_1(\text{CINN})$	0.246	0.002	0.001	0.003
$\text{N}_3\text{Cl}_3\text{-Cl}_4(\text{CICICI})$	0.362	0.008	0.012	0.02
$\text{N}_1\text{Cl}_5\text{-N}_2\text{Cl}_2(\text{CICIN})$	0.289	0.004	0.002	0.006
$\text{N}_2\text{Cl}_4\text{-Cl}_4(\text{CICICI})$	0.336	0.005	0.008	0.013
$\text{N}_4\text{Cl}_2\text{-N}_3\text{Cl}_1(\text{CINN})$	0.289	0.007	0.005	0.013
$\text{N}_3\text{Cl}_3\text{-N}_4(\text{NNN})$	0.24	0.005	0.001	0.006
$\text{N}_3\text{Cl}_3\text{-N}_1\text{Cl}_3(\text{CICICI})$	0.457	0	0.457	0.04

N ₄ Cl ₂ -N ₃ Cl ₁ (NNN)	0.267	0.006	0.003	0.009
N ₄ Cl ₂ -N ₄ (NNN)	0.247	0.011	0.004	0.015
N ₂ Cl ₄ -N ₂ Cl ₂ (CINN)	0.233	0.004	0.002	0.006
N ₂ Cl ₄ -N ₃ Cl ₁ (CINN)	0.244	0.004	0.003	0.007
N ₂ Cl ₄ -N ₁ Cl ₃ (CICICI)	0.358	0.007	0.01	0.017
N ₅ Cl ₁ -N ₄ (NNN)	0.232	0.009	0.007	0.016
N ₅ Cl ₁ -N ₃ Cl ₁ (CINN)	0.288	0.007	0.007	0.015
N ₂ Cl ₂ -N ₂ Cl ₂ (CIN)	0.483	0.003	0.012	0.016
N ₂ Cl ₂ -N ₃ Cl ₁ (CIN)	0.486	0.005	0.011	0.016
N ₂ Cl ₂ -N ₁ Cl ₃ (CIN)	0.411	0.003	0.004	0.006
N ₂ Cl ₂ -N ₁ Cl ₃ (CICI)	0.461	0.013	0.021	0.034
N ₂ Cl ₂ -N ₂ Cl ₂ (NN)	0.32	0.004	0.001	0.005
N ₃ Cl ₁ -N ₃ Cl ₁ (NN)	0.32	0.002	0	0.002
N ₃ Cl ₁ -N ₁ Cl ₃ (CIN)	0.43	0.003	0.004	0.007
N ₃ Cl ₁ -N ₂ Cl ₂ (CIN)	0.488	0.003	0.007	0.01
N ₁ Cl ₃ -N ₂ Cl ₂ (CIN)	0.41	0.003	0.004	0.007
N ₁ Cl ₃ -N ₁ Cl ₃ (CICI)	0.525	0.012	0.033	0.045
N ₂ Cl ₂ -N ₄ (NN)	0.43	0.007	0.001	0.008
N ₁ Cl ₃ -Cl ₄ (CICI)	0.5	0.006	0.03	0.036
N ₁ Cl ₃ -N ₃ Cl ₁ (CIN)	0.433	0.003	0.003	0.006
N ₁ Cl ₃ -N ₂ Cl ₂ (CICI)	0.531	0	0.531	0.04
N ₂ Cl ₂ -N ₃ Cl ₁ (NN)	0.375	0.004	0.001	0.005
N ₂ Cl ₂ -Cl ₄ (CICI)	0.546	0.006	0.016	0.022
N ₃ Cl ₁ -N ₃ Cl ₁ (CIN)	0.457	0.009	0.014	0.022
Cl ₄ -N ₁ Cl ₃ (CICI)	0.406	0.005	0.016	0.021
Cl ₄ -Cl ₄ (CICI)	0.322	0.004	0.003	0.007
Cl ₄ -N ₂ Cl ₂ (CICI)	0.412	0.008	0.019	0.027
N ₃ Cl ₁ -N ₂ Cl ₂ (NN)	0.366	0.005	0.002	0.006
N ₄ -N ₂ Cl ₂ (NN)	0.419	0.005	0.005	0.01
N ₄ -N ₃ Cl ₁ (NN)	0.328	0.003	0.001	0.004
N ₄ -N ₄ (NN)	0.321	0.003	0.002	0.005
N ₁ Cl ₃ -N ₁ Cl ₃ (CIN)	0.294	0.002	0	0.003
N ₃ Cl ₁ -N ₄ (NN)	0.333	0.003	0.002	0.005
N ₂ Cl ₂ -N ₄ Cl ₂ (CINN)	0.384	0.004	0.001	0.005
N ₂ Cl ₂ -N ₃ Cl ₃ (CICIN)	0.464	0.004	0.003	0.007
N ₂ Cl ₂ -N ₃ Cl ₃ (CINN)	0.359	0.003	0.004	0.007
N ₂ Cl ₂ -N ₁ Cl ₅ (CICIN)	0.379	0.006	0.009	0.014
N ₃ Cl ₁ -N ₆ (NNN)	0.329	0.005	0	0.005
N ₃ Cl ₁ -N ₃ Cl ₃ (CINN)	0.322	0.003	0.001	0.004
N ₁ Cl ₃ -N ₂ Cl ₄ (CICIN)	0.344	0.003	0	0.004
N ₁ Cl ₃ -N ₁ Cl ₅ (CICICI)	0.49	0.007	0.018	0.025
N ₁ Cl ₃ -N ₄ Cl ₂ (CICIN)	0.433	0.009	0.005	0.014
N ₂ Cl ₂ -N ₂ Cl ₄ (CICIN)	0.398	0.005	0.007	0.012
N ₂ Cl ₂ -N ₅ Cl ₁ (CINN)	0.408	0.007	0.001	0.008
N ₂ Cl ₂ -N ₂ Cl ₄ (CINN)	0.333	0.007	0.001	0.008
N ₁ Cl ₃ -N ₃ Cl ₃ (CICIN)	0.362	0.003	0.002	0.006

Cl ₄ -N ₂ Cl ₄ (CICICI)	0.341	0.005	0.006	0.011
Cl ₄ -N ₁ Cl ₅ (CICICI)	0.277	0.003	0.002	0.005
N ₃ Cl ₁ -N ₄ Cl ₂ (CINN)	0.338	0.006	0	0.006
N ₄ -N ₃ Cl ₃ (NNN)	0.329	0.006	0.001	0.007
N ₄ -N ₅ Cl ₁ (NNN)	0.288	0.006	0.003	0.009
N ₁ Cl ₃ -N ₁ Cl ₅ (CICIN)	0.307	0.004	0.001	0.005
N ₃ Cl ₁ -N ₄ Cl ₂ (NNN)	0.352	0.006	0.001	0.007
N ₃ Cl ₁ -N ₂ Cl ₄ (CINN)	0.331	0.004	0.001	0.004
N ₄ -N ₄ Cl ₂ (NNN)	0.293	0.005	0.003	0.008
Cl ₄ -N ₃ Cl ₃ (CICICI)	0.351	0.01	0.018	0.027
N ₃ Cl ₁ -N ₅ Cl ₁ (NNN)	0.352	0.008	0.005	0.014
N ₂ Cl ₂ -N ₄ Cl ₂ (CICIN)	0.468	0.007	0.003	0.01
N ₁ Cl ₃ -N ₂ Cl ₄ (CICICI)	0.472	0.012	0.012	0.024
N ₁ Cl ₃ -N ₃ Cl ₃ (CICICI)	0.588	0.001	0.588	0.04
N ₃ Cl ₁ -N ₅ Cl ₁ (CINN)	0.348	0.009	0.005	0.014
Cl ₆ -Cl ₄ (CICICI)	0.279	0.005	0.001	0.006
Cl ₆ -N ₁ Cl ₃ (CICICI)	0.403	0.007	0.004	0.011
N ₆ -N ₄ (NNN)	0.234	0.007	0.012	0.019
N ₂ Cl ₂ -N ₂ Cl ₂ (CICI)	0.58	0.009	0.013	0.022
Cl ₄ -Cl ₆ (CICICI)	0.236	0.004	0.001	0.005
N ₁ Cl ₃ -Cl ₆ (CICICI)	0.479	0.008	0.014	0.022
N ₄ -N ₆ (NNN)	0.285	0.006	0.005	0.011
N ₃ Cl ₃ -N ₃ Cl ₁ (NNN)	0.248	0.005	0.005	0.01
N ₃ Cl ₁ -N ₃ Cl ₃ (NNN)	0.344	0.009	0.007	0.016

Supplementary Note 1: Potential small occupation of octahedral sites

For the structure solutions shown in Tables S4.1-4.4 and Figure S4.2 all Li was assumed occupy tetrahedral sites as our energetic considerations show that tetrahedral sites are clearly more stable and based on the structure solution that was previously obtained for Li_5NCl_2 i.e. $\text{Li}_{1.66}\text{Cl}_{0.66}\text{N}_{0.33}$.²

However, our energetic considerations would permit a small occupation of the octahedral sites at 300K. The energy difference between octahedral and tetrahedral sites may be estimated from tet-oct and oct-tet jump- E_a values. For the $\text{Li}_{1+2x}\text{Cl}_{1-x}\text{N}_x$ phases the oct sites are destabilized by on average 0.07 ± 0.01 eV versus the tetrahedral sites. According to the partition function this would result in 3 ± 1 % of Li ions occupying octahedral sites at 300 K:

$$q = 8 + 4 * \exp\left(\frac{-\Delta E_{\text{site}}(\text{oct}, \text{tet})}{kT}\right) \quad (S1)$$

Where q is the partition function, $\Delta E_{\text{site}}(\text{oct}, \text{tet})$ is the average energy difference between tet and oct sites, k is Boltzmann constant T is temperature.

$$p_{\text{oct}} = \frac{4 * \exp\left(\frac{-\Delta E_{\text{site}}(\text{oct}, \text{tet})}{kT}\right)}{q} \quad (S2)$$

where p_{oct} is the of Li occupying the octahedral sites.

We investigated how the quality of Rietveld fits would vary with Li occupying octahedral sites. As a representative of the $\text{Li}_{1+2x}\text{Cl}_{1-x}\text{N}_x$ phase we use the $\text{Li}_{1.66}\text{Cl}_{0.66}\text{N}_{0.33}$ phase. In Figure S4.14 we report on Rietveld fits of the x-ray diffraction pattern of a $\text{Li}_{1.66}\text{Cl}_{0.66}\text{N}_{0.33}$ phase assuming 0%, 3%, 5%, 10%, 20%, 40% and 60% of Li occupying the octahedral sites. Between 0% and 5% the quality of fit (as determined by the R_{wp} and χ^2 fit parameters) is hardly altered. From 10% of Li occupying octahedral sites onwards the fit quality gradually worsens. We performed the same investigation on a Neutron diffraction pattern of $\text{Li}_{1.66}\text{Cl}_{0.66}\text{N}_{0.33}$ which was additionally annealed to 600 °C for 3h and quenched in ambient temperature to improve crystallinity Figure (S4.15). The conclusions drawn from Figure S4.15 are equivalent: Between 0% and 5% the quality of fit (as determined by the R_{wp} and χ^2 fit parameters) is hardly altered. From 10% of Li occupying octahedral sites the fit quality gradually worsens. This investigation experimentally supports that the tetrahedra are indeed more stable than the octahedral sites (as our energetic considerations from DFT clearly demonstrate) however ~3% of Li ions occupying the octahedral sites may not be confirmed or excluded from neutron and x-ray Rietveld refinements and is thus conceivable. We note that a potentially (~3%) of Li ions occupying octahedral sites would not alter any of the conclusions of this study.

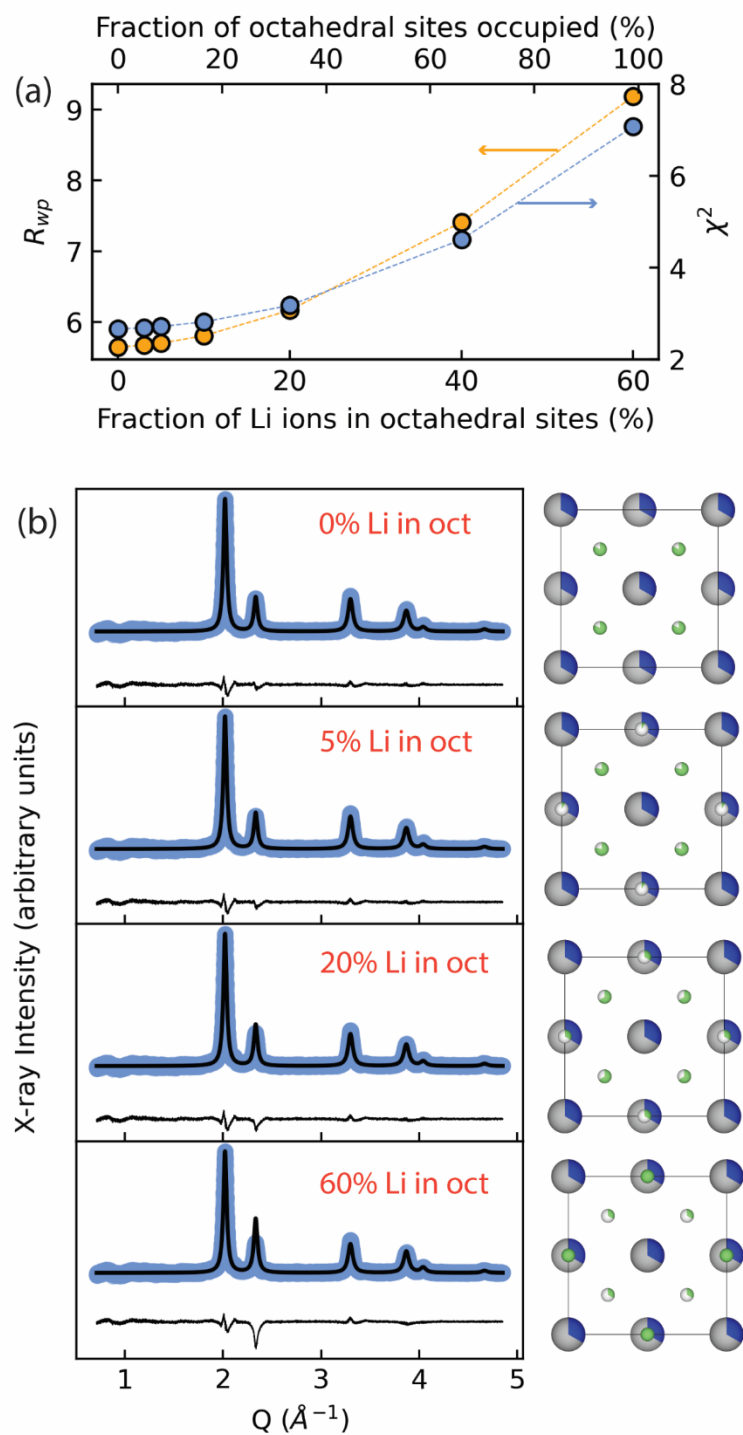


Figure S4.14. Rietveld refinements of a $\text{Li}_{1.66}\text{Cl}_{0.66}\text{N}_{0.33}$ x-ray diffraction patterns with different fractions of Li-ions occupying the tet and oct sites. (a) R_{wp} and χ^2 fit parameters as a function of the fraction of Li ions occupying the oct and tet sites respectively. (b) Rietveld fits with increasing fraction of Li ions occupying the oct sites along with the respective unit cells viewed along the [001] axis.

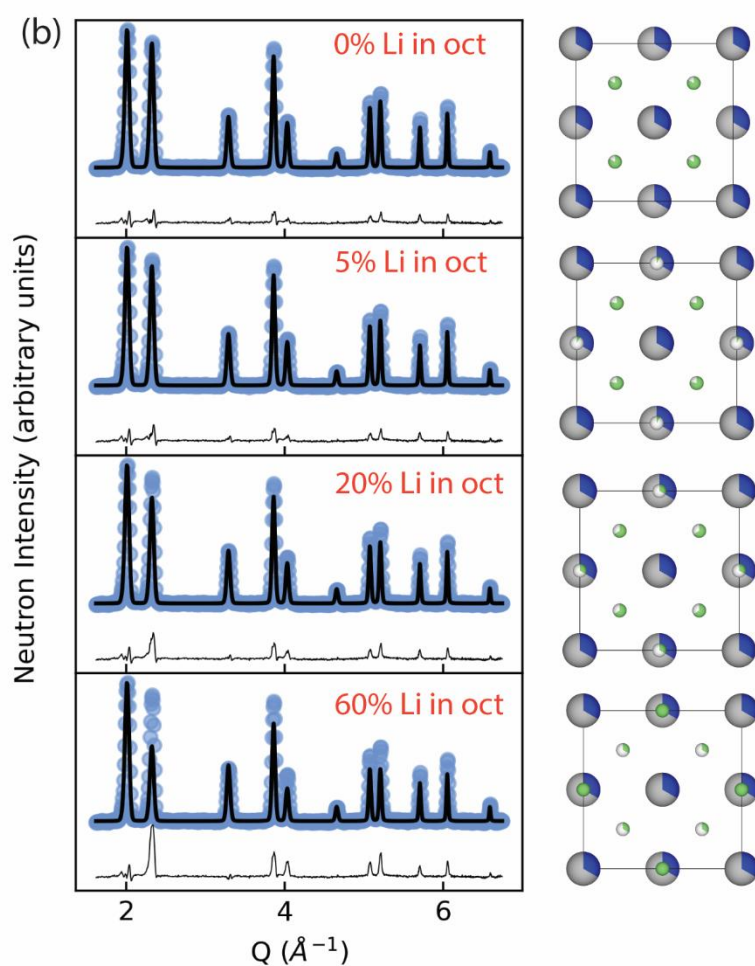
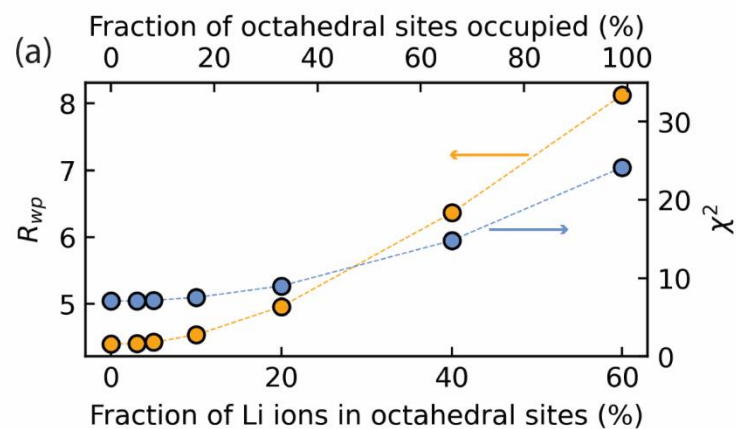


Figure S4.15. Rietveld refinements of a $\text{Li}_{1.66}\text{Cl}_{0.66}\text{N}_{0.33}$ neutron diffraction patterns with different fractions of Li-ions occupying the tet and oct sites. (a) R_{wp} and χ^2 fit parameters as a function of the fraction of Li ions occupying the oct and tet sites respectively. (b) Rietveld fits with increasing fraction of Li ions occupying the oct sites along with the respective unit cells viewed along the [001] axis.

Supplementary Note 2: tetrahedral sites in LiCl – sites or ‘merely’ positions ?

Catlow et al. proposed conditions that must be fulfilled so that ion diffusion in solids may be interpreted as ion-hops between well-defined sites.³ For crystallographic positions to qualify as sites Catlow et al. propose that the following conditions laid out in Table S4.8 need to be satisfied. Whether these conditions are fulfilled for tetrahedral and octahedral positions in LiCl was investigated via the AIMD simulations of LiCl. The results are reported in Table S4.9. As clearly identified in Table S4.9 the octahedral positions in LiCl from AIMD simulations fulfil all conditions to qualify as sites while the tetrahedral positions do not. The tetrahedral site should thus arguably more generally be referred to as ‘positions’ than ‘sites’. In this study however, we refer to both the octahedral and tetrahedral positions as sites while highlighting the high metastability of the tetrahedral position in LiCl in the main text.

Table S4.8 shows the requirements for crystallographic positions to qualify as sites defined by Catlow et al.³ T_r stands for time spent in site, T_h stands for time of hopping between sites, ν^* stands for the attempt frequency d stands for the distance between two sites and a for the vibrational amplitude in the site. ΔE_{hop} stands for the hop activation energy. All these properties may be extracted from AIMD simulations.

Property
$T_r \gg T_h$
$T_r \gg (\nu^*)^{-1}$
$d \gg a$
$\Delta E_{hop} \gg kT$

Table S4.9 shows whether the requirements defined in Table S4.8 are fulfilled for oct and tet sites in LiCl obtained from AIMD simulation of LiCl.

Property	Oct-site	Tet site	Conditions for site fulfilled [oct,tet]
T_r/T_h	892.8	0.12	[Yes, No]
$T_r/(\nu^*)^{-1}$	1863	0.26	[Yes, No]
d/a	5.79	5.79	[Yes, Yes]
$\Delta E_{hop}/kT$	25	1.2	[Yes, No]

Supplementary Note 3: Calculating the max ion radius that fits in a tetrahedral site

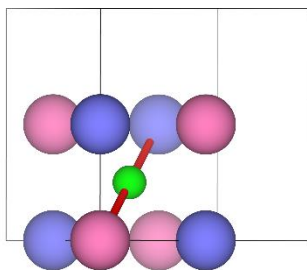


Figure S4.16 . Schematic of how the maximum ion radius fitting in a specific tetrahedral site may be obtained. An ion fitting in the tetrahedron spanned by the blue spheres also fits in a tetrahedron spanned by the pink spheres so that the cube consisting of blue/grey and pink spheres may be used to calculate the max ion radius fitting in a tetrahedral site. Note this method only works for tetrahedra where the ions at the corners are all the same. The tetrahedral site is indicated by a green sphere. The red line is the cube body diagonal.

An ion fitting in a tetrahedral site spanned by the blue spheres in Figure S4.16 also fits in the tetrahedron spanned by the pink spheres (i.e. rotated by 90 degrees) and thus the cube spanned by the pink and blue spheres may be used to calculate the max ion radius that fits in a site. This method only for tetrahedra where the ions at the corner of the tetrahedron are all the same. The maximum ion radius (r_{void}) fitting in a tetrahedron may be calculated as such

$$d = 2 * (r_{\text{void}} + r_{\text{peripheral}}) \quad (\text{S3})$$

$$r_{\text{void}} = \frac{d}{2} - r_{\text{peripheral}} \quad (\text{S4})$$

Where $r_{\text{peripheral}}$ is the radius of the ions at the corner of the tetrahedron (Cl^- or N^{3-}) and d the body diagonal of the cube spanned by the positions of the peripheral ions and the peripheral ion-positions rotated by 90 around an arbitrary rotation axis going through the tetrahedron centre (Figure S4.16) (i.e. blue and pink spheres)

For LiCl this results in $r_{\text{void}} = 0.38 \text{ \AA}$ by estimating d from the unit cell of LiCl. Table S4.10 shows different r_{void} radii calculated for different phases.

Table S4.10. Max radii fitting in tetrahedra of $\text{Li}_{1+2x}\text{Cl}_{1-x}\text{N}_x$ phases

Phase	Lattice param (\AA)	Tetrahedron type	r_{void} (\AA)
LiCl	5.15	Cl_4	0.38
$\text{Li}_{1+2x}\text{Cl}_{1-x}\text{N}_x$ ($0.33 < x < 0.5$)	5.36 (on average)	Cl_4	0.48
$\text{Li}_{1+2x}\text{Cl}_{1-x}\text{N}_x$ ($0.33 < x < 0.5$)	5.36 (on average)	N_4	0.84
$\text{Li}_{1+2x}\text{Cl}_{1-x}\text{N}_x$ ($0.33 < x < 0.5$)	5.36 (on average)	$\text{Cl}_3\text{N}_1, \text{Cl}_2\text{N}_2, \text{Cl}_1\text{N}_3$	$0.48 < r_{\text{void}} < 0.84$

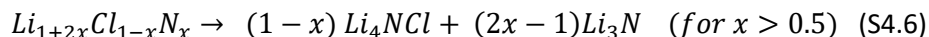
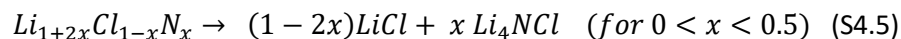
Supplementary Note 4: More details on the metastability calculations

Phase diagrams for the metastability calculations were built by leveraging the materials project database. The phases in table S4.11 are thermodynamically stable in the materials project database ⁴ on the LiCl-Li₃N and Li₂S-Li₃N tielines. In the materials project database the Li₉S₃N (mp557964) phase is slightly metastable (0.008 eV/atom above the hull). We lowered the energy of this phase to the hull since previous experimental work showed that this phase is thermodynamically stable and should be considered in phase diagrams. ^{1,5}

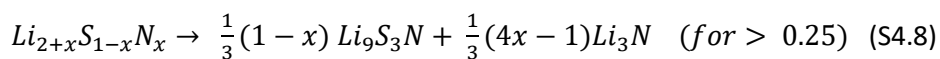
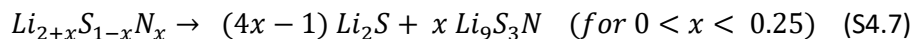
Table S4.11. Entries taken from the materials project database

Thermodynamically stable phases (space group)	Material's project ID of computed entry
LiCl (Fm-3m)	mp1185319
Li ₂ S (Fm-3m)	mp1153
Li ₃ N (P6/mmm)	mp2251
Li ₄ NCl (R-3 m h)	mp29149
Li ₉ S ₃ N (Pm-3m)	mp557964

The reactions for the LiCl-Li₃N tieline where, in the equations below Li_{1+2x}Cl_{1-x}N_x refers to antifluorite-like phases and Li₄NCl refers to the R-3mh phase:



The reactions for the Li₂S-Li₃N tieline where in the equations below Li_{2+3x}S_{1-x}N_x refers to antifluorite-like phases and Li₉S₃N refers to the Pm-3m phase:



References Appendix 3

1. Landgraf, V. *et al.* Entropy-induced high conductivity in fully-reduced electrolytes for solid-state batteries with lithium metal anodes. *ChemRxiv* (2023).
2. Marx, R. & Mayer, H. M. Preparation and Crystal Structure of Ordered and Disordered Lithium Nitride Dichloride, Li_5NCl_2 . *J. Solid State Chem.* **130**, 90–96 (1997).
3. Catlow, C. R. A. Static lattice simulation of structure and transport in superionic conductors. *Solid State Ionics* **8**, 89–107 (1983).
4. Jain, A. *et al.* Commentary: The materials project: A materials genome approach to accelerating materials innovation. *APL Mater.* **1**, 001002 (2013).
5. Marx, R., Lissner, F. & Schleid, T. $\text{Li}_9\text{N}_2\text{S}_3$: Das erste Nitridsulfid der Alkalimetalle in einer Li_2O -Typ-Variante. *Zeitschrift für Anorg. und Allg. Chemie* **632**, 2151 (2006).

Appendix 4. Supporting Information for Chapter 5

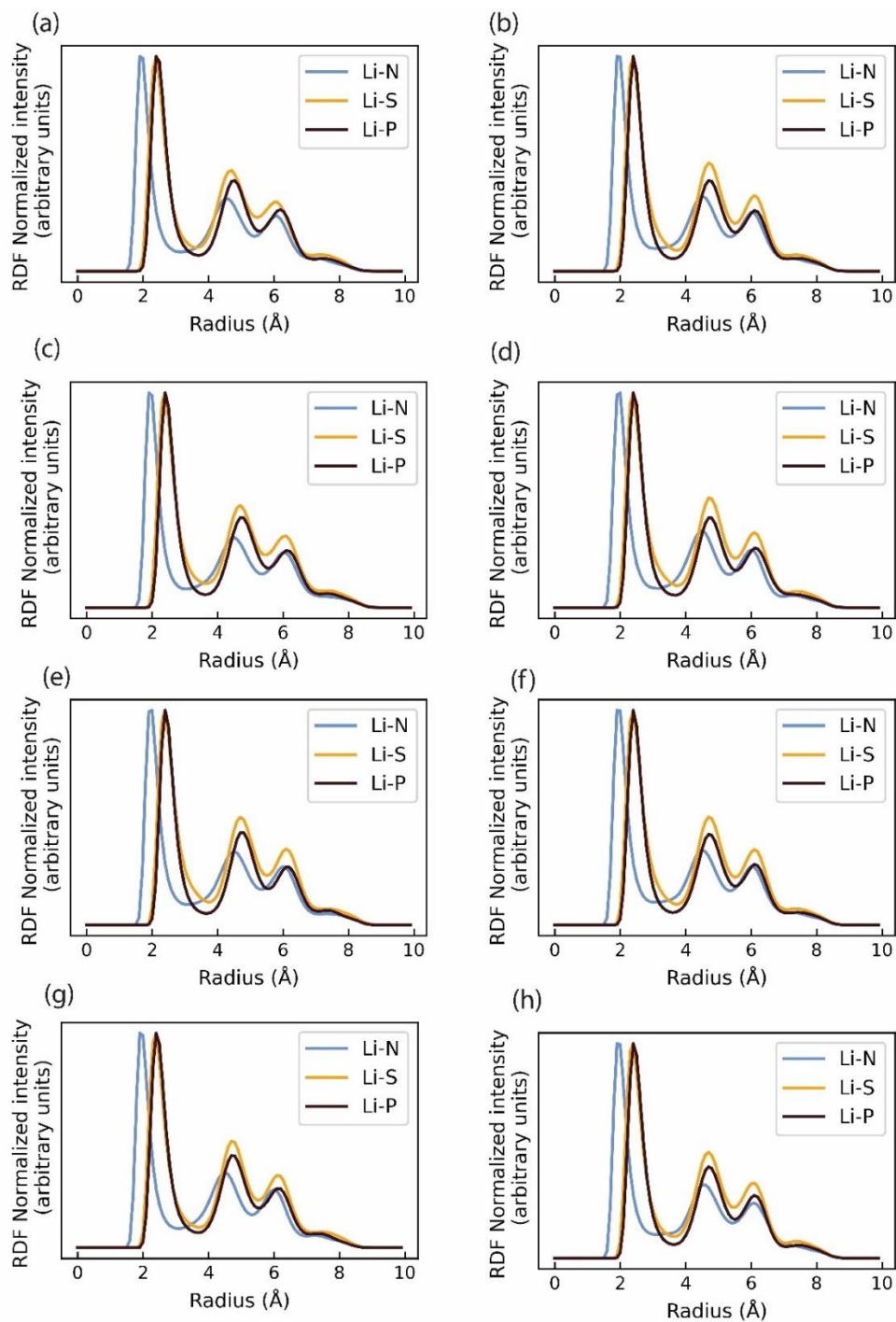


Figure S5.1. Radial distribution functions from the AIMD simulations of 8 $\text{Li}_{2.6}\text{S}_{0.4}\text{P}_{0.45}\text{N}_{0.15}$ supercells.

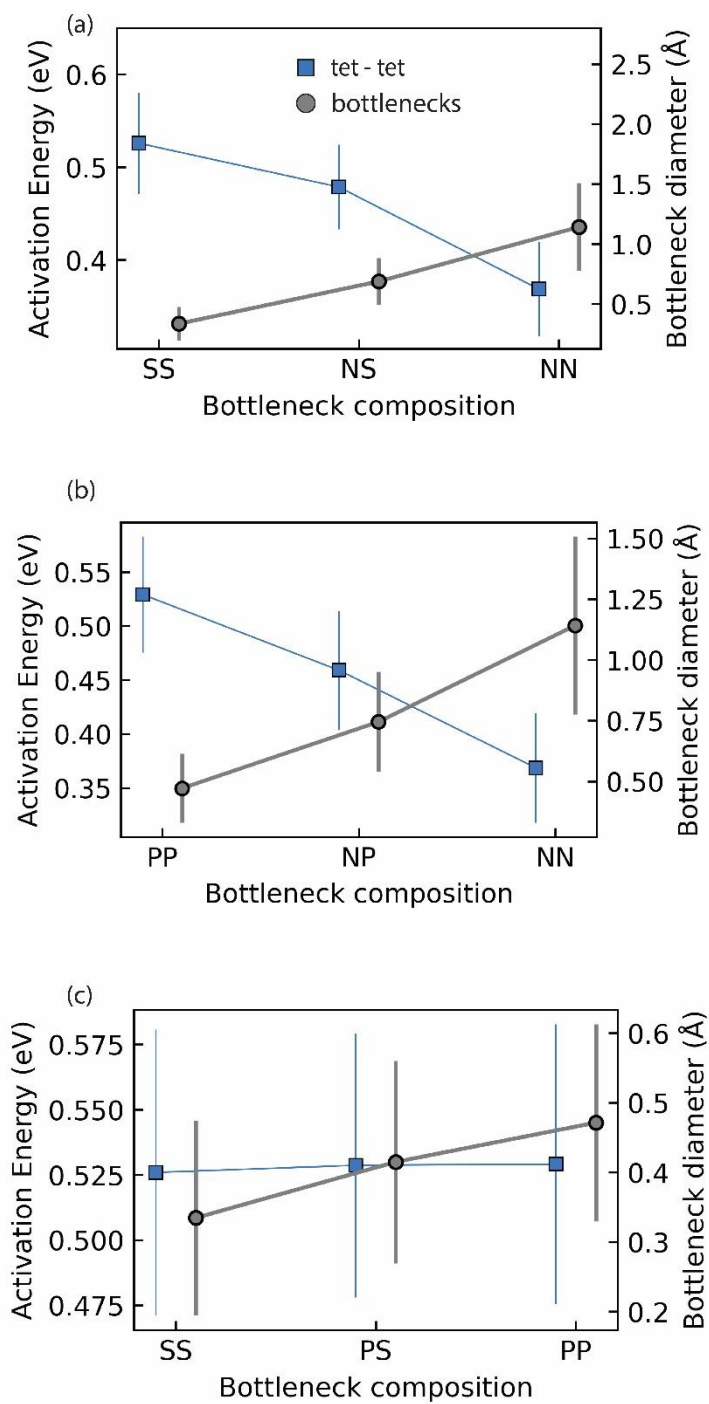


Figure S5.2. Correlation between Li-hop activation energy and bottleneck diameter as a proxy for the void size of the steric bottlenecks. (a) Effect of N_S substitution in SS bottlenecks on bottleneck diameter and Li-hop activation energies. (b) Effect of N_P substitution in PP bottlenecks on bottleneck diameter and Li-hop activation energies. (c) Effect of P_S substitution in SS bottlenecks on bottleneck diameter and Li-hop activation energies.

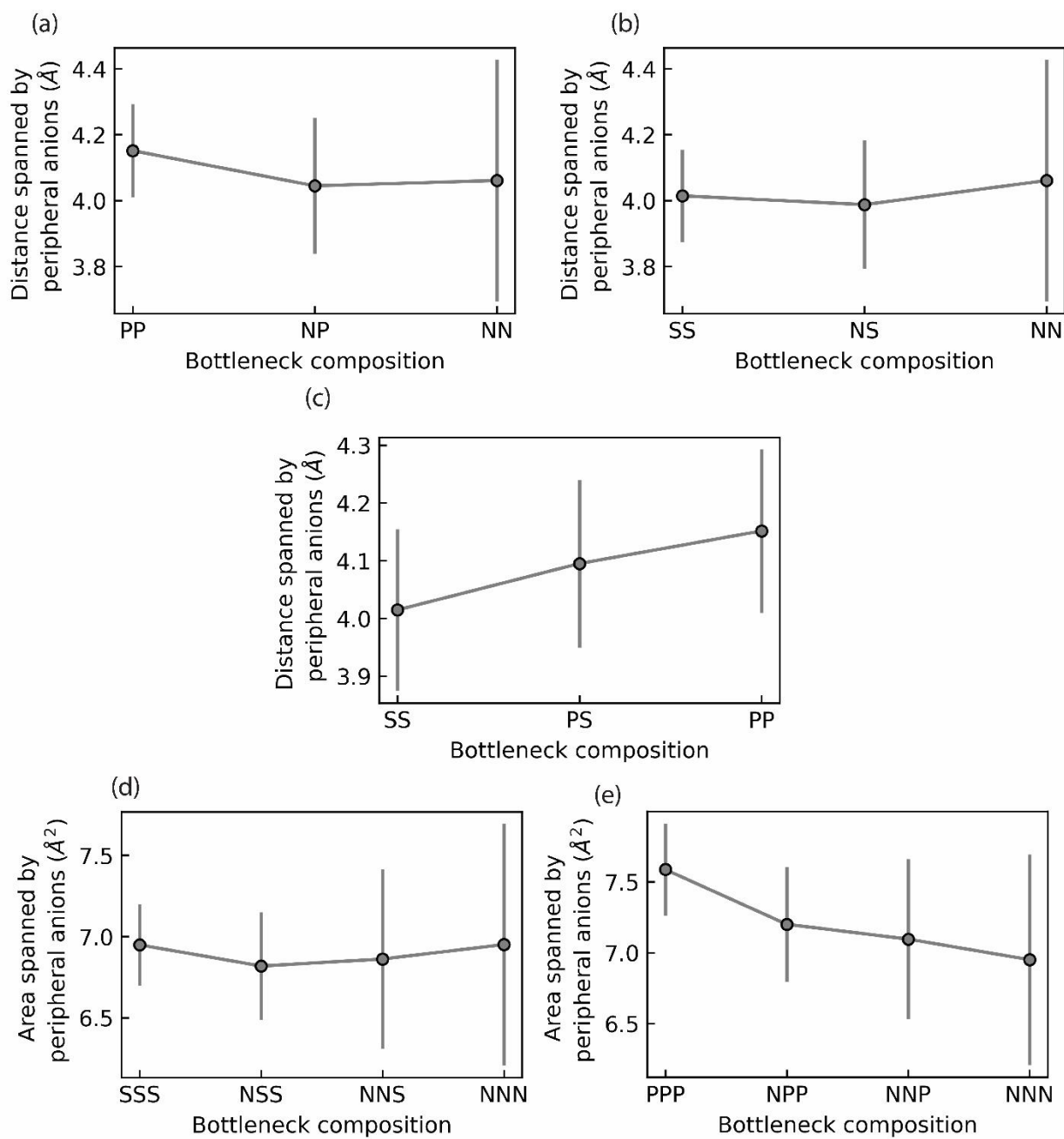


Figure S5.3. (a-c) Distance of the anions in N_P substituted PP, N_S substituted SS and P_S substituted PP bottlenecks, respectively. (d) Area of the triangle spanned by the three bottleneck anions for increased N_S substitution in SSS bottlenecks. (e) Area of the triangle spanned by the three bottleneck anions for increased N_P substitution in PPP bottlenecks.

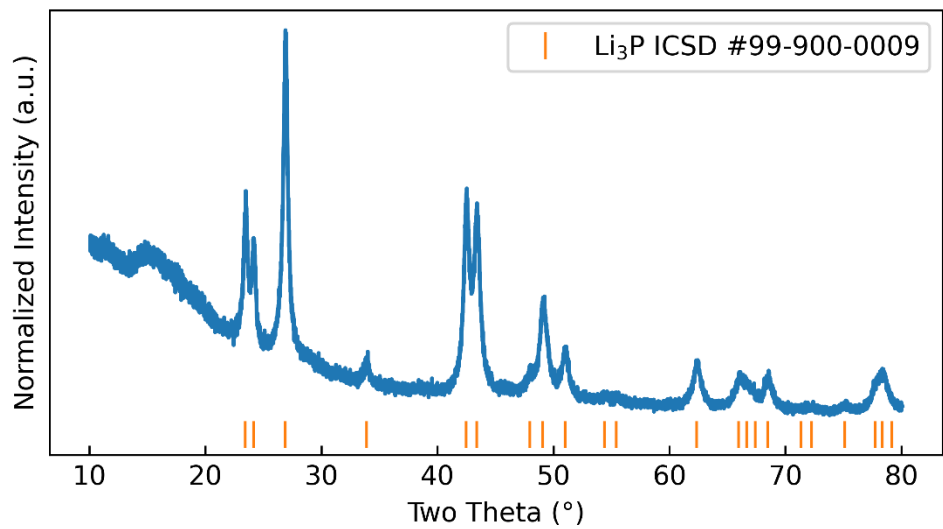


Figure S5.4. XRD pattern of the Li_3P synthesized as described in the methodology.

Table S5.1. Attempt frequency for Li-hops obtain from the oscillations around equilibrium sites from AIMD simulations of 8 supercells with $\text{Li}_{2.6}\text{S}_{0.4}\text{P}_{0.45}\text{N}_{0.15}$ stoichiometry. See ref 1 for a detailed description of how these attempt frequencies are obtained.

Supercell index	$V_0(10^{13} \text{ s}^{-1})$
1	1.06 ± 0.04
2	1.05 ± 0.04
3	1.04 ± 0.02
4	1.05 ± 0.04
5	1.05 ± 0.03
6	1.04 ± 0.02
7	1.06 ± 0.03
8	1.07 ± 0.03

Table S5.2: Refined structure solution for $Fm\bar{3}m$ - $\text{Li}_{2.6}\text{S}_{0.4}\text{P}_{0.6}$ obtained from the Rietveld refinement of X-ray diffraction patterns shown in Figure 5.5 . Lattice parameter $a = 5.96307(5) \text{ \AA}$.

Atom	x	y	z	Wyckoff	Occupancy	U_{iso}
Li-tet	0.25	0.25	0.25	8c	1	0.0130(1)
Li-oct	0.5	0.5	0.5	4b	0.6	0.1196(5)
P	0	0	0	4a	0.6	0.0101(1)
S	0	0	0	4a	0.4	0.0101(1)

Table S5.3: Refined structure solution for $Fm\bar{3}m$ - $\text{Li}_{2.6}\text{S}_{0.4}\text{P}_{0.45}\text{N}_{0.15}$ obtained from the Rietveld refinement of X-ray diffraction patterns shown in Figure 5.5 . Lattice parameter $a = 5.93939(5) \text{ \AA}$.

Atom	x	y	z	Wyckoff	Occupancy	U_{iso}
Li-tet	0.25	0.25	0.25	8c	1	0.08496(5)
Li-oct	0.5	0.5	0.5	4b	0.6	0.20038(4)
P	0	0	0	4a	0.45	0.01700(2)
S	0	0	0	4a	0.4	0.01700(2)
N	0	0	0	4a	0.15	0.01700(2)

Table S5.4: Refined structure solution for $Fm\bar{3}m$ -Li_{2.6}S_{0.4}P_{0.35}N_{0.25} obtained from the Rietveld refinement of X-ray diffraction patterns shown in Figure 5.5 . Lattice parameter a = 5.86983(2) Å.

Atom	x	y	z	Wyckoff	Occupancy	U _{iso}
Li-tet	0.25	0.25	0.25	8c	1	0.12085(1)
Li-oct	0.5	0.5	0.5	4b	0.6	0.12011(3)
P	0	0	0	4a	0.35	0.01800(3)
S	0	0	0	4a	0.4	0.01800(3)
N	0	0	0	4a	0.25	0.01800(3)

Table S5.5. Ionic conductivities of fully-reduced (i.e. irreducible) phases reported in literature and their respective ionic conductivities.

Halide	Spacegroup	Conductivity (S cm ⁻¹)	Reference
LiF	Fm-3m	1*10 ⁻⁹	2
LiCl	Fm-3m	1*10 ⁻⁹	3
LiBr	Fm-3m	n/a	n/a
LiI	Fm-3m	2*10 ⁻⁸	4
Chalcogenides	Spacegroup	Conductivity (S cm ⁻¹)	Reference
Li ₂ S	Fm-3m	1*10 ⁻⁹	5
Li ₂ Se	Fm-3m	n/a -- but computations suggest that it is higher than Li ₂ S see ref ⁶	6
Li ₂ Te	Fm-3m	n/a	n/a
Pnictides	Spacegroup	Conductivity (S cm ⁻¹)	Reference
Li ₃ N	P63/mmc	1*10 ⁻⁴	2,5,7,8
Li ₃ P	P63/mmc	1*10 ⁻⁷ - 1*10 ⁻⁴	2,9
Li ₃ As	P63/mmc	1*10 ⁻² (Electronic conductor!)	7
Mixed anions	Spacegroup	Conductivity (S cm ⁻¹)	Reference
Li _{1+2x} Cl _{1-x} N _x (0.33<x<0.5) (comprises Li ₉ N ₂ Cl ₃ and Li ₅ NCl ₂)	Fm-3m	1*10 ⁻⁵ - 5*10 ⁻⁵	3,10,11
Li _{2+x} S _{1-x} N _x (0 <x<0.55)	Fm-3m	1*10 ⁻⁹ - 2*10 ⁻⁴	5,12
Li _{2+x} S _{1-x} P _x (0 <x<0.75)	Fm-3m	1*10 ⁻⁹ - 2*10 ⁻⁴	9
Li _{2.6} S _{0.4} P _{0.45} N _{0.15}	Fm-3m	6.4*10 ⁻⁴	This work
Li _{2.6} S _{0.4} P _{0.35} N _{0.25}	Fm-3m	7.3*10 ⁻⁴	This work
Li ₇ N ₂ I	F-43m	3*10 ⁻⁴	13
Li ₉ S ₃ N (Pm-3m)	Pm-3m	~1*10 ⁻⁶	5,14
Antiperovskites	Spacegroup	Conductivity (S cm ⁻¹)	Reference
Li ₃ OX (X=Cl, Br)	Pm-3m	1*10 ⁻⁸ - 1*10 ⁻⁵	15

References Appendix 4

- (1) De Klerk, N. J. J.; Van Der Maas, E.; Wagemaker, M. Analysis of Diffusion in Solid-State Electrolytes through MD Simulations, Improvement of the Li-Ion Conductivity in β -Li₃PS₄ as an Example. *ACS Appl. Energy Mater.* **2018**, *1* (7), 3230–3242.
- (2) Park, S.; Chaudhary, R.; Han, S. A.; Qutaish, H.; Moon, J.; Park, M.-S.; Kim, J. H. Ionic Conductivity and Mechanical Properties of the Solid Electrolyte Interphase in Lithium Metal Batteries. *ENERGY Mater.* **2023**, *3* (1).
- (3) Landgraf, V.; Tu, M.; Cheng, Z.; Vasileiadis, A.; Wagemaker, M.; Famprikis, T. Compositional Flexibility in Irreducible Antifluorite Electrolytes for Next-Generation Battery Anodes. *Journal Materials Chemistry A* **2025**.
- (4) Poulsen, F. W. Ionic Conductivity of Solid Lithium Iodide and Its Monohydrate. *Solid State Ionics* **1981**, *2* (1), 53–57.
- (5) Landgraf, V.; Tu, M.; Zhao, W.; Lavrinenko, A.; Cheng, Z.; Canals, J.; de Leeuw, J.; Ganapathy, S.; Vasileiadis, A.; Wagemaker, M. Disorder-Mediated Ionic Conductivity in Irreducible Solid Electrolytes. **2024**.
- (6) Yang, W.; Tang, S.; Yang, X.; Zheng, X.; Wu, Y.; Zheng, C.; Chen, G.; Gong, Z.; Yang, Y. Li₂Se: A High Ionic Conductivity Interface to Inhibit the Growth of Lithium Dendrites in Garnet Solid Electrolytes. *ACS Appl. Mater. Interfaces* **2022**, *14* (45), 50710–50717.
- (7) Nazri, G. Preparation, Characterization and Conductivity of Li₃N, Li₃P and Li₃As. *MRS Online Proc. Libr.* **1988**, *135*, 117.
- (8) Li, W.; Wu, G.; Araújo, C. M.; Scheicher, R. H.; Blomqvist, A.; Ahuja, R.; Xiong, Z.; Feng, Y.; Chen, P. Li⁺ Ion Conductivity and Diffusion Mechanism in α -Li₃N and β -Li₃N. *Energy Environ. Sci.* **2010**, *3* (10), 1524–1530.
- (9) Szczuka, C.; Karasulu, B.; Groh, M. F.; Sayed, F. N.; Sherman, T. J.; Bocarsly, J. D.; Vema, S.; Menkin, S.; Emge, S. P.; Morris, A. J.; Grey, C. P. Forced Disorder in the Solid Solution Li₃P–Li₂S: A New Class of Fully Reduced Solid Electrolytes for Lithium Metal Anodes. *J. Am. Chem. Soc.* **2022**, *144* (36), 16350–16365.
- (10) Landgraf, V.; Famprikis, T.; Leeuw, J. De; Bannenberg, L. J.; Ganapathy, S. Li₅NCl₂: A Fully-Reduced, Highly-Disordered Nitride-Halide Electrolyte for Solid-State Batteries with Lithium-Metal Anodes. *ACS Applied Energy Materials*, **2023**, *6*(3), 1661-1672.
- (11) Li, W.; Li, M.; Chien, P.-H.; Wang, S.; Yu, C.; King, G.; Hu, Y.; Xiao, Q.; Shakouri, M.; Feng, R. Lithium-Compatible and Air-Stable Vacancy-Rich Li₉N₂Cl₃ for High-Areal Capacity, Long-Cycling All-Solid-State Lithium Metal Batteries. *Sci. Adv.* **2023**, *9* (42), eadh4626.
- (12) Yu, P.; Zhang, H.; Hussain, F.; Luo, J.; Tang, W.; Lei, J.; Gao, L.; Butenko, D.; Wang, C.; Zhu, J.; Yin, W.; Zhang, H.; Han, S.; Zou, R.; Chen, W.; Zhao, Y.; Xia, W.; Sun, X. Lithium Metal-Compatible Antifluorite Electrolytes for Solid-State Batteries. *J. Am. Chem. Soc.* **2024**.
- (13) Wang, Z.; Xia, J.; Ji, X.; Liu, Y.; Zhang, J.; He, X.; Zhang, W.; Wan, H.; Wang, C. Lithium Anode Interlayer Design for All-Solid-State Lithium-Metal Batteries. *Nat. Energy* **2024**, *9* (3), 251–262.
- (14) Miara, L. J.; Suzuki, N.; Richards, W. D.; Wang, Y.; Kim, J. C.; Ceder, G. Li-Ion Conductivity in Li₉S₃N. *J. Mater. Chem. A* **2015**, *3* (40), 20338–20344.
- (15) Zheng, J.; Perry, B.; Wu, Y. Antiperovskite Superionic Conductors: A Critical Review. *ACS Mater. Au* **2021**, *1* (2), 92–106.

Summary

Solid-state batteries currently receive ample attention due to their potential to outperform lithium-ion batteries in terms of energy density when featuring next-generation anodes such as Li metal or silicon. One key remaining challenge is identifying solid electrolytes that combine high ionic conductivity with stability in contact with the highly reducing potentials of next-generation anodes. An interesting subset of phases that are intrinsically stable even at the ultralow potential of Li metal are fully-reduced phases. Fully-reduced (lithium-)phases have lithium as their only cation and all anions in their lowest-permitted oxidation state and are thus irreducible. Many fully-reduced phases are known, but before the commencement of this thesis none (with the exception of the Li_3N phase) featured a Li-ion conductivity $> 0.01 \text{ mS cm}^{-1}$. The main findings in this thesis spread across chapters 2-5 may be broadly split into four categories: (1) Discovery of new highly-conducting fully-reduced antifluorite phases (2) Optimizing lithium diffusion in fully-reduced antifluorite phases (3) electrochemical stability windows of the newly-discovered phases and (4) discussion of potential applications for these materials. The findings in the above four categories will be further summarized below.

Discovery of new fully-reduced antifluorite phases: Combining experiments and ab initio DFT calculations we discovered new irreducible antifluorite-like electrolytes. These new irreducible solid electrolytes are all characterized by two or more anions sharing the anion site in the antifluorite phase in a disorderly manner and were obtained by mechanochemical synthesis. We discovered a solid solution of antifluorite-like phases on the $\text{Li}_2\text{S-Li}_3\text{N}$ tie line ($\text{Li}_{2+x}\text{S}_{1-x}\text{N}_x$, Chapter 3) and on the $\text{LiCl-Li}_3\text{N}$ tieline ($\text{Li}_{1+2x}\text{Cl}_{1-x}\text{N}_x$, Chapter 4) with conductivities almost on a par with that of Li_3N ($\sim 0.5 \text{ mS cm}^{-1}$). Further we found that antifluorite-like phases with four anions (Cl^- , Br^- , S^{2-} , N^{3-}) sharing the anion site may be synthesized (Chapter 4) indicating the high compositional flexibility of fully-reduced antifluorite-like phases that will allow for property optimizations of these materials. In Chapter 5 we discovered that P^{3-} and N^{3-} can also share the anion sites in irreducible antifluorite-like phases. The $\text{Li}_{2.6}\text{S}_{0.4}\text{P}_{0.35}\text{N}_{0.25}$ nitridophosphide phase we synthesized in chapter 5 is the best-conducting fully reduced solid electrolyte known today.

Lithium diffusion in fully-reduced antifluorite phases : Our DFT simulations on the newly-discovered antifluorite-like phases (Chapters 2,3,4 and 5) show that lithium diffusion is promoted by ion jumps between tetrahedral sites and ion jumps between octahedral and tetrahedral lithium sites. The new irreducible phases we discovered all feature several different jump-types due to the disordering of the anions. Thus a wide distribution of hop activation energies exists in these phases, —with a distinct hop activation energy for each jump type. This range of hop activation energies can span from $\sim 0.2 \text{ eV}$ to $\sim 0.6 \text{ eV}$. In Chapter 2 we found that this wide distribution of hop activation energies could explain the different activation energies for Li diffusion obtained from nuclear magnetic resonance line narrowing measurements ($\sim 0.25 \text{ eV}$) and electrochemical impedance spectroscopy (0.47 eV); while local fast diffusion may exist between sites connected by low hop activation energies, the macroscopic conductivity probed by electrochemical impedance spectroscopy seems to be limited by higher hop activation energies. In Chapter 3 a comparison between two very similar phases,— a disordered antifluorite-like phase with stoichiometry of $\text{Li}_9\text{S}_3\text{N}$ and an almost equivalent phase but with an ordered S/N arrangement — demonstrates the mechanism of the diffusion-boosting effect that disordering may entail: while the ordered $\text{Li}_9\text{S}_3\text{N}$ phase only features 6 discreet jump types with six associated hop activation energies the disordering of N/S in the disordered $\text{Li}_9\text{S}_3\text{N}$ phase introduced a wide distribution of jump types and hop activation energies promoting the existence of percolation paths with lower energy thresholds. Further

the analysis of lithium diffusion in all newly-discovered irreducible antifluorite-like phases (Chapters 2, 3, 4, and 5) indicates that N substitution, be it N_S , N_{Cl} , N_P , N_{Br} , increases Li diffusivity through the steric diffusion bottlenecks; the small anion radius of N^{3-} (1.49 Å) compared to Cl^- , S^{2-} , P^{3-} , Br^- (1.81 Å- 1.96 Å) increases the void space in these steric bottlenecks facilitating Li diffusion.

Electrochemical stability windows of the discovered phases: All newly-discovered phases investigated in this study are electrochemically stable against Li metal (that is 0 V vs Li). Their oxidation limits vary but are all below 2 V (vs Li). The investigations in Chapter 3 indicate that the oxidation limit correlates with the (meta)stability of phases: the more metastable the phase the lower the oxidation limit. Interestingly however, this anticorrelation of oxidation limit and metastability is only valid for similar phases for example within the $Li_{2+x}S_{1-x}N_x$ and the $Li_{1+2x}Cl_{1-x}N_x$ solid solutions. When comparing different structures this trend does not hold potentially because the electrochemical decomposition mechanism may be different; for example the antifluorite-like $Li_{2+x}S_{1-x}N_x$ phases are metastable but have larger oxidation limits than hexagonal Li_3N which is one of their thermodynamically stable decomposition products.

Potential applications of the newly discovered fully-reduced antifluorite-like phases: Due to their modest oxidation limits the likeliest application of the newly-discovered fully-reduced antifluorite-like phases will be as anolytes in bi- or multilayer separators. Compared to the long-known irreducible Li_3N phase, the newly discovered irreducible antifluorite electrolytes have several projected advantages. Mechanical and microstructural properties of anolytes play a key role, for instance in dendrite formation with metal anodes; the large compositional flexibility of irreducible antifluorite phases shown in chapter 3 may enable tunability of these properties. Additionally, chemical compatibilities of anolytes with the paired catholytes also need to be considered. It was shown in chapter 2 that the antifluorite-like $Li_{1.66}Cl_{0.66}N_{0.33}$ phase is chemically less reactive with potential catholytes than Li_3N . The antifluorite-like $Li_{2+x}S_{1-x}N_x$ phases developed in chapter 3 have stability windows that match the operation window of Si (0.01 V-1.1 V vs Li) and may hence be a better fit as anolytes against Si electrodes than Li_3N which oxidizes beyond 0.8 V (vs Li). Finally, Li_3N has reasonably high conductivity of $\sim 0.5 \text{ mS cm}^{-1}$ but exceeding this conductivity could be beneficial especially if anolytes are intended to be used in composite anodes; the large compositional flexibility of irreducible antifluorite phases discovered in this thesis enables the design of phases that exceed the conductivity of Li_3N such as the antifluorite-like nitridophosphide phases developed in chapter 5. All of the above highlights the importance of developing and understanding new irreducible solid electrolytes to which this thesis hopes to have significantly contributed.

While much could be achieved in the course of this thesis, much work in the field of fully-reduced antifluorite electrolytes remains to be done. Firstly, the integration of these electrolytes in full cells needs to be further explored. Secondly, a large phase space of fully-reduced antifluorite-like phases remains to be explored including potentially non-lithium phases based on sodium, potassium or other cations. New fully-reduced phases can be systematically discovered by exploring the phase diagrams of fully-reduced precursors which are typically different salts of the same metal; combining fully-reduced precursors of the same metal always results in fully-reduced reaction products. *For example*, new fully-reduced magnesium (Mg) - electrolytes could be discovered by exploring the tieline between $MgCl_2$ and MgS or the phase diagram spanned by $MgCl_2$, MgS and Mg_3N_2 .

The author of this thesis wishes anyone deciding to continue investigating fully-reduced phases exciting scientific endeavors.

Samenvatting

Vastestofbatterijen krijgen momenteel veel aandacht vanwege hun potentieel om lithium-ionbatterijen te overtreffen qua energiedichtheid, met name wanneer ze worden gecombineerd met next-gen anodes, zoals lithium-metaal of silicium. Een belangrijke resterende uitdaging is het identificeren van vaste elektrolyten die een hoge ionische geleidbaarheid combineren met stabiliteit bij contact met de sterk reducerende potentiaal van next-gen anodes. Een interessante subset van fasen die intrinsiek stabiel zijn, zelfs bij de ultralage potentiaal van lithium-metaal, zijn volledig-gereduceerde fasen. Volledig-gereduceerde (lithium-)fasen hebben lithium als hun enige kation en alle anionen in hun laagst toegestane oxidatietoestand en zijn dus niet verder te reduceren. Veel volledig-gereduceerde fasen zijn bekend, maar vóór aanvang van dit proefschrift had geen enkele (met uitzondering van de Li₃N-fase) een Li-iongeleiding $> 0,01 \text{ mS cm}^{-1}$. De belangrijkste bevindingen in dit proefschrift, verspreid over hoofdstukken 2-5, kunnen grofweg in vier categorieën worden verdeeld: (1) Ontdekking van nieuwe hooggeleidende volledig-gereduceerde antifuorietfasen. (2) Optimalisatie van lithiumdiffusie in volledig-gereduceerde antifuorietfasen. (3) Elektrochemische stabiliteitsvensters van de nieuw ontdekte fasen. (4) Discussie over potentiële toepassingen van deze materialen. De bevindingen in de bovengenoemde vier categorieën worden hieronder verder samengevat.

Ontdekking van nieuwe volledig-gereduceerde antifuorietfasen: Door experimenten en ab initio DFT-berekeningen te combineren, hebben we talrijke nieuwe niet-reduceerbare elektrolyten met een antifuoriet-achtige structuur ontdekt. Deze nieuwe niet-reduceerbare vaste elektrolyten worden gekarakteriseerd door twee of meer anionen die op een wanordelijke manier de anionpositie in de antifuorietfase delen en werden verkregen via mechanochemische synthese. We ontdekten een vaste oplossing van antifuoriet-achtige fasen op de Li₂S-Li₃N-bindlijn (Li_{2+x}S_{1-x}N_x, Hoofdstuk 3) en op de LiCl-Li₃N-bindlijn (Li_{1+2x}Cl_{1-x}N_x, Hoofdstuk 4) met geleidbaarheden bijna vergelijkbaar met die van Li₃N ($\sim 0,5 \text{ mS cm}^{-1}$). Verder vonden we dat antifuoriet-achtige fasen met vier anionen (Cl⁻, Br⁻, S²⁻, N³⁻) die de anionpositie delen, kunnen worden gesynthetiseerd (Hoofdstuk 4), wat wijst op de hoge samenstellingsflexibiliteit van volledig-gereduceerde antifuoriet-achtige fasen. Dit maakt optimalisaties van de materiaaleigenschappen mogelijk. In Hoofdstuk 5 ontdekten we dat ook P³⁻ en N³⁻ de anionposities kunnen delen in niet-reduceerbare antifuoriet-achtige fasen. De in Hoofdstuk 5 gesynthetiseerde Li_{2,6}S_{0,4}P_{0,35}N_{0,25}-nitridofosfidefase is de best geleidende volledig-gereduceerde vaste elektrolyt die tot nu toe bekend is.

Lithiumdiffusie in volledig-gereduceerde antifuorietfasen: Onze DFT-simulaties van de nieuw ontdekte antifuoriet-achtige fasen (Hoofdstukken 2, 3, 4 en 5) tonen aan dat lithiumdiffusie wordt bevorderd door ionensprongen tussen tetraëdrische en octaëdrische lithiumposities. De nieuw ontdekte niet-reduceerbare fasen bevatten allemaal verschillende sprongtypen dankzij de wanordelijke verdeling van de anionen. Dit leidt tot een breed scala aan activeringsenergieën voor de sprongen, variërend van $\sim 0,2 \text{ eV}$ tot $\sim 0,6 \text{ eV}$. In Hoofdstuk 2 bleek dat deze spreiding in activeringsenergieën het verschil kan verklaren tussen de activeringsenergieën voor Li-diffusie verkregen uit NMR-metingen ($\sim 0,25 \text{ eV}$) en elektrochemische impedantiespectroscopie ($0,47 \text{ eV}$). In Hoofdstuk 3 wordt aangetoond dat wanorde de diffusie kan bevorderen: terwijl de geordende Li₉S₃N-fase slechts zes discrete sprongtypen heeft, introduceert de wanorde van S/N in de ongeordende Li₉S₃N-fase een breed scala aan sprongtypen en lagere energiedrempels voor percolatiepaden. Substitutie met N, zoals N_S, N_{Cl}, N_P en N_{Br}, vergroot

bovendien de lithiumdiffusie door de sterische bottlenecks te verminderen, dankzij de kleine anionradius van N^{3-} (1,49 Å) vergeleken met Cl^{-} , S^{2-} , P^{3-} en Br^{-} (1,81-1,96 Å).

Elektrochemische stabiliteitsvensters van de ontdekte fasen: Alle nieuw ontdekte fasen die in dit onderzoek zijn onderzocht, zijn elektrochemisch stabiel tegen lithium-metaal (0 V vs. Li). Hun oxidatiegrenzen variëren, maar liggen allemaal onder 2 V (vs. Li). In Hoofdstuk 3 bleek dat de oxidatiegrens correleert met de (meta)stabiliteit van fasen: hoe metastabieler de fase, hoe lager de oxidatiegrens. Dit patroon geldt echter alleen binnen vergelijkbare structuren.

Potentiële toepassingen van volledig-gereduceerde antifuorietfasen: Vanwege hun beperkte oxidatiegrenzen zijn de nieuw ontdekte fasen het meest geschikt als anolieten in tweelags of meerlaagse scheidingslagen. De grote samenstellingsflexibiliteit van antifuorietfasen kan leiden tot betere mechanische eigenschappen en chemische compatibiliteit met catholieten. In Hoofdstuk 5 is aangetoond dat bepaalde antifuoriet-achtige fasen hogere geleidbaarheid hebben dan Li_3N ($\sim 0,5 \text{ mS cm}^{-1}$), wat belangrijk kan zijn in composietanodes.

Dit proefschrift heeft bijgedragen aan de ontwikkeling van nieuwe niet-reduceerbare vaste elektrolyten en biedt een basis voor verdere onderzoek naar volledig-gereduceerde antifuorietfasen, inclusief mogelijke toepassingen met andere kationen zoals natrium of kalium.

Acknowledgments

First and foremost, I am deeply grateful to Marnix for his academic guidance and for giving me the opportunity to complete my PhD in his group at the TU Delft. His support has been foundational to my work. Special thanks also go to Theo for his supervision and for consistently asking the important questions, I might have overlooked. Thanks Theo!

I would like to acknowledge the technical staff in the SEE group: Frans, Katarina, Jouke, Nirmal, and Dan. Your expertise and assistance have been crucial.

I'd like to thank Piero and Jerry for an instructive and enjoyable time during my visit at the University of Houston.

A warm thank you to Zhu and Alexandros for your scientific insights and support whenever it was needed. Zhu, in addition to your scientific input I am grateful for your master classes on the tennis court.

I'd also like to thank Mengfu, Anastasiia, Wenxuan and Jef for excellent collaborations. Working alongside you all has been a pleasure and an enriching experience. To Mengfu, Xavier, Peter, Biffo, Shengnan and Wenxuan—it's great to share an office with you!

A big thank you to Pier, Hanan, Biffo, Pranav, Hao, Chaofan, Mark, Remco, Qidi, Chenglong, Tammo, Albert, Pedro, Lars, Xuehang, Swapna, Lucas & Luca, Rijk, Ajay, Robert, Meera, Hao, Joris, Ming, and Zhaolong. You have all been wonderful colleagues and friends over the years, and I am grateful for our time together.

To Apoorva, thank you for your unwavering support and for being by my side throughout this four-year journey.

Lastly, I am incredibly thankful to my family—my sisters, Liora and Zoe, and my parents Annette and Martin—for their encouragement and constant support.

My time at the TU Delft has been both highly instructive and highly enjoyable, and I am grateful to everyone who has been a part of it.

Curriculum Vitae Victor Landgraf

Victor Ruben Landgraf was born in Brussels in 1997. After completing high school at the European School Brussels I, Victor pursued undergraduate and postgraduate studies in Chemistry at Imperial College London and ETH Zurich. Early on in his chemistry studies Victor developed a keen interest for electrochemistry. He was intrigued by the interplay of chemistry and electric currents and by the relevance of electrochemical applications (batteries, fuel cells, electrolyzers) to circumvent a climate catastrophe. At ETH Zurich Victor received extensive training in electrochemistry and he completed his thesis in Prof Petr Novak's lab on inverse opal carbon electrodes for Li-S batteries. Following the completion of his MSc degree, Victor joined the Fraunhofer Institute for Interfacial Engineering and Biotechnology to work on electrochemical CO₂ reduction. Soon after, Victor joined the Storage of Electrochemical Energy lab of Prof Marnix Wagemaker at the Technological University Delft to complete his PhD co-supervised by Dr Theodosios Famprikis. At the TU Delft, Victor combined theoretical calculations and experimental work to explore new phases that would be at once thermodynamically stable against highly reactive Li metal and highly ion conductive. While completing his thesis, Victor spent 6 months at the cutting-edge battery labs of Tesla at the Gigafactory in Berlin and 1 month at the University of Houston in Prof Pieremanuele Canepa's lab to further-develop a kinetic Monte Carlo python package in conjunction with Prof Zeyu Deng from the National University of Singapore. After completing his doctoral degree, Victor joined the European Patent Office as an examiner for Batteries and Fuel Cells.